



RETURNING MATERIALS:
Place in book drop to
remove this checkout from
your record. FINES will
be charged if book is
returned after the date
stamped below.

--	--	--

**INTERACTION OF ELECTROMAGNETIC WAVES WITH
HETEROGENEOUS BODIES OF
ARBITRARY SHAPE AND PARAMETERS**

by

Huei Wang

A DISSERTATION

Submitted to
Michigan State University
in partial fulfillment of the requirements
for the degree of

DOCTOR OF PHILOSOPHY

Department of Electrical Engineering and
Systems Science

1987

ABSTRACT

INTERACTION OF ELECTROMAGNETIC WAVES WITH HETEROGENEOUS BODIES OF ARBITRARY SHAPE AND PARAMETERS

By

Huei Wang

This thesis consists of two parts: The first part deals with the quantification of interaction of electromagnetic fields with finite heterogeneous bodies, and the second part presents an application of electromagnetic waves for detecting a small movement of a biological body behind a barrier.

In the study on the quantification of interaction of electromagnetic fields with finite non-magnetic lossy bodies, some new numerical methods have been developed. These new methods improve the numerical accuracy of the existing tensor integral equation method. The induced electric field of electric mode which is excited by the symmetrical part of incident electric field can be solved accurately from the tensor electric field integral equation with the method of moment and pulse basis expansion. However, the induced electric field of the magnetic mode excited by the antisymmetrical part of incident electric field can not be determined accurately by the same method. The solution of magnetic mode can be improved by using an iterative loop-EMF method which is designed to calculate the induced electric field of magnetic mode by the incident magnetic field. Another alternative is to introduce an equivalent magnetic current to compensate for the discontinuity of the tangential component of electric field

at the boundary created by using the pulse-basis expansion.

The EM fields with finite lossy magnetic bodies has also been investigated in this research. A set of coupled tensor integral equations has been derived to solve for the induced EM field in a finite heterogeneous body which is irradiated by an incident EM field. This set of equations can be decoupled into a separate tensor electric field integral equation (EFIE) and a tensor magnetic integral equation (MFIE). Numerical solutions of the coupled integral equations and decoupled EFIE are compared. The procedures for calculating numerical solutions of these integral equations are also included.

In the study of an application of electromagnetic waves for detecting a small movement of a biological body behind a barrier, a series of experiments were conducted to measure the breathing and heart signals of a human subject behind a thick layer of bricks with microwave life detection systems. A theory was developed to predict the transmission of a non-uniform plane wave passing through a wall. Experimental results on the detection of breathing and heart signals of human subjects behind brick walls of various thicknesses are presented. The basic principle of the microwave life-detection system is also included for completeness.

To My Family

ACKNOWLEDGMENTS

I offer my most grateful thanks to many persons who helped me on this thesis. Special thanks are extended to Dr. Kun-Mu Chen for his sincere guidance and financial support during my graduate study, under whose supervision this research was conducted.

Thanks are extended to the members of my guidance committee, Dr. Dennis P. Nyquist, Dr. Hassan Khalil and Dr. Byron Drachman for their comments and suggestions.

Thanks go to Mr. Y. Q. Liang for his beneficial discussions in the research work, also to Dr. D. Misra and Dr. H. R. Chuang for their guidance and help in conducting experiments.

I sincerely thank my family members for their encouragement, especially my wife Yun, whose patience and understanding are truly appreciated.

Finally, I owe many thanks to my departed father.

Table of Contents

LIST OF TABLES	vi
LIST OF FIGURES	vii
I. INTRODUCTION	1
II. NEW METHODS FOR QUANTIFICATION OF INDUCED EM FIELDS IN FINITE, NON-MAGNETIC AND LOSSY BODIES	6
2.1 Tensor Electric Field Integral Equation (Tensor EFIE)	6
2.2 The Limitation of the Existing Tensor Integral Equation Method	12
2.3 Iterative Loop-EMF Method	16
2.4 Equivalent Magnetic Current Compensation Method	21
2.5 Numerical Comparison between the New Methods and Existing Method	28
III. INTERACTION OF EM FIELDS WITH FINITE, HETEROGENEOUS, DIELECTRIC, MAGNETIC AND LOSSY BODIES	45
3.1 Coupled Tensor Integral Equations	46
3.2 Decoupled Electric Field Integral Equation (EFIE) and Magnetic Field Integral Equation (MFIE)	52
3.3 Coupled and Decoupled Integral Equations in Terms of Free Space Scalar Green's Function	58
3.4 Numerical Solutions of Various Integral Equations with Pulse- Basis Expansion and Point-matching	67
3.5 Discussions	79
IV. PLANE WAVE SPECTRUM ANALYSIS OF A NONUNIFORM PLANE WAVE PASSING THROUGH A LAYER OF LOSSY MATERIAL	128
4.1 Plane Wave Spectrum Analysis	129

V.

AF

CO

BID

4.2 Predictions of Field Distributions for a Nonuniform Plane Wave Passing through a Layer of Lossy Material	135
4.3 Brief Description of Microwave Life Detection Systems	152
4.4 Experimental Results of Detecting Movements of a Human Body behind a Wall by Using Microwave Life Detection Systems	155
V. SUMMARY	172
APPENDICES	175
COMPUTER PROGRAMS	186
BIBLIOGRAPHY	208

3.1

3.1

List of Tables

3.1	Summary of agreement and convergence properties for the coupled tensor IE and tensor EFIE (I)	123
3.1a	Summary of agreement and convergence properties for the coupled tensor IE and tensor EFIE (II)	124

List of Figures

2.1	An arbitrarily shaped non-magnetic lossy body in free space illuminated by an incident plane wave.	8
2.2	Electric mode distribution of the x- component of the induced electric fields in the body based on 216-cell division and 512-cell division.	14
2.3	Magnetic mode distribution of the x- component of the induced electric fields in the body based on 216-cell division and 512-cell division.	15
2.4	A single layer of non-magnetic lossy body regarded as an impedance network system with N loops.	18
2.5	Illustration of the equivalent surface charge and the equivalent magnetic current created by the discontinuity of the electric field between neighboring cells.	24
2.6	A homogeneous rectangular biological model with dimensions 6x6x1 cm illuminated by an EM wave at end-on incidence.	26
2.7	Conventional EFIE solutions based on 36-cell division. (electric mode, f = 100 MHz)	31
2.8	Conventional EFIE solutions based on 288-cell division. (electric mode, f = 100 MHz)	31
2.9	Conventional EFIE solutions based on 36-cell division. (magnetic mode, f = 100 MHz)	32
2.10	Conventional EFIE solutions based on 288-cell division. (magnetic mode, f = 100 MHz)	32
2.11	Iterative loop-EMF solutions based on 36-cell division. (magnetic mode, f = 100 MHz)	33
2.12	Equivalent magnetic current method solutions based on 36-cell division. (magnetic mode, f = 100 MHz)	33
2.13	Conventional EFIE solutions based on 36-cell division. (magnetic mode, f = 300 MHz)	35
2.14	Conventional EFIE solutions based on 288-cell division. (magnetic mode, f = 300 MHz)	35

2.15	Iterative loop-EMF solutions based on 36-cell division. (magnetic mode, $f = 300$ MHz)	36
2.16	Equivalent magnetic current method solutions based on 36-cell division. (magnetic mode, $f = 300$ MHz)	36
2.17	Conventional EFIE solutions based on 36-cell division. (magnetic mode, $f = 500$ MHz)	37
2.18	Conventional EFIE solutions based on 288-cell division. (magnetic mode, $f = 500$ MHz)	37
2.19	Iterative loop-EMF solutions based on 36-cell division. (magnetic mode, $f = 500$ MHz)	38
2.20	Equivalent magnetic current method solutions based on 36-cell division. (magnetic mode, $f = 500$ MHz)	38
2.21	Conventional EFIE solutions based on 36-cell division. (magnetic mode, $f = 700$ MHz)	39
2.22	Conventional EFIE solutions based on 288-cell division. (magnetic mode, $f = 700$ MHz)	39
2.23	Iterative loop-EMF solutions based on 36-cell division. (magnetic mode, $f = 700$ MHz)	40
2.24	Equivalent magnetic current method solutions based on 36-cell division. (magnetic mode, $f = 700$ MHz)	40
2.25	A heterogeneous body of dimensions 6x6x1 cm with the parameters specified in the shaded and unshaded regions.	41
2.26	Iterative loop-EMF solutions in the heterogeneous body with the impedances determined by the complex conductivity of each cell.	43
2.27	Iterative loop-EMF solutions in the heterogeneous body with the impedances determined by the average of the complex conductivities between two adjacent cells.	44
3.1	An arbitrarily shaped magnetic lossy body in free space illuminated by an incident EM wave.	47
3.2	Illustration of the equivalent sources induced by the incident EM wave in the volume region v and on the enclosing surface s	59
3.3	A symmetric body partitioned into symmetrical octants, denoted by Roman numerals. The origin of the coordinate system is located at the center of the body.	77
3.4	A homogeneous cubic body of dimensions 6x6x6 cm illuminated by an	

	incident plane EM wave.	80
3.5	Solutions for the symmetric mode of induced electric field obtained from the coupled tensor integral equations based on 216-cell division in the magnetic body. (x- component of electric field)	82
3.6	Solutions for the symmetric mode of induced electric field obtained from the coupled tensor integral equations based on 216-cell division in the non-magnetic body. (x- component of electric field)	83
3.7	Solutions for the antisymmetric mode of induced electric field obtained from the coupled tensor integral equations based on 216-cell division in the magnetic body. (x- component of electric field)	85
3.8	Solutions for the antisymmetric mode of induced electric field obtained from the coupled tensor integral equations based on 216-cell division in the magnetic body. (z- component of electric field)	86
3.9	Solutions for the antisymmetric mode of induced electric field obtained from the coupled tensor integral equations based on 216-cell division in the non-magnetic body. (x- component of electric field)	87
3.10	Solutions for the antisymmetric mode of induced electric field obtained from the coupled tensor integral equations based on 216-cell division in the non-magnetic body. (z- component of electric field)	88
3.11	Solutions for the symmetric mode of induced electric field obtained from the tensor EFIE based on 216-cell division in the magnetic body. (x- component of electric field)	89
3.12	Solutions for the antisymmetric mode of induced electric field obtained from the tensor EFIE based on 216-cell division in the magnetic body. (x- component of electric field)	90
3.13	Solutions for the antisymmetric mode of induced electric field obtained from the tensor EFIE based on 216-cell division in the magnetic body. (z- component of electric field)	91
3.14	Solutions for the antisymmetric mode of induced electric field obtained from the coupled tensor integral equations based on	

	512-cell division in the magnetic body. (x- component of electric field)	93
3.15	Solutions for the antisymmetric mode of induced electric field obtained from the coupled tensor integral equations based on 512-cell division in the magnetic body. (z- component of electric field)	94
3.16	Solutions for the antisymmetric mode of induced electric field obtained from the coupled tensor integral equations based on 1000-cell division in the magnetic body. (x- component of electric field)	95
3.17	Solutions for the antisymmetric mode of induced electric field obtained from the coupled tensor integral equations based on 1000-cell division in the magnetic body. (z- component of electric field)	97
3.18	Solutions for the antisymmetric mode of induced electric field obtained from the tensor EFIE based on 512-cell division in the magnetic body. (x- component of electric field)	99
3.19	Solutions for the antisymmetric mode of induced electric field obtained from the tensor EFIE based on 512-cell division in the magnetic body. (z- component of electric field)	100
3.20	Solutions for the antisymmetric mode of induced electric field obtained from the tensor EFIE based on 1000-cell division in the magnetic body. (x- component of electric field)	101
3.21	Solutions for the antisymmetric mode of induced electric field obtained from the tensor EFIE based on 1000-cell division in the magnetic body. (z- component of electric field)	103
3.22	A homogeneous cubic body of dimensions 12x12x6 cm illuminated by an incident plane EM wave.	106
3.23	Solutions for the symmetric mode of induced electric field obtained from the coupled tensor integral equations in the rectangular magnetic body. (x- component of electric field)	107
3.24	Solutions for the symmetric mode of induced electric field obtained from the tensor EFIE in the rectangular magnetic body. (x- component of electric field)	108

3.25	Solutions for the antisymmetric mode of induced electric field obtained from the coupled tensor integral equations in the rectangular magnetic body. (x- component of electric field)	109
3.26	Solutions for the antisymmetric mode of induced electric field obtained from the coupled tensor integral equations in the rectangular magnetic body. (z- component of electric field)	110
3.27	Solutions for the antisymmetric mode of induced electric field obtained from the tensor EFIE in the rectangular magnetic body. (x- component of electric field)	111
3.28	Solutions for the antisymmetric mode of induced electric field obtained from the tensor EFIE in the rectangular magnetic body. (z- component of electric field)	112
3.29	Solutions for the antisymmetric mode of induced electric field obtained from the tensor EFIE in the rectangular non-magnetic body. (x- component of electric field)	113
3.30	Solutions for the antisymmetric mode of induced electric field obtained from the tensor EFIE in the rectangular non-magnetic body. (z- component of electric field)	114
3.31	A heterogeneous cubic body of dimensions 6x6x1 cm with different parameters specified in the shaded and unshaded regions.	116
3.32	Solutions for the antisymmetric mode of induced EM field obtained from the coupled tensor integral equations in the heterogeneous body.	117
3.33	Solutions for the antisymmetric mode of induced EM field obtained from the coupled tensor integral equations in the non-magnetic homogeneous body.	118
3.34	Solutions for the antisymmetric mode of induced EM field obtained from the coupled tensor integral equations based on 512 cell division in the heterogeneous body. (x- component of electric field)	120
3.35	Solutions for the antisymmetric mode of induced EM field obtained from the coupled tensor integral equations based on 512 cell division in the heterogeneous body. (z- component of electric field)	121
3.36	Solutions for the antisymmetric mode of induced EM field	

obtained from the coupled tensor integral equations based on 512 cell division in the heterogeneous body. (y- component of magnetic field)	122
4.1 An incident plane EM wave on a lossy layer of thickness d	132
4.2 Equivalent circuit for a lossy dielectric layer.	132
4.3 The front view and side view of the antenna aperture located next to the lossy layer.	136
4.4 The magnitude of the x- component of plane wave spectrum behind the barrier ($d = 0.2$ m).	139
4.5 The magnitude of the x- component of electric field distribution behind the barrier ($d = 0.2$ m) at a distance of 0.2 m.	141
4.6 The magnitude of the z- component of plane wave spectrum behind the barrier ($d = 0.2$ m).	142
4.7 The magnitude of the z- component of electric field distribution behind the barrier ($d = 0.2$ m) at a distance of 0.4 m.	143
4.8 The magnitude of the x- component of electric field distribution behind the barrier ($d = 0.2$ m) at a distance of 0.2 m.	144
4.9 The magnitude of the z- component of electric field distribution behind the barrier ($d = 0.2$ m) at a distance of 0.2 m.	145
4.10 The magnitude of the x- component of plane wave spectrum behind the barrier ($d = 0.5$ m).	146
4.11 The magnitude of the x- component of electric field distribution behind the barrier ($d = 0.5$ m) at a distance of 0.2 m.	147
4.12 The magnitude of the z- component of plane wave spectrum behind the barrier ($d = 0.5$ m).	148
4.13 The magnitude of the z- component of electric field distribution behind the barrier ($d = 0.5$ m) at a distance of 0.2 m.	149
4.14 The magnitude of the x- component of electric field distribution behind the barrier ($d = 0.5$ m) at a distance of 0.4 m.	150
4.15 The magnitude of the z- component of electric field distribution behind the barrier ($d = 0.5$ m) at a distance of 0.4 m.	151
4.16 Circuit diagram of the microwave life detection system.	154
4.17 Experimental set up for the measurement of heart and breathing signals of a human object through brick wall, using microwave life detection system.	157
4.18 Heart and breathing signals of a human subject measured through brick walls of various thicknesses using the 10 GHz life detection	

system.	158
4.19 Heart and breathing signals of a human subject measured through brick walls of various thicknesses using the 10 GHz life detection system.	159
4.20 Heart and breathing signals of a human subject measured through brick walls of various thicknesses using the 2 GHz life detection system.	160
4.21 Heart and breathing signals of a human subject measured through brick walls of various thicknesses using the 2 GHz life detection system.	161
4.22 Heart and breathing signals of a human subject measured through brick walls of various thicknesses using the 10 GHz life detection system. One layer of wet bricks severely hampered the penetration of the microwave beam.	163
4.23 Heart and breathing signals of a human subject measured through brick walls of various thicknesses using the 2 GHz life detection system. One layer of wet bricks had a considerable effect on the penetration of the microwave beam.	164
4.24 Experimental set up for the measurement of heart and breathing signals of a human object under layers of bricks, using microwave life detection system.	165
4.25 Heart and breathing signals of a human subject, lying with face-up or face-down position under 3 layers of bricks, measured by the 10 GHz life detection system.	167
4.26 Heart and breathing signals of a human subject, lying with face-up or face-down position under 4 layers of bricks, measured by the 10 GHz life detection system.	168
4.27 Heart and breathing signals of a human subject, lying with face-up or face-down position under 5 layers of bricks, measured by the 2 GHz life detection system.	169
4.28 Heart and breathing signals of a human subject, lying with face-up or face-down position under 6 layers of bricks, measured by the 2 GHz life detection system.	170
4.29 Heart and breathing signals of a human subject, lying with face-up or face-down position under 7 layers of bricks, measured by the 2 GHz life detection system.	171
A.1 Different notations of the parameters and variables in a permeable body used by Tai and this thesis when it is illuminated by a plane	

	wave.	178
A.2	Illustration of the exclusion of a small region which contains the singularity point when evaluating the principal integration.	184

i
h
u
w
m
in
fie

easy
this
and
the r
const
to ex
Dirac-
tion o

CHAPTER I

INTRODUCTION

The interaction of an electromagnetic (EM) field with a heterogeneous material body, with arbitrary electric and magnetic parameters and finite physical dimensions, is a fundamental and important research subject. This subject has received attentions of many researchers because of its relevance in medical and engineering applications. For example, the induced EM field in a human body when it is irradiated by an incident EM wave is an important piece of information in the assessment of potential health hazard, or in some medical applications such as the hyperthermia cancer therapy using EM radiation. In the field of engineering, the knowledge of interaction of EM waves with a finite body of arbitrary compositions has direct applications in the modification of radar scattering from space vehicles. This knowledge is also relevant in other electronic fields whenever a material body of a device is exposed to an EM field.

To quantify the induced EM field in an irradiated heterogeneous body is not an easy task. The mathematical complexity of three-dimension computation exacerbates this problem. A tensor electric field integral equation (EFIE) was derived by Livesay and Chen to quantify the induced fields in a non-magnetic and lossy body [1], where the method of moment (MOM) was used for the numerical calculation, the piecewise constant functions (or pulse functions) were chosen as basis functions (trial functions) to expand the components of unknown induced electric field distribution and the Dirac-Delta functions were selected as weighting functions (it is the so called collocation or point-matching testing procedure). Some researchers [26], [27] solved this

problem by an equivalent EFIE in terms of free space scalar Green's function, with the choice of some other basis and weighting functions for the method of moment. The results of the latter approach, when compared with the analytical solution of the induced electric field distribution in a homogeneous non-magnetic lossy sphere, seem to improve over the results of Livesay and Chen [1]. However, to use the pulse-basis expansion and point-matching in the method of moment is still advantageous over other choices of basis and weighting functions from the viewpoint of the simplicity in the procedures of calculation. There are some limitation of solving this EFIE with pulse-basis expansion and point-matching which have been reported [5], [6]. A reported problem [6] states that induced electric field of electric mode which is excited by symmetrical part of incident electric field can be solved accurately but the induced electric field of magnetic mode which is excited by the antisymmetrical part of incident electric field can not be determined accurately unless a large number of partition of the body is used. This thesis presents some methods, namely, the iterative loop-EMF method and the equivalent magnetic current compensation method, to improve the efficiency and accuracy of the existing method (solving tensor EFIE with pulse-basis expansion and point-matching). The results of these new methods in the frequency range of several hundred MHz are compared with the results of Livesay and Chen [1].

To study the interaction of EM waves with magnetic and lossy bodies, a set of coupled tensor integral equations [3], [14] have been derived based on the method of equivalent polarized currents to relate the induced EM fields with incident EM fields. Since the unknown induced electric and magnetic fields are coupled together in this set of equations, we need to solve them simultaneously. In order to reduce the number of unknowns, we can decouple this set of equations into a separated tensor EFIE and a separated tensor magnetic field integral equation (MFIE) in which case the electric and

magnetic field distributions can be solved separately and only one half of unknowns need to be handled in the procedure of numerical calculation. The method of moment solutions of coupled and decoupled tensor integral equations are compared and the effect of induced fields due to the magnetic material is investigated. These tensor integral equations are constructed in terms of free space dyadic Green's functions and can be transformed into integral equations in terms of free space scalar Green's functions. Similar numerical results can be obtained by solving the integral equations in terms of the scalar Green's functions.

A study of an application of electromagnetic waves for detecting a small movement of a biological body located at a distance or behind a barrier is also presented in this thesis. The so called microwave life detection systems are developed to measure the small movements due to breathing or heartbeats of a human subject at a distant away or behind a barrier. The original purpose of the systems was that Navy needed a system to indicate whether a wounded soldier on the battlefield is still alive or not. Such a system can prevent fellow soldiers from taking risks attempting to help a dead combatant. It turns out that there are many other applications. For example, this system can be used to find out whether there are people under a collapsed building after an earthquake or it can be used as an alarm system to monitor intruders into a room.

The basic principle of the systems is to illuminate the human subject with a low intensity microwave beam and then extract the body movement of the subject from the modulated back-scattered wave with a detecting system. Two different operating frequencies have been selected to construct the systems, one is 10 GHz (X-band) and the other is 2 GHz (L-band). The L-band system is specially designed for detecting small body vibrations behind a thick wall because of the better penetration ability of the EM wave of the lower frequency. Plane wave spectrum theory [17], [18] is used to analyze the nonuniform plane wave from the antenna passing through a layer of lossy

material and to predict the electric field distribution on the other side of the barrier. The predicted electric field distributions and experimental results for the detection of breathing and heart signals of a human subject behind brick wall of various thicknesses are presented.

In chapter II, a brief outline of the derivation of the tensor EFIE which can be used to quantify the induced electric field distribution in a non-magnetic body is given in the beginning and then an example is given to show the limitation of the MOM solution with pulse-basis expansion and point-matching of this equation. We introduce two new methods to improve the accuracy and efficiency of the tensor EFIE method. The iterative loop-EMF method and the equivalent magnetic current methods are discussed in sections 2.3 and 2.4, respectively. For the iterative loop-EMF method, we use the concepts of impedance networks and Faraday's law to relate the induced currents and the induced EM fields, then apply a coupled tensor integral equation to perform the iterative process. For the equivalent magnetic current compensation method, an equivalent magnetic current on each adjacent cell boundary is introduced to compensate the discontinuity of the tangential component of the induced electric field distribution which is artificially produced by the pulse-basis expansion. Discussions and numerical results are included at the end of chapter.

Chapter III discusses the interaction of EM fields with magnetic bodies. An outline of the derivation of the coupled tensor integral equations which can be used to quantify the induced EM field distribution in a magnetic body is given in section 3.1. The transformation from this set of coupled equations into a separate tensor EFIE and a separate tensor MFIE in various forms [13], [16] are presented next. These sets of integral equations in terms of the free space scalar Green's function, rather than the dyadic Green's function, can be derived from the concept of potential functions maintained by equivalent current and charge densities. The derivations are given in section

3.3. Numerical solutions of the coupled equations and decoupled equations are compared and the effects of the induced EM fields due to the magnetic material are investigated in this chapter. Both the advantages and disadvantages of each set of the integral equations are also discussed.

Chapter IV is devoted to the study of the application of electromagnetic wave for detecting a small movement of a biological body located at a distance or behind a barrier. Plane wave spectrum analysis is outlined in the beginning of chapter and followed by some numerical simulations of the predicted electric field distributions for a nonuniform plane wave passing through a layer of lossy barrier. The description of the microwave life detection systems, along with the circuit diagram and the principle of operation, is included in section 4.3. Finally, a series of experimental results for the detection of the breathing and heartbeats of a human subject behind a brick wall are presented.

CHAPTER II

NEW METHODS FOR QUANTIFICATION OF INDUCED EM FIELDS

IN

FINITE, NON-MAGNETIC AND LOSSY BODIES

Some new numerical methods for quantifying the induced EM field in a finite, heterogeneous, non-magnetic body irradiated by an incident EM field are investigated in this chapter. The numerical solutions of the tensor electric field integral equation (tensor EFIE) [1] by using conventional pulse-basis expansion with point-matching are compared with the results of the new methods. In the first two sections, we introduce the derivation of the tensor EFIE and discuss some limitation of this method. Section 2.3 and 2.4 illustrate the new methods, i.e., the iterative loop-EMF method and the equivalent magnetic current method, to improve the accuracy of the numerical solutions of the induced EM field distribution. For the iterative loop-EMF method, we use the concepts of impedance networks and Faraday's law to relate the induced currents and the induced EM fields, then apply a coupled tensor integral equation to perform the iterative process. In the equivalent magnetic current method, an equivalent magnetic current is introduced to compensate the discontinuity of the tangential component of the induced electric field distribution which is produced by the pulse-basis expansion. The comparisons and comments between various methods are presented in section 2.5.

2.1 Tensor Electric Field Integral Equation (Tensor EFIE)

A brief outline of derivation of the well known tensor EFIE is given in this section. Fig-2.1 shows a finite heterogeneous system composed of dielectric, and lossy medium with arbitrary shape, being irritated by an incident EM field \mathbf{E}^i and \mathbf{H}^i of angular frequency ω . The conductivity σ and permittivity ϵ of the medium consisting this system are both functions of location, i.e.,

$$\sigma = \sigma(\mathbf{r}) \quad (2.1.1)$$

$$\epsilon = \epsilon(\mathbf{r}) \quad (2.1.2)$$

where \mathbf{r} is the position vector in R^3 .

The incident fields $\mathbf{E}^i, \mathbf{H}^i$ must satisfy Maxwell's equations in free space:

$$\nabla \times \mathbf{E}^i(\mathbf{r}) = i\omega\mu_0 \mathbf{H}^i(\mathbf{r}) \quad (2.1.3)$$

$$\nabla \times \mathbf{H}^i(\mathbf{r}) = -i\omega\epsilon_0 \mathbf{E}^i(\mathbf{r}) \quad (2.1.4)$$

where

$$i = \sqrt{-1} , \quad (2.1.5)$$

the time harmonic factor $e^{-i\omega t}$ is assumed and ϵ_0, μ_0 are the permittivity and permeability of the free space, respectively.

The total fields \mathbf{E} and \mathbf{H} inside the system which is induced by incident fields should also satisfy Maxwell's equations:

$$\nabla \times \mathbf{E}(\mathbf{r}) = i\omega\mu_0 \mathbf{H}(\mathbf{r}) \quad (2.1.6)$$

$$\nabla \times \mathbf{H}(\mathbf{r}) = \sigma(\mathbf{r})\mathbf{E}(\mathbf{r}) - i\omega\epsilon(\mathbf{r})\mathbf{E}(\mathbf{r}) . \quad (2.1.7)$$

The scattered fields are defined as the total fields subtracted by the incident fields, that is,

$$\mathbf{E}^s(\mathbf{r}) = \mathbf{E}(\mathbf{r}) - \mathbf{E}^i(\mathbf{r}) \quad (2.1.8)$$

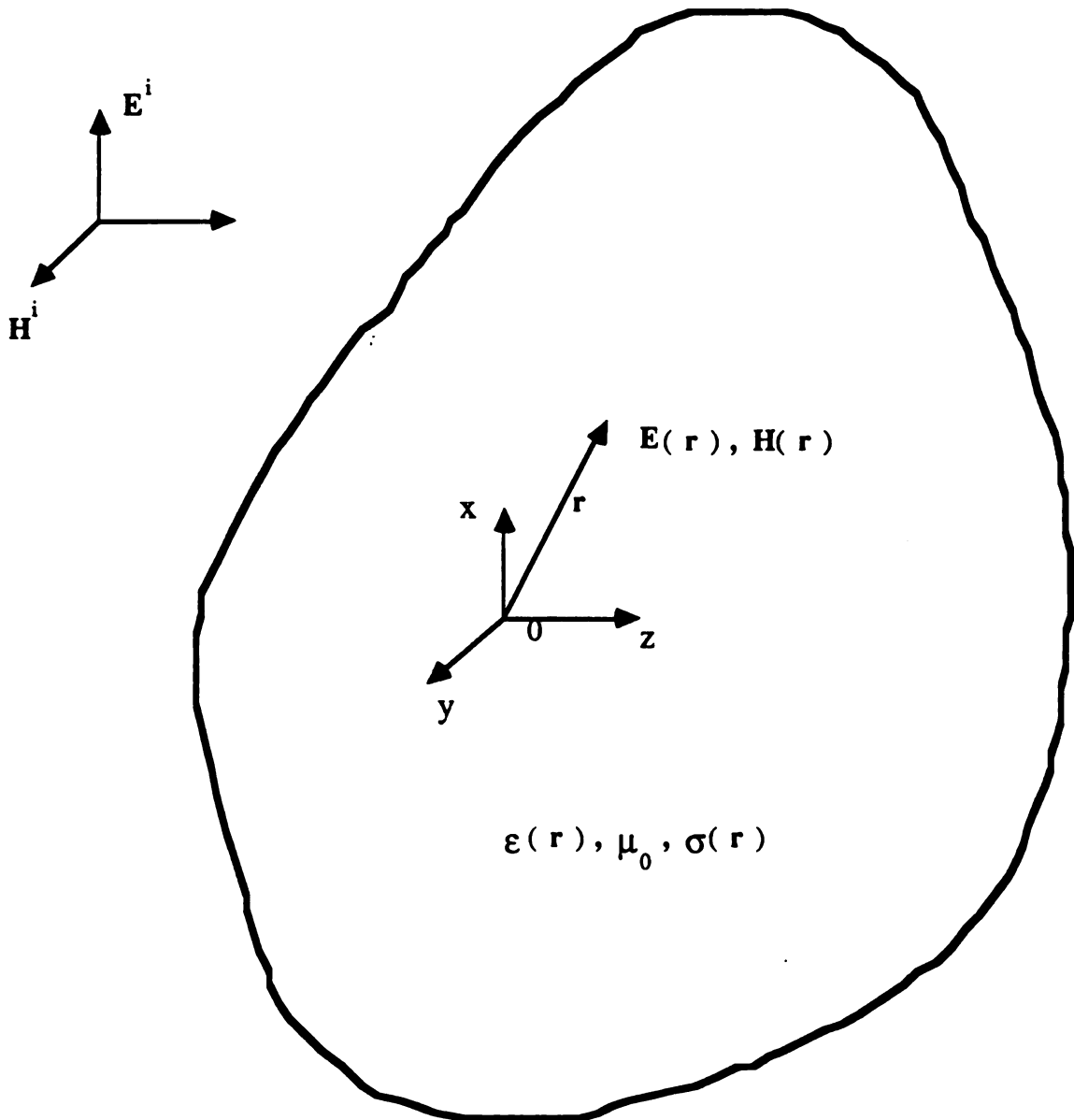


Fig-2.1 An arbitrarily shaped non-magnetic lossy body in free space illuminated by an incident plane wave.

$$\mathbf{H}^s(\mathbf{r}) = \mathbf{H}(\mathbf{r}) - \mathbf{H}^i(\mathbf{r}) . \quad (2.1.9)$$

From the set of equations (2.1.3), (2.1.4) and (2.1.6), (2.1.7), and using (2.1.8), (2.1.9), the following equations are easily obtained:

$$\nabla \times \mathbf{E}^s(\mathbf{r}) = i\omega\mu_0 \mathbf{H}^s(\mathbf{r}) \quad (2.1.10)$$

$$\nabla \times \mathbf{H}^s(\mathbf{r}) = \left\{ \sigma(\mathbf{r}) - i\omega \left[\varepsilon(\mathbf{r}) - \varepsilon_0 \right] \right\} \mathbf{E}(\mathbf{r}) - i\omega\varepsilon_0 \mathbf{E}^s(\mathbf{r}) . \quad (2.1.11)$$

Suppose we define an equivalent volume current density as

$$\mathbf{J}_{eq}(\mathbf{r}) = \tau(\mathbf{r})\mathbf{E}(\mathbf{r}) , \quad (2.1.12)$$

where

$$\tau(\mathbf{r}) = \sigma(\mathbf{r}) - i\omega \left[\varepsilon(\mathbf{r}) - \varepsilon_0 \right] \quad (2.1.13)$$

is the equivalent complex conductivity of the medium, then we can rewrite (2.1.10) and (2.1.11) as

$$\nabla \times \mathbf{E}^s(\mathbf{r}) = i\omega\mu_0 \mathbf{H}^s(\mathbf{r}) \quad (2.1.14)$$

$$\nabla \times \mathbf{H}^s(\mathbf{r}) = \mathbf{J}_{eq}(\mathbf{r}) - i\omega\varepsilon_0 \mathbf{E}^s(\mathbf{r}) . \quad (2.1.15)$$

We can determine \mathbf{E}^s in terms of \mathbf{J}_{eq} from (2.1.14) and (2.1.15) now. By taking curl operation in both side of (2.1.14) and making use of (2.1.15), a differential equation is obtained:

$$\nabla \times \nabla \times \mathbf{E}^s(\mathbf{r}) - k_0^2 \mathbf{E}^s(\mathbf{r}) = i\omega\mu_0 \mathbf{J}_{eq}(\mathbf{r}) \quad \text{for all } \mathbf{r} , \quad (2.1.16)$$

where

$$k_0 = \omega\sqrt{\mu_0\varepsilon_0} \quad (2.1.17)$$

is the wave number of free space.

To find the solution of this equation, we can find the Green's function first. The Green's function \vec{G}_0 is a tensor quantity and must satisfy the following dyadic differential equation in free space:

$$\nabla \times \nabla \times \vec{G}_0(\mathbf{r}, \mathbf{r}') - k_0^2 \vec{G}_0(\mathbf{r}, \mathbf{r}') = \vec{I} \delta(\mathbf{r} - \mathbf{r}') \quad (2.1.18)$$

where

$$\vec{I} = \mathbf{xx} + \mathbf{yy} + \mathbf{zz} \quad (2.1.19)$$

is the unit dyad and \mathbf{x} , \mathbf{y} , \mathbf{z} , are the unit vectors in x -, y -, z - direction, respectively. The free space dyadic Green's function \vec{G}_0 must also satisfy the radiation condition at infinity.

\vec{G}_0 can be determined as [4]:

$$\vec{G}_0(\mathbf{r}, \mathbf{r}') = \left(\vec{I} + \frac{1}{k_0^2} \nabla \nabla \right) \phi(\mathbf{r}, \mathbf{r}') \quad \text{for } \mathbf{r} \neq \mathbf{r}' \quad (2.1.20)$$

where

$$\phi(\mathbf{r}, \mathbf{r}') = \frac{e^{ik_0 R}}{4\pi R} \quad \text{for } \mathbf{r} \neq \mathbf{r}' \quad (2.1.21)$$

is the free space scalar Green's function and

$$R = |\mathbf{r} - \mathbf{r}'| . \quad (2.1.22)$$

Thus, the solution of (2.1.16) is

$$\mathbf{E}^s(\mathbf{r}) = \int_v i\omega\mu_0 \mathbf{J}_{eq}(\mathbf{r}') \cdot \vec{G}_0(\mathbf{r}, \mathbf{r}') dv' \quad (2.1.23)$$

where v is the volume of the body.

Since the integrand of (2.1.23) is not in the L^1 space, i.e., not integrable, this integration is valid only in the sense of Cauchy principal value and a correction term is needed to overcome the singularity problem, [1], [2], i.e.,

$$\mathbf{E}^s(\mathbf{r}) = P.V. \int_{\nu} i\omega\mu_0 \mathbf{J}_{eq}(\mathbf{r}') \cdot \vec{\mathcal{G}}_0(\mathbf{r}, \mathbf{r}') d\nu' + \frac{\mathbf{J}_{eq}(\mathbf{r})}{3i\omega\epsilon_0}. \quad (2.1.24)$$

From (2.1.8) and (2.1.24), we can easily obtain the well known tensor EFIE:

$$\left[1 + \frac{i\tau(\mathbf{r})}{3\omega\epsilon_0} \right] \mathbf{E}(\mathbf{r}) - P.V. \int_{\nu} i\omega\mu_0 \tau(\mathbf{r}') \mathbf{E}(\mathbf{r}') \cdot \vec{\mathcal{G}}_0(\mathbf{r}, \mathbf{r}') d\nu' = \mathbf{E}^i(\mathbf{r}). \quad (2.1.25)$$

This integral equation can be transformed into a system of linear algebraic equations by applying pulse-basis expansion and point-matching and then solved numerically. The details of the transformation are shown in section 2.4 where we will illustrate the differences between this method and the equivalent magnetic current method.

Another integral equation, which will be used in the iterative loop-EMF method in section 2.3, in terms of incident magnetic field can be derived by taking curl operation of (2.1.23) and utilizing (2.1.9) and (2.1.14):

$$\nabla \times \mathbf{E}^s(\mathbf{r}) = \nabla \times \int_{\nu} i\omega\mu_0 \tau(\mathbf{r}') \mathbf{E}(\mathbf{r}') \cdot \vec{\mathcal{G}}_0(\mathbf{r}, \mathbf{r}') d\nu'. \quad (2.1.26)$$

Using equations (2.1.14), we have

$$\mathbf{H}^s(\mathbf{r}) = -\frac{i}{\omega\mu_0} \nabla \times \mathbf{E}^s(\mathbf{r}), \quad (2.1.27)$$

then (2.1.27) becomes

$$\mathbf{H}^s(\mathbf{r}) = - \int_{\nu} \tau(\mathbf{r}') \mathbf{E}(\mathbf{r}') \cdot [\nabla \times \vec{\mathcal{G}}_0(\mathbf{r}, \mathbf{r}')] d\nu'. \quad (2.1.28)$$

By applying (2.1.9) and (2.1.28), we can obtain a coupled tensor integral equation in terms of \mathbf{H}^i :

$$\mathbf{H}(\mathbf{r}) + \int_{\nu} \tau(\mathbf{r}') \mathbf{E}(\mathbf{r}') \cdot [\nabla \times \vec{\mathcal{G}}_0(\mathbf{r}, \mathbf{r}')] d\nu' = \mathbf{H}^i(\mathbf{r}). \quad (2.1.29)$$

We will make use of this equation to establish the iterative process in the iterative loop-EMF method since the induced magnetic field $\mathbf{H}(\mathbf{r})$ is easily obtained via

numerical integration provided the induced electric field distribution $\mathbf{E}(\mathbf{r})$ and the incident magnetic field $\mathbf{H}^i(\mathbf{r})$ are known. More details are presented in section 2.3.

2.2 The Limitation of the Existing Tensor Integral Equation Method

The limitation of the Existing Tensor Integral Equation Method has been discussed by several researchers [5], [6]. One limitation is concerned with the specific absorption rate of energy (SAR). It was reported that the tensor EFIE method with pulse-basis expansion and point-matching gives good values for whole-body average SAR, but the convergence of the solutions for the electric field distribution and the SAR distributions is questionable. The convergence problem has also been indicated by Chen and Rukspollmuang [6] by using a cubic body as an example. This example is given here to illustrate the limitation of the tensor EFIE. An incident plane electromagnetic wave of frequency ω ,

$$\mathbf{E}^i = \mathbf{x} E_0 e^{ik_0 z} \quad (2.2.1)$$

$$\mathbf{H}^i = \mathbf{y} H_0 e^{ik_0 z}, \quad (2.2.2)$$

where E_0 and H_0 are some complex constants, can be decomposed into two standing waves as

$$\mathbf{E}^i = \mathbf{E}_e^i + \mathbf{E}_m^i \quad (2.2.3)$$

$$\mathbf{H}^i = \mathbf{H}_e^i + \mathbf{H}_m^i, \quad (2.2.4)$$

where

$$\mathbf{E}_e^i = \mathbf{x} E_0 \cos(k_0 z) \quad (2.2.5)$$

$$\mathbf{E}_m^i = x iE_0 \sin(k_0 z) \quad (2.2.6)$$

$$\mathbf{H}_e^i = y i \frac{E_0}{\zeta} \sin(k_0 z) \quad (2.2.7)$$

$$\mathbf{H}_m^i = y \frac{E_0}{\zeta} \cos(k_0 z) \quad (2.2.8)$$

and

$$\zeta = \sqrt{\frac{\mu_0}{\epsilon_0}} \quad (2.2.9)$$

is the free space wave impedance. The induced electric field \mathbf{E} due to \mathbf{E}_e^i is called the electric mode solution, while the induced electric field \mathbf{E} due to \mathbf{E}_m^i is called the magnetic mode solution.

Two sets of numerical solutions of electric mode and magnetic mode field distributions in a cubic body obtained by solving the tensor EFIE with pulse-basis expansion and point-matching are shown in Fig-2.2 and Fig-2.3, respectively. Fig-2.2 shows the x - components of the amplitude of the induced electric fields $|E_x|$ inside a $4 \times 4 \times 4 \text{ cm}$ cube with the conductivity $\sigma = 4.5 \text{ S/m}$ and the relative permittivity $\epsilon_r = 50$, excited by a symmetrically impressed electric field $\mathbf{E}^i = x \cos(k_0 z)$ of frequency 750 MHz. The middle part of Fig-2.2 shows the distribution of the amplitude of E_x within one eighth of the cube, obtained when the cube was subdivided into 216 cubic cells. In the lower part of Fig-2.2 the distribution of the amplitude of E_x within one eighth of the cube obtained with 512-cell subdivision is shown.

Fig-2.3 shows the distribution the amplitude of E_x inside the same cube excited by an antisymmetrically impressed electric field $\mathbf{E}^i = x i \sin(k_0 z)$ of frequency 750 MHz. The numerical results for the amplitude of E_x are given in Fig-2.3 for the cases of 216-cell subdivision and the 512-cell subdivision. It is noticed that the electric

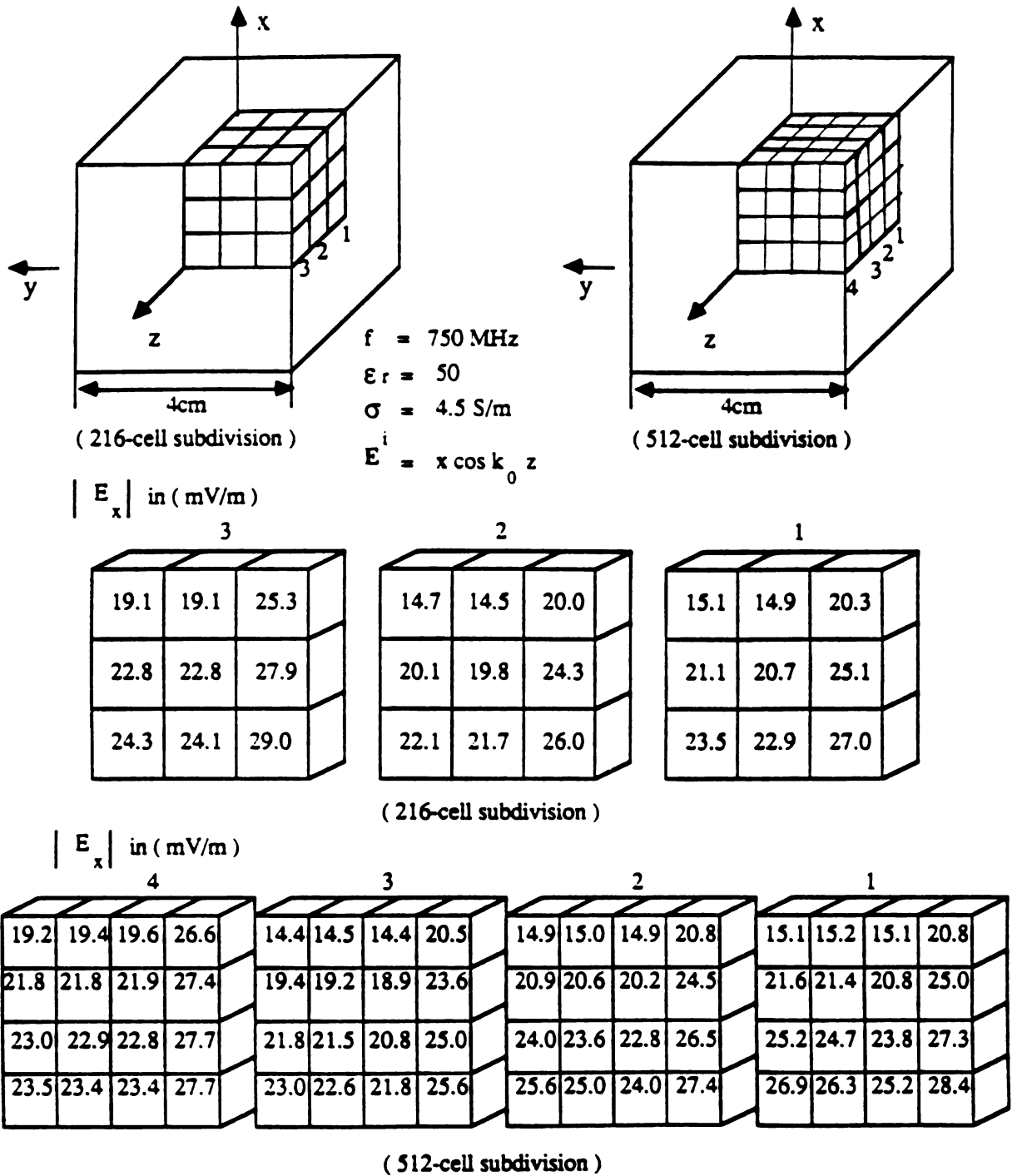


Fig-2.2 Electric mode distribution of the x-component of the induced electric fields in the body based on 216-cell division and 512-cell division.

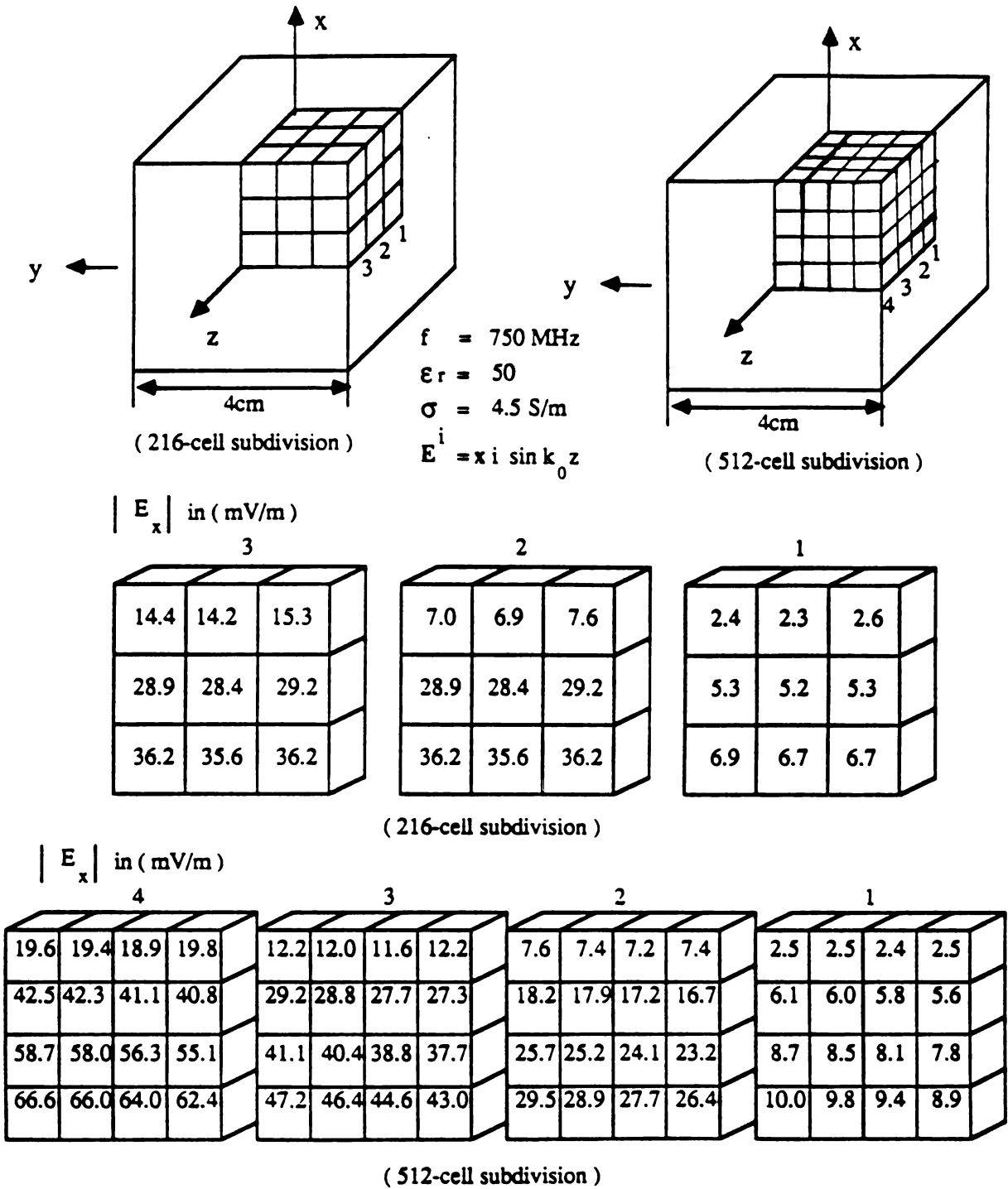


Fig-2.3 Magnetic mode distribution of the x-component of the induced electric fields in the body based on 216-cell division and 512-cell division.

mode solution exhibits a good convergence but the magnetic mode results for the 512-cell subdivision deviate significantly from those of the 216-cell subdivision, especially at the outer layer of the cube. A simple physical explanation is that the electric mode solution is induced by a symmetrically impressed electric field so that it is linear in nature while the magnetic mode solution is induced by an antisymmetrically impressed electric field so that it is circulatory in nature. Intuitively, for the latter case, we do not expect good results with the pulse-basis expansion which is linear in nature. To produce accurate results for the magnetic mode of induced electric field field, the cell size should be smaller in comparison with the case of the electric mode shown in Fig-2.2.

2.3 Iterative loop-EMF method

A finite body can be considered as an impedance network system from the viewpoint of electric voltage and current [7], [8]. The body is subdivided into a number of cells, each of which is then replaced by an equivalent impedance loop. One can find the induced current distribution of this network when it is exposed to an incident field with the applications of Faraday's law and Kirchhoff's circuit theory to the network. The electric field distribution of the body can thus be determined by the relation:

$$\mathbf{J}_{eq}(\mathbf{r}) = \tau(\mathbf{r})\mathbf{E}(\mathbf{r}) . \quad (2.1.12)$$

An iterative process can be added to improve the accuracy of the induced currents in the resulting network and hence the induced electric fields inside the body by using the coupled integral equation (2.1.29). The iterative loop-EMF method is based on the

concept of impedance network combined with the iterative process. The procedures of this method are given in this section.

Fig-2.4 is an example of a single layer of body illuminated by an antisymmetric incident electric field \mathbf{E}_m^i of

$$\mathbf{E}_m^i = x iE_0 \sin(k_0 z) , \quad (2.2.6)$$

which has the associated magnetic field \mathbf{H}_m^i of

$$\mathbf{H}_m^i = y \frac{E_0}{\zeta} \cos(k_0 z) . \quad (2.2.8)$$

The single layer body is cut into N cubic cells of width d while we regard each cell as a loop in the whole system. In each loop, say the n -th one, we define a loop current,

$$J_n = \tau_n E_n \quad (2.3.1)$$

where E_n can be considered as a loop electric field in the n -th cell and τ_n is the equivalent complex conductivity of this cell. This loop current can be calculated in terms of magnetic field by Faraday's law:

$$\int_c \mathbf{E} \cdot d\mathbf{l} = i\omega\mu_0 \int_{\Delta s} \mathbf{H} \cdot d\mathbf{s} . \quad (2.3.2)$$

Let us apply (2.3.2) in the i -th cell for illustration. From (2.1.12) we have

$$\mathbf{E}(\mathbf{r}) = \frac{\mathbf{J}_{eq}(\mathbf{r})}{\tau(\mathbf{r})} , \quad (2.3.3)$$

then (2.3.2) and (2.3.3) give

$$\frac{J_i}{\tau_i} 4d - \frac{J_j}{\tau_j} d - \frac{J_k}{\tau_k} d - \frac{J_l}{\tau_l} d = i\omega\mu_0 (H_i)_y d^2 , \quad (2.3.4)$$

or in other words,

$$4E_i - E_j - E_k - E_l = i\omega\mu_0 (H_i)_y d , \quad (2.3.5)$$

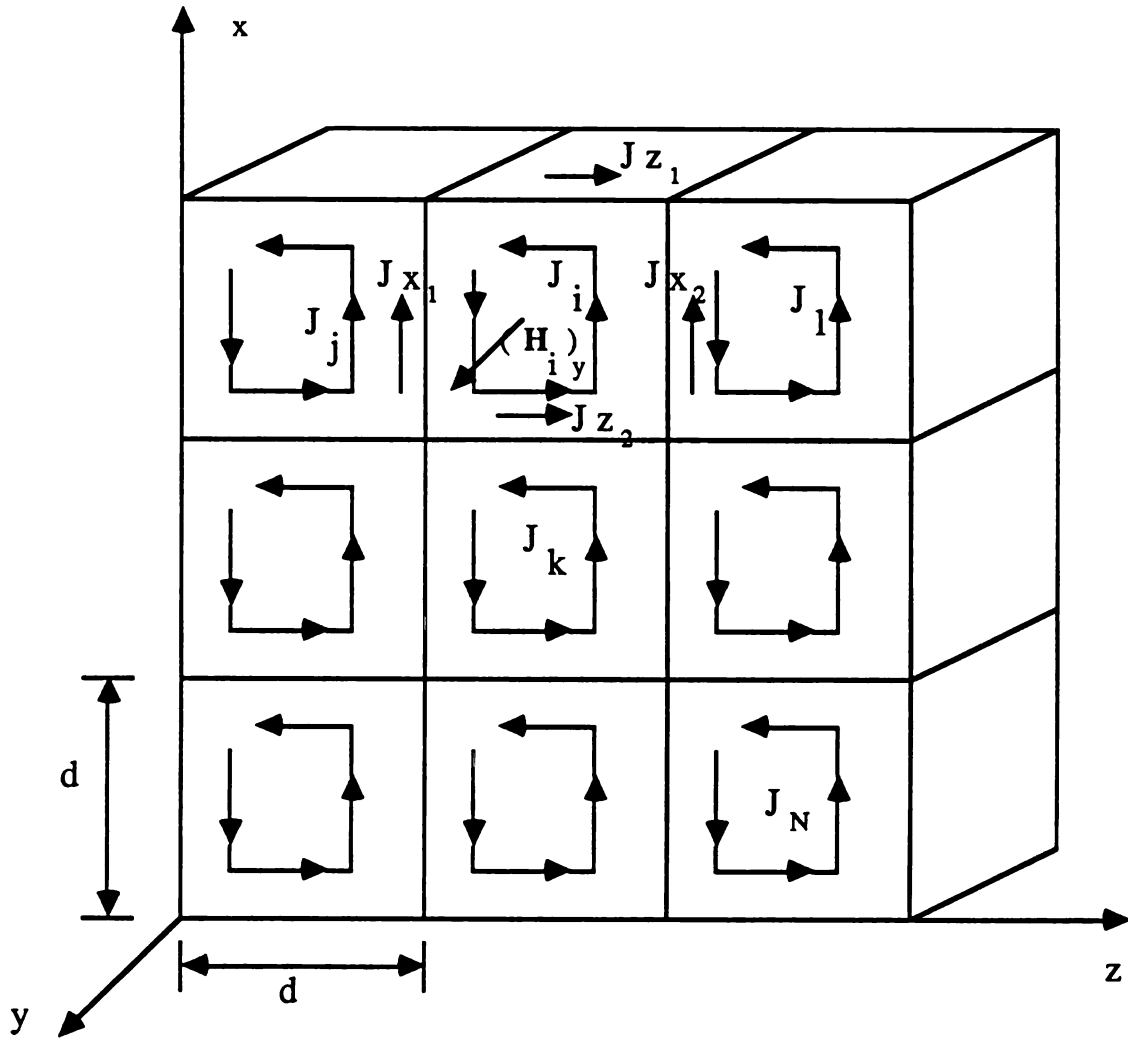


Fig-2.4 A single layer of non-magnetic lossy body regarded as an impedance network system with N loops.

where $(H_n)_y$ is the y - component of the \mathbf{H} field for the n -th cell. Eventually, (2.3.4) can be thought as the application of Kirchoff's voltage law while J_i 's are correspondent to mesh currents and $\frac{d}{\tau_i}$ correspondent to branch impedances along the sides of the cell.

The application of (2.3.5) to all the cells will give rise to

$$\begin{bmatrix} a_{11} & a_{12} & \dots & a_{1N} \\ a_{21} & a_{22} & \dots & a_{2N} \\ \vdots & \vdots & \ddots & \vdots \\ \vdots & \vdots & \ddots & \vdots \\ a_{N1} & a_{N2} & \dots & a_{NN} \end{bmatrix} \begin{bmatrix} E_1 \\ E_2 \\ \vdots \\ \vdots \\ E_N \end{bmatrix} = \begin{bmatrix} (H_1)_y \\ (H_2)_y \\ \vdots \\ \vdots \\ (H_N)_y \end{bmatrix} \quad (2.3.6)$$

where

$$a_{mn} = c L_{mn} \quad \text{for } m=1,2,\dots,N \quad n=1,2,\dots,N \quad (2.3.7)$$

$$c = \frac{d}{i\omega\mu_0} \quad (2.3.8)$$

and L_{mn} belonging to the set $\{-4,-3,-2,-1,0,1,2,3,4\}$, is dependent on the relative location of the loop in the network system.

We can obtain E_n in terms of $(H_n)_y$ by solving the system of simultaneous linear algebraic equations (2.3.6). After that the loop current density of each cell J_n is simply obtained as

$$J_n = \tau_n E_n . \quad (2.3.9)$$

The actual current density along the side of each cell can be found by subtracting those loop current densities of the adjacent cells. For example, in Fig-2.4, J_{x1} , J_{z1} , J_{x2} and J_{z2} are the actual current density of four sides along the i -th cell respectively, and can be expressed as follows:

distrib

which

(2.1.2)

in the

is the

F

zeroth-

are the

tively.

The

(2.3.10)

field at

the sides

$$J_{z1} = -J_i \quad (2.3.10)$$

$$J_{x1} = J_j - J_i \quad (2.3.11)$$

$$J_{z2} = J_i - J_k \quad (2.3.12)$$

$$J_{x2} = J_i - J_l \quad (2.3.13)$$

Once we know the actual current distribution, we can easily find the electric field distribution by (2.3.3).

The remaining problem is that we still do not have the magnetic field distribution which is needed to apply (2.3.2). Thus, an iterative process is developed by using (2.1.29) to estimate the \mathbf{H} field. We can choose the initial guess as

$$\mathbf{H}^{(0)} = \mathbf{H}^i \quad (2.3.14)$$

in the zeroth-iteration, where

$$\mathbf{H}^{(k)}, \quad \text{for } k=0,1,2,\dots, \quad (2.3.15)$$

is the estimated magnetic field distribution in the k -th iteration.

From (2.3.6), we are able to calculate for the loop electric field $E_n^{(0)}$ in this zeroth-iteration, and thus for the loop current $J_n^{(0)}$, where

$$E_n^{(k)} \text{ and } J_n^{(k)}, \quad \text{for } k=0,1,2,\dots, \quad (2.3.16)$$

are the loop electric field and loop current of the n -th cell in the k -th iteration, respectively.

The actual electric field distribution can be easily constructed similarly to that in (2.3.10) to (2.3.13) in this zeroth-iteration. In order to make use of the actual electric field at the center in each cell, we can approximate that by averaging the values along the sides of each cell, for example,

$$E_{ix} = \frac{(E_{x1} + E_{x2})}{2} \quad (2.3.17)$$

$$E_{iz} = \frac{(E_{z1} + E_{z2})}{2} \quad (2.3.18)$$

for the i -th cell as shown in Fig-2.4, where E_{ix} and E_{iz} are x - and z - components of electric field at the center in the cell. So $\mathbf{E}^{(0)}$, the zeroth E field distribution, is constructed automatically.

Now we are on the way to proceed the iteration process. For the first-iteration, $\mathbf{H}^{(1)}$ can be calculated from (2.1.29):

$$\mathbf{H}^{(1)}(\mathbf{r}) = \mathbf{H}^i(\mathbf{r}) - \int_v \tau(\mathbf{r}') \mathbf{E}^{(0)}(\mathbf{r}') \cdot [\nabla \times \vec{G}_0(\mathbf{r}, \mathbf{r}')] dv' , \quad (2.3.19)$$

where the integration in (2.3.19) should be carried out numerically. Again, we can obtain $E_n^{(1)}$ from (2.3.6) by using $\mathbf{H}^{(1)}$.

Similarly, for the k th-iteration:

$$\mathbf{H}^{(k)}(\mathbf{r}) = \mathbf{H}^i(\mathbf{r}) - \int_v \tau(\mathbf{r}') \mathbf{E}^{(k-1)}(\mathbf{r}') \cdot [\nabla \times \vec{G}_0(\mathbf{r}, \mathbf{r}')] dv' , \quad (2.3.20)$$

and then $E_n^{(k)}$ can also be obtain from (2.3.6) with $\mathbf{H}^{(k)}$ calculated from the $(k-1)$ -th iteration.

This iteration process should continue until both E_n and \mathbf{H} converge.

As we can observe, a nearly uniform, incident magnetic field will enable us to apply the Faraday's law accurately and thus will give better approximation in this method. This process, as described above, will be more accurate and efficient if we applied it on an electrically small size body with an antisymmetric incident electric field.

2.4 Equivalent Magnetic Current Compensation Method

When (2.1.25) is solved numerically with pulse-basis expansion in a finite body, this body is partitioned into a finite number of cells and the induced field in each cell is assumed to be uniform. In this way, we allow the induced electric fields to vary from cell to cell. Obviously, this assumption creates a discontinuity of \mathbf{E} field between adjacent cells.

In a homogeneous region, the induced \mathbf{E} fields need to be continuous everywhere but the consequence of the above assumption clearly violates this fact. When point-matching is applied as the testing procedure, there is a physical explanation for the discontinuity of the normal component of the \mathbf{E} field [9] and a brief discussion is given here.

In (2.1.18), the dyadic Green's function can be regarded as the \mathbf{E} field generated by a current element and a pair of opposite charges at the ends of the element. A source region with conventional current and charge density can be considered as an ensemble of small cells each containing a current element or an electric dipole of certain magnitude and orientation. Based on this picture, two adjoining cells containing current elements of different magnitudes or orientations will result in a net charge at the boundary of these cells. On the other hand, the discontinuity of the normal component of the \mathbf{E} field between two adjacent cells as we mentioned earlier will also yield a net charge at the interface by applying the boundary condition of the Maxwell's equations.

From this argument, we say the discontinuity of the normal component of \mathbf{E} field is compensated by the equivalent surface charge at the boundary which effect is taken into account by the free space tensor Green's function \vec{G}_0 .

The discontinuity of the tangential components of \mathbf{E} fields, however, still exists between adjacent cells. An equivalent magnetic surface current \mathbf{K}_m is proposed at the

cell

of th

neig!

we h

where

adjoin

mainta

Thus (

Therefo

where \bar{s}

face enc

Eq

modifica

In

a matrix

cell boundary to compensate for this discontinuity. Fig-2.5 illustrates a rough picture of the equivalent surface charge and the equivalent magnetic surface current between neighboring cells.

By definition of magnetic surface current and the principle of equivalence [10], we have:

$$\mathbf{K}_m = -\mathbf{n} \times \mathbf{E} = (\mathbf{n}_1 \times \mathbf{E}_1 + \mathbf{n}_2 \times \mathbf{E}_2) \quad (2.4.1)$$

where \mathbf{n} is the unit normal vector and $\mathbf{n}_1, \mathbf{n}_2$, are the unit normal vectors on the adjoining surface of cell 1 and cell 2 respectively, as shown in Fig-2.5. This \mathbf{K}_m will maintain another scattering electric field:

$$\mathbf{E}^{s'}(\mathbf{r}) = -\int_{\bar{s}} (\mathbf{n} \times \mathbf{E}(\mathbf{r}')) \times \nabla \phi(\mathbf{r}, \mathbf{r}') ds' . \quad (2.4.2)$$

Thus (2.1.8) becomes

$$\mathbf{E} = \mathbf{E}^i + \mathbf{E}^s + \mathbf{E}^{s'} . \quad (2.4.3)$$

Therefore the tensor EFIE (2.1.25), is then modified as follows:

$$\left[1 + \frac{i\tau(\mathbf{r})}{3\omega\epsilon_0} \right] \mathbf{E}(\mathbf{r}) - P.V. \int_{\nu} i\omega\mu_0\tau(\mathbf{r}') \mathbf{E}(\mathbf{r}') \cdot \vec{\mathcal{G}}_0(\mathbf{r}, \mathbf{r}') d\nu' \\ + \int_{\bar{s}} (\mathbf{n} \times \mathbf{E}(\mathbf{r}')) \times \nabla \phi(\mathbf{r}, \mathbf{r}') ds' = \mathbf{E}^i(\mathbf{r}) , \quad (2.4.4)$$

where \bar{s} represents all the six surfaces of each cell except the outmost boundary surface enclosing ν .

Equation (2.4.4) can be solved numerically in a similar way as before with a modification in the matrix elements, as described below.

In the tensor EFIE (2.1.25), the inner product $\mathbf{E}(\mathbf{r}') \cdot \vec{\mathcal{G}}_0(\mathbf{r}, \mathbf{r}')$ can be represented as a matrix product as

$$\mathbf{E}(\mathbf{r}') \cdot \vec{\mathcal{G}}_0(\mathbf{r}, \mathbf{r}')$$

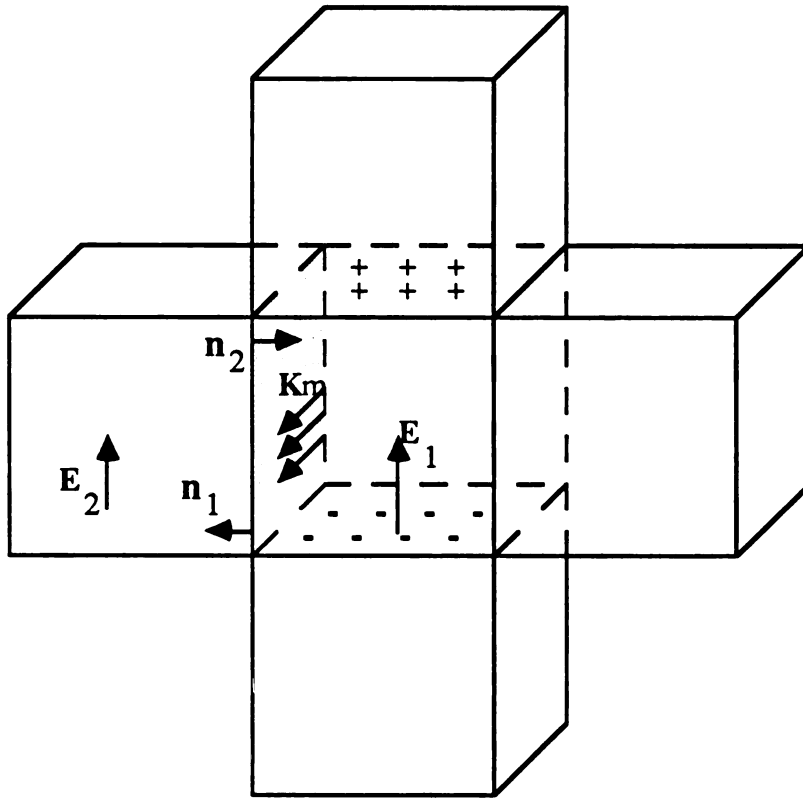


Fig-2.5 Illustration of the equivalent surface charge and the equivalent magnetic current created by the discontinuity of the electric field between neighboring cells.

w

for

E_2

r_n

then

where

The e

$$= \begin{bmatrix} \phi(\mathbf{r}, \mathbf{r}') + \frac{1}{k_0^2} \phi_{xx}(\mathbf{r}, \mathbf{r}') & \frac{1}{k_0^2} \phi_{xy}(\mathbf{r}, \mathbf{r}') & \frac{1}{k_0^2} \phi_{xz}(\mathbf{r}, \mathbf{r}') \\ \frac{1}{k_0^2} \phi_{yx}(\mathbf{r}, \mathbf{r}') & \phi(\mathbf{r}, \mathbf{r}') + \frac{1}{k_0^2} \phi_{yy}(\mathbf{r}, \mathbf{r}') & \frac{1}{k_0^2} \phi_{yz}(\mathbf{r}, \mathbf{r}') \\ \frac{1}{k_0^2} \phi_{zx}(\mathbf{r}, \mathbf{r}') & \frac{1}{k_0^2} \phi_{zy}(\mathbf{r}, \mathbf{r}') & \phi(\mathbf{r}, \mathbf{r}') + \frac{1}{k_0^2} \phi_{zz}(\mathbf{r}, \mathbf{r}') \end{bmatrix} \begin{bmatrix} E_x(\mathbf{r}') \\ E_y(\mathbf{r}') \\ E_z(\mathbf{r}') \end{bmatrix} \quad (2.4.5)$$

where

$$\begin{aligned} \phi_{x_p x_q}(\mathbf{r}, \mathbf{r}') &= \frac{\partial^2}{\partial x_p \partial x_q} \phi(\mathbf{r}, \mathbf{r}') \\ &= \frac{k_0^2 e^{ik_0 R}}{4\pi R^3} \left\{ \left[(k_0 R)^2 - 1 + ik_0 R \right] \delta_{pq} + \frac{(x_p - x_p')(x_q - x_q')}{R^2} \left[3 - (k_0 R)^2 - 3ik_0 R \right] \right\} \end{aligned} \quad (2.4.6)$$

for $p, q=1, 2, 3$, and x_1, x_2, x_3 stand for x, y, z , respectively for convenience, E_x, E_y and E_z are x -, y -, and z - components of the electric field \mathbf{E} . Note that δ_{pq} is defined as

$$\delta_{pq} = \begin{cases} 1 & p=q \\ 0 & \text{otherwise} \end{cases} \quad (2.4.7)$$

Suppose the body is divided into N cells with the center of each cell \mathbf{v}_n located at \mathbf{r}_n , $n=1, 2, \dots, N$. After applying pulse-basis expansion and point-matching, (2.1.25) is then transformed into a system of linear equations of order $3N$:

$$\begin{bmatrix} G_{11} & G_{12} & G_{13} \\ G_{21} & G_{22} & G_{23} \\ G_{31} & G_{32} & G_{33} \end{bmatrix} \begin{bmatrix} E_1 \\ E_2 \\ E_3 \end{bmatrix} = \begin{bmatrix} E_1^i \\ E_2^i \\ E_3^i \end{bmatrix} \quad (2.4.8)$$

where G_{pq} is an $N \times N$ matrix, E_p and E_p^i are $N \times 1$ column vectors, for $p, q=1, 2, 3$.

The elements of those matrices and vectors are

c

T

w

w

is

Th

inte

for

$$\begin{aligned}
(G_{pq})_{mn} &= \delta_{pq} \delta_{mn} \left[1 + \frac{i\tau(\mathbf{r}_n)}{3\omega\epsilon_0} \right] \\
&+ i\omega\mu_0 \text{P.V.} \int_{v_n} \tau(\mathbf{r}') [\delta_{pq} \phi(\mathbf{r}_n, \mathbf{r}') + \frac{1}{k_0^2} \phi_{x_p x_q}(\mathbf{r}_n, \mathbf{r}')] dv', \\
m, n &= 1, 2, \dots, N
\end{aligned} \tag{2.4.9}$$

$$(E_p)_n = E_{x_p}(\mathbf{r}_n), \quad n=1, 2, \dots, N \tag{2.4.10}$$

$$(E_p^i)_n = E_{x_p^i}(\mathbf{r}_n), \quad n=1, 2, \dots, N \tag{2.4.11}$$

Note that the integration in (2.4.9) has the singularity problem when $m = n$. A correction term and the Cauchy principal integration are needed to evaluate $(G_{pq})_{nn}$. The results of $(G_{pq})_{nn}$ can be obtained analytically by approximating v_n as a sphere with the same center and an identical volume [12]:

$$(G_{pq})_{nn} = \delta_{pq} \left\{ \frac{2i\omega\mu_0\tau(\mathbf{r}_n)}{3k_0^2} [e^{ik_0 a_n}(1 - ik_0 a_n) - 1] + \left[1 + \frac{i\tau(\mathbf{r}_n)}{3\omega\epsilon_0} \right] \right\}, \tag{2.4.12}$$

where

$$a_n = \left[\frac{3V_n}{4\pi} \right]^{1/3} \tag{2.4.13}$$

is the radius of the approximated sphere and V_n stands for the volume of the n -th cell. The rest of elements in G_{pq} can be carried out numerically.

Now in the modified integral equation (2.4.4), the integrand of the surface integration $(\mathbf{n} \times \mathbf{E}(\mathbf{r}')) \times \nabla\phi(\mathbf{r}, \mathbf{r}')$ can also be represented in another matrix product form:

$$(\mathbf{n} \times \mathbf{E}(\mathbf{r}')) \times \nabla\phi(\mathbf{r}, \mathbf{r}')$$

$$= \begin{bmatrix} n_2\phi_y(\mathbf{r},\mathbf{r}') + n_3\phi_z(\mathbf{r},\mathbf{r}') & -n_1\phi_y(\mathbf{r},\mathbf{r}') & -n_1\phi_z(\mathbf{r},\mathbf{r}') \\ -n_2\phi_x(\mathbf{r},\mathbf{r}') & n_1\phi_x(\mathbf{r},\mathbf{r}') + n_3\phi_z(\mathbf{r},\mathbf{r}') & -n_2\phi_z(\mathbf{r},\mathbf{r}') \\ -n_3\phi_x(\mathbf{r},\mathbf{r}') & -n_3\phi_y(\mathbf{r},\mathbf{r}') & n_1\phi_x(\mathbf{r},\mathbf{r}') + n_2\phi_y(\mathbf{r},\mathbf{r}') \end{bmatrix} \begin{bmatrix} E_x(\mathbf{r}') \\ E_y(\mathbf{r}') \\ E_z(\mathbf{r}') \end{bmatrix} \quad (2.4.14)$$

where n_1 , n_2 and n_3 are x -, y - and z - components of the unit normal vector \mathbf{n} , i.e.,

$$\mathbf{n} = n_1\mathbf{x} + n_2\mathbf{y} + n_3\mathbf{z} \quad (2.4.15)$$

$$n_1^2 + n_2^2 + n_3^2 = 1, \quad (2.4.16)$$

and

$$\phi_{x_p}(\mathbf{r},\mathbf{r}') = \frac{\partial}{\partial x_p} \phi(\mathbf{r},\mathbf{r}') = \frac{e^{ik_0R}}{4\pi R^2} \frac{(x_p - x_p')}{R} (1 - ik_0R) \quad (2.4.17)$$

for $p=1,2,3$.

Suppose we apply pulse-basis expansion and point-matching at the center of each cell, the system of linear algebraic equations will become

$$\begin{bmatrix} \bar{G}_{11} & \bar{G}_{12} & \bar{G}_{13} \\ \bar{G}_{21} & \bar{G}_{22} & \bar{G}_{23} \\ \bar{G}_{31} & \bar{G}_{32} & \bar{G}_{33} \end{bmatrix} \begin{bmatrix} E_1 \\ E_2 \\ E_3 \end{bmatrix} = \begin{bmatrix} E_1^i \\ E_2^i \\ E_3^i \end{bmatrix} \quad (2.4.18)$$

where \bar{G}_{pq} is again a $N \times N$ matrix, the elements of the matrices for $p,q=1,2,3$ are

$$\begin{aligned} (\bar{G}_{pq})_{mn} &= \delta_{pq} \delta_{mn} \left[1 + \frac{i\tau(\mathbf{r}_n)}{3\omega\epsilon_0} \right] \\ &+ i\omega\mu_0 P.V. \int_{v_n} \tau(\mathbf{r}') [\delta_{pq} \phi(\mathbf{r}_n, \mathbf{r}') + \frac{1}{k_0^2} \phi_{x_p x_q}(\mathbf{r}_n, \mathbf{r}')] dv' \\ &+ \int_{\bar{s}_m} [\delta_{pq} \sum_{\substack{i \neq q \\ i=1}}^3 n_i \phi_{x_i}(\mathbf{r}_n, \mathbf{r}') - (1 - \delta_{pq}) n_p \phi_{x_q}(\mathbf{r}_n, \mathbf{r}')] ds', \\ &m, n = 1, 2, \dots, N \end{aligned} \quad (2.4.19)$$

where \bar{s}_m represents the six surfaces of v_m , except for those surfaces which belong to the outmost surface s , and of course, n_p depends on \bar{s}_m . The surface integration in (2.4.19) should also be carried out numerically.

Now we can find the electric field at the center of each cell by solving the above matrix equation. Numerical examples will be shown in section 2.5.

2.5 Numerical Comparison between the New Methods and the Existing Method

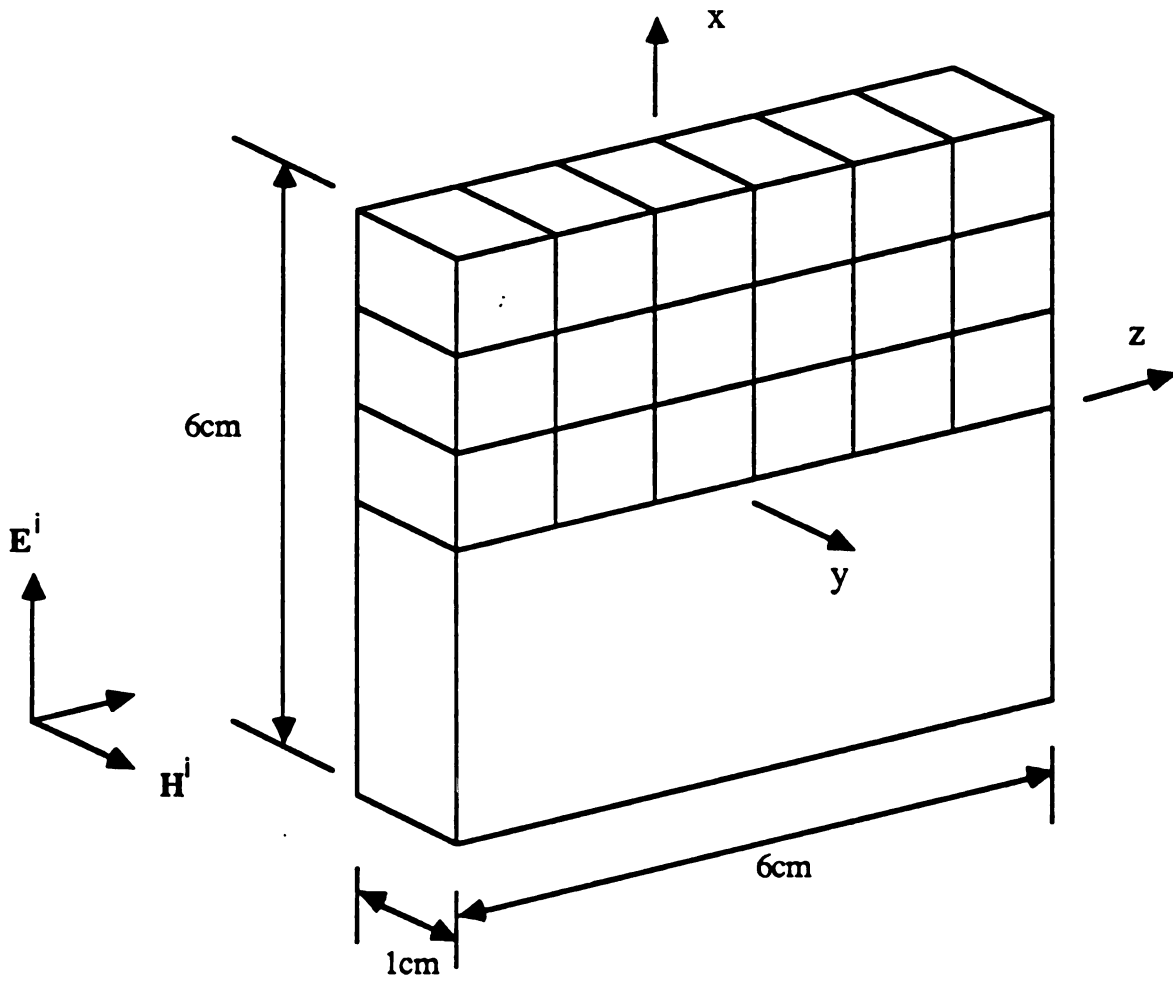
Several sets of numerical solutions of induced electromagnetic fields inside some block models solved by the new methods described in this chapter are compared with the corresponding induced fields obtained from the tensor integral equation method. This comparison is shown in Fig-2.6 to Fig-2.24 and is the subject matter of discussion in this section.

In Fig-2.6, a single layer, homogeneous rectangular biological model with dimensions of $6 \times 6 \times 1$ cm is illuminated by a plane wave with a vertically polarized field at end-on incidence. The total volume is divided into 36 subvolumes and each of them is $1 \times 1 \times 1$ cm in dimensions. Fig-2.7 indicates the numerical solutions of the tensor integral equation due to symmetric part of the incident electric field,

$$\mathbf{E}^i = \mathbf{E}_e^i = \mathbf{x} \cos(k_0 z) \quad (2.5.1)$$

with a frequency $f = 100$ MHz.

Those numbers in the figure are the x - and z - components of the total induced field at the centers of the cells. The y - component is very small compared with the other two components so that it can be disregarded. In this calculation, the conductivity σ is assumed to be 0.889 S/m and the permittivity ϵ is assumed to be $71.7\epsilon_0$.



$$\epsilon_r = 71.7$$

$$\sigma = 0.889 \text{ S/m}$$

$$\mu_r = 1$$

Fig-2.6 A homogeneous rectangular biological model with dimensions $6 \times 6 \times 1 \text{ cm}$ illuminated by an EM wave at end-on incidence.

Due to the symmetry of the geometry and hence the field distribution [11], [12], only the values of the induced fields in the first quadrant of the model are shown in Fig-2.7. Fig-2.8 shows the solutions of a model with the same dimension and material which was subdivided into 288 cells with each subvolume of dimensions $0.5 \times 0.5 \times 0.5 \text{ cm}$ exposed to the same incident field as Fig-2.7. Each numerical value is obtained by taking average of the fields at the centers of eight neighboring subcells which are included in the original 1 cm^3 cubic cell in order to compare with the numerical values in Fig-2.7. Fig-2.9 and Fig-2.10 are the similar results as those shown in Fig-2.7 and Fig-2.8 except that the incident electric field is antisymmetrical:

$$\mathbf{E}^i = \mathbf{E}_m^i = \mathbf{x} \sin(k_0 z) . \quad (2.5.2)$$

It is observed that the values in Fig-2.7 are quite close to those in Fig-2.8, but the values in Fig-2.9 are only about one third to one half of those in Fig-2.10 which are regarded as more accurate solutions. This is not surprising since we have already seen an example in section 2.2.

Fig-2.11 shows the field distribution obtained by the iterative loop-EMF method in the same body with an antisymmetrical incident electric field of frequency 100 MHz. Here the body is subdivided into 36 cells of size 1 cm^3 . We find that the values in this figure are closer to those in Fig-2.10 than those in Fig-2.9.

Fig-2.12 presents the results of the equivalent magnetic current method, with the same body and the same incident fields as the case of Fig-2.11. The body is again cut into 36 cells and we have added the effect due to the equivalent magnetic current between adjacent cells. The improvement in this case is not very significant since the electric field distribution is not changing rapidly and hence the effect due to the discontinuity assumption by using pulse-basis expansion is also not very noticeable.

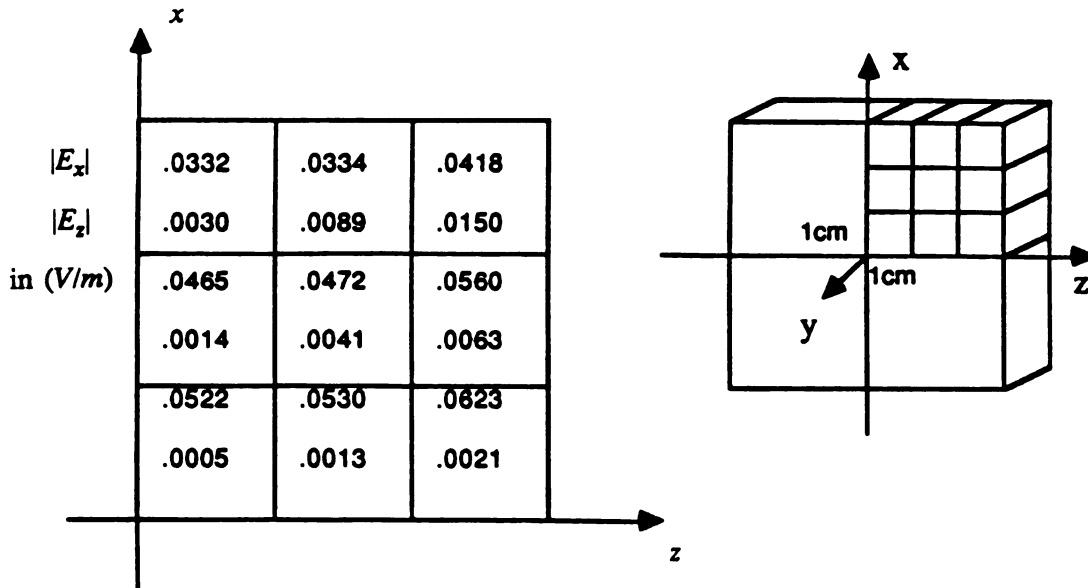


Fig-2.7 Conventional EFIE solutions based on 36-cell division.

$$E^i = x \cos(k_0 z)$$

$$f = 100 \text{ MHz}$$

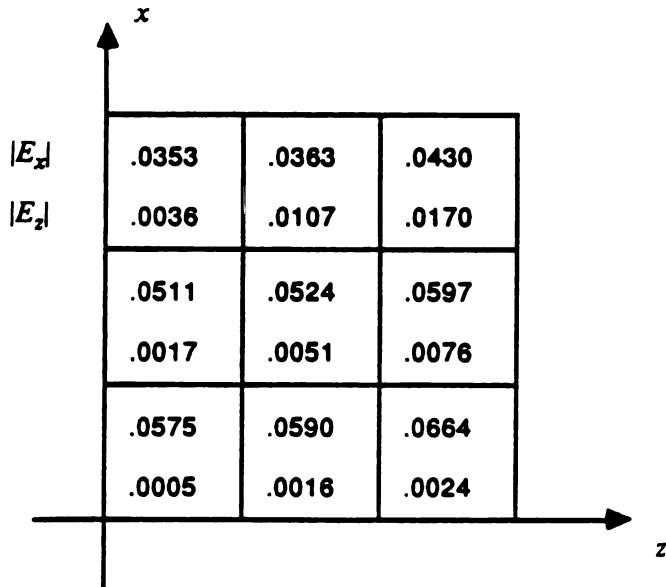


Fig-2.8 Conventional EFIE solutions based on 288-cell division.

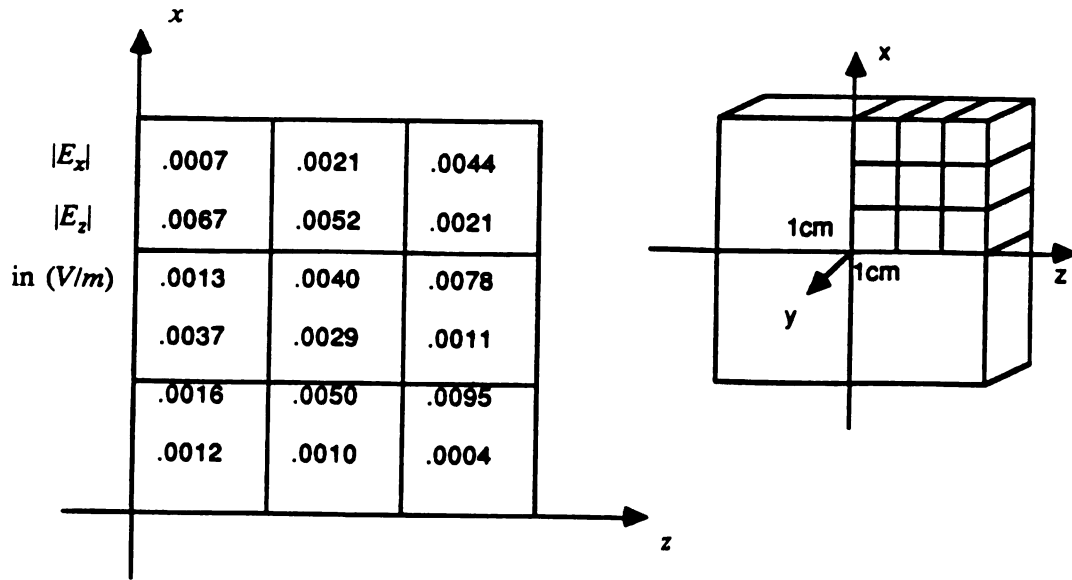


Fig-2.9 Conventional EFIE solutions based on 36-cell division.

$$E^i = x \sin(k_0 z)$$

$$f = 100 \text{ MHz}$$

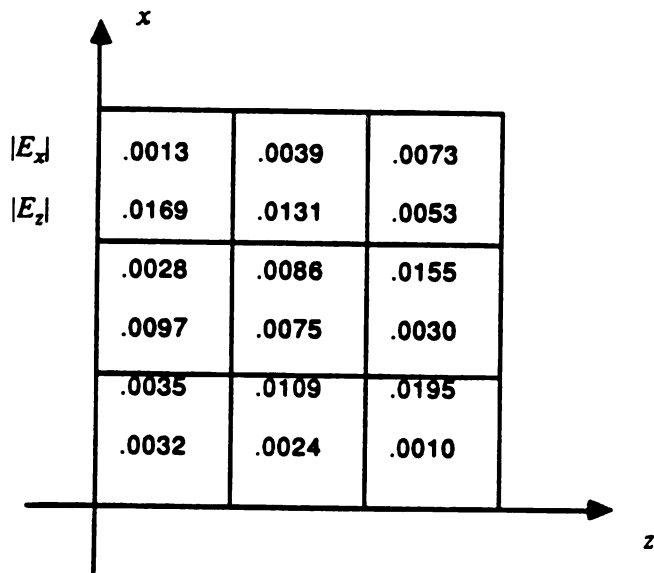


Fig-2.10 Conventional EFIE solutions based on 288-cell division.

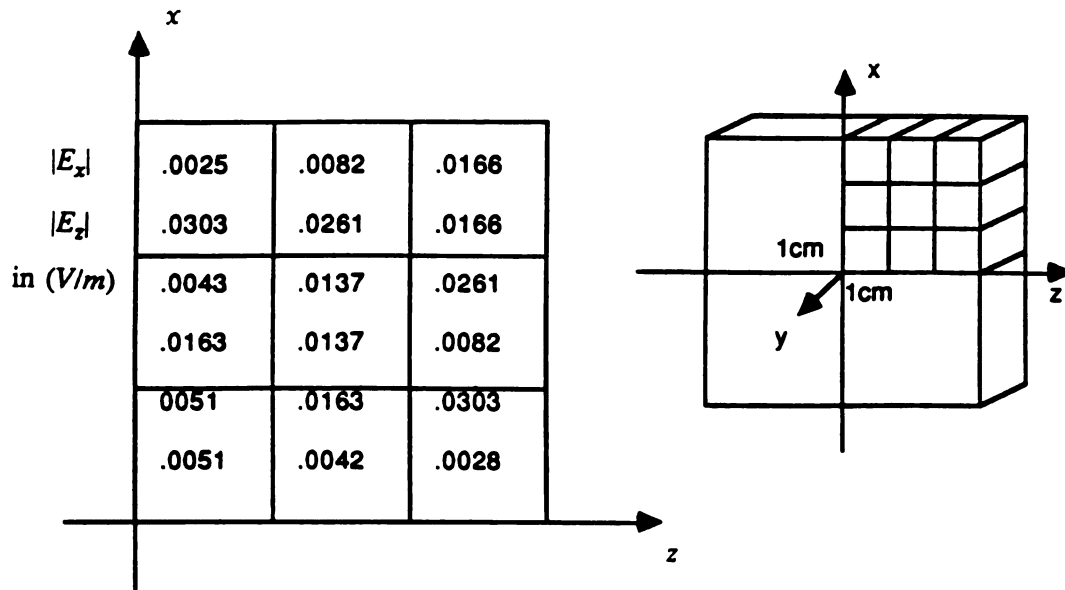


Fig-2.11 Iterative loop-EMF solutions based on 36-cell division.

$$E^i = x \sin(k_0 z)$$

$$f = 100 \text{ MHz}$$

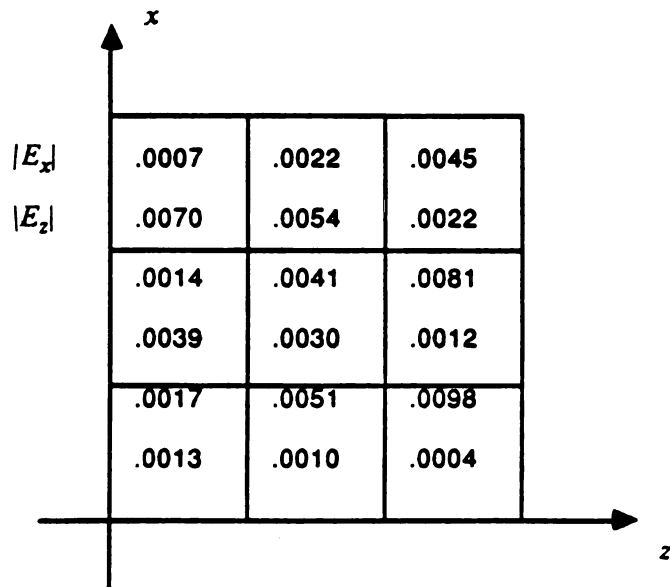


Fig-2.12 Equivalent magnetic current method solutions based on 36-cell division.

a
s
m
lo
It
exp
rap
crea
meth

antis
ment
freque
MHz,
discus
the res
case.

A
this se
in this
again.
and pe
antisym
this cas
are of

Fig-2.13 to Fig-2.16 show the induced fields in the same body illuminated by an antisymmetrical incident electric field of frequency 300 MHz. Fig-2.13 shows the solution of tensor EFIE method with 36 cells, Fig-2.14 indicates the solution of same method with 288 cells, while Fig-2.15 and Fig-2.16 depict the solutions by iterative loop-EMF method and equivalent magnetic current method, respectively, with 36 cells. It is obvious that the improvements by the new methods are increased. The physical explanation is that as the frequency goes up, the electric field distribution varies more rapidly and hence those new methods will give more compensations to the inaccuracy created by the piece-wise constant assumption of fields in each cell in the conventional method.

Fig-2.17 to Fig-2.24 illustrate the induced field in the same body, exposed to antisymmetric incident electric field of frequencies 500 and 700 MHz. The improvement of the iterative loop-EMF method is quite significant as we can observe when the frequency is 500 MHz. The effect is not so significant when the frequency is 700 MHz, as we observe in the figure, since there are certain limitations of this method as discussed at the end of section 2.3. The equivalent magnetic current method improves the results about 20 to 30 percents on the amplitude of the field distribution in each case.

An example of the induced field in a heterogeneous body is given at the end of this section. The iterative loop-EMF method is used to calculate the field distribution in this example. Fig-2.25 shows a heterogeneous body of dimensions $6 \times 6 \times 1$ cm again. The shaded region indicates different material of conductivity $\sigma = 0.048$ S/m and permittivity $\epsilon = 7.45\epsilon_0$, the remaining part is the same as the previous cases. An antisymmetrical incident electric field of frequency 500 MHz is used. The difficulty of this case is the determination of the impedance at the boundaries of those cells which are of different materials. The impedances which are related to the complex

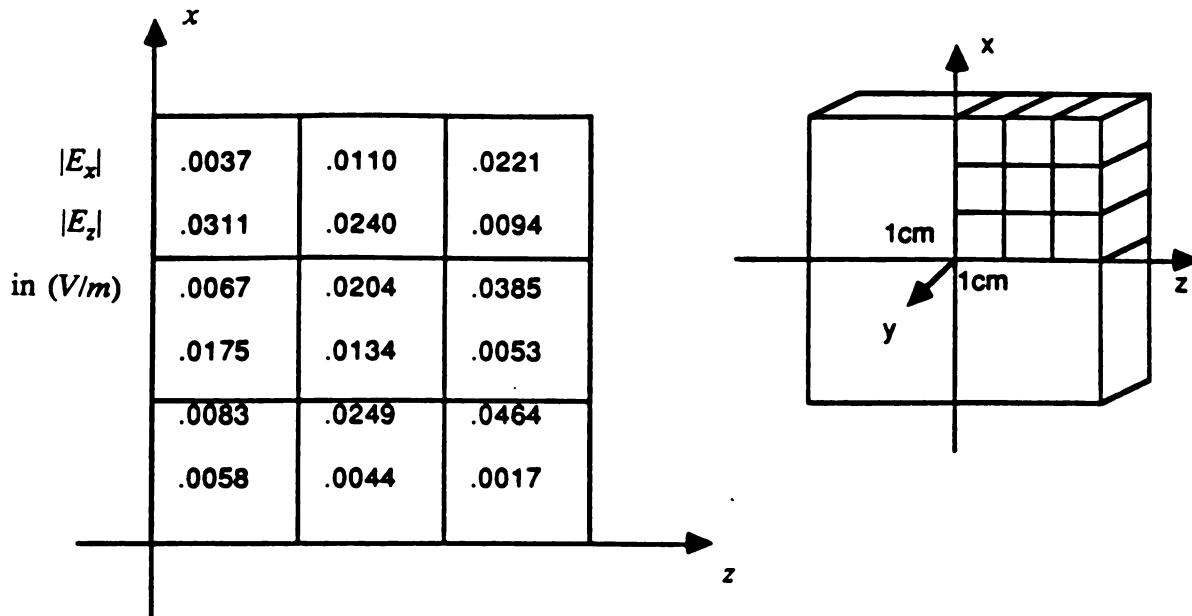


Fig-2.13 Conventional EFIE solutions based on 36-cell division.

$$E^i = x \sin(k_0 z)$$

$$f = 300 \text{ MHz}$$

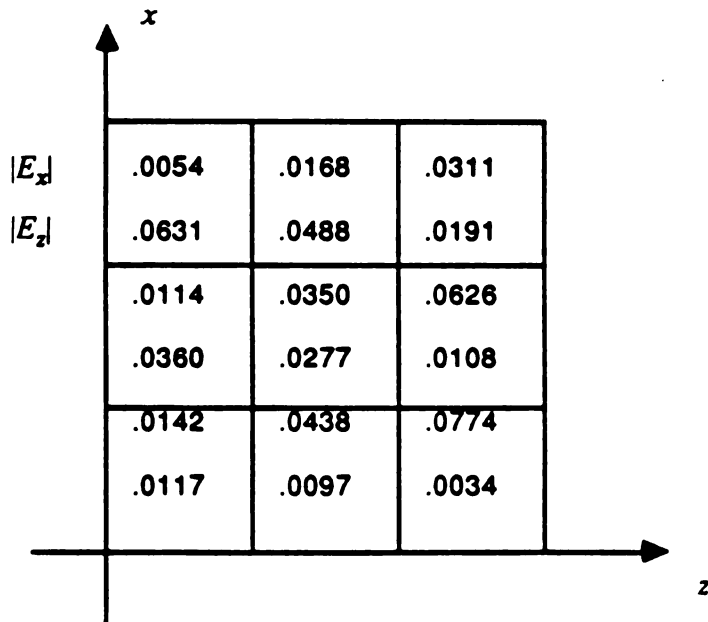


Fig-2.14 Conventional EFIE solutions based on 288-cell division.

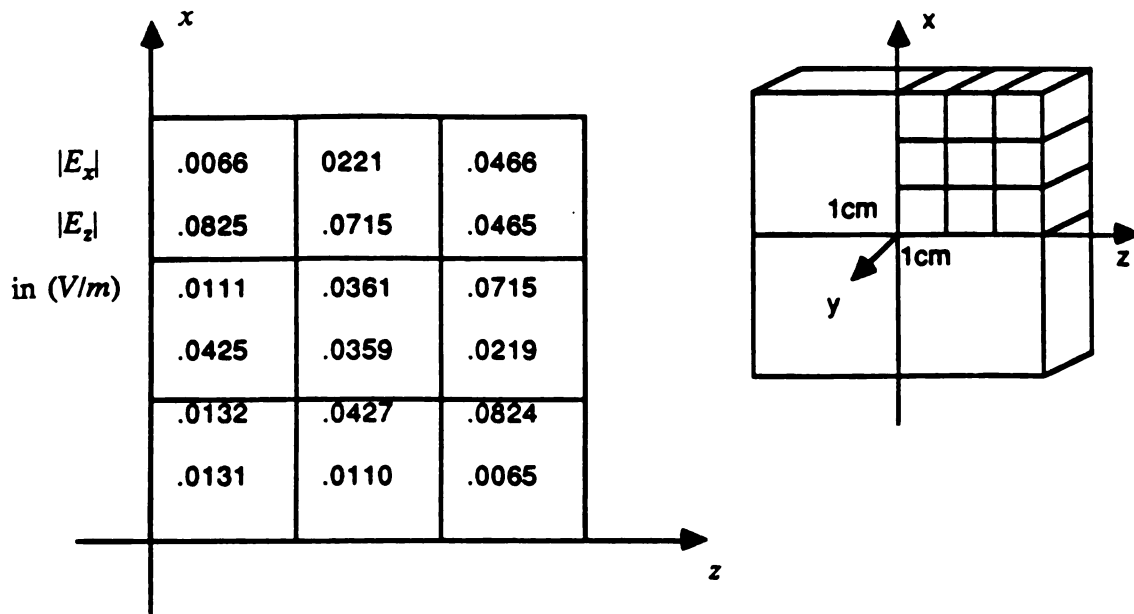


Fig-2.15 Iterative loop-EMF solutions based on 36-cell division.

$$E^i = x \sin(k_0 z)$$

$$f = 300 \text{ MHz}$$

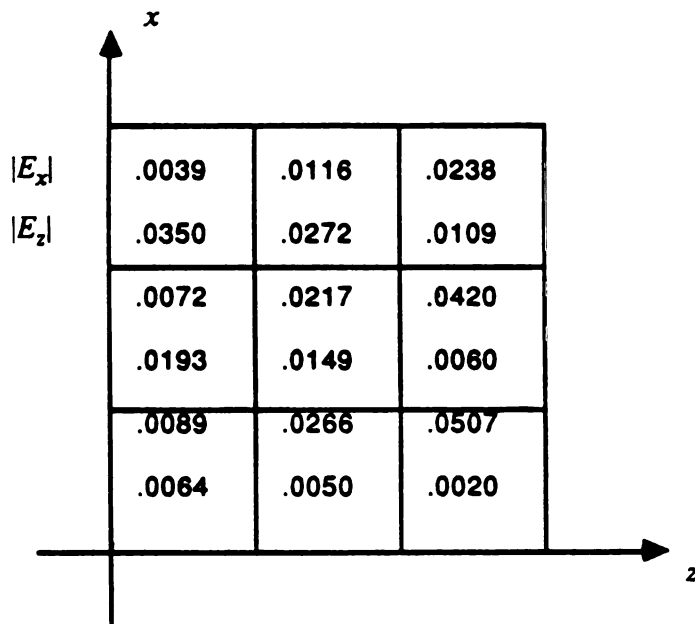


Fig-2.16 Equivalent magnetic current method solutions based on 36-cell division.

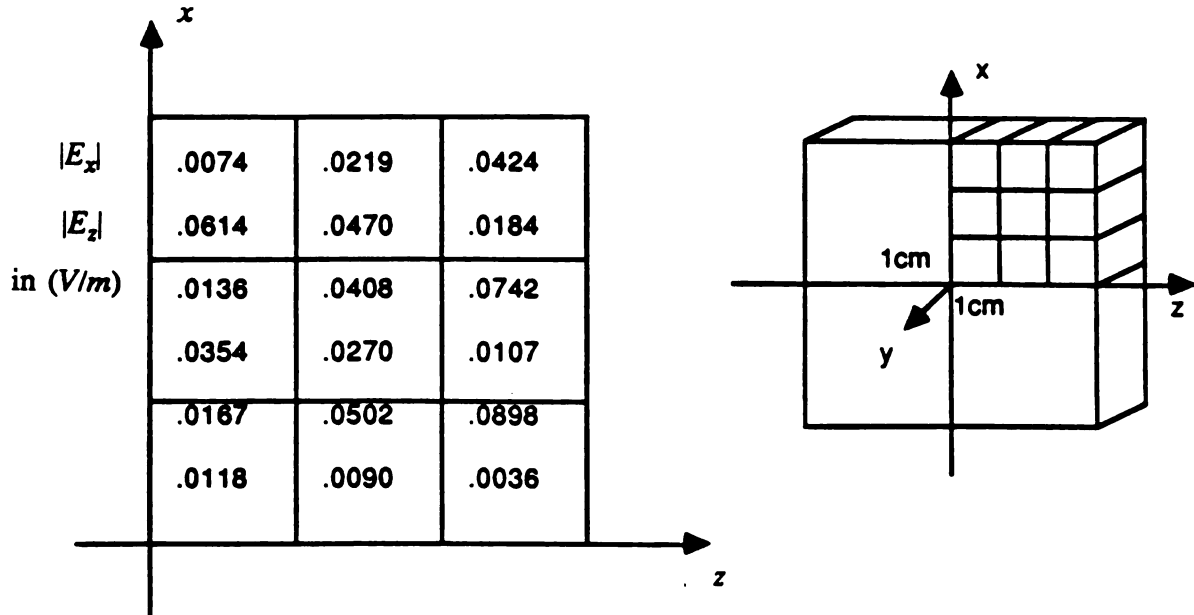


Fig-2.17 Conventional EFIE solutions based on 36-cell division.

$$E^i = x \sin(k_0 z)$$

$$f = 500 \text{ MHz}$$

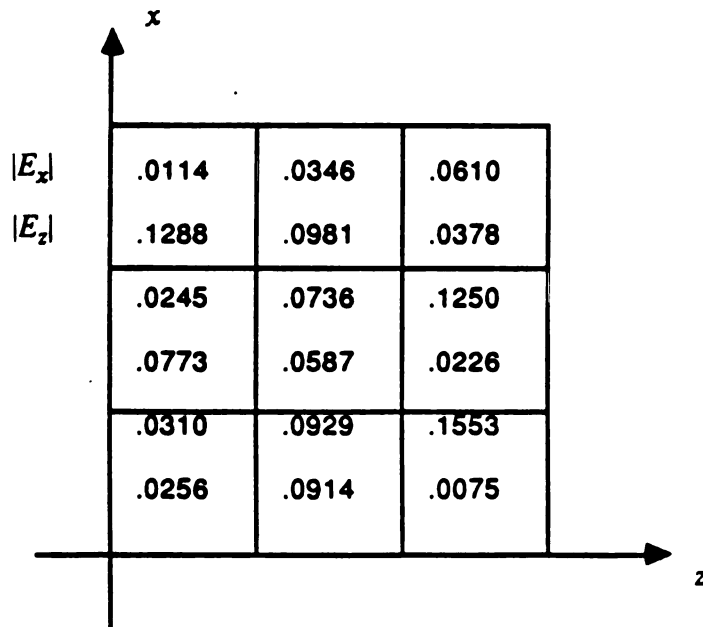


Fig-2.18 Conventional EFIE solutions based on 288-cell division.

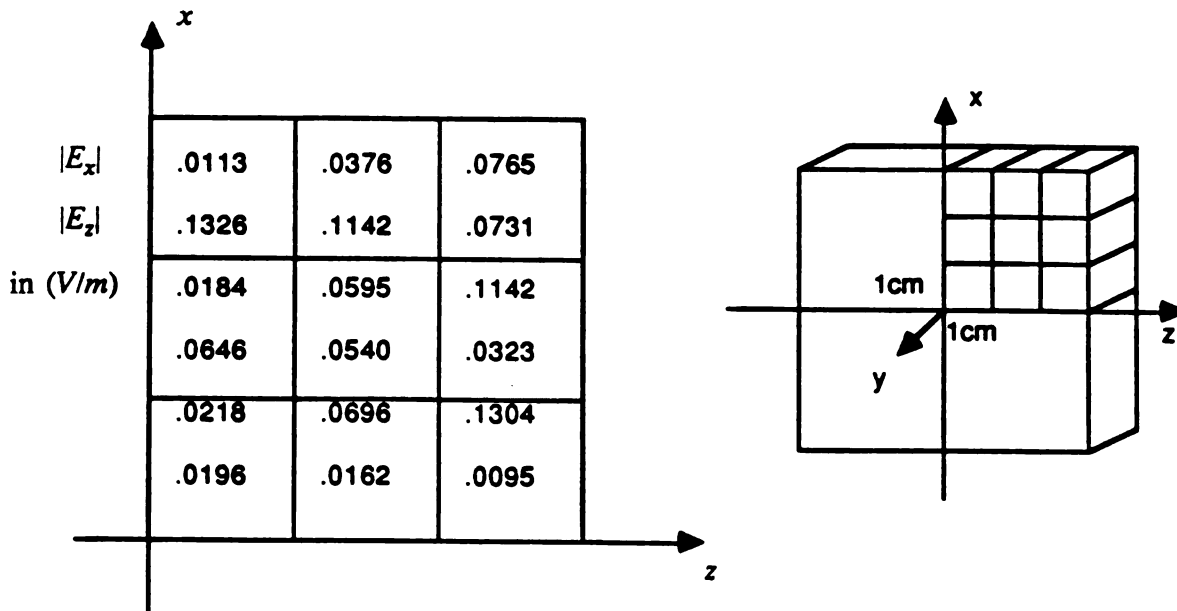


Fig-2.19 Iterative loop-EMF solutions based on 36-cell division.

$$E^i = x \sin(k_0 z)$$

$$f = 500 \text{ MHz}$$

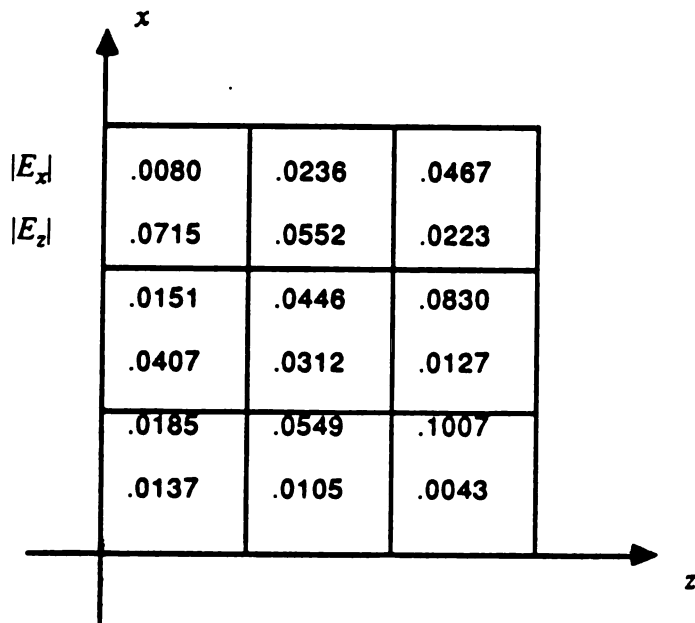


Fig-2.20 Equivalent magnetic current method solutions based on 36-cell division.

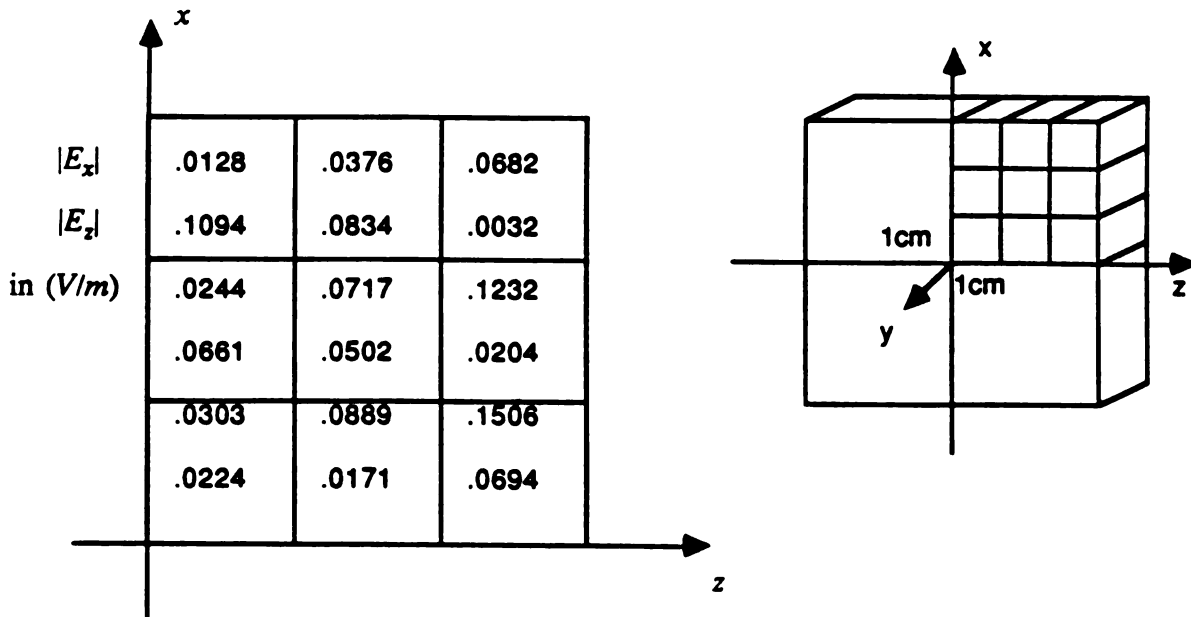


Fig-2.21 Conventional EFIE solutions based on 36-cell division.

$$E^i = x \sin(k_0 z)$$

$$f = 700 \text{ MHz}$$

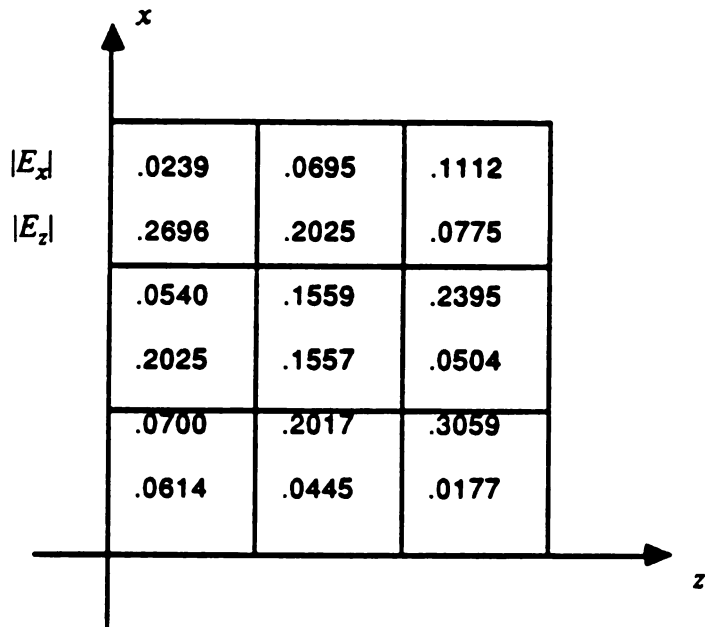


Fig-2.22 Conventional EFIE solutions based on 288-cell division.

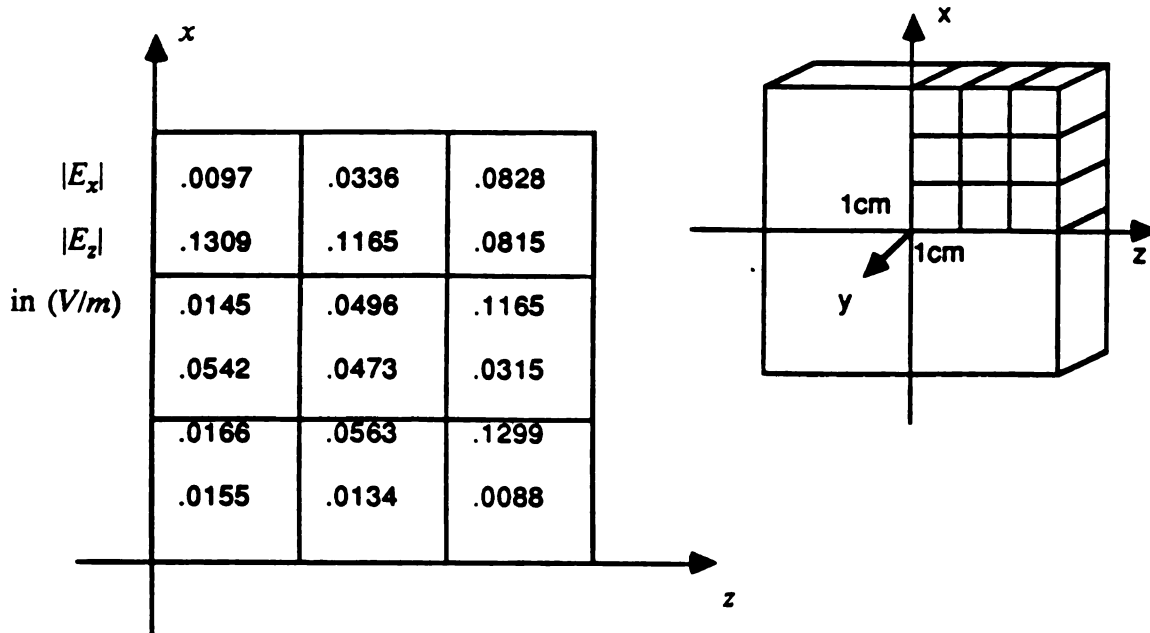


Fig-2.23 Iterative loop-EMF solutions based on 36-cell division.

$$E^i = x \sin(k_0 z)$$

$$f = 700 \text{ MHz}$$

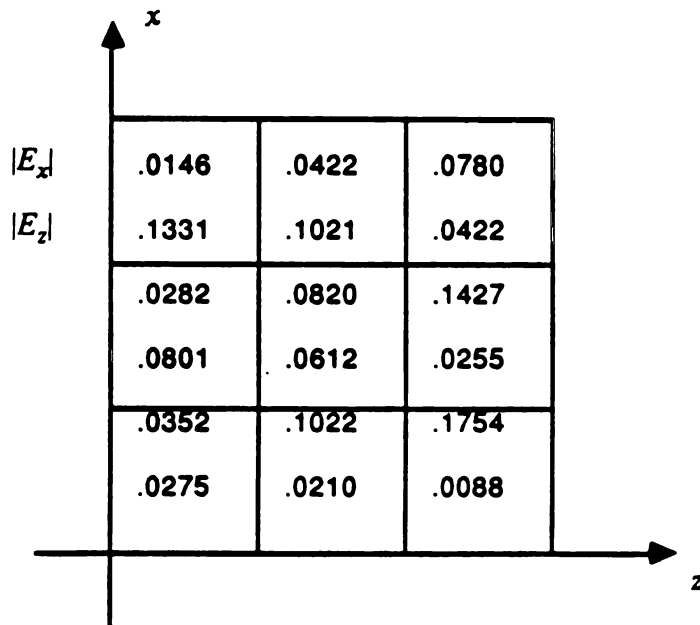
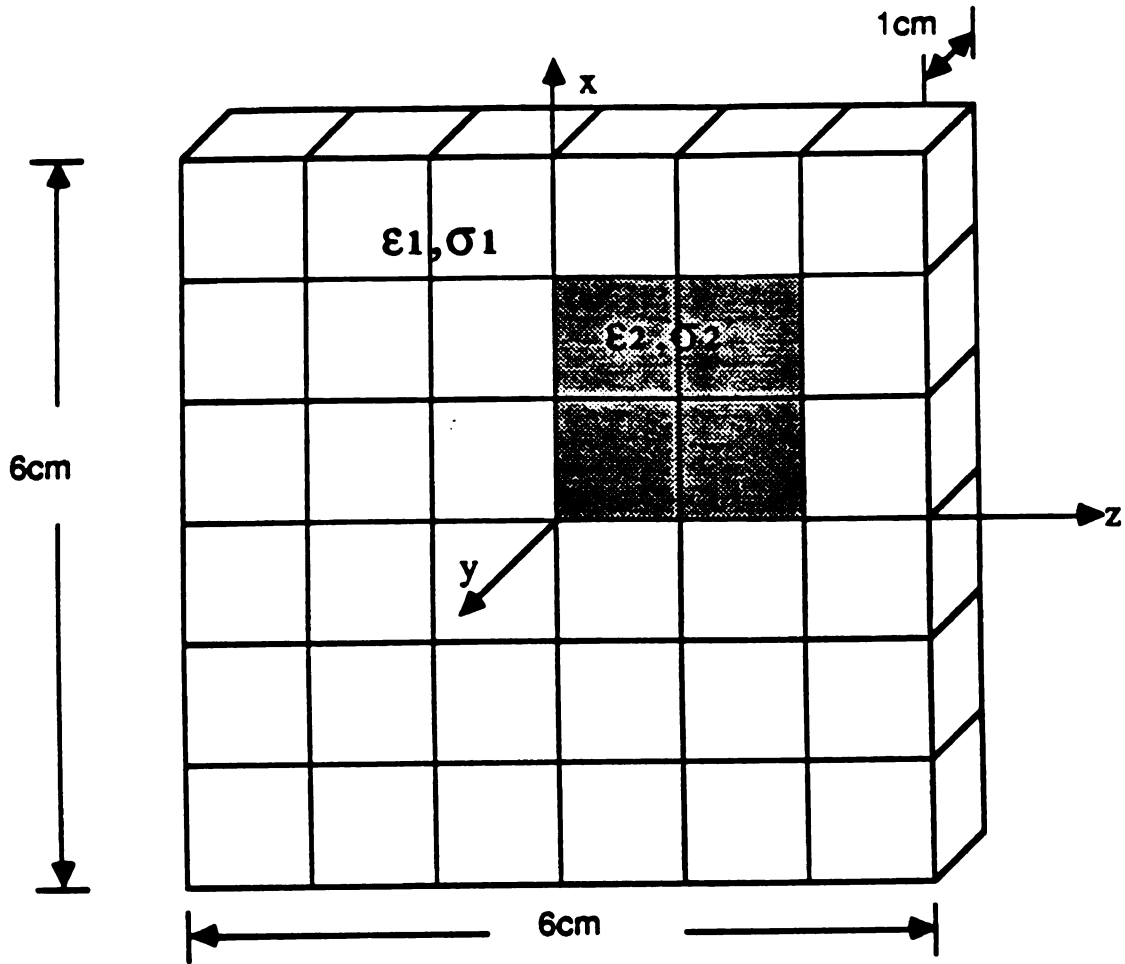


Fig-2.24 Equivalent magnetic current method solutions based on 36-cell division.



$$\epsilon_1 = 71.7 \epsilon_0$$

$$\sigma_1 = 0.889 \text{ S/m}$$

$$\epsilon_2 = 7.45 \epsilon_0$$

$$\sigma_2 = 0.048 \text{ S/m}$$

Fig-2.25 A heterogeneous body of dimensions $6 \times 6 \times 1 \text{ cm}$ with the parameters specified in the shaded and unshaded regions.

conductivities at boundaries of heterogeneous cells can be determined by two different approaches which do not yield the same result. The first approach simply uses the complex conductivity in each cell itself in the evaluation of the left hand side of Faraday's law (2.3.2). The second approach takes the average of the two different complex conductivities of two adjacent heterogeneous cells for the impedance of the common side. Fig-2.26 and Fig-2.27 are the numerical results of these two different approaches. It is observed that the field distribution is about the same in the region away from the heterogeneity but is somewhat different in the area near the heterogeneity. Further study is needed to determine which approach is more accurate.

$ E_x $.0163	.0018	.0212	.0212	.0018	.0163
$ E_z $.0027	.0208	.0050	.0004	.0018	.0027
in (V/m)	.0208	.0023	.0212	.0783	.0266	.0018
	.0009	.0059	.0005	.0533	.1671	.0009
$E^i = x \sin(k_0 z)$.0221	.0023	.0225	.0744	.0218	.0019
$f=500 \text{ MHz}$.0005	.0014	.0005	.0476	.2366	.0005
	.0221	.0023	.0266	.0266	.0023	.0221
	.0005	.0014	.0005	.0046	.0189	.0005
	.0208	.0023	.0257	.0257	.0023	.0208
	.0009	.0059	.0005	.0005	.0059	.0009
	.0163	.0018	.0212	.0212	.0018	.0163
	.0027	.0208	.0050	.0050	.0208	.0027

Fig-2.26 Iterative loop-EMF solutions in the heterogeneous body with the impedances determined by the complex conductivity of each cell.

$ E_x $.0178	.0001	.0196	.0148	.0027	.0124
$ E_z $.0015	.0236	.0008	.0041	.0076	.0043
in (V/m)	.0236	.0023	.0196	.0797	.0973	.0079
$E' = x \sin(k_0 z)$.0015	.0073	.0035	.0691	.0531	.0003
$f = 500 \text{ MHz}$.0251	.0022	.0209	.0776	.0974	.0079
	.0002	.0005	.0023	.0660	.1033	.0001
	.0241	.0002	.0257	.0181	.0028	.0165
	.0012	.0033	.0049	.0084	.0113	.0005
	.0218	.0015	.0261	.0228	.0005	.0192
	.0018	.0075	.0030	.0032	.0007	.0009
	.0166	.0014	.0214	.0203	.0013	.0158
	.0022	.0218	.0037	.0043	.0192	.0037

Fig-2.27 Iterative loop-EMF solutions in the heterogeneous body with the impedances determined by the average of the complex conductivities between two adjacent cells.

CHAPTER III

INTERACTION OF ELECTROMAGNETIC FIELDS

WITH

FINITE, HETEROGENEOUS, DIELECTRIC, MAGNETIC AND LOSSY BODIES

The induced EM fields in a finite, heterogeneous, dielectric, magnetic and lossy body irradiated by an incident plane EM wave are investigated in this chapter. Field integral equations of various forms are used to solve this problem. The first formulation is based on the method of equivalent polarized currents that yield a set of coupled tensor integral equations [3], [14]. Another set of coupled integral equations can be derived using the free space scalar Green's functions and the concepts of scalar and vector potentials maintained by equivalent currents and charges. These two sets of coupled integral equations are essentially equivalent and a proof will be given. The coupled tensor integral equations can be decoupled into a separated tensor electric field integral equation (Tensor EFIE) and a separated tensor magnetic field integral equation (Tensor MFIE) in different but equivalent forms [13], [16]. The separated tensor field integral equations can also be expressed in terms of free space scalar Green's functions instead of dyadic Green's functions in forms of more conventional EFIE and MFIE. Derivations of the integral equations and relations of different formulations are presented. The numerical comparisons of various integral equations are also included. In section 3.1, we introduce the derivation of the coupled tensor integral equations. Section 3.2 illustrates the procedures of decoupling the set of equations derived in section 3.1 and the relations with another set of decoupled integral equations developed by Tai [13]. Those integral equations in terms of free space scalar Green's function are presented in section 3.3. We will discuss and compare the numerical solutions of

these different equations in the last two sections.

3.1 Coupled Tensor Integral Equations

A set of coupled tensor integral equation has been derived by Chen [3] in 1981 to relate the induced EM fields inside a finite, arbitrarily shaped, heterogeneous body with the EM fields of an incident time harmonic plane wave. A brief outline of derivation is given in this section. Fig-3.1 shows a finite heterogeneous system composed of dielectric, magnetic and lossy medium with arbitrary shape, being exposed to an incident plane EM wave (\mathbf{E}^i , \mathbf{H}^i) with an angular frequency ω . The conductivity, permittivity and permeability of medium consisting this system are all functions of location, i.e.,

$$\sigma = \sigma(\mathbf{r}) \quad (3.1.1)$$

$$\epsilon = \epsilon(\mathbf{r}) \quad (3.1.2)$$

$$\mu = \mu(\mathbf{r}) , \quad (3.1.3)$$

where μ is a complex number since the system is assumed to possess some magnetic loss.

The generalized Maxwell's equations govern the electric and magnetic fields, \mathbf{E} and \mathbf{H} , maintained by a time harmonic source consisting of an electric current density \mathbf{J}^e and a magnetic current density \mathbf{J}^m in a medium with permittivity ϵ and permeability μ :

$$\nabla \times \mathbf{E}(\mathbf{r}) = -\mathbf{J}^m(\mathbf{r}) + i\omega\mu(\mathbf{r})\mathbf{H}(\mathbf{r}) \quad (3.1.4)$$

$$\nabla \times \mathbf{H}(\mathbf{r}) = \mathbf{J}^e(\mathbf{r}) - i\omega\epsilon(\mathbf{r})\mathbf{E}(\mathbf{r}) \quad (3.1.5)$$

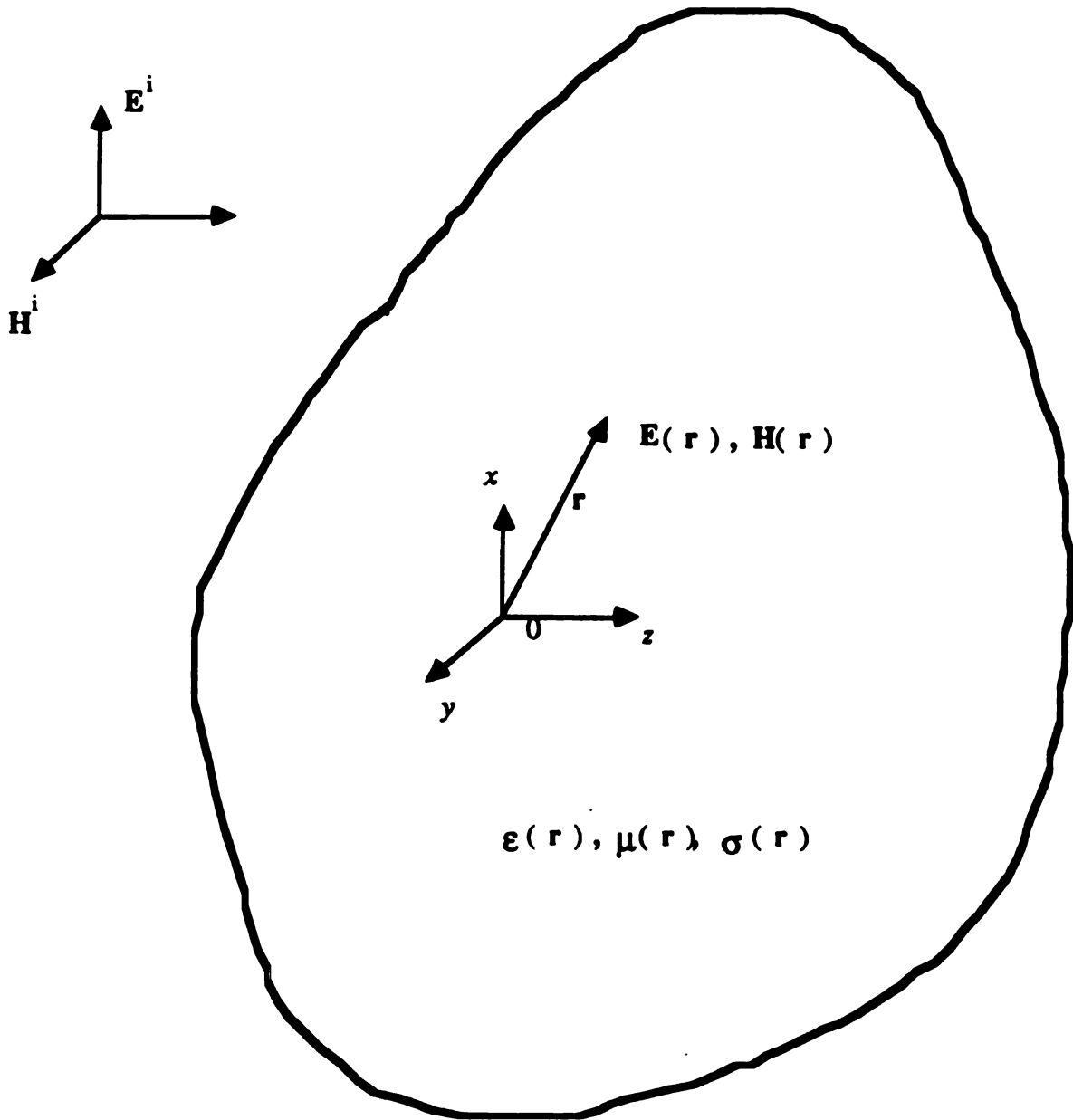


Fig-3.1 An arbitrarily shaped magnetic lossy body in free space illuminated by an incident EM wave.

$$\nabla \cdot [\mu(\mathbf{r})\mathbf{H}(\mathbf{r})] = \rho^m(\mathbf{r}) \quad (3.1.6)$$

$$\nabla \cdot [\varepsilon(\mathbf{r})\mathbf{E}(\mathbf{r})] = \rho^e(\mathbf{r}) , \quad (3.1.7)$$

where the time harmonic factor $e^{-i\omega t}$ is assumed and ρ^e , ρ^m are electric and magnetic volume charge density, respectively. The charge densities and current densities are related by the continuity equations as

$$\nabla \cdot \mathbf{J}^e(\mathbf{r}) - i\omega\rho^e(\mathbf{r}) = 0 \quad (3.1.8)$$

$$\nabla \cdot \mathbf{J}^m(\mathbf{r}) - i\omega\rho^m(\mathbf{r}) = 0 . \quad (3.1.9)$$

Our derivation is based on (3.1.4) to (3.1.9). In a source free region of free space, or in absence of the body, the incident electric and magnetic fields \mathbf{E}^i and \mathbf{H}^i must satisfy the following equations:

$$\nabla \times \mathbf{E}^i(\mathbf{r}) = i\omega\mu_0 \mathbf{H}^i(\mathbf{r}) \quad (3.1.10)$$

$$\nabla \times \mathbf{H}^i(\mathbf{r}) = -i\omega\varepsilon_0 \mathbf{E}^i(\mathbf{r}) . \quad (3.1.11)$$

The internal fields \mathbf{E} and \mathbf{H} inside the system which are induced by incident fields should also satisfy Maxwell's equations:

$$\nabla \times \mathbf{E}(\mathbf{r}) = i\omega\mu(\mathbf{r}) \mathbf{H}(\mathbf{r}) \quad (3.1.12)$$

$$\nabla \times \mathbf{H}(\mathbf{r}) = \sigma(\mathbf{r})\mathbf{E}(\mathbf{r}) - i\omega\varepsilon(\mathbf{r}) \mathbf{E}(\mathbf{r}) , \quad (3.1.13)$$

or we can rewrite them as

$$\nabla \times \mathbf{E}(\mathbf{r}) = -\mathbf{J}_{eq}^m(\mathbf{r}) + i\omega\mu_0\mathbf{H}(\mathbf{r}) \quad (3.1.14)$$

$$\nabla \times \mathbf{H}(\mathbf{r}) = \mathbf{J}_{eq}^e(\mathbf{r}) - i\omega\varepsilon_0\mathbf{E}(\mathbf{r}) , \quad (3.1.15)$$

where

$$\mathbf{J}_{eq}^e(\mathbf{r}) = \tau_e(\mathbf{r})\mathbf{E}(\mathbf{r}) = \left\{ \sigma(\mathbf{r}) - i\omega[\varepsilon(\mathbf{r}) - \varepsilon_0] \right\} \mathbf{E}(\mathbf{r}) \quad (3.1.16)$$

$$\mathbf{J}_{eq}^m(\mathbf{r}) = \tau_m(\mathbf{r})\mathbf{H}(\mathbf{r}) = -i\omega[\mu(\mathbf{r}) - \mu_0] \mathbf{H}(\mathbf{r}) \quad (3.1.17)$$

are defined as equivalent electric current density and equivalent magnetic current density, τ_e and τ_m are complex electric and magnetic conductivities, respectively. The scattered fields \mathbf{E}^s and \mathbf{H}^s are defined as follows:

$$\mathbf{E}^s(\mathbf{r}) = \mathbf{E}(\mathbf{r}) - \mathbf{E}^i(\mathbf{r}) \quad (3.1.18)$$

$$\mathbf{H}^s(\mathbf{r}) = \mathbf{H}(\mathbf{r}) - \mathbf{H}^i(\mathbf{r}) . \quad (3.1.19)$$

Subtracting (3.1.10) and (3.1.11) from (3.1.14) and (3.1.15), we can obtain equations in terms of \mathbf{E}^s and \mathbf{H}^s :

$$\nabla \times \mathbf{E}^s(\mathbf{r}) = -\mathbf{J}_{eq}^m(\mathbf{r}) + i\omega\mu_0\mathbf{H}^s(\mathbf{r}) \quad (3.1.20)$$

$$\nabla \times \mathbf{H}^s(\mathbf{r}) = \mathbf{J}_{eq}^e(\mathbf{r}) - i\omega\epsilon_0\mathbf{E}^s(\mathbf{r}) . \quad (3.1.21)$$

It is advantageous to express the scattering fields \mathbf{E}^s and \mathbf{H}^s as the sum of the electric mode fields, \mathbf{E}_e^s and \mathbf{H}_e^s , which are excited by \mathbf{J}_{eq}^e , and the magnetic mode fields, \mathbf{E}_m^s and \mathbf{H}_m^s , which are excited by \mathbf{J}_{eq}^m :

$$\mathbf{E}^s = \mathbf{E}_e^s + \mathbf{E}_m^s \quad (3.1.22)$$

$$\mathbf{H}^s = \mathbf{H}_e^s + \mathbf{H}_m^s . \quad (3.1.23)$$

Therefore (3.1.20) and (3.1.21) can be divided into two sets of differential equations of the electric mode and the magnetic mode:

$$\nabla \times \mathbf{E}_e^s(\mathbf{r}) = i\omega\mu_0\mathbf{H}_e^s(\mathbf{r}) \quad (3.1.24)$$

$$\nabla \times \mathbf{H}_e^s(\mathbf{r}) = \mathbf{J}_{eq}^e(\mathbf{r}) - i\omega\epsilon_0\mathbf{E}_e^s(\mathbf{r}) \quad (3.1.25)$$

and

$$\nabla \times \mathbf{E}_m^s(\mathbf{r}) = -\mathbf{J}_{eq}^m(\mathbf{r}) - i\omega\mu_0\mathbf{H}_m^s(\mathbf{r}) \quad (3.1.26)$$

$$\nabla \times \mathbf{H}_m^s(\mathbf{r}) = -i\omega\epsilon_0\mathbf{E}_m^s(\mathbf{r}) . \quad (3.1.27)$$

Now we can solve \mathbf{E}^s and \mathbf{H}^s in terms of \mathbf{J}_{eq}^e and \mathbf{J}_{eq}^m . From (3.1.24) and (3.1.25), we have

$$\nabla \times \nabla \times \mathbf{E}_e^s(\mathbf{r}) - k_0^2 \mathbf{E}_e^s(\mathbf{r}) = i\omega\mu_0 \mathbf{J}_{eq}^e(\mathbf{r}) \quad (3.1.28)$$

$$\nabla \times \nabla \times \mathbf{H}_e^s(\mathbf{r}) - k_0^2 \mathbf{H}_e^s(\mathbf{r}) = \nabla \times \mathbf{J}_{eq}^e(\mathbf{r}) . \quad (3.1.29)$$

Similarly from (3.1.26) and (3.1.27), we have

$$\nabla \times \nabla \times \mathbf{H}_m^s(\mathbf{r}) - k_0^2 \mathbf{H}_m^s(\mathbf{r}) = i\omega\epsilon_0 \mathbf{J}_{eq}^m(\mathbf{r}) \quad (3.1.30)$$

$$\nabla \times \nabla \times \mathbf{E}_m^s(\mathbf{r}) - k_0^2 \mathbf{E}_m^s(\mathbf{r}) = -\nabla \times \mathbf{J}_{eq}^m(\mathbf{r}) . \quad (3.1.31)$$

As mentioned in chapter II, the free space dyadic Green's function $\vec{\mathcal{G}}_0$ must satisfy the differential equation,

$$\nabla \times \nabla \times \vec{\mathcal{G}}_0(\mathbf{r}, \mathbf{r}') - k_0^2 \vec{\mathcal{G}}_0(\mathbf{r}, \mathbf{r}') = \vec{\mathcal{I}} \delta(\mathbf{r} - \mathbf{r}') , \quad (3.1.32)$$

and by Tai [4],

$$\vec{\mathcal{G}}_0(\mathbf{r}, \mathbf{r}') = \left(\vec{\mathcal{I}} + \frac{1}{k_0^2} \nabla \nabla \right) \phi(\mathbf{r}, \mathbf{r}') \quad \text{for } \mathbf{r} \neq \mathbf{r}' , \quad (3.1.33)$$

where $\phi(\mathbf{r}, \mathbf{r}')$ is the free space scalar Green's function. By the definition of the Green's function and the discussion of the singularity problem, that is, the correction term and the principal value integration, we obtain the expression of \mathbf{E}_e^s and \mathbf{H}_m^s [3] as

$$\begin{aligned} \mathbf{E}_e^s(\mathbf{r}) &= \int_v i\omega\mu_0 \mathbf{J}_{eq}^e(\mathbf{r}') \cdot \vec{\mathcal{G}}_0(\mathbf{r}, \mathbf{r}') dv' \\ &= P.V. \int_v i\omega\mu_0 \mathbf{J}_{eq}^e(\mathbf{r}') \cdot \vec{\mathcal{G}}_0(\mathbf{r}, \mathbf{r}') dv' + \frac{\mathbf{J}_{eq}^e(\mathbf{r})}{3i\omega\epsilon_0} \end{aligned} \quad (3.1.34)$$

$$\begin{aligned} \mathbf{H}_m^s(\mathbf{r}) &= \int_v i\omega\epsilon_0 \mathbf{J}_{eq}^m(\mathbf{r}') \cdot \vec{\mathcal{G}}_0(\mathbf{r}, \mathbf{r}') dv' \\ &= P.V. \int_v i\omega\epsilon_0 \mathbf{J}_{eq}^m(\mathbf{r}') \cdot \vec{\mathcal{G}}_0(\mathbf{r}, \mathbf{r}') dv' + \frac{\mathbf{J}_{eq}^m(\mathbf{r})}{3i\omega\mu_0} . \end{aligned} \quad (3.1.35)$$

\mathbf{E}_m^s and \mathbf{H}_e^s can be determined by using (3.1.24) and (3.1.27):

$$\begin{aligned}
\mathbf{H}_e^s(\mathbf{r}) &= -\frac{i}{\omega\mu_0} \nabla \times \mathbf{E}_e^s(\mathbf{r}) \\
&= \int_v [\nabla \times \vec{\mathcal{G}}_0(\mathbf{r}, \mathbf{r}')] \cdot \mathbf{J}_{eq}^e(\mathbf{r}') dv' \quad (3.1.36)
\end{aligned}$$

$$\begin{aligned}
\mathbf{E}_m^s(\mathbf{r}) &= \frac{i}{\omega\epsilon_0} \nabla \times \mathbf{H}_m^s(\mathbf{r}) \\
&= -\int_v [\nabla \times \vec{\mathcal{G}}_0(\mathbf{r}, \mathbf{r}')] \cdot \mathbf{J}_{eq}^m(\mathbf{r}') dv' . \quad (3.1.37)
\end{aligned}$$

The principle of superposition gives

$$\mathbf{E}(\mathbf{r}) = \mathbf{E}^i(\mathbf{r}) + \mathbf{E}^s(\mathbf{r}) = \mathbf{E}^i(\mathbf{r}) + \mathbf{E}_e^s(\mathbf{r}) + \mathbf{E}_m^s(\mathbf{r}) \quad (3.1.38)$$

$$\mathbf{H}(\mathbf{r}) = \mathbf{H}^i(\mathbf{r}) + \mathbf{H}^s(\mathbf{r}) = \mathbf{H}^i(\mathbf{r}) + \mathbf{H}_e^s(\mathbf{r}) + \mathbf{H}_m^s(\mathbf{r}) , \quad (3.1.39)$$

and this leads to the final results of the coupled tensor integral equations, i.e.,

$$\begin{aligned}
\left[1 + \frac{i\tau_e(\mathbf{r})}{3\omega\epsilon_0} \right] \mathbf{E}(\mathbf{r}) - P.V. \int_v i\omega\mu_0\tau_e(\mathbf{r}')\mathbf{E}(\mathbf{r}') \cdot \vec{\mathcal{G}}_0(\mathbf{r}, \mathbf{r}') dv' \\
- \int_v \tau_m(\mathbf{r}')\mathbf{H}(\mathbf{r}') \cdot [\nabla \times \vec{\mathcal{G}}_0(\mathbf{r}, \mathbf{r}')] dv' = \mathbf{E}^i(\mathbf{r}) \quad (3.1.40)
\end{aligned}$$

$$\begin{aligned}
\left[1 + \frac{i\tau_m(\mathbf{r})}{3\omega\mu_0} \right] \mathbf{H}(\mathbf{r}) - P.V. \int_v i\omega\epsilon_0\tau_m(\mathbf{r}')\mathbf{H}(\mathbf{r}') \cdot \vec{\mathcal{G}}_0(\mathbf{r}, \mathbf{r}') dv' \\
+ \int_v \tau_e(\mathbf{r}')\mathbf{E}(\mathbf{r}') \cdot [\nabla \times \vec{\mathcal{G}}_0(\mathbf{r}, \mathbf{r}')] dv' = \mathbf{H}^i(\mathbf{r}) . \quad (3.1.41)
\end{aligned}$$

Suppose we define

$$\vec{\mathcal{G}}_e^e(\mathbf{r}, \mathbf{r}') = i\omega\mu_0\vec{\mathcal{G}}_0(\mathbf{r}, \mathbf{r}') \quad (3.1.42)$$

$$\vec{\mathcal{G}}_m^m(\mathbf{r}, \mathbf{r}') = i\omega\epsilon_0\vec{\mathcal{G}}_0(\mathbf{r}, \mathbf{r}') \quad (3.1.43)$$

$$\vec{\mathcal{G}}_e^m(\mathbf{r}, \mathbf{r}') = -\vec{\mathcal{G}}_m^e(\mathbf{r}, \mathbf{r}') = \nabla \times \vec{\mathcal{G}}_0(\mathbf{r}, \mathbf{r}') = \nabla\phi(\mathbf{r}, \mathbf{r}') \times \vec{I} , \quad (3.1.44)$$

then (3.1.40) and (3.1.41) can be written as

$$\begin{aligned} \left[1 + \frac{i\tau_e(\mathbf{r})}{3\omega\epsilon_0} \right] \mathbf{E}(\mathbf{r}) - P.V. \int_v \tau_e(\mathbf{r}') \mathbf{E}(\mathbf{r}') \cdot \overleftrightarrow{\mathbf{G}}_e^e(\mathbf{r}, \mathbf{r}') dv' \\ + \int_v \tau_m(\mathbf{r}') \mathbf{H}(\mathbf{r}') \cdot \overleftrightarrow{\mathbf{G}}_m^e(\mathbf{r}, \mathbf{r}') dv' = \mathbf{E}^i(\mathbf{r}) \end{aligned} \quad (3.1.45)$$

$$\begin{aligned} \left[1 + \frac{i\tau_m(\mathbf{r})}{3\omega\mu_0} \right] \mathbf{H}(\mathbf{r}) - P.V. \int_v \tau_m(\mathbf{r}') \mathbf{H}(\mathbf{r}') \cdot \overleftrightarrow{\mathbf{G}}_m^m(\mathbf{r}, \mathbf{r}') dv' \\ + \int_v \tau_e(\mathbf{r}') \mathbf{E}(\mathbf{r}') \cdot \overleftrightarrow{\mathbf{G}}_e^m(\mathbf{r}, \mathbf{r}') dv' = \mathbf{H}^i(\mathbf{r}) . \end{aligned} \quad (3.1.46)$$

Equations (3.1.45) and (3.1.46) are the so called coupled tensor integral equations and can be transformed into a system of linear algebraic equations via pulse-basis expansion and point-matching. Both the electric and magnetic field distributions, $\mathbf{E}(\mathbf{r})$ and $\mathbf{H}(\mathbf{r})$, can thus be solved simultaneously. More descriptions about the transformation will be presented in section 3.4.

3.2 Decoupled Electric Field Integral Equation (EFIE) and Magnetic Field Integral Equation (MFIE)

The coupled tensor integral equations (3.1.45) and (3.1.46) which we have derived in the preceding section can be decomposed into a separated EFIE and a separated MFIE. Let's derive the tensor EFIE from (3.1.45) first. Rewriting (3.1.45):

$$\begin{aligned} \left[1 + \frac{i\tau_e(\mathbf{r})}{3\omega\epsilon_0} \right] \mathbf{E}(\mathbf{r}) - P.V. \int_v \tau_e(\mathbf{r}') \mathbf{E}(\mathbf{r}') \cdot \overleftrightarrow{\mathbf{G}}_e^e(\mathbf{r}, \mathbf{r}') dv' \\ + \int_v \tau_m(\mathbf{r}') \mathbf{H}(\mathbf{r}') \cdot \overleftrightarrow{\mathbf{G}}_m^e(\mathbf{r}, \mathbf{r}') dv' = \mathbf{E}^i(\mathbf{r}) . \end{aligned} \quad (3.1.45)$$

Equation (3.1.45) has the unknown \mathbf{H} in the second integral of the left hand side.

To eliminate \mathbf{H} , we can apply the Maxwell's equation:

$$\mathbf{H}(\mathbf{r}') = - \frac{i}{\omega\mu(\mathbf{r}')} \nabla' \times \mathbf{E}(\mathbf{r}') . \quad (3.2.1)$$

The integrand of the integral can then be written as

$$\tau_m(\mathbf{r}') \mathbf{H}(\mathbf{r}') \cdot \overleftrightarrow{\mathbf{G}}_m^e(\mathbf{r}, \mathbf{r}') = - \frac{i\tau_m(\mathbf{r}')}{\omega\mu(\mathbf{r}')} [\nabla' \times \mathbf{E}(\mathbf{r}')] \cdot \overleftrightarrow{\mathbf{G}}_m^e(\mathbf{r}, \mathbf{r}') . \quad (3.2.2)$$

We need to make use of the following dyadic and vector identities [15] to remove the curl operation on \mathbf{E} :

$$\nabla \cdot (\mathbf{A} \times \overleftrightarrow{\mathbf{G}}) = (\nabla \times \mathbf{A}) \cdot \overleftrightarrow{\mathbf{G}} - \mathbf{A} \cdot (\nabla \times \overleftrightarrow{\mathbf{G}}) \quad (3.2.3)$$

$$\nabla \times (\phi \mathbf{A}) = (\nabla \phi) \times \mathbf{A} + \phi (\nabla \times \mathbf{A}) . \quad (3.2.4)$$

Equation (3.2.2) then becomes

$$\begin{aligned} & \tau_m(\mathbf{r}') \mathbf{H}(\mathbf{r}') \cdot \overleftrightarrow{\mathbf{G}}_m^e(\mathbf{r}, \mathbf{r}') \\ &= \left\{ \nabla' \cdot \left[\frac{i\tau_m(\mathbf{r}')}{\omega\mu(\mathbf{r}')} \times \mathbf{E}(\mathbf{r}') \right] \right\} \cdot \overleftrightarrow{\mathbf{G}}_m^e(\mathbf{r}, \mathbf{r}') - \left\{ \nabla' \times \left[\frac{i\tau_m(\mathbf{r}')}{\omega\mu(\mathbf{r}')} \mathbf{E}(\mathbf{r}') \right] \right\} \cdot \overleftrightarrow{\mathbf{G}}_m^e(\mathbf{r}, \mathbf{r}') \\ &= \left\{ \nabla' \cdot \left[\frac{i\tau_m(\mathbf{r}')}{\omega\mu(\mathbf{r}')} \times \mathbf{E}(\mathbf{r}') \right] \right\} \cdot \overleftrightarrow{\mathbf{G}}_m^e(\mathbf{r}, \mathbf{r}') - \frac{i\tau_m(\mathbf{r}')}{\omega\mu(\mathbf{r}')} \mathbf{E}(\mathbf{r}') \cdot [\nabla' \times \overleftrightarrow{\mathbf{G}}_m^e(\mathbf{r}, \mathbf{r}')] \\ & \quad - \nabla' \cdot \left[\frac{i\tau_m(\mathbf{r}')}{\omega\mu(\mathbf{r}')} \mathbf{E}(\mathbf{r}') \times \overleftrightarrow{\mathbf{G}}_m^e(\mathbf{r}, \mathbf{r}') \right] . \end{aligned} \quad (3.2.5)$$

Since

$$\nabla' \times \overleftrightarrow{\mathbf{G}}_m^e(\mathbf{r}, \mathbf{r}') = \nabla' \times \nabla' \times \overleftrightarrow{\mathbf{G}}_0(\mathbf{r}, \mathbf{r}') = k_0^2 \overleftrightarrow{\mathbf{G}}_0(\mathbf{r}, \mathbf{r}') + \delta(\mathbf{r} - \mathbf{r}') \overleftrightarrow{\mathbf{I}} , \quad (3.2.6)$$

by integrating both sides of (3.2.5) over v and applying the divergence theorem to the last term of the right hand side, we have

$$\int_v \tau_m(\mathbf{r}') \mathbf{H}(\mathbf{r}') \cdot \overleftrightarrow{\mathbf{G}}_m^e(\mathbf{r}, \mathbf{r}') dv'$$

$$\begin{aligned}
&= \int_{\nu} \left\{ \nabla' \left[\frac{i\tau_m(\mathbf{r}')}{\omega\mu(\mathbf{r}')} \right] \times \mathbf{E}(\mathbf{r}') \right\} \cdot \overleftrightarrow{G}_m^e(\mathbf{r}, \mathbf{r}') d\nu' - \int_{\nu} k_0^2 \frac{i\tau_m(\mathbf{r}')}{\omega\mu(\mathbf{r}')} \mathbf{E}(\mathbf{r}') \cdot \overleftrightarrow{G}_0(\mathbf{r}, \mathbf{r}') d\nu' \\
&- \frac{i\tau_m(\mathbf{r})}{\omega\mu(\mathbf{r})} \mathbf{E}(\mathbf{r}) - \int_s \mathbf{n} \cdot \left[\frac{i\tau_m(\mathbf{r}')}{\omega\mu(\mathbf{r}')} \mathbf{E}(\mathbf{r}') \times \overleftrightarrow{G}_m^e(\mathbf{r}, \mathbf{r}') \right] ds' . \tag{3.2.7}
\end{aligned}$$

Note that the second volume integral in the right hand side of (3.2.7) is valid in the sense of Cauchy principal value, a correction term is again needed to overcome the singularity problem, i.e.,

$$\begin{aligned}
\int_{\nu} k_0^2 \frac{i\tau_m(\mathbf{r}')}{\omega\mu(\mathbf{r}')} \mathbf{E}(\mathbf{r}') \cdot \overleftrightarrow{G}_0(\mathbf{r}, \mathbf{r}') d\nu' &= P.V. \int_{\nu} \frac{\epsilon_0 \tau_m(\mathbf{r}')}{\mu(\mathbf{r}')} \mathbf{E}(\mathbf{r}') \cdot \overleftrightarrow{G}_e^e(\mathbf{r}, \mathbf{r}') d\nu' \\
&+ \frac{\tau_m(\mathbf{r})}{i3\omega\mu(\mathbf{r})} \mathbf{E}(\mathbf{r}) . \tag{3.2.8}
\end{aligned}$$

Substituting (3.2.7) and (3.2.8) into (3.1.45) and arranging terms, the decoupled EFIE can be written

$$\begin{aligned}
&\left[\frac{2\mu_0}{3\mu(\mathbf{r})} + \frac{\epsilon^*(\mathbf{r})}{3\epsilon_0} \right] \mathbf{E}(\mathbf{r}) + P.V. \int_{\nu} i\omega \left[\epsilon^*(\mathbf{r}') - \frac{\epsilon_0\mu_0}{\mu(\mathbf{r}')} \right] \mathbf{E}(\mathbf{r}') \cdot \overleftrightarrow{G}_e^e(\mathbf{r}, \mathbf{r}') d\nu' \\
&+ \int_{\nu} \nabla' \left[\frac{\mu(\mathbf{r}') - \mu_0}{\mu(\mathbf{r}')} \right] \times \mathbf{E}(\mathbf{r}') \cdot \overleftrightarrow{G}_m^e(\mathbf{r}, \mathbf{r}') d\nu' \\
&- \int_s \mathbf{n} \cdot \left[\frac{i\tau_m(\mathbf{r}')}{\omega\mu(\mathbf{r}')} \mathbf{E}(\mathbf{r}') \times \overleftrightarrow{G}_m^e(\mathbf{r}, \mathbf{r}') \right] ds' = \mathbf{E}^i(\mathbf{r}) , \tag{3.2.9}
\end{aligned}$$

where

$$\epsilon^*(\mathbf{r}) = \epsilon(\mathbf{r}) + \frac{i\sigma(\mathbf{r})}{\omega} . \tag{3.2.10}$$

The decoupled MFIE can be derived through a similar procedure. Rewriting (3.1.46):

$$\left[1 + \frac{i\tau_m(\mathbf{r})}{3\omega\mu_0} \right] \mathbf{H}(\mathbf{r}) - P.V. \int_{\nu} \tau_m(\mathbf{r}') \mathbf{H}(\mathbf{r}') \cdot \overleftrightarrow{G}_m^m(\mathbf{r}, \mathbf{r}') d\nu'$$

$$+ \int_{\nu} \tau_e(\mathbf{r}') \mathbf{E}(\mathbf{r}') \cdot \overleftrightarrow{G}_e^m(\mathbf{r}, \mathbf{r}') d\nu' = \mathbf{H}^i(\mathbf{r}) . \quad (3.1.46)$$

To eliminate \mathbf{E} in the second integral of the left hand side, we can apply the Maxwell's equation:

$$\mathbf{E}(\mathbf{r}') = \frac{i}{\omega \epsilon^*(\mathbf{r}')} \nabla' \times \mathbf{H}(\mathbf{r}') , \quad (3.2.11)$$

then its integrand can be written as

$$\tau_e(\mathbf{r}') \mathbf{E}(\mathbf{r}') \cdot \overleftrightarrow{G}_e^m(\mathbf{r}, \mathbf{r}') = - \frac{i\tau_e(\mathbf{r}')}{\omega \epsilon^*(\mathbf{r}')} [\nabla' \times \mathbf{H}(\mathbf{r}')] \cdot \overleftrightarrow{G}_e^m(\mathbf{r}, \mathbf{r}') . \quad (3.2.12)$$

By using the dyadic and vector identities (3.2.3) and (3.2.4), (3.2.12) then become:

$$\begin{aligned} & \tau_e(\mathbf{r}') \mathbf{E}(\mathbf{r}') \cdot \overleftrightarrow{G}_e^m(\mathbf{r}, \mathbf{r}') \\ &= \left\{ \nabla' \cdot \left[\frac{i\tau_e(\mathbf{r}')}{\omega \epsilon^*(\mathbf{r}')} \right] \times \mathbf{H}(\mathbf{r}') \right\} \overleftrightarrow{G}_e^m(\mathbf{r}, \mathbf{r}') - \left\{ \nabla' \times \left[\frac{i\tau_e(\mathbf{r}')}{\omega \epsilon^*(\mathbf{r}')} \mathbf{H}(\mathbf{r}') \right] \right\} \overleftrightarrow{G}_e^m(\mathbf{r}, \mathbf{r}') \\ &= \left\{ \nabla' \cdot \left[\frac{i\tau_e(\mathbf{r}')}{\omega \epsilon^*(\mathbf{r}')} \right] \times \mathbf{H}(\mathbf{r}') \right\} \overleftrightarrow{G}_e^m(\mathbf{r}, \mathbf{r}') - \frac{i\tau_e(\mathbf{r}')}{\omega \epsilon^*(\mathbf{r}')} \mathbf{H}(\mathbf{r}') \cdot [\nabla' \times \overleftrightarrow{G}_e^m(\mathbf{r}, \mathbf{r}')] \\ & \quad - \nabla' \cdot \left[\frac{i\tau_e(\mathbf{r}')}{\omega \epsilon^*(\mathbf{r}')} \mathbf{H}(\mathbf{r}') \times \overleftrightarrow{G}_e^m(\mathbf{r}, \mathbf{r}') \right] . \end{aligned} \quad (3.2.13)$$

Now since

$$\nabla' \times \overleftrightarrow{G}_e^m(\mathbf{r}, \mathbf{r}') = - \nabla' \times \nabla' \times \overleftrightarrow{G}_0(\mathbf{r}, \mathbf{r}') = - k_0^2 \overleftrightarrow{G}_0(\mathbf{r}, \mathbf{r}') - \delta(\mathbf{r} - \mathbf{r}') \overleftrightarrow{I} , \quad (3.2.14)$$

by integrating both sides of (3.2.13) over ν and applying the divergence theorem to the last term of the right hand side, we have

$$\begin{aligned} & \int_{\nu} \tau_e(\mathbf{r}') \mathbf{E}(\mathbf{r}') \cdot \overleftrightarrow{G}_e^m(\mathbf{r}, \mathbf{r}') d\nu' \\ &= - \int_{\nu} \left\{ \nabla' \cdot \left[\frac{i\tau_e(\mathbf{r}')}{\omega \epsilon^*(\mathbf{r}')} \right] \times \mathbf{H}(\mathbf{r}') \right\} \overleftrightarrow{G}_e^m(\mathbf{r}, \mathbf{r}') d\nu' - \int_{\nu} k_0^2 \frac{i\tau_e(\mathbf{r}')}{\omega \epsilon^*(\mathbf{r}')} \mathbf{H}(\mathbf{r}') \cdot \overleftrightarrow{G}_0(\mathbf{r}, \mathbf{r}') d\nu' \end{aligned}$$

$$-\frac{i\tau_e(\mathbf{r})}{\omega\epsilon^*(\mathbf{r})}\mathbf{H}(\mathbf{r}) + \int_s \mathbf{n} \cdot \left[\frac{i\tau_e(\mathbf{r}')}{\omega\epsilon^*(\mathbf{r}')} \mathbf{H}(\mathbf{r}') \times \vec{G}_e^m(\mathbf{r}, \mathbf{r}') \right] ds' \quad (3.2.15)$$

The second volume integral in the right hand side of (3.2.15) again needs a correction term and the principal value integration to overcome the singularity problem. This leads to

$$\begin{aligned} \int_v k_0^2 \frac{i\tau_e(\mathbf{r}')}{\omega\epsilon^*(\mathbf{r}')} \mathbf{H}(\mathbf{r}') \cdot \vec{G}_0(\mathbf{r}, \mathbf{r}') dv' &= P.V. \int_v \frac{\mu_0 \tau_e(\mathbf{r}')}{\epsilon^*(\mathbf{r}')} \mathbf{H}(\mathbf{r}') \cdot \vec{G}_m^m(\mathbf{r}, \mathbf{r}') dv' \\ &+ \frac{\tau_e(\mathbf{r})}{i3\omega\epsilon^*(\mathbf{r})} \mathbf{H}(\mathbf{r}) . \end{aligned} \quad (3.2.16)$$

Substituting (3.2.15) and (3.2.16) into (3.1.46) and arranging terms, the decoupled MFIE can be written as

$$\begin{aligned} \left[\frac{2\epsilon_0}{3\epsilon^*(\mathbf{r})} + \frac{\mu(\mathbf{r})}{3\mu_0} \right] \mathbf{H}(\mathbf{r}) + P.V. \int_v i\omega \left[\mu(\mathbf{r}') - \frac{\epsilon_0\mu_0}{\epsilon^*(\mathbf{r}')} \right] \mathbf{H}(\mathbf{r}') \cdot \vec{G}_m^m(\mathbf{r}, \mathbf{r}') dv' \\ + \int_v \nabla' \cdot \left[\frac{\epsilon^*(\mathbf{r}') - \epsilon_0}{\epsilon^*(\mathbf{r}')} \right] \times \mathbf{H}(\mathbf{r}') \cdot \vec{G}_e^m(\mathbf{r}, \mathbf{r}') dv' \\ - \int_s \mathbf{n} \cdot \left[\frac{i\tau_e(\mathbf{r}')}{\omega\epsilon^*(\mathbf{r}')} \mathbf{H}(\mathbf{r}') \times \vec{G}_e^m(\mathbf{r}, \mathbf{r}') \right] ds' = \mathbf{H}^i(\mathbf{r}) . \end{aligned} \quad (3.2.17)$$

To summarize the results, we rewrite (3.2.9) and (3.2.17) as

$$\begin{aligned} \left[\frac{2\mu_0}{3\mu(\mathbf{r})} + \frac{\epsilon^*(\mathbf{r})}{3\epsilon_0} \right] \mathbf{E}(\mathbf{r}) - P.V. \int_v k_0^2 \left[\frac{\epsilon^*(\mathbf{r}')}{\epsilon_0} - \frac{\mu_0}{\mu(\mathbf{r}')} \right] \mathbf{E}(\mathbf{r}') \cdot \vec{G}_0(\mathbf{r}, \mathbf{r}') dv' \\ - \int_v \mathbf{E}(\mathbf{r}') \times \nabla' \cdot \left[\frac{\mu(\mathbf{r}') - \mu_0}{\mu(\mathbf{r}')} \right] \cdot [\nabla' \times \vec{G}_0(\mathbf{r}, \mathbf{r}')] dv' \\ - \int_s \left[\frac{\mu(\mathbf{r}') - \mu_0}{\mu(\mathbf{r}')} \right] [\mathbf{n} \times \mathbf{E}(\mathbf{r}')] \cdot [\nabla' \times \vec{G}_0(\mathbf{r}, \mathbf{r}')] ds' = \mathbf{E}^i(\mathbf{r}) \end{aligned} \quad (3.2.18)$$

$$\left[\frac{2\epsilon_0}{3\epsilon^*(\mathbf{r})} + \frac{\mu(\mathbf{r})}{3\mu_0} \right] \mathbf{H}(\mathbf{r}) - P.V. \int_v k_0^2 \left[\frac{\mu(\mathbf{r}')}{\mu_0} - \frac{\epsilon_0}{\epsilon^*(\mathbf{r}')} \right] \mathbf{H}(\mathbf{r}') \cdot \vec{G}_0(\mathbf{r}, \mathbf{r}') dv'$$

$$\begin{aligned}
& - \int_v \mathbf{H}(\mathbf{r}') \times \nabla' \left[\frac{\epsilon^*(\mathbf{r}') - \epsilon_0}{\epsilon^*(\mathbf{r}')} \right] \cdot [\nabla' \times \vec{G}_0(\mathbf{r}, \mathbf{r}')] dv' \\
& - \int_s \left[\frac{\epsilon^*(\mathbf{r}') - \epsilon_0}{\epsilon^*(\mathbf{r}')} \right] [\mathbf{n} \times \mathbf{H}(\mathbf{r}')] \cdot [\nabla' \times \vec{G}_0(\mathbf{r}, \mathbf{r}')] ds' = \mathbf{H}^i(\mathbf{r}) \quad (3.2.19)
\end{aligned}$$

Equations (3.2.18) and (3.2.19) are decoupled tensor EFIE and MFIE, and can be transformed into two systems of linear algebraic equations with a proper choice of basis functions. The electric field and magnetic field distributions are computed numerically in section 3.4.

To check the validity of (3.2.18) and (3.2.19), they are compared with a set of decoupled integral equations for homogeneous body derived by Tai [13] here. Tai's integral equations are:

$$\begin{aligned}
\mathbf{E}(\mathbf{r}) - (k^2 - k_0^2) \int_v \vec{G}_0(\mathbf{r}, \mathbf{r}') \cdot \mathbf{E}(\mathbf{r}') dv' \\
+ \left[\frac{\mu - \mu_0}{\mu} \right] \int_s \vec{G}_0(\mathbf{r}, \mathbf{r}') \cdot [\mathbf{n} \times \nabla' \times \mathbf{E}(\mathbf{r}')] ds' = \mathbf{E}^i(\mathbf{r}) \quad (3.2.20)
\end{aligned}$$

$$\begin{aligned}
\mathbf{H}(\mathbf{r}) - (k^2 - k_0^2) \int_v \vec{G}_0(\mathbf{r}, \mathbf{r}') \cdot \mathbf{H}(\mathbf{r}') dv' \\
+ \left[\frac{\epsilon^* - \epsilon_0}{\epsilon^*} \right] \int_s \vec{G}_0(\mathbf{r}, \mathbf{r}') \cdot [\mathbf{n} \times \nabla' \times \mathbf{H}(\mathbf{r}')] ds' = \mathbf{H}^i(\mathbf{r}) \quad (3.2.21)
\end{aligned}$$

where the complex permittivity ϵ^* and the complex permeability μ are both constants inside the body and

$$k = \sqrt{\omega^2 \mu \epsilon^*} . \quad (3.2.22)$$

is the wave number in the homogeneous medium.

He started from the fact that the EM fields both inside and outside the body must satisfy the Maxwell's equations, then applied the vector-dyadic Green's theorem, finally matched the boundary conditions to obtain the above equations. This set of

equations can be proved to be equivalent to the equations derived in this section when the body is homogeneous. The proof is given in the appendix A.1. More discussions about the decoupled tensor integral equations are presented in section 3.5.

3.3 Coupled and Decoupled Integral Equations in Terms of Free Space Scalar Green's Function

The problem of solving induced EM fields in a finite, heterogeneous, dielectric, magnetic and lossy body due to an incident plane EM wave as described in the beginning of this chapter can be solved through another approach. When such a body is exposed to an incident EM field, there must exist induced electric and magnetic volume current densities and induced electric and magnetic volume charge densities inside the body, in addition to induced electric and magnetic surface charge densities on the boundary as indicated in Fig-3.2. We can then treat these induced currents and charges as equivalent sources in free space, and the scattered fields maintained by these sources are determined via the concept of potentials. In Fig-3.2, \mathbf{J}_{eq}^e , \mathbf{J}_{eq}^m , ρ_{eq}^e , ρ_{eq}^m represent volume equivalent electric, magnetic current densities and volume electric, magnetic charge densities, respectively, while ρ_s^e and ρ_s^m stand for the electric and magnetic surface charge densities, respectively.

The scalar and vector potentials, Φ^e and \mathbf{A}^e , due to the electric sources can be expressed as:

$$\Phi^e(\mathbf{r}) = \frac{1}{\epsilon_0} \int_v \rho_{eq}^e(\mathbf{r}') \phi(\mathbf{r}, \mathbf{r}') dv' + \frac{1}{\epsilon_0} \int_s \rho_s^e(\mathbf{r}') \phi(\mathbf{r}, \mathbf{r}') ds' \quad (3.3.1)$$

$$\mathbf{A}^e(\mathbf{r}) = \int_v \mathbf{J}_{eq}^e(\mathbf{r}') \phi(\mathbf{r}, \mathbf{r}') dv' , \quad (3.3.2)$$

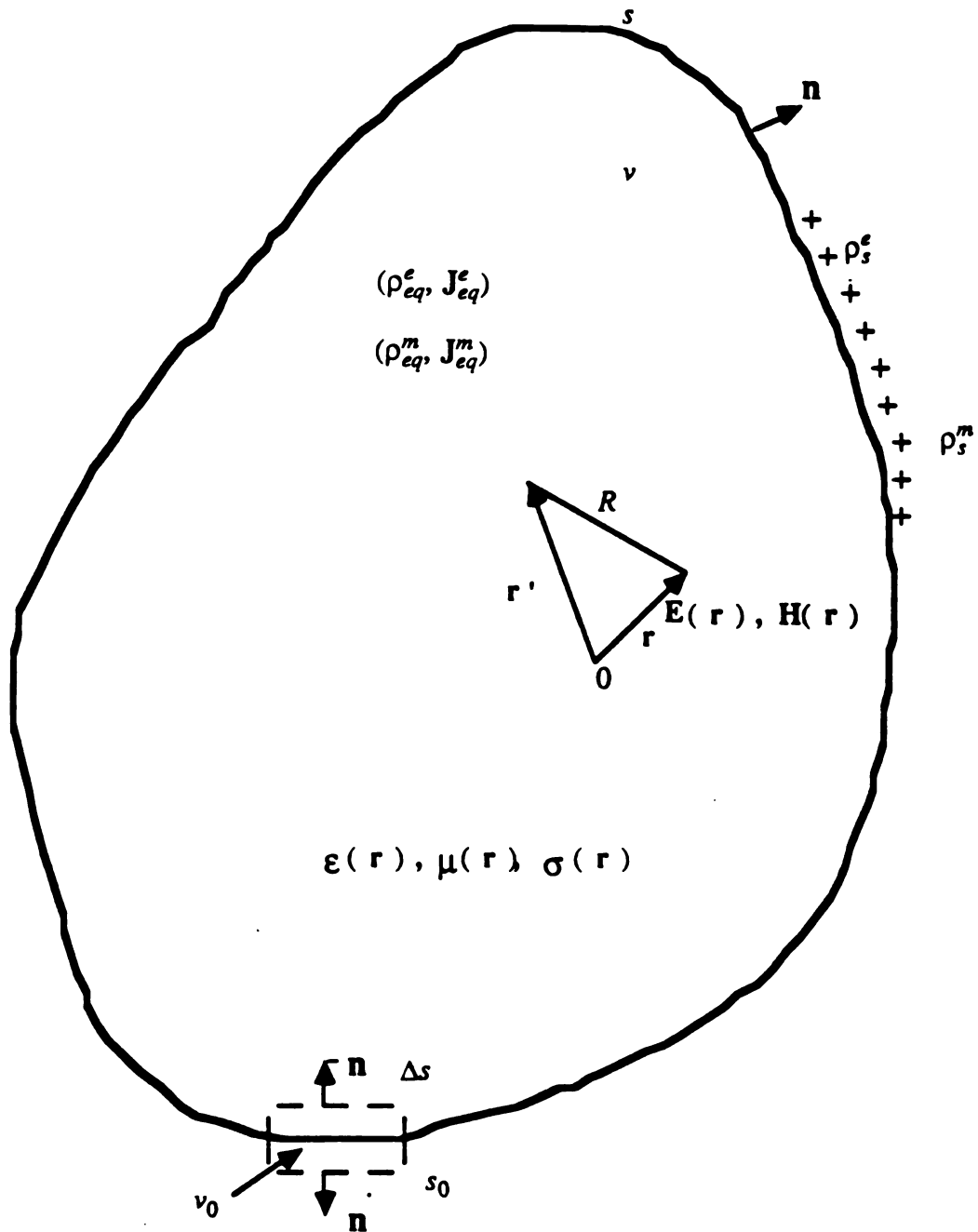


Fig-3.2 Illustration of the equivalent sources induced by the incident EM wave in the volume region v and on the enclosing surface s .

where v stands for the volume source region and s for the closed boundary surface enclosing region v , and

$$\phi(\mathbf{r}, \mathbf{r}') = \frac{e^{ik_0R}}{4\pi R} \quad (3.3.3)$$

is the free space scalar Green's function.

Similarly, the scalar and vector potentials, Φ^m and \mathbf{A}^m , due to the magnetic sources are

$$\Phi^m(\mathbf{r}) = \frac{1}{\mu_0} \int_v \rho_{eq}^m(\mathbf{r}') \phi(\mathbf{r}, \mathbf{r}') dv' + \frac{1}{\mu_0} \int_s \rho_s^m(\mathbf{r}') \phi(\mathbf{r}, \mathbf{r}') ds' \quad (3.3.4)$$

$$\mathbf{A}^m(\mathbf{r}) = \int_v \mathbf{J}_{eq}^m(\mathbf{r}') \phi(\mathbf{r}, \mathbf{r}') dv' . \quad (3.3.5)$$

The equivalent volume current densities have the following relations with the induced EM fields:

$$\mathbf{J}_{eq}^e(\mathbf{r}) = \tau_e(\mathbf{r})\mathbf{E}(\mathbf{r}) \quad (3.3.6)$$

$$\mathbf{J}_{eq}^m(\mathbf{r}) = \tau_m(\mathbf{r})\mathbf{H}(\mathbf{r}) \quad (3.3.7)$$

where

$$\tau_e(\mathbf{r}) = -i\omega(\epsilon^*(\mathbf{r}) - \epsilon_0) \quad (3.3.8)$$

$$\tau_m(\mathbf{r}) = -i\omega(\mu^*(\mathbf{r}) - \mu_0) \quad (3.3.9)$$

are the complex electric and magnetic conductivities and

$$\epsilon^*(\mathbf{r}) = \epsilon(\mathbf{r}) + \frac{i\sigma(\mathbf{r})}{\omega} \quad (3.3.10)$$

$$\mu^*(\mathbf{r}) = \mu(\mathbf{r}) \quad (3.3.11)$$

are the complex permittivity and permeability of the medium.

The scattered EM fields can be determined by knowing those scalar and vector potentials, namely,

$$\mathbf{E}^s(\mathbf{r}) = -\nabla\Phi^e(\mathbf{r}) + i\omega\mu_0\mathbf{A}^e(\mathbf{r}) - \nabla \times \mathbf{A}^m(\mathbf{r}) \quad (3.3.12)$$

$$\mathbf{H}^s(\mathbf{r}) = \nabla \times \mathbf{A}^e(\mathbf{r}) - \nabla\Phi^m(\mathbf{r}) + i\omega\epsilon_0\mathbf{A}^m(\mathbf{r}) . \quad (3.3.13)$$

The volume charge densities are related to the volume current densities by the continuity equations:

$$\rho_{eq}^e(\mathbf{r}') = -\frac{i}{\omega}\nabla' \cdot \mathbf{J}_{eq}^e(\mathbf{r}') \quad (3.3.14)$$

$$\rho_{eq}^m(\mathbf{r}') = -\frac{i}{\omega}\nabla' \cdot \mathbf{J}_{eq}^m(\mathbf{r}') . \quad (3.3.15)$$

Integrating (3.3.14) and (3.3.15) over the small pillowbox volume v_0 as shown in Fig-3.2, we obtain

$$\int_{v_0} \rho_{eq}^e(\mathbf{r}') dv' = -\frac{i}{\omega} \int_{v_0} \nabla' \cdot \mathbf{J}_{eq}^e(\mathbf{r}') dv' \quad (3.3.16)$$

$$\int_{v_0} \rho_{eq}^m(\mathbf{r}') dv' = -\frac{i}{\omega} \int_{v_0} \nabla' \cdot \mathbf{J}_{eq}^m(\mathbf{r}') dv' . \quad (3.3.17)$$

After the application of the divergence theorem to the right hand sides of (3.3.16) and (3.3.17), the results are simply

$$[-\mathbf{n} \cdot \mathbf{J}_{eq}^e(\mathbf{r}')]\Delta s = i\omega\rho_s^e\Delta s \quad (3.3.18)$$

$$[-\mathbf{n} \cdot \mathbf{J}_{eq}^m(\mathbf{r}')]\Delta s = i\omega\rho_s^m\Delta s , \quad (3.3.19)$$

where Δs is the inner surface of s_0 enclosing v_0 as shown in Fig 3.2. The surface charge densities are thus

$$\rho_s^e(\mathbf{r}') = \frac{i}{\omega} \mathbf{n} \cdot \mathbf{J}_{eq}^e(\mathbf{r}') \quad (3.3.20)$$

$$\rho_s^m(\mathbf{r}') = \frac{i}{\omega} \mathbf{n} \cdot \mathbf{J}_{eq}^m(\mathbf{r}') \quad (3.3.21)$$

over the exterior boundary s .

Since

$$\begin{aligned}\nabla \times [\mathbf{J}_{eq}^e(\mathbf{r}')\phi(\mathbf{r},\mathbf{r}')] &= \phi(\mathbf{r},\mathbf{r}') [\nabla \times \mathbf{J}_{eq}^e(\mathbf{r}')] + \nabla\phi(\mathbf{r},\mathbf{r}') \times \mathbf{J}_{eq}^e(\mathbf{r}') \\ &= - \mathbf{J}_{eq}^e(\mathbf{r}') \times \nabla\phi(\mathbf{r},\mathbf{r}')\end{aligned}\quad (3.3.22)$$

$$\begin{aligned}\nabla \times [\mathbf{J}_{eq}^m(\mathbf{r}')\phi(\mathbf{r},\mathbf{r}')] &= \phi(\mathbf{r},\mathbf{r}') [\nabla \times \mathbf{J}_{eq}^m(\mathbf{r}')] + \nabla\phi(\mathbf{r},\mathbf{r}') \times \mathbf{J}_{eq}^m(\mathbf{r}') \\ &= - \mathbf{J}_{eq}^m(\mathbf{r}') \times \nabla\phi(\mathbf{r},\mathbf{r}')\end{aligned}\quad (3.3.23)$$

and from (3.3.12), (3.3.13), we can to express the scattering fields, \mathbf{E}^s and \mathbf{H}^s , in terms of the equivalent volume current densities:

$$\begin{aligned}\mathbf{E}^s(\mathbf{r}) &= \int_v \left[\frac{i}{\omega\epsilon_0} (\nabla' \cdot \mathbf{J}_{eq}^e(\mathbf{r}')) \nabla\phi(\mathbf{r},\mathbf{r}') + i\omega\mu_0 \mathbf{J}_{eq}^e(\mathbf{r}')\phi(\mathbf{r},\mathbf{r}') \right] dv' \\ &\quad - \int_s \frac{i}{\omega\epsilon_0} (\mathbf{n} \cdot \mathbf{J}_{eq}^e(\mathbf{r}')) \nabla\phi(\mathbf{r},\mathbf{r}') ds' - \int_v \nabla\phi(\mathbf{r},\mathbf{r}') \times \mathbf{J}_{eq}^m(\mathbf{r}') dv'\end{aligned}\quad (3.3.24)$$

$$\begin{aligned}\mathbf{H}^s(\mathbf{r}) &= \int_v \nabla\phi(\mathbf{r},\mathbf{r}') \times \mathbf{J}_{eq}^e(\mathbf{r}') dv' - \int_s \frac{i}{\omega\mu_0} (\mathbf{n} \cdot \mathbf{J}_{eq}^m(\mathbf{r}')) \nabla\phi(\mathbf{r},\mathbf{r}') ds' \\ &\quad + \int_v \left[\frac{i}{\omega\mu_0} (\nabla' \cdot \mathbf{J}_{eq}^m(\mathbf{r}')) \nabla\phi(\mathbf{r},\mathbf{r}') + i\omega\epsilon_0 \mathbf{J}_{eq}^m(\mathbf{r}')\phi \right] dv' .\end{aligned}\quad (3.3.25)$$

Again by the definitions of scattered fields,

$$\mathbf{E} - \mathbf{E}^s = \mathbf{E}^i \quad (3.3.26)$$

$$\mathbf{H} - \mathbf{H}^s = \mathbf{H}^i , \quad (3.3.27)$$

in addition to the relations (3.3.6), (3.3.7) and (3.3.24), (3.3.25) we have just derived, another set of coupled integral equations are constructed as

$$\mathbf{E}(\mathbf{r}) - \frac{i\zeta}{k_0} \int_v \left\{ [\nabla' \cdot (\tau_e(\mathbf{r}')\mathbf{E}(\mathbf{r}'))] \nabla\phi(\mathbf{r},\mathbf{r}') + k_0^2 \tau_e(\mathbf{r}')\mathbf{E}(\mathbf{r}')\phi(\mathbf{r},\mathbf{r}') \right\} dv'$$

$$\begin{aligned}
& + \frac{i\zeta}{k_0} \int_s [\mathbf{n} \cdot (\boldsymbol{\tau}_e(\mathbf{r}') \mathbf{E}(\mathbf{r}'))] \nabla \phi(\mathbf{r}, \mathbf{r}') ds' + \int_v \boldsymbol{\tau}_m(\mathbf{r}') \mathbf{H}(\mathbf{r}') \times \nabla \phi(\mathbf{r}, \mathbf{r}') dv' \\
& = \mathbf{E}^i(\mathbf{r}) \tag{3.3.28}
\end{aligned}$$

$$\begin{aligned}
\mathbf{H}(\mathbf{r}) - \frac{i}{\zeta k_0} \int_v \left\{ [\nabla' \cdot (\boldsymbol{\tau}_m(\mathbf{r}') \mathbf{H}(\mathbf{r}'))] \nabla \phi(\mathbf{r}, \mathbf{r}') + k_0^2 \boldsymbol{\tau}_m(\mathbf{r}') \mathbf{H}(\mathbf{r}') \phi(\mathbf{r}, \mathbf{r}') \right\} dv' \\
+ \frac{i}{\zeta k_0} \int_s [\mathbf{n} \cdot (\boldsymbol{\tau}_m(\mathbf{r}') \mathbf{H}(\mathbf{r}'))] \nabla \phi(\mathbf{r}, \mathbf{r}') ds' - \int_v \boldsymbol{\tau}_e(\mathbf{r}') \mathbf{E}(\mathbf{r}') \times \nabla \phi(\mathbf{r}, \mathbf{r}') dv' \\
= \mathbf{H}^i(\mathbf{r}) , \tag{3.3.29}
\end{aligned}$$

where

$$\zeta = \sqrt{\frac{\mu_0}{\epsilon_0}} \tag{3.3.30}$$

is the wave impedance in the free space.

Equation (3.3.28) and (3.3.29) are the coupled integral equations in terms of free space scalar Green's function. They can also be transformed into a system of linear algebraic equations in a similar way as will be discussed in a latter section.

The two different formulations of the coupled integral equations derived in section 3.1 and here are actually equivalent. The proof is given in the appendix A.2.

The decoupled Tensor EFIE and MFIE (3.2.18) and (3.2.19) can also be expressed in terms of the free space scalar Green's function instead of the free space dyadic Green's functions. Since

$$\vec{G}_0(\mathbf{r}, \mathbf{r}') = \left(\vec{I} + \frac{1}{k_0^2} \nabla \nabla \right) \phi(\mathbf{r}, \mathbf{r}') , \tag{3.1.33}$$

(3.2.18) can be rewritten as

$$\begin{aligned}
& \left[\frac{2\mu_0}{3\mu(\mathbf{r})} + \frac{\epsilon^*(\mathbf{r})}{3\epsilon_0} \right] \mathbf{E}(\mathbf{r}) - \int_v k_0^2 \left[\frac{\epsilon^*(\mathbf{r}')}{\epsilon_0} - \frac{\mu_0}{\mu(\mathbf{r}')} \right] \mathbf{E}(\mathbf{r}') \phi(\mathbf{r}, \mathbf{r}') dv' \\
& - P.V. \int_v \left[\frac{\epsilon^*(\mathbf{r}')}{\epsilon_0} - \frac{\mu_0}{\mu(\mathbf{r}')} \right] \mathbf{E}(\mathbf{r}') \cdot \nabla \nabla \phi(\mathbf{r}, \mathbf{r}') dv' \\
& - \int_v \mathbf{E}(\mathbf{r}') \times \nabla' \left[\frac{\mu(\mathbf{r}') - \mu_0}{\mu(\mathbf{r}')} \right] \cdot [\nabla' \times \vec{G}_0(\mathbf{r}, \mathbf{r}')] dv' \\
& - \int_s \left[\frac{\mu(\mathbf{r}') - \mu_0}{\mu(\mathbf{r}')} \right] [\mathbf{n} \times \mathbf{E}(\mathbf{r}')] \cdot [\nabla' \times \vec{G}_0(\mathbf{r}, \mathbf{r}')] ds' = \mathbf{E}^i(\mathbf{r}) \quad (3.3.31)
\end{aligned}$$

In appendix A.2, we have shown that

$$\begin{aligned}
& \int_v [\nabla' \cdot \mathbf{A}(\mathbf{r}')] \nabla \phi(\mathbf{r}, \mathbf{r}') dv' - \int_s [\mathbf{n} \cdot \mathbf{A}(\mathbf{r}')] \nabla \phi(\mathbf{r}, \mathbf{r}') ds' \\
& = P.V. \int_v \mathbf{A}(\mathbf{r}') \cdot \nabla \nabla \phi(\mathbf{r}, \mathbf{r}') dv' - \frac{\mathbf{A}(\mathbf{r})}{3}, \quad (A2.1)
\end{aligned}$$

the second integral in the left hand side of (3.3.31), denoted as I_1 , can be written as

$$\begin{aligned}
I_1 &= \int_v \left\{ \nabla' \cdot \left[\left[\frac{\epsilon^*(\mathbf{r}')}{\epsilon_0} - \frac{\mu_0}{\mu(\mathbf{r}')} \right] \mathbf{E}(\mathbf{r}') \right] \right\} \nabla \phi(\mathbf{r}, \mathbf{r}') dv' \\
& - \int_s \left[\mathbf{n} \cdot \left[\frac{\epsilon^*(\mathbf{r}')}{\epsilon_0} - \frac{\mu_0}{\mu(\mathbf{r}')} \right] \mathbf{E}(\mathbf{r}') \right] \nabla \phi(\mathbf{r}, \mathbf{r}') ds' \\
& + \frac{1}{3} \left[\frac{\epsilon^*(\mathbf{r})}{\epsilon_0} - \frac{\mu_0}{\mu(\mathbf{r})} \right] \mathbf{E}(\mathbf{r}). \quad (3.3.32)
\end{aligned}$$

By using (A2.12),

$$\mathbf{A}(\mathbf{r}') \cdot [\nabla \times \vec{G}_0(\mathbf{r}, \mathbf{r}')] = \mathbf{A}(\mathbf{r}') \cdot [\nabla \phi(\mathbf{r}, \mathbf{r}') \times \vec{\mathcal{J}}] = \mathbf{A}(\mathbf{r}') \times \nabla \phi(\mathbf{r}, \mathbf{r}'). \quad (A2.12)$$

the third and fourth integrals in the left hand side of (3.3.31), can be rewritten in terms of the free space scalar Green's function.

Substituting (3.3.32) into (3.2.18) and using (A2.12), the decoupled EFIE can be expressed as follows:

$$\begin{aligned}
& \frac{\mu_0}{\mu(\mathbf{r})} \mathbf{E}(\mathbf{r}) - \int_{\nu} k_0^2 \left[\frac{\boldsymbol{\varepsilon}^*(\mathbf{r}')}{\varepsilon_0} - \frac{\mu_0}{\mu(\mathbf{r}')} \right] \mathbf{E}(\mathbf{r}') \phi(\mathbf{r}, \mathbf{r}') d\nu' \\
& - \int_{\nu} \left\{ \nabla' \cdot \left[\left[\frac{\boldsymbol{\varepsilon}^*(\mathbf{r}')}{\varepsilon_0} - \frac{\mu_0}{\mu(\mathbf{r}')} \right] \mathbf{E}(\mathbf{r}') \right] \right\} \nabla \phi(\mathbf{r}, \mathbf{r}') d\nu' \\
& + \int_s \left[\mathbf{n} \cdot \left[\frac{\boldsymbol{\varepsilon}^*(\mathbf{r}')}{\varepsilon_0} - \frac{\mu_0}{\mu(\mathbf{r}')} \right] \mathbf{E}(\mathbf{r}') \right] \nabla \phi(\mathbf{r}, \mathbf{r}') ds' \\
& - \int_{\nu} \mathbf{E}(\mathbf{r}') \times \nabla' \left[\frac{\mu(\mathbf{r}') - \mu_0}{\mu(\mathbf{r})} \right] \times \nabla \phi(\mathbf{r}, \mathbf{r}') d\nu' \\
& - \int_s \left[\frac{\mu(\mathbf{r}') - \mu_0}{\mu(\mathbf{r}')} \right] [\mathbf{n} \times \mathbf{E}(\mathbf{r}')] \times \nabla \phi(\mathbf{r}, \mathbf{r}') ds' = \mathbf{E}^i(\mathbf{r}) \quad (3.3.33)
\end{aligned}$$

Similarly the decoupled MFIE (3.2.19) can be rewritten as

$$\begin{aligned}
& \left[\frac{2\varepsilon_0}{3\varepsilon^*(\mathbf{r})} + \frac{\mu(\mathbf{r})}{3\mu_0} \right] \mathbf{H}(\mathbf{r}) - \int_{\nu} k_0^2 \left[\frac{\mu(\mathbf{r}')}{\mu_0} - \frac{\varepsilon_0}{\varepsilon^*(\mathbf{r}')} \right] \mathbf{H}(\mathbf{r}') \phi(\mathbf{r}, \mathbf{r}') d\nu' \\
& - P.V. \int_{\nu} \left[\frac{\mu(\mathbf{r}')}{\mu_0} - \frac{\varepsilon_0}{\varepsilon^*(\mathbf{r}')} \right] \mathbf{H}(\mathbf{r}') \cdot \nabla \nabla \phi(\mathbf{r}, \mathbf{r}') d\nu' \\
& - \int_{\nu} \mathbf{H}(\mathbf{r}') \times \nabla' \left[\frac{\varepsilon^*(\mathbf{r}') - \varepsilon_0}{\varepsilon^*(\mathbf{r}')} \right] \cdot [\nabla' \times \vec{G}_0(\mathbf{r}, \mathbf{r}')] d\nu' \\
& - \int_s \left[\frac{\varepsilon^*(\mathbf{r}') - \varepsilon_0}{\varepsilon^*(\mathbf{r}')} \right] [\mathbf{n} \times \mathbf{H}(\mathbf{r}')] \cdot [\nabla' \times \vec{G}_0(\mathbf{r}, \mathbf{r}')] ds' = \mathbf{H}^i(\mathbf{r}) \quad (3.3.34)
\end{aligned}$$

Suppose we make use of (A2.1) again, the second integral in the left hand side of (3.3.34), denoted as I_2 , can be written:

$$I_2 = \int_{\nu} \left\{ \nabla' \cdot \left[\left[\frac{\mu(\mathbf{r}')}{\mu_0} - \frac{\varepsilon_0}{\varepsilon^*(\mathbf{r}')} \right] \mathbf{H}(\mathbf{r}') \right] \right\} \nabla \phi(\mathbf{r}, \mathbf{r}') d\nu'$$

hand

tion.

expr

spa

can

and

$$\begin{aligned}
& - \int_s \left[\mathbf{n} \cdot \left[\frac{\mu(\mathbf{r}')}{\mu_0} - \frac{\epsilon_0}{\epsilon^*(\mathbf{r}')} \right] \mathbf{H}(\mathbf{r}') \right] \nabla \phi(\mathbf{r}, \mathbf{r}') ds' \\
& + \frac{1}{3} \left[\frac{\mu(\mathbf{r})}{\mu_0} - \frac{\epsilon_0}{\epsilon^*(\mathbf{r})} \right] \mathbf{H}(\mathbf{r}) . \tag{3.3.35}
\end{aligned}$$

Let us apply (A2.12) once more, then the third and fourth integrals in the left hand side of (3.3.35), can be rewritten in terms of the free space scalar Green's function.

Substituting (3.3.35) into (3.2.19) and using (A2.12), the decoupled MFIE can be expressed as follows:

$$\begin{aligned}
& \frac{\epsilon_0}{\epsilon^*(\mathbf{r})} \mathbf{H}(\mathbf{r}) - \int_v k_0^2 \left[\frac{\mu(\mathbf{r}')}{\mu_0} - \frac{\epsilon_0}{\epsilon^*(\mathbf{r}')} \right] \mathbf{H}(\mathbf{r}') \phi(\mathbf{r}, \mathbf{r}') dv' \\
& - \int_v \left\{ \nabla' \cdot \left[\left[\frac{\mu(\mathbf{r}')}{\mu_0} - \frac{\epsilon_0}{\epsilon^*(\mathbf{r}')} \right] \mathbf{H}(\mathbf{r}') \right] \right\} \nabla \phi(\mathbf{r}, \mathbf{r}') dv' \\
& + \int_s \left[\mathbf{n} \cdot \left[\frac{\mu(\mathbf{r}')}{\mu_0} - \frac{\epsilon_0}{\epsilon^*(\mathbf{r}')} \right] \mathbf{H}(\mathbf{r}') \right] \nabla \phi(\mathbf{r}, \mathbf{r}') ds' \\
& - \int_v \mathbf{H}(\mathbf{r}') \times \nabla' \left[\frac{\epsilon^*(\mathbf{r}') - \epsilon_0}{\epsilon^*(\mathbf{r}')} \right] \times \nabla \phi(\mathbf{r}, \mathbf{r}') dv' \\
& - \int_s \left[\frac{\epsilon^*(\mathbf{r}') - \epsilon_0}{\epsilon^*(\mathbf{r}')} \right] [\mathbf{n} \times \mathbf{H}(\mathbf{r}')] \times \nabla \phi(\mathbf{r}, \mathbf{r}') ds' = \mathbf{H}^i(\mathbf{r}) . \tag{3.3.36}
\end{aligned}$$

Equations (3.3.33) and (3.3.36) are decoupled EFIE and MFIE in terms of free space scalar Green's functions. Numerical solutions of these integral equations can be carried out similarly as before. It is noted that we have attempted to derive (3.3.33) and (3.3.36) directly from (3.3.28) and (3.3.29) without success.

3.4 Numerical Solutions of Various Integral Equations with Pulse-Basis Expansion and Point-matching

The various integral equations introduced from section 3.1 to 3.3 are solved numerically by pulse-basis expansion and point-matching. After the testing procedure, these integral equations can be transformed into systems of linear algebraic equations which can be solved easily in a manner as described in section 2.3. In all cases discussed in this section, the body is assumed to be partitioned into N cells, while v_n denotes the n -th cell with the center point located at \mathbf{r}_n . The field at the center of each cell is formed by solving a system of linear algebraic equations. Some symmetry properties of the problem were used to reduce the order of the system of linear algebraic equations. The coupled tensor integral equations (3.1.45) and (3.1.46) are investigated first.

Let us rewrite the coupled tensor integral equations:

$$\left[1 + \frac{i\tau_e(\mathbf{r})}{3\omega\epsilon_0} \right] \mathbf{E}(\mathbf{r}) - P.V. \int_{v} \tau_e(\mathbf{r}') \mathbf{E}(\mathbf{r}') \cdot \overleftrightarrow{G}_e^e(\mathbf{r}, \mathbf{r}') dv' \\ + \int_{v} \tau_m(\mathbf{r}') \mathbf{H}(\mathbf{r}') \cdot \overleftrightarrow{G}_m^e(\mathbf{r}, \mathbf{r}') dv' = \mathbf{E}^i(\mathbf{r}) \quad (3.1.45)$$

$$\left[1 + \frac{i\tau_m(\mathbf{r})}{3\omega\mu_0} \right] \mathbf{H}(\mathbf{r}) - P.V. \int_{v} \tau_m(\mathbf{r}') \mathbf{H}(\mathbf{r}') \cdot \overleftrightarrow{G}_m^m(\mathbf{r}, \mathbf{r}') dv' \\ + \int_{v} \tau_e(\mathbf{r}') \mathbf{E}(\mathbf{r}') \cdot \overleftrightarrow{G}_e^m(\mathbf{r}, \mathbf{r}') dv' = \mathbf{H}^i(\mathbf{r}) . \quad (3.1.46)$$

Note that

$$\overleftrightarrow{G}_e^e(\mathbf{r}, \mathbf{r}') = i\omega\mu_0 \overleftrightarrow{G}_0(\mathbf{r}, \mathbf{r}') \quad (3.1.42)$$

$$\overleftrightarrow{G}_m^m(\mathbf{r}, \mathbf{r}') = i\omega\epsilon_0 \overleftrightarrow{G}_0(\mathbf{r}, \mathbf{r}') \quad (3.1.43)$$

$$\vec{G}_e^m(\mathbf{r}, \mathbf{r}') = -\vec{G}_m^e(\mathbf{r}, \mathbf{r}') = \nabla \times \vec{G}_0(\mathbf{r}, \mathbf{r}') = \nabla \phi \times \vec{Y}. \quad (3.1.44)$$

In (3.1.45), the inner product $\mathbf{E}(\mathbf{r}') \cdot \vec{G}_0(\mathbf{r}, \mathbf{r}')$ can be represented by a matrix product as

$$\begin{aligned} & \mathbf{E}(\mathbf{r}') \cdot \vec{G}_0(\mathbf{r}, \mathbf{r}') \\ &= \begin{bmatrix} \phi(\mathbf{r}, \mathbf{r}') + \frac{1}{k_0^2} \phi_{xx}(\mathbf{r}, \mathbf{r}') & \frac{1}{k_0^2} \phi_{xy}(\mathbf{r}, \mathbf{r}') & \frac{1}{k_0^2} \phi_{xz}(\mathbf{r}, \mathbf{r}') \\ \frac{1}{k_0^2} \phi_{yx}(\mathbf{r}, \mathbf{r}') & \phi(\mathbf{r}, \mathbf{r}') + \frac{1}{k_0^2} \phi_{yy}(\mathbf{r}, \mathbf{r}') & \frac{1}{k_0^2} \phi_{yz}(\mathbf{r}, \mathbf{r}') \\ \frac{1}{k_0^2} \phi_{zx}(\mathbf{r}, \mathbf{r}') & \frac{1}{k_0^2} \phi_{zy}(\mathbf{r}, \mathbf{r}') & \phi(\mathbf{r}, \mathbf{r}') + \frac{1}{k_0^2} \phi_{zz}(\mathbf{r}, \mathbf{r}') \end{bmatrix} \begin{bmatrix} E_x(\mathbf{r}') \\ E_y(\mathbf{r}') \\ E_z(\mathbf{r}') \end{bmatrix} \end{aligned} \quad (3.4.1)$$

while the inner product $\mathbf{H}(\mathbf{r}') \cdot [\nabla \times \vec{G}_0(\mathbf{r}, \mathbf{r}')] = \mathbf{H}(\mathbf{r}') \cdot \vec{G}_e^m(\mathbf{r}, \mathbf{r}')$ can be represented by another matrix product as

$$\mathbf{H}(\mathbf{r}') \cdot [\nabla \times \vec{G}_0(\mathbf{r}, \mathbf{r}')] = \begin{bmatrix} 0 & -\phi_z(\mathbf{r}, \mathbf{r}') & \phi_y(\mathbf{r}, \mathbf{r}') \\ \phi_z(\mathbf{r}, \mathbf{r}') & 0 & -\phi_x(\mathbf{r}, \mathbf{r}') \\ -\phi_y(\mathbf{r}, \mathbf{r}') & \phi_x(\mathbf{r}, \mathbf{r}') & 0 \end{bmatrix} \begin{bmatrix} H_x(\mathbf{r}') \\ H_y(\mathbf{r}') \\ H_z(\mathbf{r}') \end{bmatrix} \quad (3.4.2)$$

Similarly in (3.1.46), the inner product $\mathbf{H}(\mathbf{r}') \cdot \vec{G}_0(\mathbf{r}, \mathbf{r}')$ can be represented by a matrix product as

$$\begin{aligned} & \mathbf{H}(\mathbf{r}') \cdot \vec{G}_0(\mathbf{r}, \mathbf{r}') \\ &= \begin{bmatrix} \phi(\mathbf{r}, \mathbf{r}') + \frac{1}{k_0^2} \phi_{xx}(\mathbf{r}, \mathbf{r}') & \frac{1}{k_0^2} \phi_{xy}(\mathbf{r}, \mathbf{r}') & \frac{1}{k_0^2} \phi_{xz}(\mathbf{r}, \mathbf{r}') \\ \frac{1}{k_0^2} \phi_{yx}(\mathbf{r}, \mathbf{r}') & \phi(\mathbf{r}, \mathbf{r}') + \frac{1}{k_0^2} \phi_{yy}(\mathbf{r}, \mathbf{r}') & \frac{1}{k_0^2} \phi_{yz}(\mathbf{r}, \mathbf{r}') \\ \frac{1}{k_0^2} \phi_{zx}(\mathbf{r}, \mathbf{r}') & \frac{1}{k_0^2} \phi_{zy}(\mathbf{r}, \mathbf{r}') & \phi(\mathbf{r}, \mathbf{r}') + \frac{1}{k_0^2} \phi_{zz}(\mathbf{r}, \mathbf{r}') \end{bmatrix} \begin{bmatrix} H_x(\mathbf{r}') \\ H_y(\mathbf{r}') \\ H_z(\mathbf{r}') \end{bmatrix} \end{aligned} \quad (3.4.3)$$

while the inner product $\mathbf{E}(\mathbf{r}') \cdot [\nabla \times \vec{G}_0(\mathbf{r}, \mathbf{r}')]]$ can be represented by another matrix product as

$$\mathbf{E}(\mathbf{r}') \cdot [\nabla \times \vec{G}_0(\mathbf{r}, \mathbf{r}')]] = \begin{bmatrix} 0 & -\phi_z(\mathbf{r}, \mathbf{r}') & \phi_y(\mathbf{r}, \mathbf{r}') \\ \phi_z(\mathbf{r}, \mathbf{r}') & 0 & -\phi_x(\mathbf{r}, \mathbf{r}') \\ -\phi_y(\mathbf{r}, \mathbf{r}') & \phi_x(\mathbf{r}, \mathbf{r}') & 0 \end{bmatrix} \begin{bmatrix} E_x(\mathbf{r}') \\ E_y(\mathbf{r}') \\ E_z(\mathbf{r}') \end{bmatrix} \quad (3.4.4)$$

where $\phi_{x_p x_q}(\mathbf{r}, \mathbf{r}')$, $\phi_{x_p}(\mathbf{r}, \mathbf{r}')$ and x_1, x_2, x_3 are the same as defined in section 2.4.

After applying pulse-basis expansion and point-matching, the coupled tensor integral equations become a system of linear algebraic equations of order $6N$:

$$\begin{bmatrix} A & B \\ C & D \end{bmatrix} \begin{bmatrix} E \\ H \end{bmatrix} = \begin{bmatrix} E^i \\ H^i \end{bmatrix} \quad (3.4.5)$$

where each of A, B, C and D is $3N \times 3N$ matrix, E, H, E^i and H^i are $3N \times 1$ column vectors. These matrices and vectors can be expressed as follows:

$$A = \begin{bmatrix} A_{11} & A_{12} & A_{13} \\ A_{21} & A_{22} & A_{23} \\ A_{31} & A_{32} & A_{33} \end{bmatrix} \quad B = \begin{bmatrix} B_{11} & B_{12} & B_{13} \\ B_{21} & B_{22} & B_{23} \\ B_{31} & B_{32} & B_{33} \end{bmatrix} \quad (3.4.6)$$

where A_{pq} and B_{pq} are both $N \times N$ matrices for $p, q=1,2,3$, and the elements of these matrices are

$$(A_{pq})_{mn} = \delta_{pq} \delta_{mn} \left[1 + \frac{i\tau_e(\mathbf{r}_n)}{3\omega\epsilon_0} \right] + i\omega\mu_0 \text{P.V.} \int_{v_m} \tau_e(\mathbf{r}') [\delta_{pq} \phi(\mathbf{r}_n, \mathbf{r}') + \frac{1}{k_0^2} \phi_{x_p x_q}(\mathbf{r}_n, \mathbf{r}')] dv' ,$$

$$m, n=1, 2, \dots, N \quad (3.4.7)$$

$$(B_{pq})_{mn} = \sum_{r=1}^3 \epsilon_{pqr} \int_{v_r} \tau_m(\mathbf{r}') \phi_x(\mathbf{r}, \mathbf{r}') dv' . \quad m, n=1, 2, \dots, N \quad (3.4.8)$$

Note that ϵ_{pqr} is defined as

$$\epsilon_{pqr} = \begin{cases} 1 & p, q, r \text{ form a cyclic permutation} \\ -1 & p, q, r \text{ form an anti-cyclic permutation} \\ 0 & \text{otherwise} \end{cases} \quad p, q, r = 1, 2, 3 \quad (3.4.9)$$

Matrices C and D are represented as

$$C = \begin{bmatrix} C_{11} & C_{12} & C_{13} \\ C_{21} & C_{22} & C_{23} \\ C_{31} & C_{32} & C_{33} \end{bmatrix} \quad D = \begin{bmatrix} D_{11} & D_{12} & D_{13} \\ D_{21} & D_{22} & D_{23} \\ D_{31} & D_{32} & D_{33} \end{bmatrix} \quad (3.4.10)$$

where C_{pq} and D_{pq} are also $N \times N$ matrices for $p, q = 1, 2, 3$, and the elements of these matrices are

$$(C_{pq})_{mn} = - \sum_{r=1}^3 \epsilon_{pqr} \int_v \tau_e(r') \phi_{x_r}(r, r') dv' , \quad m, n = 1, 2, \dots, N \quad (3.4.11)$$

$$(D_{pq})_{mn} = \delta_{pq} \delta_{mn} \left[1 + \frac{i\tau_m(r_n)}{3\omega\mu_0} \right] \\ + i\omega\epsilon_0 P.V. \int_{v_m} \tau_m(r') [\delta_{pq} \phi(r_n, r') + \frac{1}{k_0^2} \phi_{x_r x_r}(r_n, r')] dv' . \\ m, n = 1, 2, \dots, N \quad (3.4.12)$$

The column vectors E , E^i , H and H^i are

$$E = \begin{bmatrix} E_1 \\ E_2 \\ E_3 \end{bmatrix} \quad E^i = \begin{bmatrix} E_1^i \\ E_2^i \\ E_3^i \end{bmatrix} \quad (3.4.13)$$

$$H = \begin{bmatrix} H_1 \\ H_2 \\ H_3 \end{bmatrix} \quad H^i = \begin{bmatrix} H_1^i \\ H_2^i \\ H_3^i \end{bmatrix} \quad (3.4.14)$$

where E_p , E_p^i , H_p and H_p^i are $N \times 1$ vectors for $p = 1, 2, 3$ with the n -th elements

$$(E_p)_n = E_{x_p}(\mathbf{r}_n) , \quad n=1,2,\dots,N \quad (3.4.15)$$

$$(E_p^i)_n = E_{x_p}^i(\mathbf{r}_n) , \quad n=1,2,\dots,N \quad (3.4.16)$$

$$(H_p)_n = H_{x_p}(\mathbf{r}_n) , \quad n=1,2,\dots,N \quad (3.4.17)$$

$$(H_p^i)_n = H_{x_p}^i(\mathbf{r}_n) , \quad n=1,2,\dots,N \quad (3.4.18)$$

From the expressions above, it is noticed that the diagonal submatrices B_{pp} and C_{pp} of the matrices B and C are null matrices. The diagonals of the off-diagonal submatrices B_{pq} and C_{pq} are all zeros since the integration will be canceled out by the symmetry property.

By solving the $6N \times 6N$ matrix equation (3.4.5), we can obtain both electric and magnetic field distributions over the body simultaneously.

The decoupled tensor integral equation (3.2.18) and (3.2.19) are investigated next. For a heterogeneous body, these equations contain two terms which involve the gradients of the complex permittivity and permeability functions. This will cause difficulty especially for heterogeneous body with jump discontinuities of parameters within the body. Therefore, we will concentrate on the cases of homogeneous bodies in the discussion of the decoupled tensor integral equations.

The decoupled tensor integral equations when applied to a homogeneous body can be written:

$$\begin{aligned} & \left[\frac{2\mu_0}{3\mu} + \frac{\epsilon^*}{3\epsilon_0} \right] \mathbf{E}(\mathbf{r}) - P.V. \int_v k_0^2 \left[\frac{\epsilon^*}{\epsilon_0} - \frac{\mu_0}{\mu} \right] \mathbf{E}(\mathbf{r}') \cdot \vec{G}_0(\mathbf{r}, \mathbf{r}') dv' \\ & - \int_s \left[\frac{\mu - \mu_0}{\mu} \right] [\mathbf{n} \times \mathbf{E}(\mathbf{r}') \cdot [\nabla' \times \vec{G}_0(\mathbf{r}, \mathbf{r}')] ds' = \mathbf{E}^i(\mathbf{r}) \quad (3.4.19) \\ & \left[\frac{2\epsilon_0}{3\epsilon^*} + \frac{\mu}{3\mu_0} \right] \mathbf{H}(\mathbf{r}) - P.V. \int_v k_0^2 \left[\frac{\mu}{\mu_0} - \frac{\epsilon_0}{\epsilon^*} \right] \mathbf{H}(\mathbf{r}') \cdot \vec{G}_0(\mathbf{r}, \mathbf{r}') dv' \end{aligned}$$

$$- \int_s \left[\frac{\epsilon^* - \epsilon_0}{\epsilon^*} \right] [\mathbf{n} \times \mathbf{H}(\mathbf{r}')] \cdot [\nabla' \times \vec{G}_0(\mathbf{r}, \mathbf{r}')] ds' = \mathbf{H}^i(\mathbf{r}) . \quad (3.4.20)$$

It is sufficient to analyze the tensor EFIE only since the tensor MFIE can be handled similarly.

In the tensor EFIE (3.4.19), the inner product $\mathbf{E}(\mathbf{r}') \cdot \vec{G}_0(\mathbf{r}, \mathbf{r}')$ is exactly the same as that shown in (3.4.1) while the inner product $[\mathbf{n} \times \mathbf{E}(\mathbf{r}')] \cdot [\nabla' \times \vec{G}_0(\mathbf{r}, \mathbf{r}')] can be expressed in the following matrix product form:$

$$\begin{aligned} & [\mathbf{n} \times \mathbf{E}(\mathbf{r}')] \cdot [\nabla' \times \vec{G}_0(\mathbf{r}, \mathbf{r}')] \\ &= - \begin{bmatrix} n_2\phi_y(\mathbf{r}, \mathbf{r}') + n_3\phi_z(\mathbf{r}, \mathbf{r}') & -n_1\phi_y(\mathbf{r}, \mathbf{r}') & -n_1\phi_z(\mathbf{r}, \mathbf{r}') \\ -n_2\phi_x(\mathbf{r}, \mathbf{r}') & n_1\phi_x(\mathbf{r}, \mathbf{r}') + n_3\phi_z(\mathbf{r}, \mathbf{r}') & -n_2\phi_z(\mathbf{r}, \mathbf{r}') \\ -n_3\phi_x(\mathbf{r}, \mathbf{r}') & -n_3\phi_y(\mathbf{r}, \mathbf{r}') & n_1\phi_x(\mathbf{r}, \mathbf{r}') + n_2\phi_y(\mathbf{r}, \mathbf{r}') \end{bmatrix} \begin{bmatrix} E_x(\mathbf{r}') \\ E_y(\mathbf{r}') \\ E_z(\mathbf{r}') \end{bmatrix} \end{aligned} \quad (3.4.21)$$

where n_1 , n_2 and n_3 are the three components of the unit normal vector \mathbf{n} as defined in section 2.4. Applying similar testing procedure as before, we can transform (3.4.19) into a $3N \times 3N$ matrix equation:

$$\begin{bmatrix} G_{11} & G_{12} & G_{13} \\ G_{21} & G_{22} & G_{23} \\ G_{31} & G_{32} & G_{33} \end{bmatrix} \begin{bmatrix} E_1 \\ E_2 \\ E_3 \end{bmatrix} = \begin{bmatrix} E_1^i \\ E_2^i \\ E_3^i \end{bmatrix} \quad (3.4.22)$$

The elements of the $N \times N$ matrix G_{pq} for $p, q=1, 2, 3$ are:

$$\begin{aligned} (G_{pq})_{mn} &= c_1 \delta_{pq} \delta_{mn} + c_2 P.V. \int_{v_m} [\delta_{pq} \phi(\mathbf{r}_n, \mathbf{r}') + \frac{1}{k_0^2} \phi_{x_p x_q}(\mathbf{r}_n, \mathbf{r}')] dv' \\ &+ c_3 \int_{s_m} [\delta_{pq} \sum_{i=1}^3 n_i \phi_{x_i}(\mathbf{r}_n, \mathbf{r}') - (1 - \delta_{pq}) n_p \phi_{x_q}(\mathbf{r}_n, \mathbf{r}')] ds' , \\ &m, n=1, 2, \dots, N \end{aligned} \quad (3.4.23)$$

where

$$c_1 = \frac{2\mu_0}{3\mu} + \frac{\epsilon^*}{3\epsilon_0} \quad (3.4.24)$$

$$c_2 = -k_0^2 \left[\frac{\epsilon^*}{\epsilon_0} - \frac{\mu_0}{\mu} \right] \quad (3.4.25)$$

$$c_3 = \frac{\mu - \mu_0}{\mu} \quad (3.4.26)$$

and s_m stands for the surface of m -th cell which are common with the closed surface s enclosing v .

We can now solve the matrix equation (3.4.22) to obtain the electric field distribution of the body. Similarly we can obtain the magnetic field distribution if we follow the same procedure to transform the MFIE into a matrix equation.

The numerical solutions of the coupled tensor integral equations and decoupled tensor integral equations are compared in section 3.5.

The coupled integral equations with scalar Green's function (3.3.28) and (3.3.29) can be transformed similarly. Since these two equations contain the terms involving the divergences of \mathbf{E} and \mathbf{H} , they are in fact integro-differential equations instead of pure integral equations. To avoid the complexity of the equations, we again discuss this set of equations for the case of a homogeneous body where the volume charge density should vanish inside the body. Furthermore, the pulse-basis expansion of the induced field distributions will satisfy this charge-free condition inside each cell automatically except on the adjacent boundaries of the cells. Those boundaries of the adjacent cells are then assumed to contain some surface charge so that we should extend the domain of the surface integration when the pulse-basis expansion is applied. The set of integral equations when applied on a homogeneous body then becomes:

$$\begin{aligned} \mathbf{E}(\mathbf{r}) - i\zeta k_0 \int_V \tau_e \mathbf{E}(\mathbf{r}') \phi(\mathbf{r}, \mathbf{r}') dV' + \frac{i\zeta}{k_0} \int_S [\mathbf{n} \cdot (\tau_e \mathbf{E}(\mathbf{r}'))] \nabla \phi(\mathbf{r}, \mathbf{r}') ds' \\ + \int_V \tau_m \mathbf{H}(\mathbf{r}') \times \nabla \phi(\mathbf{r}, \mathbf{r}') dV' = \mathbf{E}^i(\mathbf{r}) \end{aligned} \quad (3.4.27)$$

$$\begin{aligned} \mathbf{H}(\mathbf{r}) - \frac{ik_0}{\zeta} \int_V \tau_m \mathbf{H}(\mathbf{r}') \phi(\mathbf{r}, \mathbf{r}') dV' + \frac{i}{\zeta k_0} \int_S [\mathbf{n} \cdot (\tau_m \mathbf{H}(\mathbf{r}'))] \nabla \phi(\mathbf{r}, \mathbf{r}') ds' \\ - \int_V \tau_e \mathbf{E}(\mathbf{r}') \times \nabla \phi(\mathbf{r}, \mathbf{r}') dV' = \mathbf{H}^i(\mathbf{r}), \end{aligned} \quad (3.4.28)$$

where τ_e and τ_m are both constants inside the body now.

In (3.4.27) and (3.4.28), the inner products $[\mathbf{n} \cdot \mathbf{E}(\mathbf{r}')] \nabla \phi(\mathbf{r}, \mathbf{r}')$ and $[\mathbf{n} \cdot \mathbf{H}(\mathbf{r}')] \nabla \phi(\mathbf{r}, \mathbf{r}')$ are expressed in matrix forms as

$$[\mathbf{n} \cdot \mathbf{E}(\mathbf{r}')] \nabla \phi(\mathbf{r}, \mathbf{r}') = \begin{bmatrix} n_x \phi_x(\mathbf{r}, \mathbf{r}') & n_y \phi_x(\mathbf{r}, \mathbf{r}') & n_z \phi_x(\mathbf{r}, \mathbf{r}') \\ n_x \phi_y(\mathbf{r}, \mathbf{r}') & n_y \phi_y(\mathbf{r}, \mathbf{r}') & n_z \phi_y(\mathbf{r}, \mathbf{r}') \\ n_x \phi_z(\mathbf{r}, \mathbf{r}') & n_y \phi_z(\mathbf{r}, \mathbf{r}') & n_z \phi_z(\mathbf{r}, \mathbf{r}') \end{bmatrix} \begin{bmatrix} E_x(\mathbf{r}') \\ E_y(\mathbf{r}') \\ E_z(\mathbf{r}') \end{bmatrix} \quad (3.4.29)$$

$$[\mathbf{n} \cdot \mathbf{H}(\mathbf{r}')] \nabla \phi(\mathbf{r}, \mathbf{r}') = \begin{bmatrix} n_x \phi_x(\mathbf{r}, \mathbf{r}') & n_y \phi_x(\mathbf{r}, \mathbf{r}') & n_z \phi_x(\mathbf{r}, \mathbf{r}') \\ n_x \phi_y(\mathbf{r}, \mathbf{r}') & n_y \phi_y(\mathbf{r}, \mathbf{r}') & n_z \phi_y(\mathbf{r}, \mathbf{r}') \\ n_x \phi_z(\mathbf{r}, \mathbf{r}') & n_y \phi_z(\mathbf{r}, \mathbf{r}') & n_z \phi_z(\mathbf{r}, \mathbf{r}') \end{bmatrix} \begin{bmatrix} H_x(\mathbf{r}') \\ H_y(\mathbf{r}') \\ H_z(\mathbf{r}') \end{bmatrix} \quad (3.4.30)$$

while $\mathbf{H}(\mathbf{r}') \times \nabla \phi(\mathbf{r}, \mathbf{r}')$ and $\mathbf{E}(\mathbf{r}') \times \nabla \phi(\mathbf{r}, \mathbf{r}')$ can be represented by the same matrix product forms as those in (3.4.2) and (3.4.4).

The system of linear algebraic equations of order $6N$ obtained after we applied pulse-basis expansion and point-matching is then

$$\begin{bmatrix} \bar{A} & C \\ B & \bar{D} \end{bmatrix} \begin{bmatrix} E \\ H \end{bmatrix} = \begin{bmatrix} E^i \\ H^i \end{bmatrix} \quad (3.4.31)$$

where the matrices B , C , and the column vectors E , H , E^i and H^i are the same as those in (3.4.5). \bar{A} and \bar{D} are also $3N \times 3N$ matrices:

$$\bar{A} = \begin{bmatrix} \bar{A}_{11} & \bar{A}_{12} & \bar{A}_{13} \\ \bar{A}_{21} & \bar{A}_{22} & \bar{A}_{23} \\ \bar{A}_{31} & \bar{A}_{23} & \bar{A}_{33} \end{bmatrix} \quad \bar{D} = \begin{bmatrix} \bar{D}_{11} & \bar{D}_{12} & \bar{D}_{13} \\ \bar{D}_{21} & \bar{D}_{22} & \bar{D}_{23} \\ \bar{D}_{31} & \bar{D}_{23} & \bar{D}_{33} \end{bmatrix} \quad (3.4.32)$$

\bar{A}_{pq} and \bar{D}_{pq} are both $N \times N$ matrices for $p, q=1, 2, 3$ with elements

$$\begin{aligned} (\bar{A}_{pq})_{mn} = & \delta_{pq} \left[\delta_{mn} - i\zeta k_0 \tau_e \int_{v_m} \phi(\mathbf{r}_n, \mathbf{r}') dv' \right] \\ & + \frac{i\zeta \tau_e}{k_0} \int_{\bar{s}_m} n_q \phi_{x_p}(\mathbf{r}_n, \mathbf{r}') ds', \quad m, n=1, 2, \dots, N \end{aligned} \quad (3.4.33)$$

$$\begin{aligned} (\bar{D}_{pq})_{mn} = & \delta_{pq} \left[\delta_{mn} - \frac{ik_0 \tau_m}{\zeta} \int_{v_m} \phi(\mathbf{r}_n, \mathbf{r}') dv' \right] \\ & + \frac{i\zeta \tau_m}{\zeta k_0} \int_{\bar{s}_m} n_q \phi_{x_p}(\mathbf{r}_n, \mathbf{r}') ds', \quad m, n=1, 2, \dots, N \end{aligned} \quad (3.4.34)$$

where \bar{s}_m stands for all the surrounding surfaces of the m -th cell.

Again, the electric and magnetic field distributions can be obtained simultaneously by solving the matrix equation (3.4.31). The reason we extend the domain of the surface integration in (3.4.33) and (3.4.34) is related with some physical picture, more discussion will be presented in section 3.5.

The transformation procedure of the decoupled EFIE and MFIE with free space scalar Green's function into matrix equations is very similar to that of coupled integral equations (3.4.27) and (3.4.28) so that we will omit it here. Since both the equations (3.3.33) and (3.3.36) contain the terms involving the divergence of \mathbf{E} and \mathbf{H} , we will apply this set of equations to homogeneous bodies for the time being and also note that the surface integration in the equations should also be handled in the same way as that in (3.4.33) and (3.4.34).

The transformed matrix equations are of order $6N$ for coupled integral equations and $3N$ for decoupled integral equations. However, if there are some symmetry properties in the geometry of the body and the incident EM fields, the induced EM field distributions will also be symmetric along certain directions. Therefore we should be able to reduce the number of unknowns in the system of linear algebraic equations and

hence the size of matrix. The symmetry properties of the induced electric field $\mathbf{E}(\mathbf{r})$ have been studied by previous researchers [11], [12] while the symmetry properties of the induced magnetic field $\mathbf{H}(\mathbf{r})$ can be inspected similarly and confirmed by numerical calculation also.

Suppose the body is symmetric about its center, as shown in Fig-3.3, we can locate the origin of the coordinate system at the center of the body. The planes $x=0$, $y=0$ and $z=0$ divide the body into eight octants. The material parameters are distributed symmetrically in each octant, that is,

$$\tau_e(\mathbf{r}_1) = \tau_e(\mathbf{r}_2) = \dots = \tau_e(\mathbf{r}_8) \quad (3.4.35)$$

$$\tau_m(\mathbf{r}_1) = \tau_m(\mathbf{r}_2) = \dots = \tau_m(\mathbf{r}_8) \quad (3.4.36)$$

where \mathbf{r}_i stands for the position vector in the i -th octant for $i=1,2,\dots,8$.

An incident plane EM wave with EM fields $\mathbf{E}^i(\mathbf{r})$ and $\mathbf{H}^i(\mathbf{r})$ can be decomposed into two standing wave as mentioned in section 2.2. Let $(\mathbf{E}_e^i, \mathbf{H}_e^i) = (\mathbf{E}_s^i, \mathbf{H}_s^i) = (x E_0 \cos(k_0 z), y i \frac{E_0}{\zeta} \sin(k_0 z))$ be the symmetric mode of $(\mathbf{E}^i, \mathbf{H}^i)$ and $(\mathbf{E}_m^i, \mathbf{H}_m^i) = (\mathbf{E}_a^i, \mathbf{H}_a^i) = (x i E_0 \sin(k_0 z), y \frac{E_0}{\zeta} \cos(k_0 z))$ be the antisymmetric mode of $(\mathbf{E}^i, \mathbf{H}^i)$. The subscripts s and a stand for the words symmetric and antisymmetric, and simply mean that the incident electric field is either symmetric or antisymmetric with respect to the x - y plane. It is noted that the incident magnetic field will be antisymmetric for the subscript s and symmetric for the subscript a .

Now let $\mathbf{E}_s(\mathbf{r})$ and $\mathbf{H}_s(\mathbf{r})$ denote the EM fields induced by the symmetric mode of $\mathbf{E}^i(\mathbf{r})$ and $\mathbf{H}^i(\mathbf{r})$, then the three components of $\mathbf{E}_s(\mathbf{r})$ and $\mathbf{H}_s(\mathbf{r})$, denoted as $E_{xs}(\mathbf{r})$, $E_{ys}(\mathbf{r})$, $E_{zs}(\mathbf{r})$ and $H_{xs}(\mathbf{r})$, $H_{ys}(\mathbf{r})$, $H_{zs}(\mathbf{r})$, will obey the following relations:

$$E_{xs}(\mathbf{r}_1) = E_{xs}(\mathbf{r}_2) = E_{xs}(\mathbf{r}_3) = E_{xs}(\mathbf{r}_4) = E_{xs}(\mathbf{r}_5) = E_{xs}(\mathbf{r}_6) = E_{xs}(\mathbf{r}_7) = E_{xs}(\mathbf{r}_8)$$

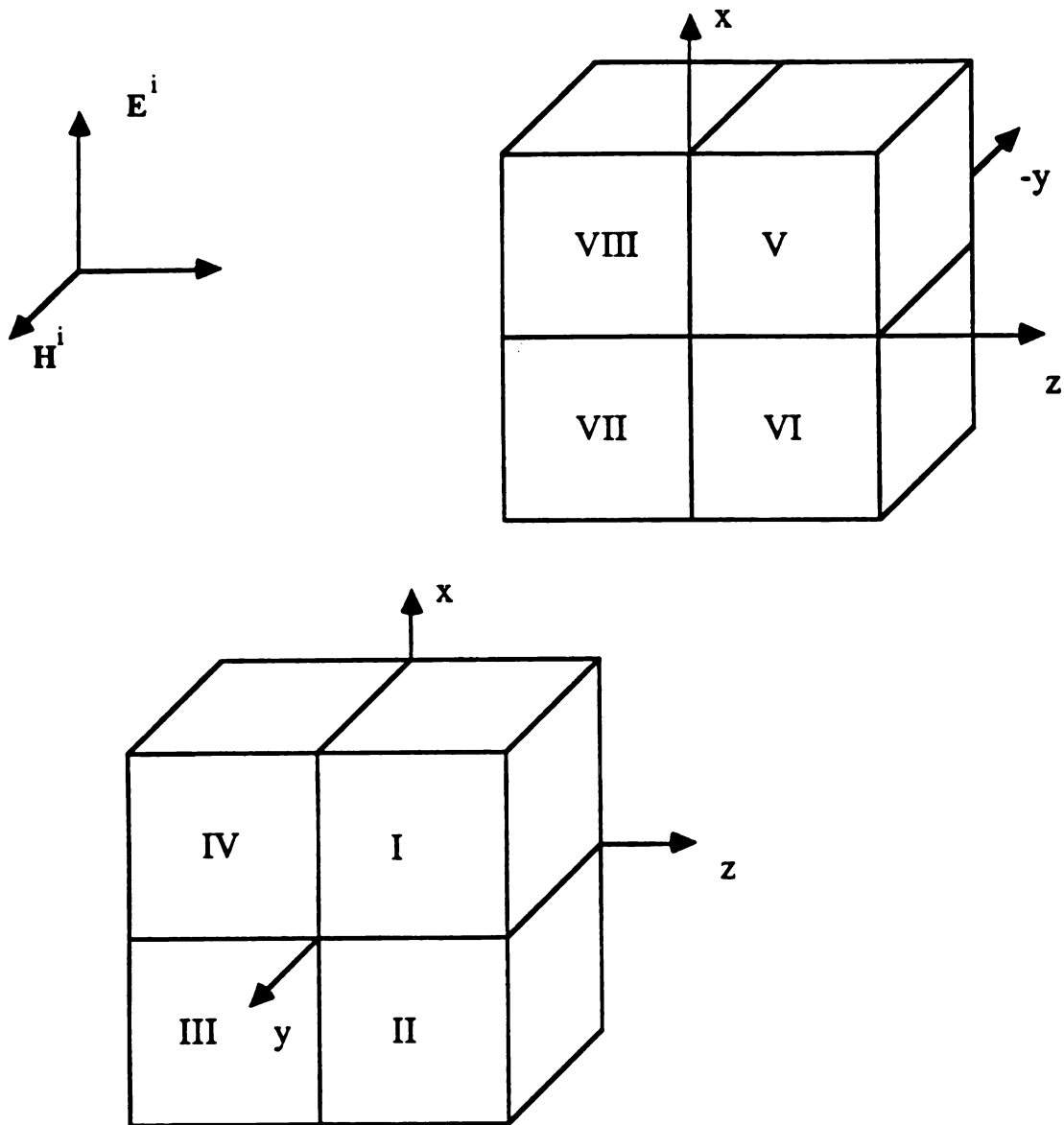


Fig-3.3 A symmetric body partitioned into symmetrical octants, denoted by Roman numerals. The origin of the coordinate system is located at the center of the body.

(3.4.37)

$$E_{ys}(\mathbf{r}_1) = -E_{ys}(\mathbf{r}_2) = E_{ys}(\mathbf{r}_3) = -E_{ys}(\mathbf{r}_4) = E_{ys}(\mathbf{r}_5) = -E_{ys}(\mathbf{r}_6) = E_{ys}(\mathbf{r}_7) = -E_{ys}(\mathbf{r}_8)$$

(3.4.38)

$$E_{zs}(\mathbf{r}_1) = -E_{zs}(\mathbf{r}_2) = -E_{zs}(\mathbf{r}_3) = E_{zs}(\mathbf{r}_4) = -E_{zs}(\mathbf{r}_5) = E_{zs}(\mathbf{r}_6) = E_{zs}(\mathbf{r}_7) = -E_{zs}(\mathbf{r}_8)$$

(3.4.39)

$$H_{xs}(\mathbf{r}_1) = -H_{xs}(\mathbf{r}_2) = H_{xs}(\mathbf{r}_3) = -H_{xs}(\mathbf{r}_4) = -H_{xs}(\mathbf{r}_5) = H_{xs}(\mathbf{r}_6) = -H_{xs}(\mathbf{r}_7) = H_{xs}(\mathbf{r}_8)$$

(3.4.40)

$$H_{ys}(\mathbf{r}_1) = -H_{ys}(\mathbf{r}_2) = H_{ys}(\mathbf{r}_3) = -H_{ys}(\mathbf{r}_4) = H_{ys}(\mathbf{r}_5) = -H_{ys}(\mathbf{r}_6) = H_{ys}(\mathbf{r}_7) = -H_{ys}(\mathbf{r}_8)$$

(3.4.41)

$$H_{zs}(\mathbf{r}_1) = H_{zs}(\mathbf{r}_2) = -H_{zs}(\mathbf{r}_3) = -H_{zs}(\mathbf{r}_4) = H_{zs}(\mathbf{r}_5) = H_{zs}(\mathbf{r}_6) = -H_{zs}(\mathbf{r}_7) = -H_{zs}(\mathbf{r}_8)$$

(3.4.42)

Similarly, let $\mathbf{E}_a(\mathbf{r})$ and $\mathbf{H}_a(\mathbf{r})$ denote the EM fields induced by the anti-symmetric mode of $\mathbf{E}^i(\mathbf{r})$ and $\mathbf{H}^i(\mathbf{r})$, then the three components of $\mathbf{E}_a(\mathbf{r})$ and $\mathbf{H}_a(\mathbf{r})$, denoted as $E_{xa}(\mathbf{r})$, $E_{ya}(\mathbf{r})$, $E_{za}(\mathbf{r})$ and $H_{xa}(\mathbf{r})$, $H_{ya}(\mathbf{r})$, $H_{za}(\mathbf{r})$, will obey the following relations:

$$E_{xa}(\mathbf{r}_1) = E_{xa}(\mathbf{r}_2) = E_{xa}(\mathbf{r}_3) = E_{xa}(\mathbf{r}_4) = -E_{xa}(\mathbf{r}_5) = -E_{xa}(\mathbf{r}_6) = -E_{xa}(\mathbf{r}_7) = -E_{xa}(\mathbf{r}_8)$$

(3.4.43)

$$E_{ya}(\mathbf{r}_1) = -E_{ya}(\mathbf{r}_2) = E_{ya}(\mathbf{r}_3) = -E_{ya}(\mathbf{r}_4) = -E_{ya}(\mathbf{r}_5) = E_{ya}(\mathbf{r}_6) = -E_{ya}(\mathbf{r}_7) = E_{ya}(\mathbf{r}_8)$$

(3.4.44)

$$E_{za}(\mathbf{r}_1) = -E_{za}(\mathbf{r}_2) = -E_{za}(\mathbf{r}_3) = E_{za}(\mathbf{r}_4) = E_{za}(\mathbf{r}_5) = -E_{za}(\mathbf{r}_6) = -E_{za}(\mathbf{r}_7) = E_{za}(\mathbf{r}_8)$$

(3.4.45)

$$H_{xa}(\mathbf{r}_1) = -H_{xa}(\mathbf{r}_2) = H_{xa}(\mathbf{r}_3) = -H_{xa}(\mathbf{r}_4) = H_{xa}(\mathbf{r}_5) = -H_{xa}(\mathbf{r}_6) = H_{xa}(\mathbf{r}_7) = -H_{xa}(\mathbf{r}_8)$$

(3.4.46)

$$H_{ya}(\mathbf{r}_1) = H_{ya}(\mathbf{r}_2) = H_{ya}(\mathbf{r}_3) = H_{ya}(\mathbf{r}_4) = H_{ya}(\mathbf{r}_5) = H_{ya}(\mathbf{r}_6) = H_{ya}(\mathbf{r}_7) = H_{ya}(\mathbf{r}_8)$$

(3.4.47)

$$H_{za}(\mathbf{r}_1) = H_{za}(\mathbf{r}_2) = -H_{za}(\mathbf{r}_3) = -H_{za}(\mathbf{r}_4) = -H_{za}(\mathbf{r}_5) = -H_{za}(\mathbf{r}_6) = H_{za}(\mathbf{r}_7) = H_{za}(\mathbf{r}_8)$$

(3.4.48)

By using the relations (3.4.37) to (3.4.48), we can reduce the number of unknowns in the system of linear algebraic equations by a factor of eight if a particular mode of incident field is given. To manipulate the reduced systems, we only match the points at the centers of those cells in the first octant, and then rearrange those linear algebraic equations by collecting the terms which possess symmetric properties. Once we find the induced field distributions in the first octant, the distributions in other octants can be easily obtained by employing the relations of (3.4.37) to (3.4.48).

3.5 Discussions

Numerical examples of induced fields in a magnetically permeable body irradiated by an incident plane wave are presented in this section. Solutions of various integral equations applied to different bodies are investigated and some comments about each set of equations are made.

In Fig-3.4, a homogeneous cubic body of dimensions $6 \times 6 \times 6$ cm is illuminated by an incident EM plane wave. If the incident EM wave is decomposed into symmetric and antisymmetric modes, we can choose the origin of the coordinate system at the center of this cube so that we merely need to investigate the induced EM field

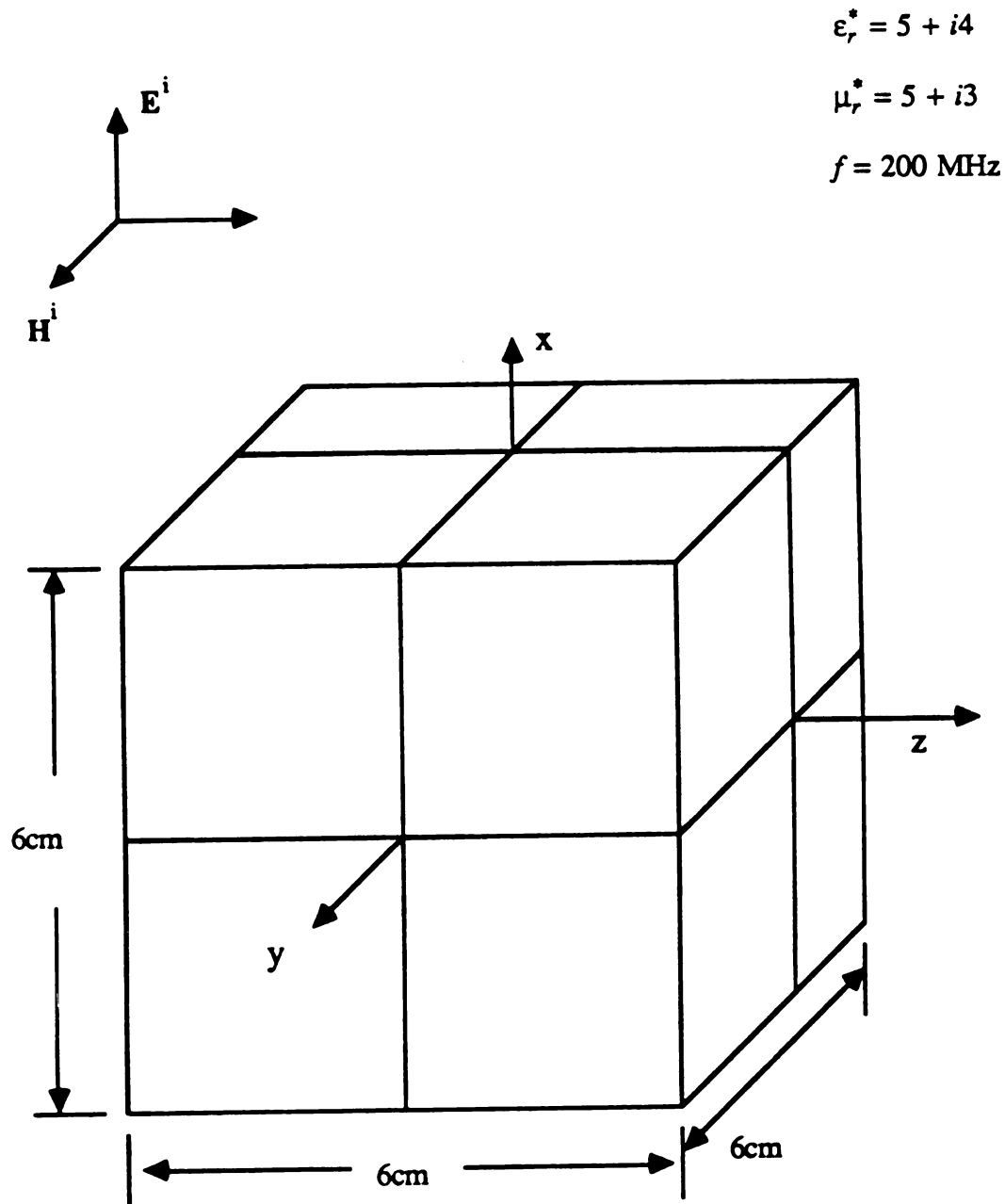
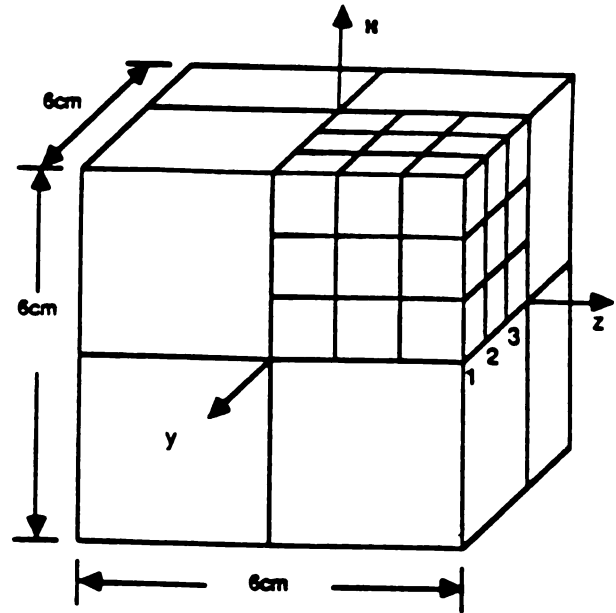
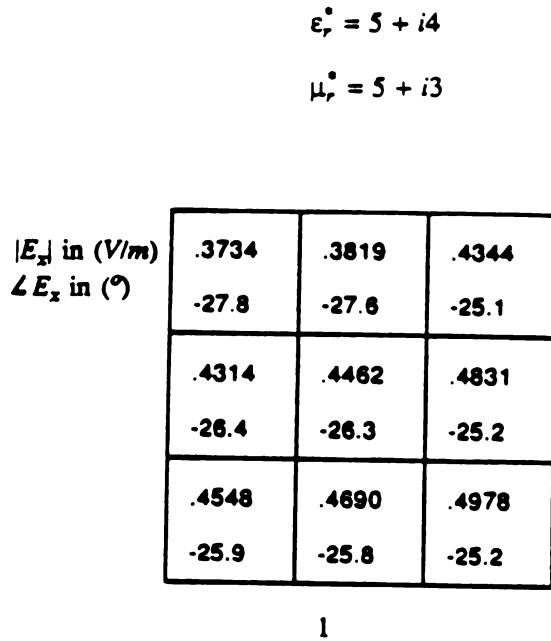


Fig-3.4 A homogeneous cubic body of dimensions $6 \times 6 \times 6 \text{ cm}$ illuminated by an incident plane EM wave.

distributions of different modes in the first octant owing to the symmetry properties.

It is noticed that when the body is non-magnetic, that is, $\mu^* = \mu_0$, the first equation of the set of coupled integral equations is decoupled automatically and we will find that (3.1.45) becomes identical to (3.2.18). Similarly in the non-dielectric case $\epsilon^* = \epsilon_0$, equation (3.1.46) will become identical to (3.2.19). We will study the numerical solutions of the coupled tensor integral equations first and then investigate the effects of the magnetic material on the induced fields. The numbers presented in Fig-3.5 to Fig-3.10 are all numerical solutions of (3.1.45) and (3.1.46).

Fig-3.5 shows the induced electric field distribution in a homogeneous body of the dimensions specified in Fig-3.4 with permittivity $\epsilon = 5\epsilon_0$, conductivity $\sigma = 0.0444 \text{ S/m}$ and complex permeability $\mu^* = (5 + i3)\mu_0$, i.e., the relative complex permittivity $\epsilon_r^* = 5 + i4$ and the relative complex permeability $\mu_r^* = 5 + i3$, excited by a symmetric mode of incident EM field $(\mathbf{E}^i, \mathbf{H}^i) = (x \cos(k_0z), y \frac{i}{\zeta} \sin(k_0z))$ of frequency at 200 MHz. The body is divided into 216 cubic cells of size $1 \times 1 \times 1 \text{ cm}$, but only the numerical solutions in the 27 cells of the first octant need to be presented. We simply indicate the amplitude (in V/m) and phase angle (in degree) of the x -component of the electric field \mathbf{E} in this figure since $|E_y|$ and $|E_z|$ are much smaller than $|E_x|$ in the symmetric mode solution. Fig-3.6 shows the distribution of E_x in a nonmagnetic cube with identical size and ϵ_r^* excited by the same incident fields. We observe that the numerical solutions in these two cases are almost the same, this tells us the magnetic property of the material does not affect too much on the induced electric field when the incident electric field is symmetric and almost constant throughout the body. The reason for this phenomenon is that the incident magnetic field is zero at the center of the body, and also the permeability is not high enough to have a significant enhancement of the induced fields.



.3138	.3221	.3777
-29.7	-29.9	-27.9
.3946	.4078	.4400
-25.9	-26.4	-26.7
.4285	.4403	.4622
-24.8	-25.5	-26.3

2

.3040	.3122	.3677
-29.4	-29.8	-28.2
.3796	.3919	.4227
-25.2	-26.1	-27.0
.4149	.4254	.4451
-24.1	-25.1	-26.6

3

Fig-3.5 Solutions for the symmetric mode of induced electric field obtained from the coupled tensor integral equations based on 216-cell division in the magnetic body. (x- component of \mathbf{E} field)

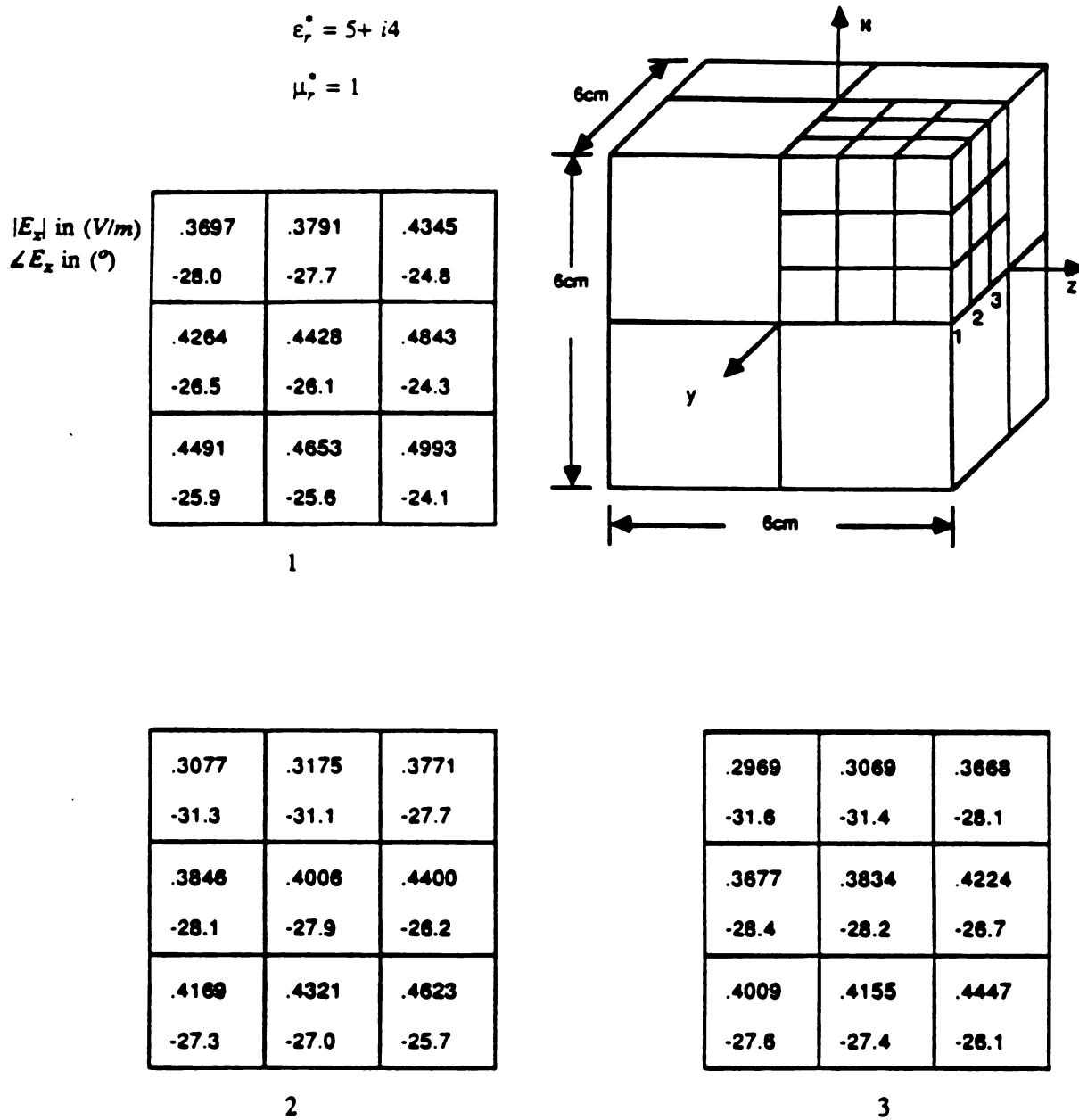


Fig-3.6 Solutions for the symmetric mode of induced electric field obtained from the coupled tensor integral equations based on 216-cell division in the non-magnetic body. (x- component of E field)

Now let us investigate the case for an incident field of the antisymmetric mode. Fig-3.7 and Fig-3.8 indicate the induced electric field distributions in the magnetic body with the same parameters and dimensions as in Fig-3.5 excited by an incident EM field $(\mathbf{E}^i, \mathbf{H}^i) = (x \text{isin}(k_0z), y \frac{1}{\zeta} \cos(k_0z))$ of frequency at 200 MHz. The body is divided as before and only the cells of the first octant are of interests. In this case only y - component of the electric field is insignificant. The distribution of E_x is presented in Fig-3.7 and E_z in Fig-3.8. The x - and z - components of the induced electric fields in the same non-magnetic body as described in Fig-3.6 excited by the same antisymmetric incident field are shown in Fig-3.9 and Fig-3.10. It is observed that the amplitude of the electric field \mathbf{E} in the magnetic material increases by a factor of 2 compared with that in the non-magnetic material. This indicates that the magnetic material plays an important roll in the induced electric field excited by the incident EM field of antisymmetric mode which has a maximum incident magnetic field at the center of the body.

Fig-3.11 to Fig-3.13 give the numerical solutions of the decoupled tensor integral equation (3.2.18) applied to the same magnetic body as described above. The distribution of E_x of symmetric mode is shown in Fig-3.11 while the distributions of E_x and E_z of the antisymmetric mode are shown in Fig-3.12 and Fig-3.13. The frequency is 200 MHz as before. We find that not only is the induced field distribution of the symmetric mode very close to that solved by the coupled tensor integral equations but also the distribution of the antisymmetric mode.

From the examples shown above, it appears that the agreement of the numerical solutions between the two different sets of tensor integral equations is satisfactory. We will investigate the convergence of the numerical solutions next.

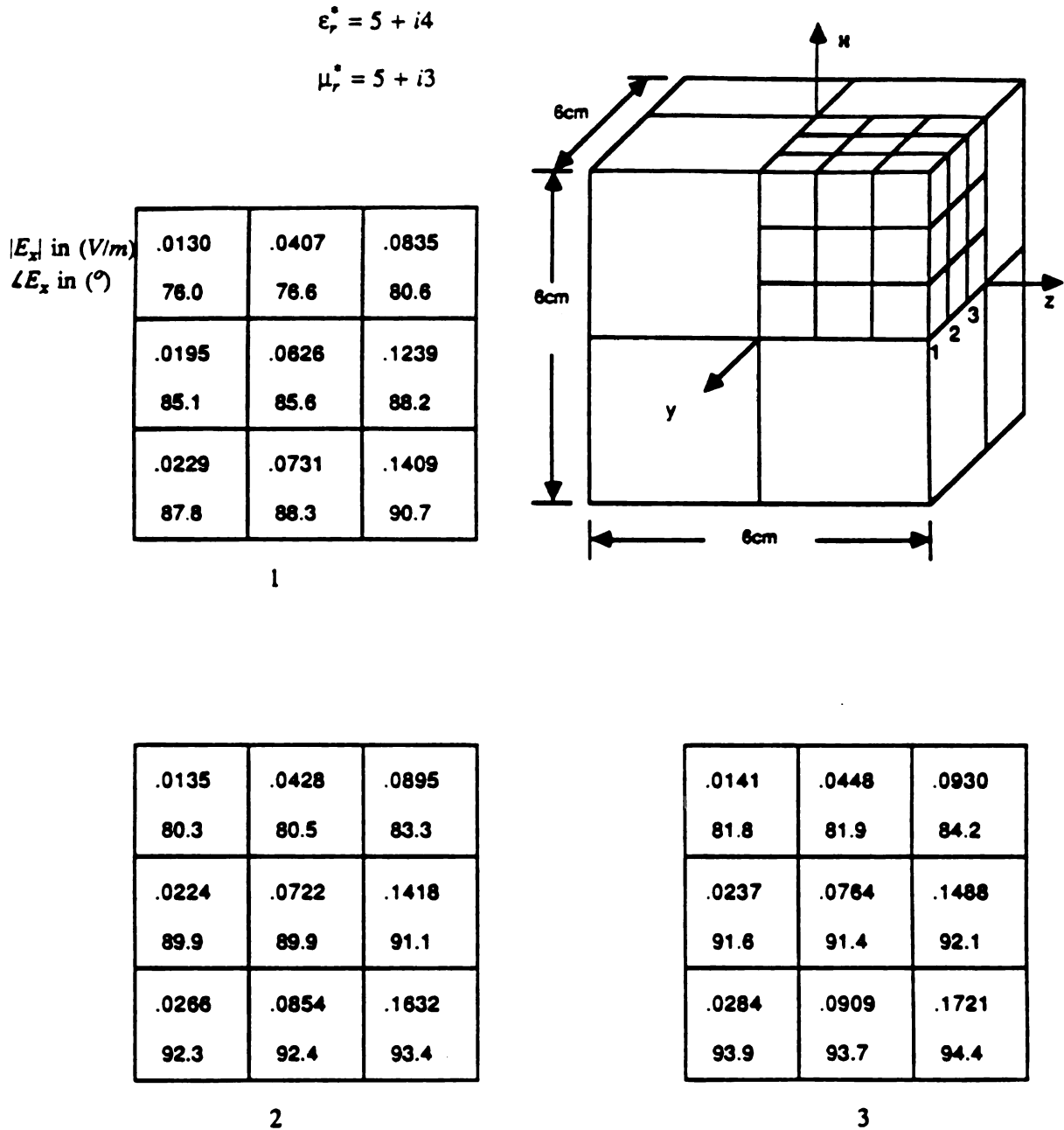


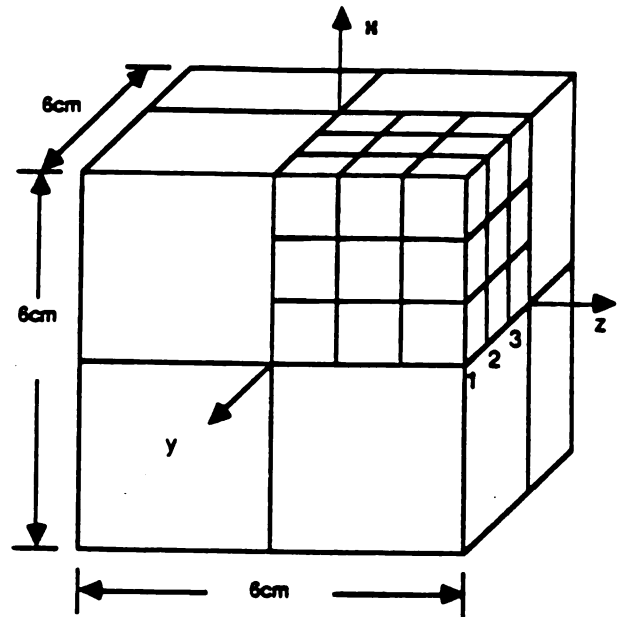
Fig-3.7 Solutions for the antisymmetric mode of induced electric field obtained from the coupled tensor integral equations based on 216-cell division in the magnetic body. (x - component of \mathbf{E} field)

$$\epsilon_r^* = 5 + i4$$

$$\mu_r^* = 5 + i3$$

$ E_z $ in (V/m)	.0978	.0781	.0339
$\angle E_z$ in ($^\circ$)	-76.7	-77.2	-77.0
	.0473	.0364	.0156
	-76.5	-76.8	-80.2
	.0143	.0109	.0048
	-75.8	-76.0	-80.6

1



.1258	.1023	.0476
-76.4	-76.8	-77.1
.0629	.0497	.0228
-75.2	-75.6	-79.1
.0191	.0150	.0069
-74.1	-74.4	-78.7

2

.1369	.1115	.0522
-76.3	-76.8	-77.4
.0696	.0553	.0256
-75.1	-75.5	-79.2
.0213	.0168	.0078
-73.9	-74.3	-78.8

3

Fig-3.8 Solutions for the antisymmetric mode of induced electric field obtained from the coupled tensor integral equations based on 216-cell division in the magnetic body. (z-component of E field)

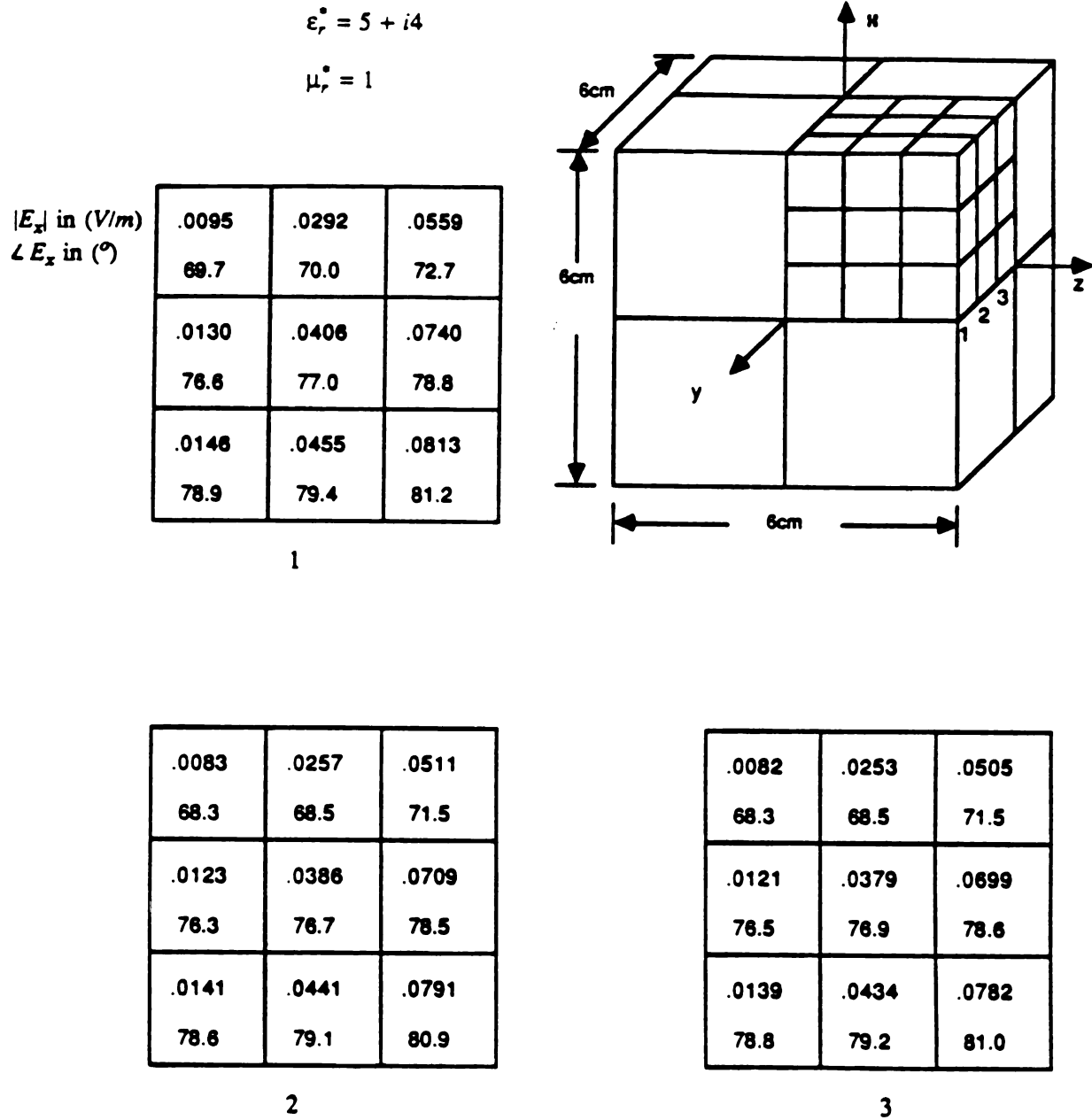
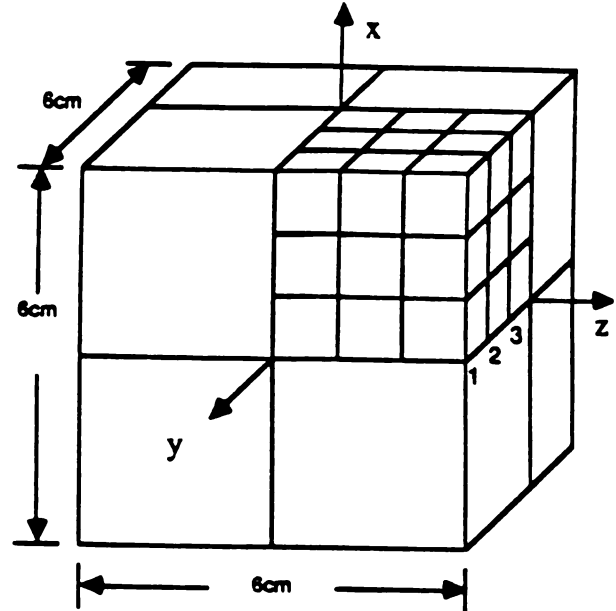


Fig-3.9 Solutions for the antisymmetric mode of induced electric field obtained from the coupled tensor integral equations based on 216-cell division in the non-magnetic body. (x - component of E field)

$\epsilon_r^* = 5 + i4$
 $\mu_r^* = 1$

$ E_x $ in (V/m)	.0353	.0258	.0062
	-76.8	-74.7	-41.4
$\angle E_x$ in ($^\circ$)	.0185	.0135	.0041
	-74.8	-72.3	-57.9
	.0057	.0042	.0013
	-73.6	-71.2	-59.7

1



.0381	.0282	.0078
-79.0	-77.0	-51.1
.0198	.0146	.0050
-76.8	-74.6	-65.0
.0061	.0045	.0015
-75.4	-73.4	-65.9

2

.0392	.0291	.0082
-79.8	-77.8	-53.3
.0203	.0150	.0052
-77.7	-75.7	-66.8
.0063	.0046	.0016
-76.3	-74.5	-67.7

3

Fig-3.10 Solutions for the antisymmetric mode of induced electric field obtained from the coupled tensor integral equations based on 216-cell division in the non-magnetic body. (x - component of E field)

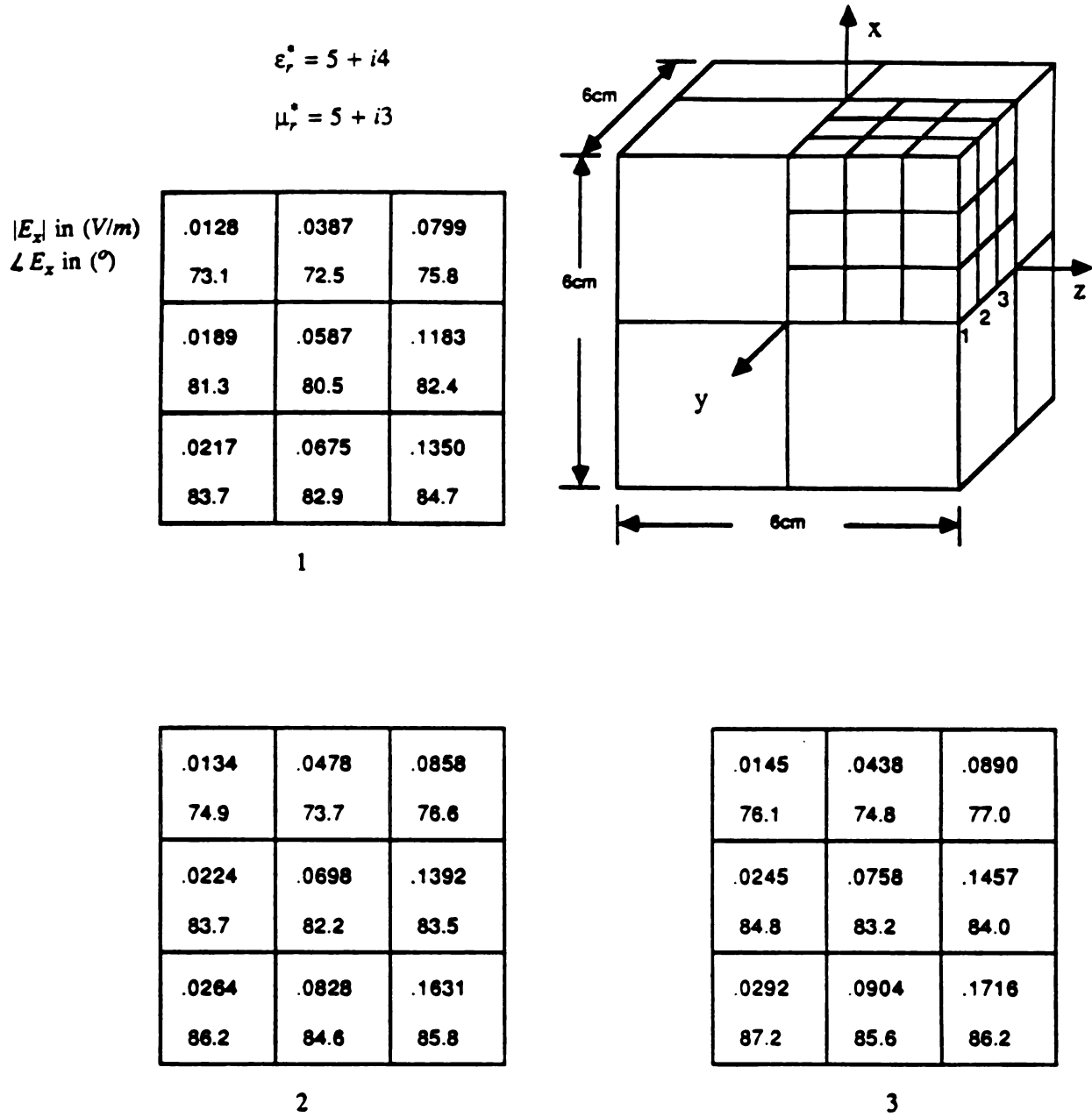


Fig-3.12 Solutions for the antisymmetric mode of induced electric field obtained from the tensor EFIE based on 216-cell division in the magnetic body. (x-component of E field)

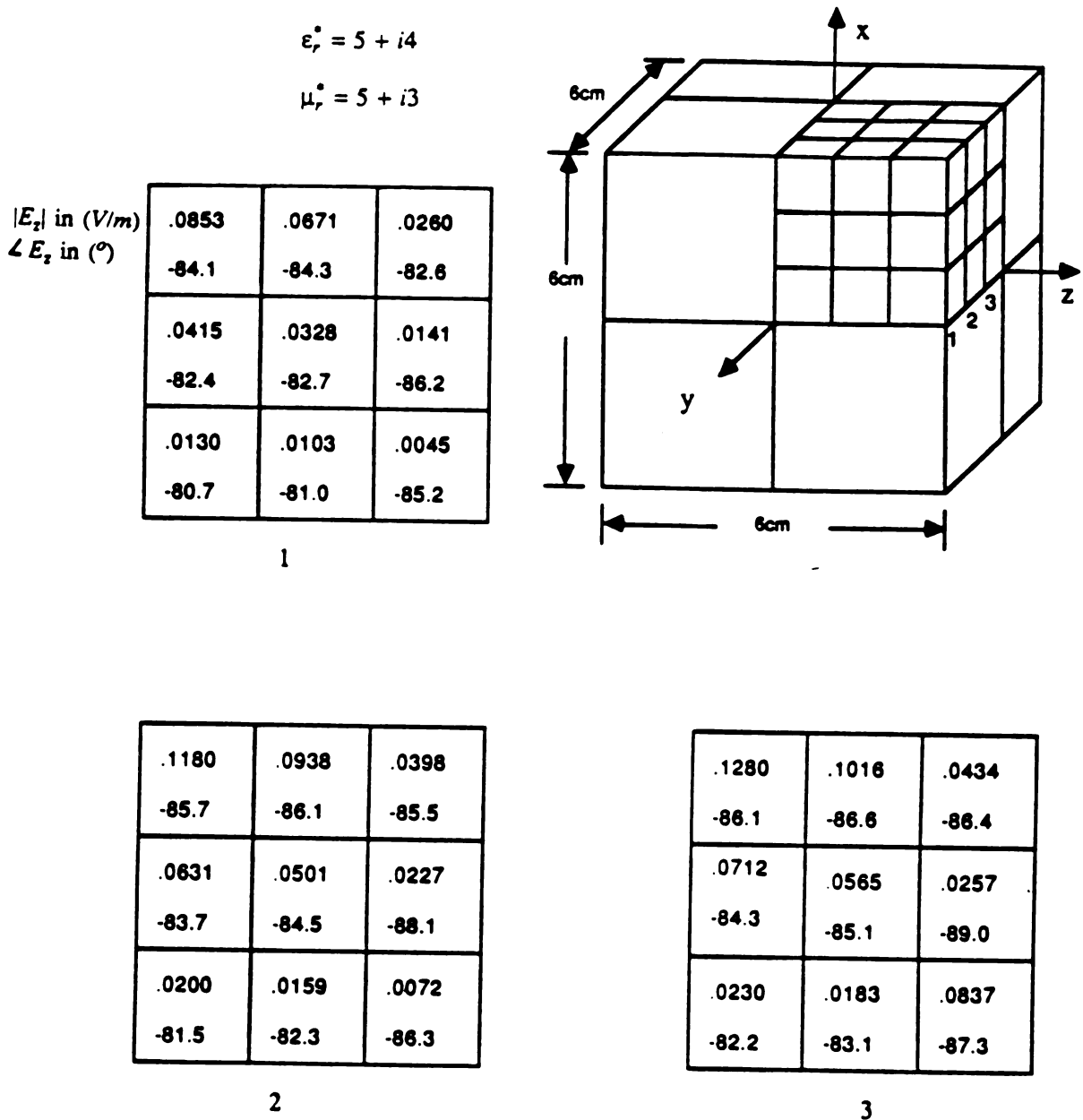
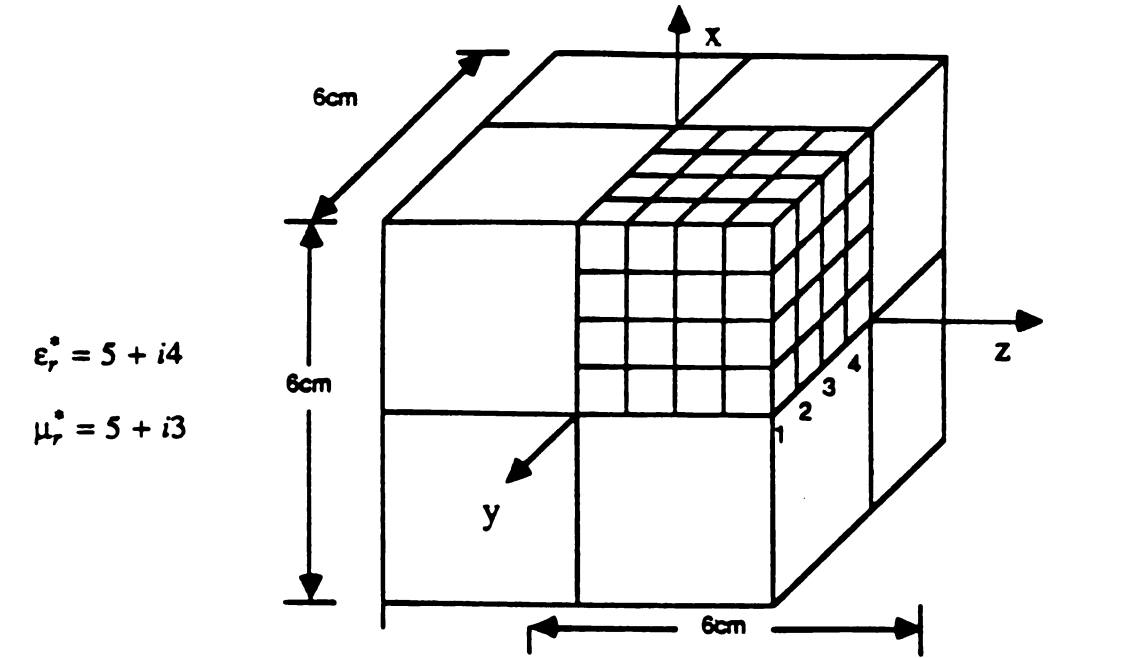


Fig-3.13 Solutions for the antisymmetric mode of induced electric field obtained from the tensor EFIE based on 216-cell division in the magnetic body. (z-component of E field)

Since for the symmetric mode of incident field, regardless of the body being permeable or not, the induced electric field distribution does not change much in the previous examples. We also know from section 2.2 that the symmetric mode solution converges quite well in the non-magnetic body hence so does the symmetric mode solution in the magnetic body. In fact the numerical results will confirm the prediction. Thus, we omit the symmetric mode case and concentrate on the cases of antisymmetric mode.

The convergence of the solutions of the coupled tensor integral equations are shown in Fig-3.14 to Fig-3.17. Fig-3.14 and Fig-3.15 show the distributions of E_x and E_z in the same magnetic body divided into 512 cubic cells excited by the same antisymmetric incident EM field. Each octant contains 64 cells and we depict the first octant distribution by dividing the octant into four 16-cell layers as shown in the figures. Each layer has a fixed y - coordinate. The numbers in Fig-3.14 are the amplitude and the phase angle of E_x and in Fig-3.15 are of E_z . We next divide the body into 1000 cells and present the first octant induced field distributions in Fig-3.16 and Fig-3.17. Now we divide the first octant into five 25-cell layers and the numbers in each cell again show the amplitude and phase of the electric field at the center of each cell. The distribution of E_x is shown in Fig-3.16 and E_z is in Fig-3.17. The agreement between these two sets of data is quite satisfactory.

Fig-3.18 to Fig-3.21 indicate the induced electric field distribution of 512 and 1000 subdivisions of the same body solved by the decoupled tensor EFIE. The incident EM field is the same antisymmetric mode with frequency at 200 MHz. The distributions of E_x and E_z of 512 subdivision are shown in Fig-3.18 and Fig-3.19 and that of 1000 subdivision are shown in Fig-3.20 and Fig-3.21. Again the results of these two divisions agree well.



$|E_x|$ in (V/m)
 $\angle E_x$ in ($^\circ$)

.0091	.0278	.0487	.0829
73.6	74.3	75.5	79.5
.0129	.0402	.0729	.1210
83.0	83.7	84.8	87.5
.0157	.0488	.0880	.1415
87.1	87.6	88.6	90.9
.0171	.0532	.0953	.1506
88.7	89.2	90.2	92.3

1

.0089	.0277	.0496	.0866
77.5	78.2	79.0	82.0
.0143	.0448	.0821	.1360
88.4	88.7	89.2	90.5
.0178	.0558	.1013	.1618
92.0	92.2	92.6	93.7
.0196	.0611	.1101	.1730
93.3	93.5	94.0	95.0

2

.0093	.0290	.0521	.0903
79.7	80.1	80.8	83.1
.0153	.0479	.0877	.1438
91.0	91.1	91.1	91.8
.0193	.0602	.1090	.1724
94.3	94.4	94.4	94.9
.0212	.0661	.1188	.1847
95.5	95.5	95.6	96.2

3

.0096	.0297	.0532	.0919
80.5	80.9	81.5	83.6
.0158	.0494	.0902	.1474
92.0	92.0	91.9	92.4
.0199	.0623	.1125	.1773
95.2	95.2	95.1	95.5
.0220	.0685	.1228	.1903
96.4	96.4	96.3	96.7

4

Fig-3.14 Solutions for the antisymmetric mode of induced electric field obtained from the coupled tensor integral equations based on 512-cell division in the magnetic body. (x- component of \vec{E} field)

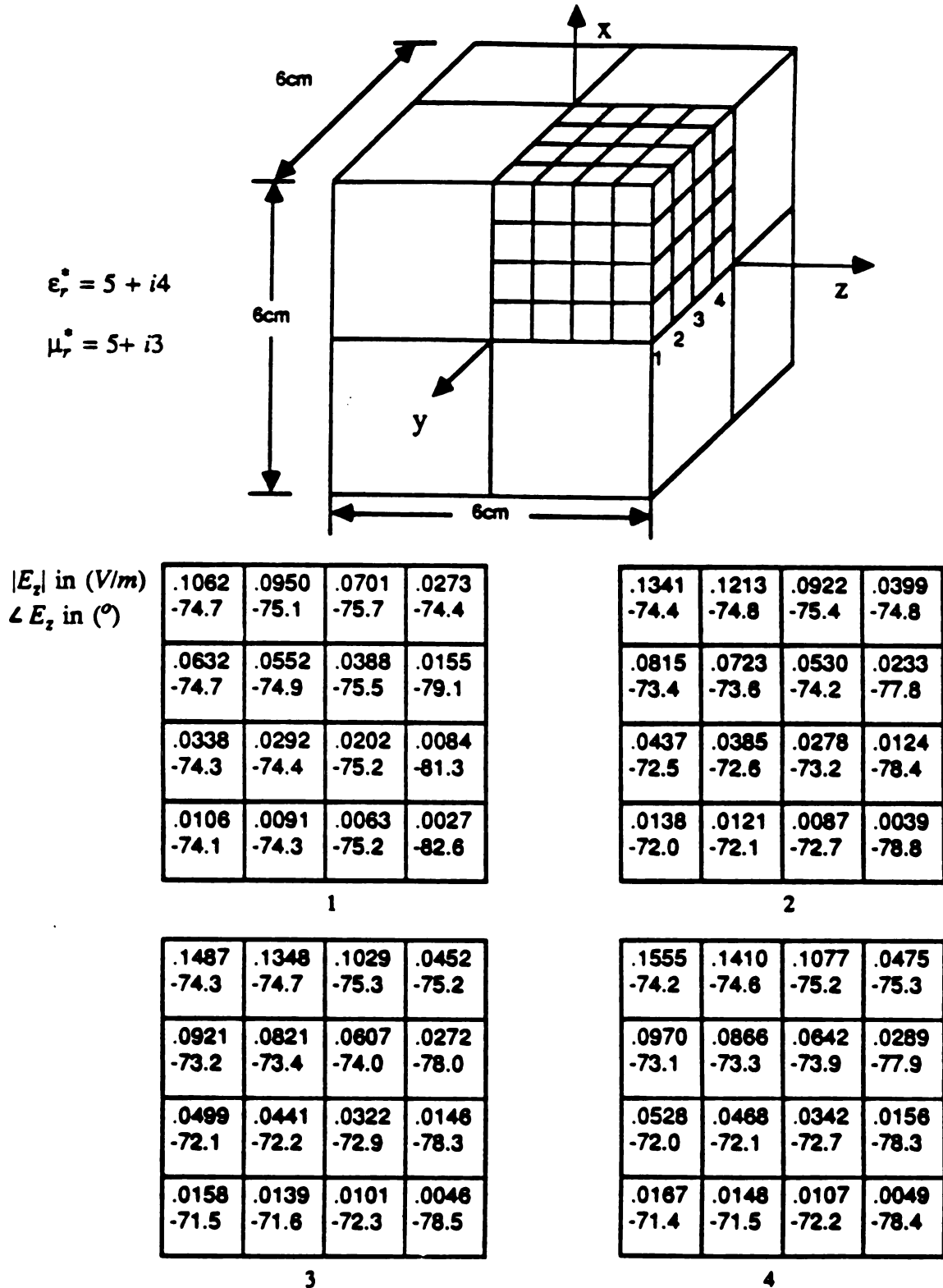


Fig-3.15 Solutions for the antisymmetric mode of induced electric field obtained from the coupled tensor integral equations based on 512-cell division in the magnetic body. (z- component of E field)

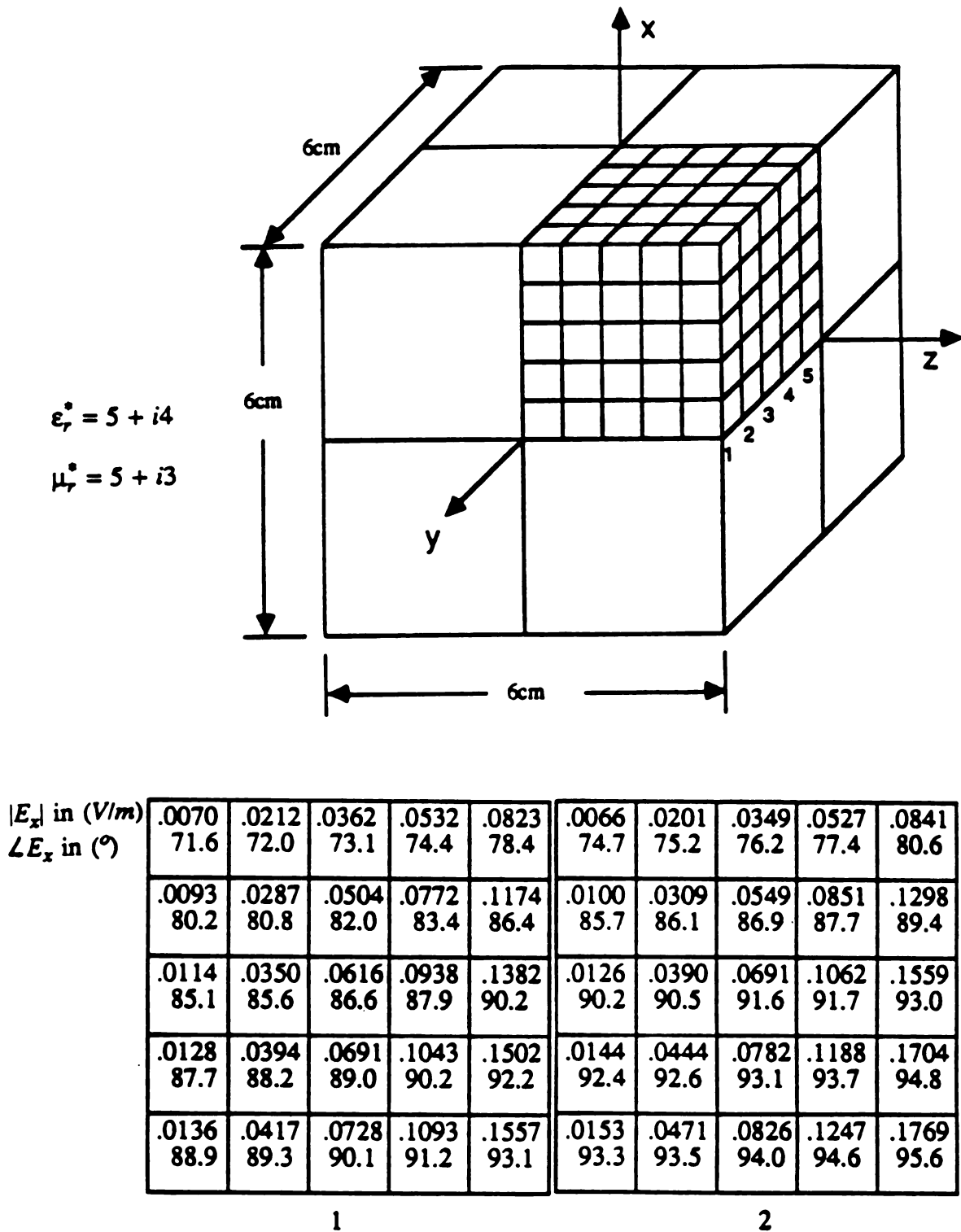


Fig-3.16 Solutions for the antisymmetric mode of induced electric field obtained from the coupled tensor integral equations based on 1000-cell division in the magnetic body. (x - component of E field)

$ E_x $ in (V/m) $\angle E_x$ in ($^\circ$)	.0068 77.1	.0209 77.5	.0364 78.3	.0551 79.2	.0873 81.8	.0070 78.2	.0215 78.6	.0374 79.3	.0565 80.1	.0892 82.3
	.0106 88.7	.0329 89.0	.0584 89.5	.0906 89.9	.1369 90.8	.0111 90.3	.0342 90.5	.0607 90.8	.0939 91.0	.1411 91.6
	.0136 93.0	.0422 93.2	.0745 93.4	.1142 93.7	.1660 94.4	.0143 94.5	.0441 94.6	.0779 94.7	.1190 94.7	.1721 95.1
	.0156 94.9	.0481 95.0	.0846 95.3	.1282 95.5	.1822 96.1	.0164 96.3	.0505 96.3	.0887 96.4	.1340 96.5	.1894 96.8
	.0166 95.7	.0511 95.8	.0895 96.0	.1348 96.3	.1894 96.8	.0174 97.0	.0536 97.1	.0938 97.1	.1410 97.3	.1972 97.5

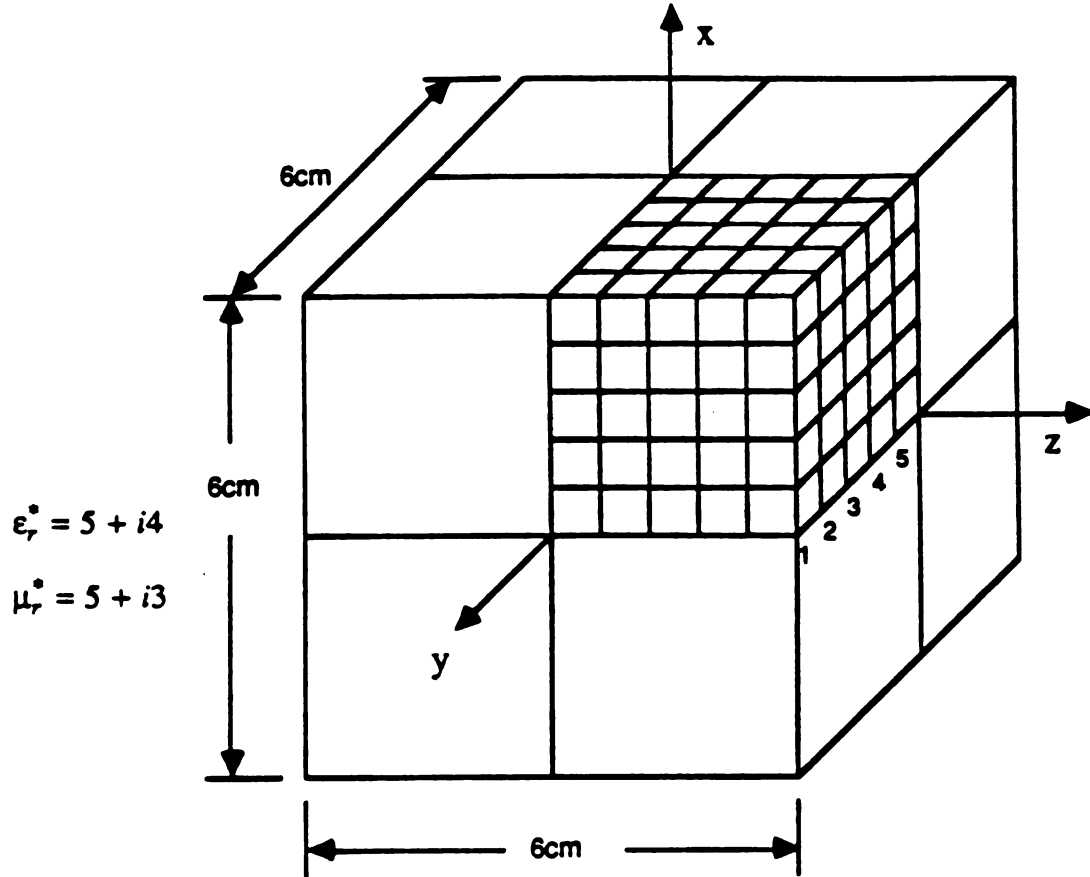
3

4

.0071 78.7	.0217 79.0	.0379 79.7	.0573 80.5	.0901 82.6
.0113 90.9	.0348 91.1	.0618 91.3	.0955 91.4	.1431 91.9
.0146 95.1	.0450 95.2	.0795 95.2	.1213 95.2	.1750 95.5
.0168 96.9	.0516 96.9	.0906 96.9	.1367 96.9	.1929 97.1
.0178 97.6	.0549 97.6	.0959 97.6	.1439 97.7	.2009 97.9

5

Fig-3.16a



$ E_z $ in (V/m)	.1105	.1035	.0882	.0621	.0216	.1368	.1290	.1120	.0820	.0332
$\angle E_z$ in ($^\circ$)	-73.6	-73.9	-74.5	-75.1	-71.9	-73.3	-73.6	-74.1	-74.7	-72.8
	.0735	.0677	.0557	.0373	.0140	.0923	.0859	.0726	.0511	.0218
	-73.7	-73.9	-74.4	-75.1	-78.7	-72.6	-72.8	-73.1	-73.7	-77.2
	.0470	.0429	.0347	.0228	.0091	.0590	.0545	.0453	.0314	.0137
	-73.6	-73.7	-74.2	-75.4	-82.4	-72.0	-72.1	-72.3	-73.1	-78.8
	.0261	.0237	.0190	.0133	.0052	.0328	.0301	.0249	.0171	.0076
	-73.5	-73.7	-74.3	-76.1	-85.1	-71.5	-71.6	-71.8	-73.0	-80.1
	.0084	.0076	.0060	.0039	.0017	.0105	.0096	.0079	.0054	.0025
	-73.5	-73.7	-74.3	-76.6	-86.5	-71.2	-71.4	-71.7	-73.0	-80.8
	1					2				

Fig-3.17 Solutions for the antisymmetric mode of induced electric field obtained from the coupled tensor integral equations based on 1000-cell division in the magnetic body. (z -component of E field)

$ E_z $ in (V/m)	.1524	.1440	.1254	.0924	.0384	.1620	.1531	.1333	.0983	.0413
$\angle E_z$ in ($^\circ$)	-73.3	-73.5	-74.1	-74.6	-73.4	-73.2	-73.4	-73.9	-74.5	-73.6
	.1046	.0977	.0831	.0593	.0259	.1122	.1049	.0894	.0640	.0283
	-72.4	-72.5	-72.9	-73.5	-77.3	-72.2	-72.4	-72.7	-73.3	-77.3
	.0675	.0626	.0525	.0369	.0165	.0728	.0676	.0569	.0402	.0182
	-71.5	-71.6	-71.8	-72.7	-78.5	-71.3	-71.4	-71.6	-72.5	-78.5
	.0377	.0348	.0290	.0202	.0092	.0409	.0378	.0316	.0221	.0102
	-70.9	-70.9	-71.2	-72.3	-79.4	-70.6	-70.7	-71.0	-72.0	-79.2
	.0121	.0112	.0093	.0064	.0030	.0132	.0121	.0101	.0071	.0033
	-70.5	-70.6	-70.8	-72.1	-79.8	-70.3	-70.3	-70.6	-71.8	-79.5

3

4

.1166	.1574	.1370	.1010	.0426
-73.1	-73.4	-73.9	-74.5	-74.7
.1159	.1083	.0923	.0662	.0293
-72.2	-72.3	-72.6	-73.3	-77.3
.0754	.0701	.0590	.0418	.0189
-71.2	-71.3	-71.5	-72.4	-78.5
.0424	.0392	.0328	.0231	.0166
-70.5	-70.6	-70.8	-71.9	-79.1
.0137	.0126	.0105	.0074	.0034
-70.2	-70.2	-70.5	-71.7	-79.5

5

Fig-3.17a

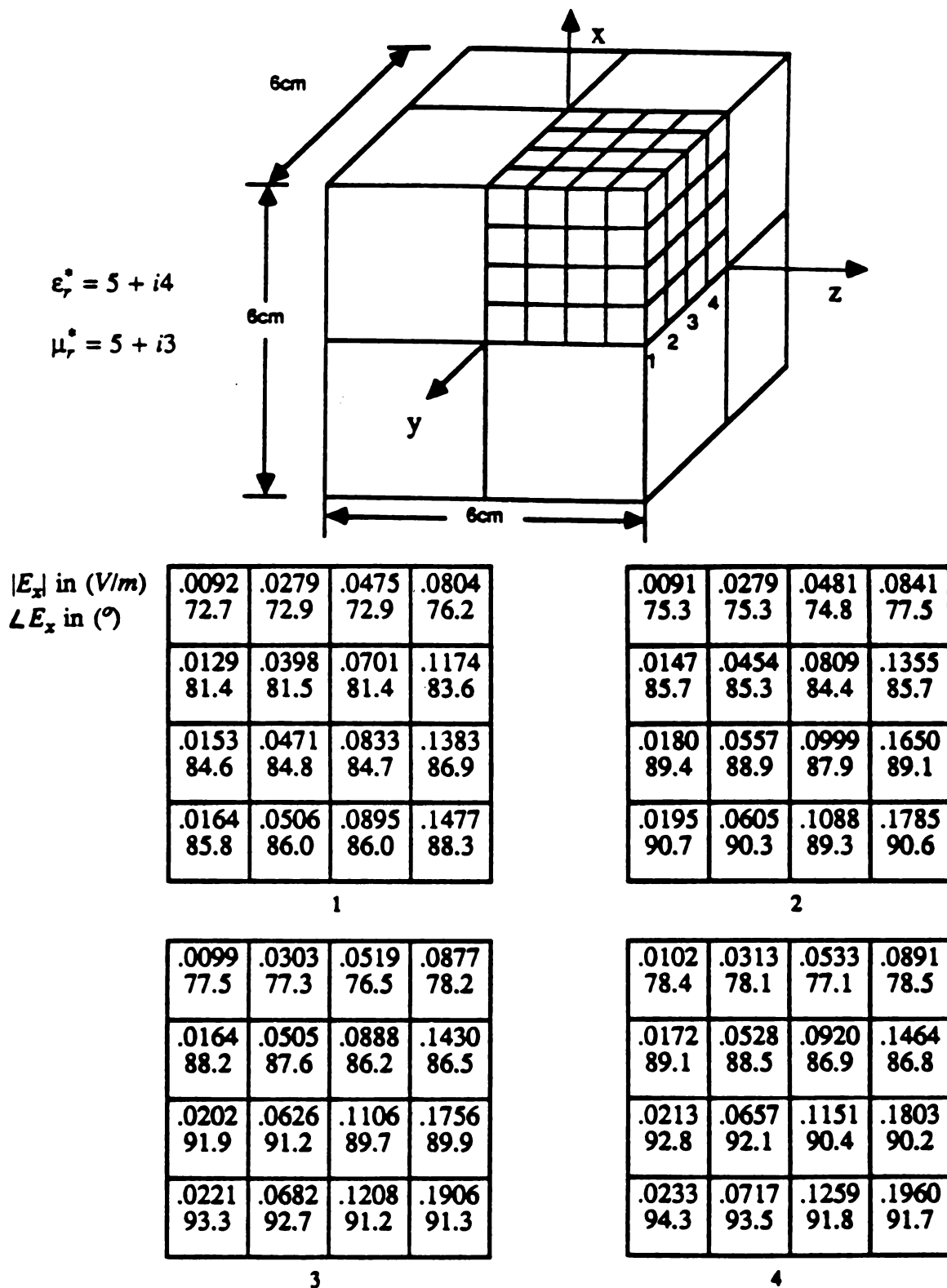
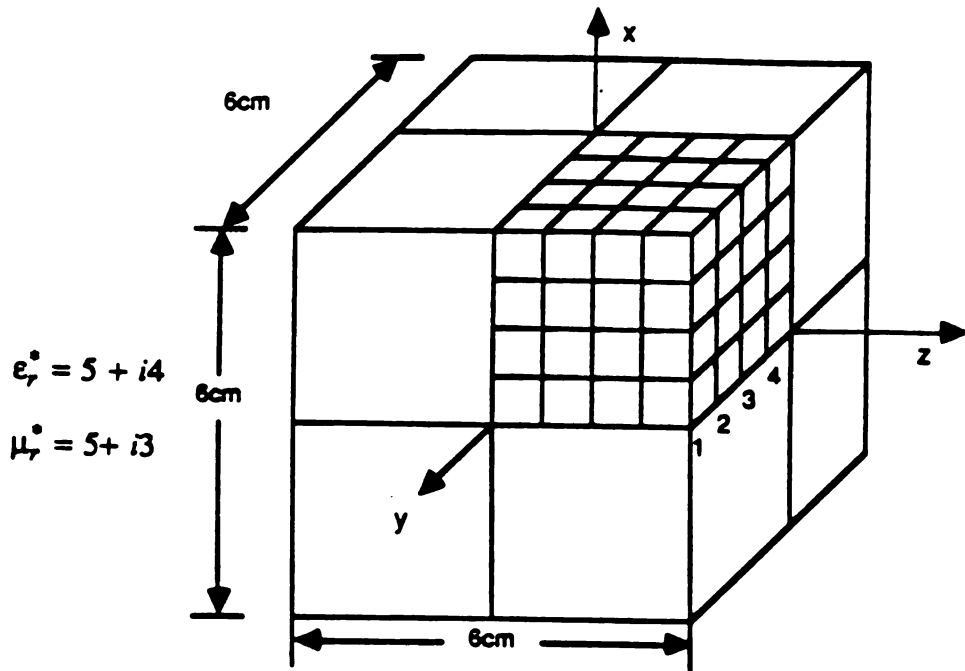


Fig-3.18 Solutions for the antisymmetric mode of induced electric field obtained from the tensor EFIE based on 512-cell division in the magnetic body. (x-component of E field)



$|E_z|$ in (V/m)
 $\angle E_z$ in ($^\circ$)

.0973	.0861	.0622	.0213
-80.0	-80.3	-80.5	-76.6
.0561	.0497	.0361	.0147
-79.4	-79.5	-79.6	-83.0
.0306	.0271	.0197	.0084
-78.2	-78.1	-78.1	-83.2
.0097	.0086	.0063	.0028
-77.7	-77.5	-77.5	-83.5

1

.1328	.1184	.0873	.0344
-80.3	-80.8	-81.3	-79.4
.0828	.0739	.0549	.0240
-78.0	-78.5	-79.4	-83.2
.0453	.0405	.0302	.0135
-75.6	-76.0	-77.0	-81.8
.0144	.0129	.0096	.0044
-74.4	-74.8	-75.7	-81.2

2

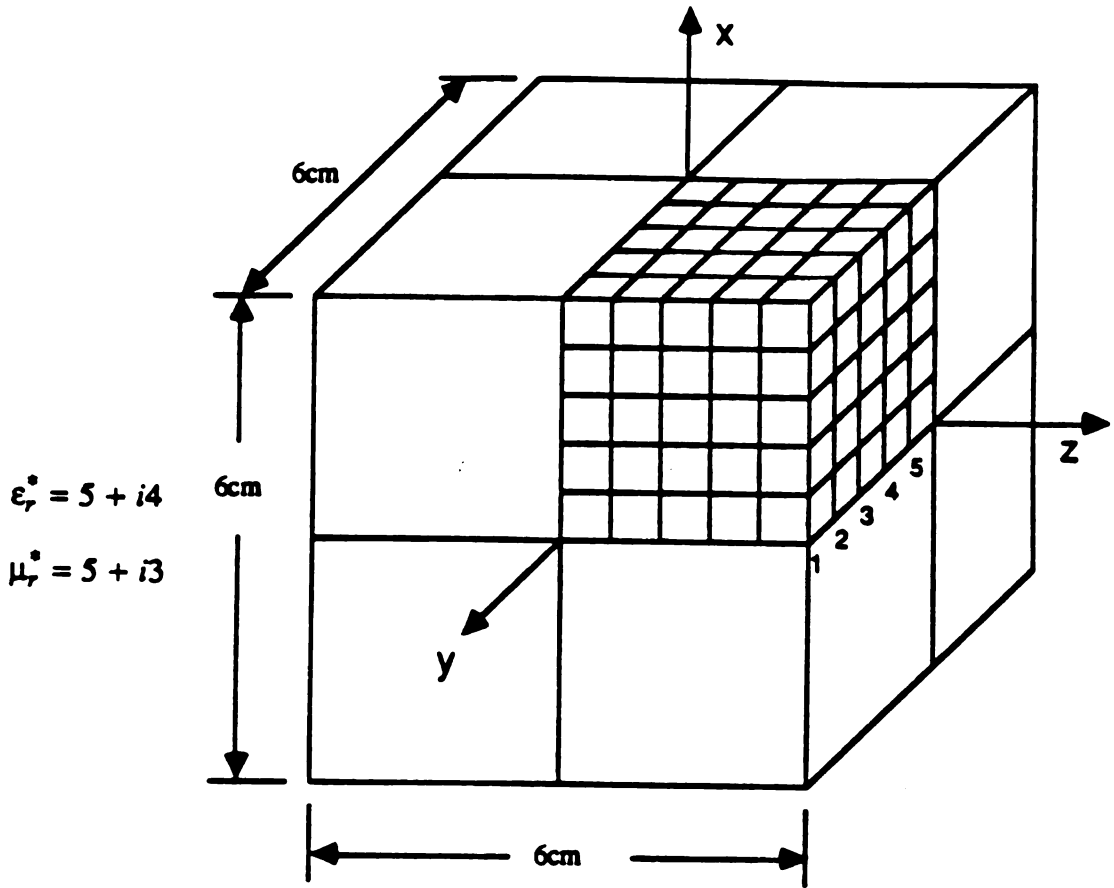
.1473	.1312	.0970	.0389
-80.6	-81.1	-81.8	-80.7
.0962	.0860	.0639	.0283
-78.0	-78.6	-79.8	-83.9
.0541	.0484	.0361	.0163
-75.3	-75.9	-77.2	-82.4
.0174	.0156	.0117	.0053
-74.0	-74.6	-75.9	-81.6

3

.1539	.1372	.1014	.0409
-80.7	-81.2	-81.9	-81.0
.1020	.0911	.0677	.0030
-78.0	-78.6	-79.9	-84.2
.0580	.0519	.0388	.0176
-75.3	-75.9	-77.3	-82.6
.1879	.0168	.0126	.0058
-73.9	-74.6	-76.0	-81.8

4

Fig-3.19 Solutions for the antisymmetric mode of induced electric field obtained from the tensor EFIE based on 512-cell division in the magnetic body. (z-component of E field)



$ E_x $ in (V/m)	.0071	.0215	.0365	.0523	.0803	.0067	.0204	.0351	.0512	.0818
	71.8	72.0	72.4	72.6	75.9	74.3	74.3	74.5	74.5	77.2
$\angle E_x$ in ($^\circ$)	.0095	.0290	.0503	.0750	.1145	.0103	.0317	.0555	.0840	.1292
	80.2	80.4	80.8	81.1	83.5	85.0	85.0	84.8	84.4	85.9
	.0113	.0346	.0602	.0901	.1358	.0127	.0392	.0695	.1050	.1590
	84.0	84.2	84.6	84.9	87.4	89.1	89.0	88.9	88.5	89.9
	.0125	.0383	.0666	.0995	.1484	.0143	.0440	.0773	.1179	.1764
	85.8	86.0	86.5	86.9	89.4	91.0	90.9	90.8	90.6	92.1
	.0131	.0402	.0697	.1040	.1542	.0150	.0462	.0812	.1240	.1845
	86.8	86.8	87.3	87.8	90.4	91.7	91.7	91.6	91.5	93.1
	1					2				

Fig-3.20 Solutions for the antisymmetric mode of induced electric field obtained from the tensor EFIE based on 1000-cell division in the magnetic body. (x-component of E field)

$ E_x $ in (V/m)	.0072	.0221	.0379	.0549	.0851	.0076	.0230	.0394	.0567	.0868
	76.9	76.8	76.7	76.3	77.9	78.4	78.2	77.9	77.2	78.4
$\angle E_x$ in ($^\circ$)	.0114	.0351	.0613	.0917	.1362	.0122	.0373	.0647	.0959	.1402
	88.3	88.0	87.5	86.5	86.8	90.1	89.7	88.9	87.6	87.4
	.0143	.0439	.0769	.1158	.1693	.0153	.0469	.0817	.1218	.1752
	92.5	92.2	91.6	90.6	90.8	94.2	93.8	93.0	91.6	91.4
	.0160	.0494	.0865	.1305	.1888	.0172	.0529	.0921	.1375	.1960
	94.5	94.2	93.6	92.7	93.0	96.2	95.8	95.0	93.7	93.5
	.0169	.0519	.0910	.1374	.1978	.0181	.0556	.0970	.1449	.2057
	95.3	95.0	94.5	93.6	94.0	97.0	96.6	95.8	94.6	94.5

3

4

.0077	.0235	.0402	.0576	.0876
79.0	78.8	78.4	77.6	75.6
.0125	.0383	.0663	.0978	.1420
90.8	90.4	89.5	88.0	87.7
.0158	.0484	.0839	.1244	.1779
95.0	94.5	93.6	92.1	91.6
.0178	.0545	.0947	.1407	.1994
97.0	96.5	95.6	94.1	93.7
.0187	.0574	.0998	.1483	.2095
97.8	97.3	96.4	95.0	94.7

5

Fig-3.20a

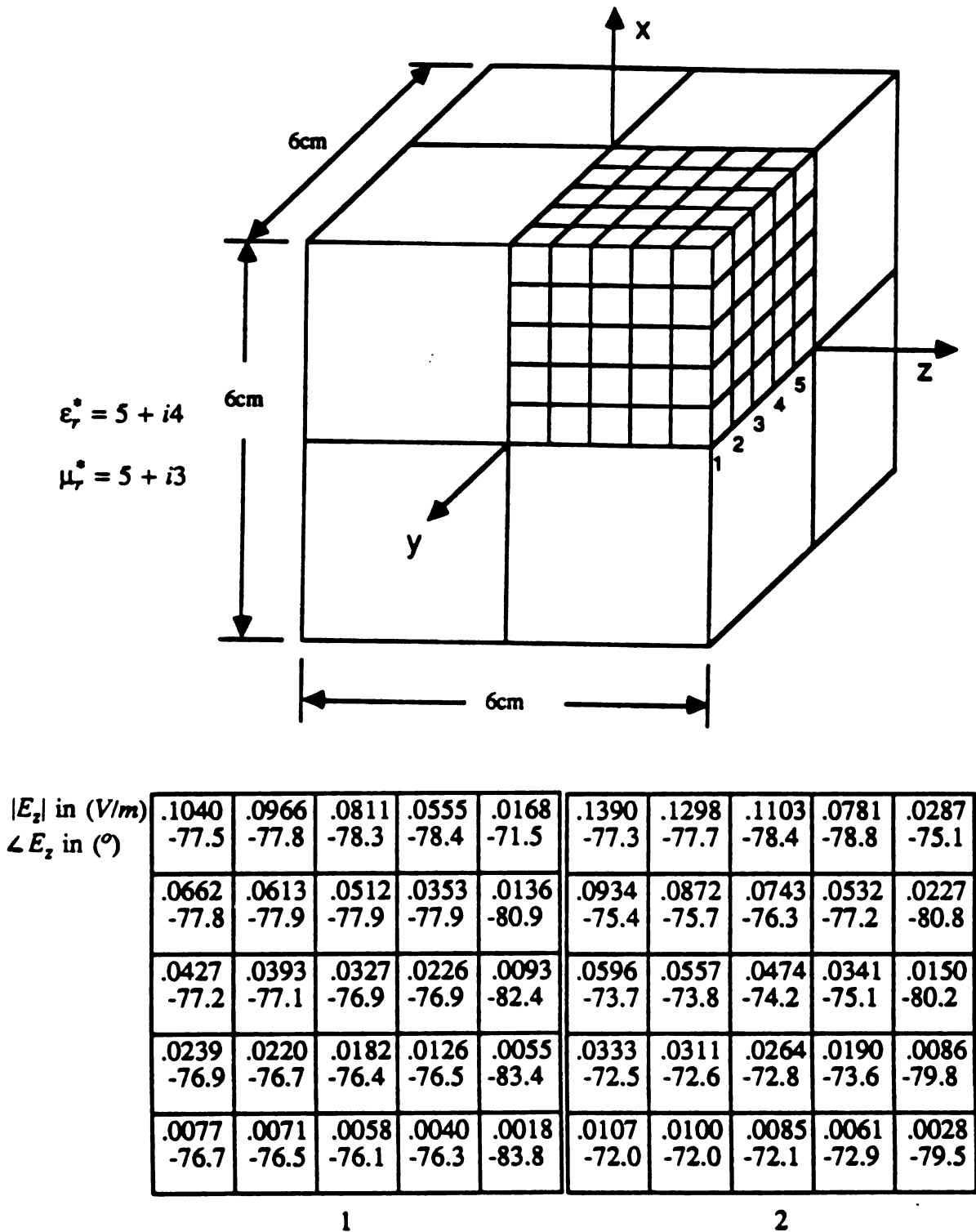


Fig-3.21 Solutions for the antisymmetric mode of induced electric field obtained from the tensor EFIE based on 1000-cell division in the magnetic body. (z-component of E field)

$ E_z $ in (V/m) $\angle E_z$ in ($^\circ$)	.1550	.1449	.1233	.0876	.0331	.1647	.1539	.1309	.0931	.0357
	-77.5	-77.9	-78.7	-79.3	-76.8	-77.6	-78.0	-78.8	-79.5	-77.3
	.1090	.1020	.0871	.0626	.0272	.1177	.1101	.0941	.0678	.0297
	-75.0	-75.4	-76.2	-77.4	-81.6	-74.9	-75.3	-76.1	-77.4	-81.8
	.0713	.0667	.0571	.0413	.0185	.0782	.0732	.0627	.0454	.0206
-72.8	-73.1	-73.7	-75.0	-80.5	-72.4	-72.8	-73.5	-75.0	-80.6	
.0402	.0376	.0322	.0233	.0107	.0445	.0417	.0357	.0260	.0121	
-71.2	-71.5	-72.0	-73.3	-79.8	-70.8	-71.1	-71.8	-73.2	-79.8	
.0130	.0121	.0104	.0075	.0035	.0144	.0135	.0116	.0084	.0040	
-70.5	-70.7	-71.2	-72.4	-79.3	-69.9	-70.2	-70.9	-72.3	-79.3	

3

4

.1693	.1582	.1345	.0957	.0369
-77.6	-78.0	-78.8	-79.5	-77.5
.1217	.1139	.0973	.0702	.0309
-74.8	-75.3	-76.1	-77.4	-81.9
.0814	.0762	.0653	.0474	.0215
-72.3	-72.7	-73.5	-74.9	-80.7
.0466	.0436	.0374	.0272	.0127
-70.6	-70.9	-71.7	-73.2	-79.8
.0151	.0142	.0122	.0089	.0042
-69.7	-70.0	-70.7	-72.2	-79.3

5

Fig-3.21a

We observe that in this particular body excited by an antisymmetric mode of incident EM field of frequency at 200 MHz, the numerical solutions of both coupled tensor integral equation and decoupled tensor EFIE achieve a good convergence as evidenced from the numbers shown in Fig-3.14 to Fig-3.21.

For practical purposes, the materials used in industry, for example, the coating materials of the airplane, are of the parameters around $\epsilon \approx 20\epsilon_0$ and $\mu \approx 10\mu_0$. Workers who are interested in the backward scattering EM fields of this kind of materials can find the induced EM fields inside the body and then calculate the EM fields outside the body from the equivalent sources which are related to the induced EM fields in the body. An example is given next.

Fig-3.22 shows a larger rectangular model of permeable material of dimensions $12 \times 6 \times 12 \text{ cm}$ with $\epsilon_r^* = 20 + i5$ and $\mu_r^* = 5 + i3$, irritated by an incident plane EM wave polarized in x - direction and propagating toward z - direction of frequency at 200 MHz.

Fig-3.23 and Fig-3.24 present the symmetric mode solutions of E_x of coupled tensor integral equations and tensor EFIE respectively. The body is divided into 256 cubic cells of dimensions $1.5 \times 1.5 \times 1.5 \text{ cm}$. Again owing to symmetry property only the distribution of the first octant is shown. It is observed that the two sets of solutions are very close to each other and in fact they are close to the induced fields of the non-magnetic case which are not presented when all the conditions remain the same except $\mu^* = \mu_0$.

The antisymmetric mode solutions of E_x and E_z of two different equations are indicated in Fig-3.25 to Fig-3.28. The non-magnetic case is shown in Fig-3.29 and Fig-3.30 for reference. We observe the agreement of the numerical solutions between the two sets of integral equations from the comparison of the numbers shown in those

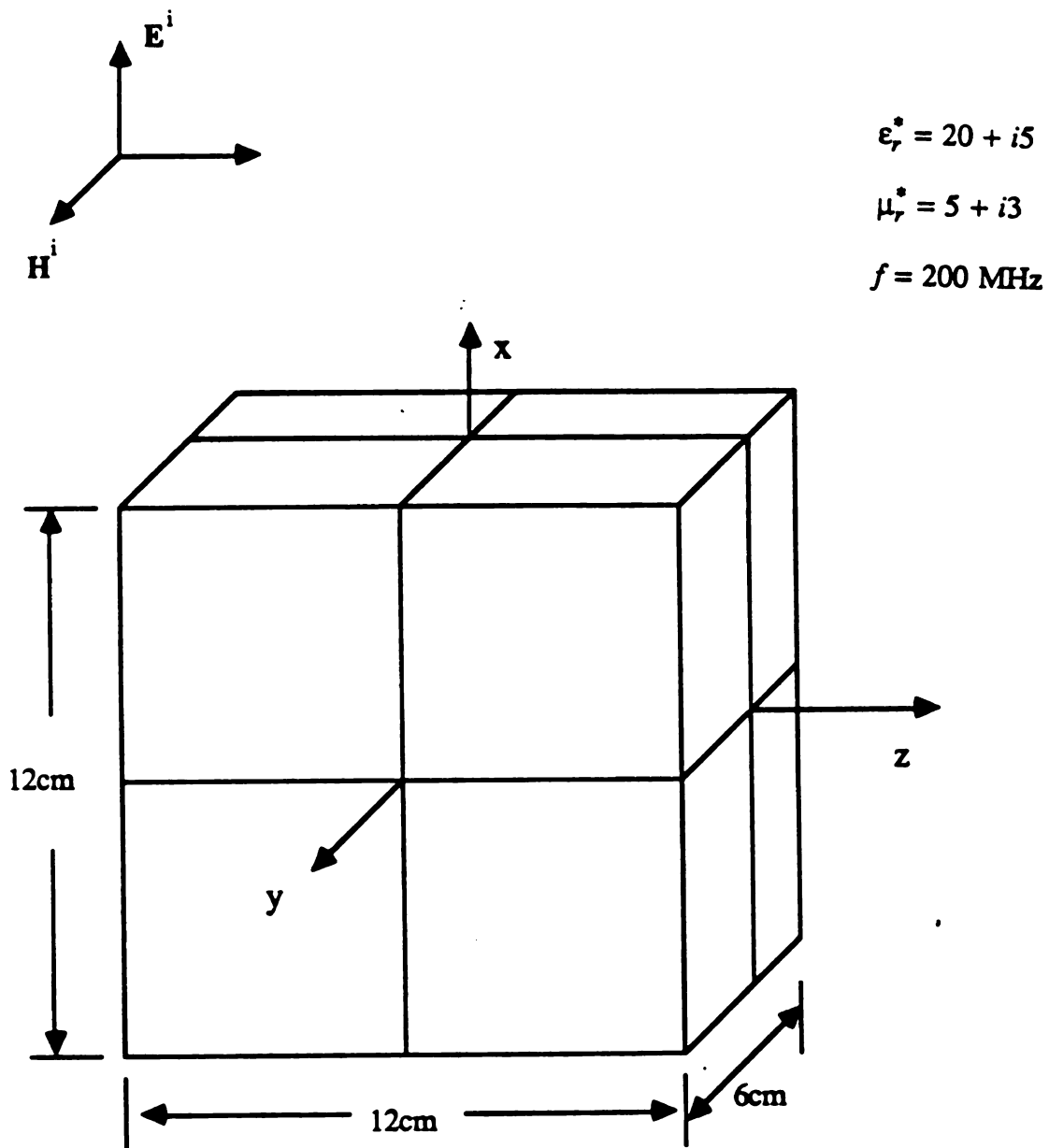
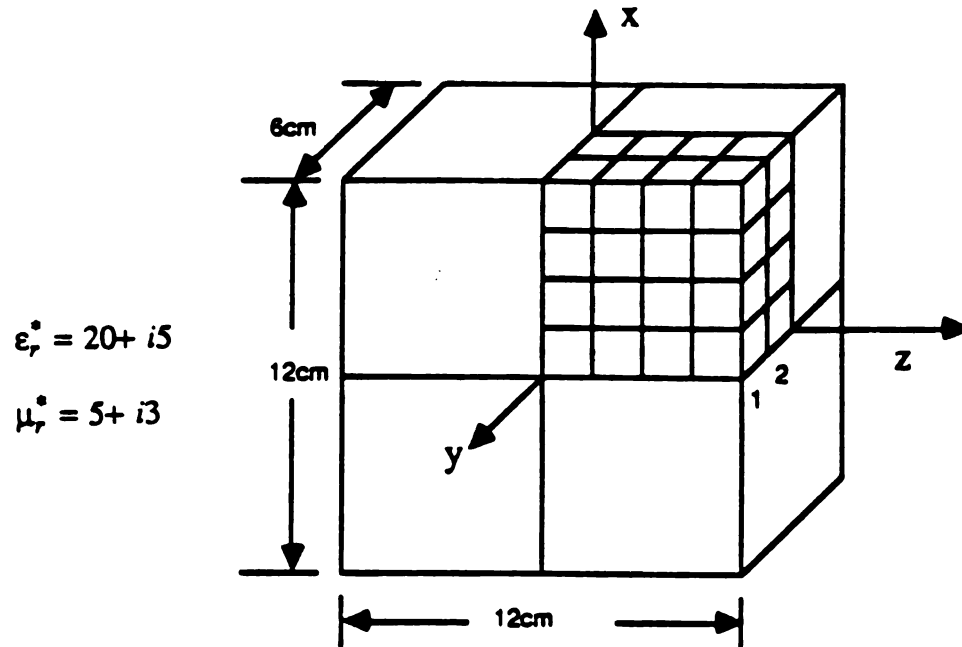
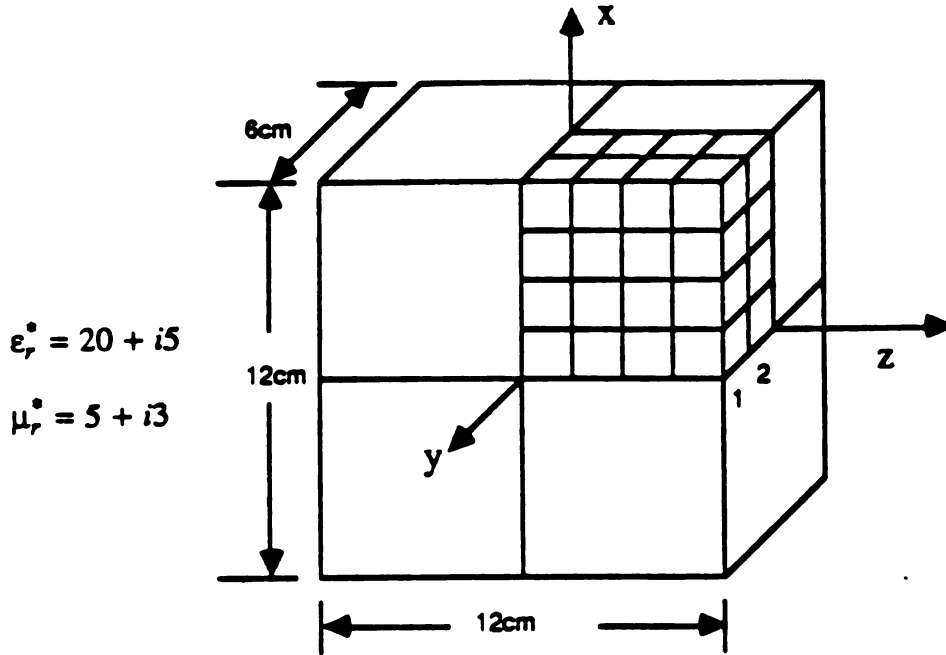


Fig-3.22 A homogeneous cubic body of dimensions $12 \times 12 \times 6 \text{ cm}$ illuminated by an incident plane EM wave.



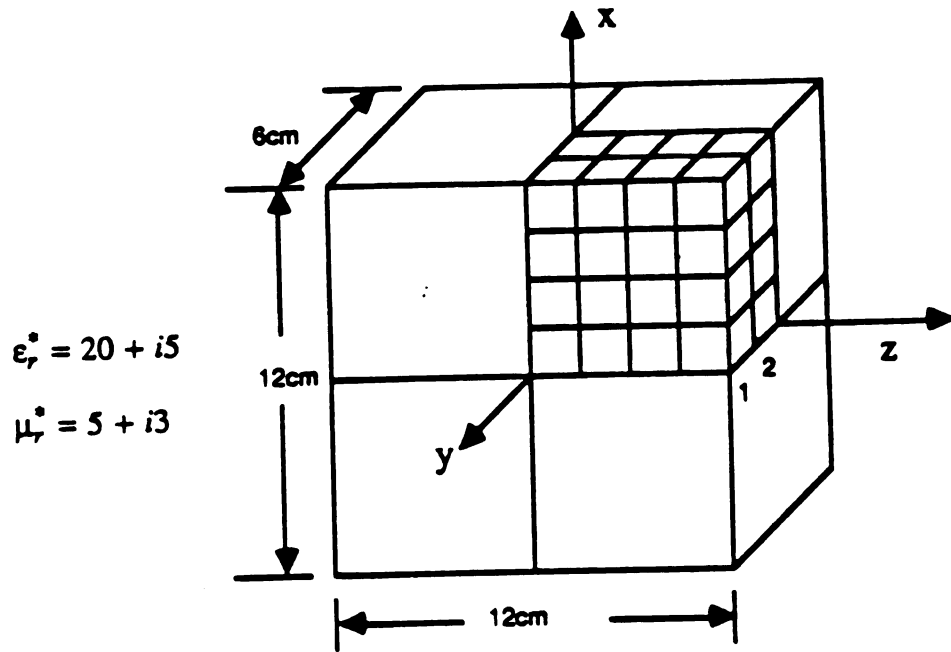
$ E_x $ in (V/m)	.1691	.1692	.1688	.1932	.1512	.1497	.1451	.1617
$\angle E_x$ in ($^\circ$)	-9.8	-10.3	-11.3	-12.5	-3.9	-5.1	-7.7	-12.4
	.2127	.2108	.2069	.2090	.2242	.2184	.2055	.1917
	-9.1	-10.0	-12.1	-15.6	-0.6	-2.4	-6.5	-14.5
	.2369	.2332	.2251	.2150	.2650	.2559	.2355	.2051
	-8.7	-9.9	-12.6	-17.5	0.8	-1.2	-6.0	-15.8
	.2483	.2437	.2334	.2174	.2845	.2737	.2496	.2112
	-8.5	-9.9	-12.8	-18.5	1.4	-0.7	-5.7	-16.4
	1				2			

Fig-3.23 Solutions for the symmetric mode of induced electric field obtained from the coupled tensor integral equations in the rectangular magnetic body. (x -component of E field)



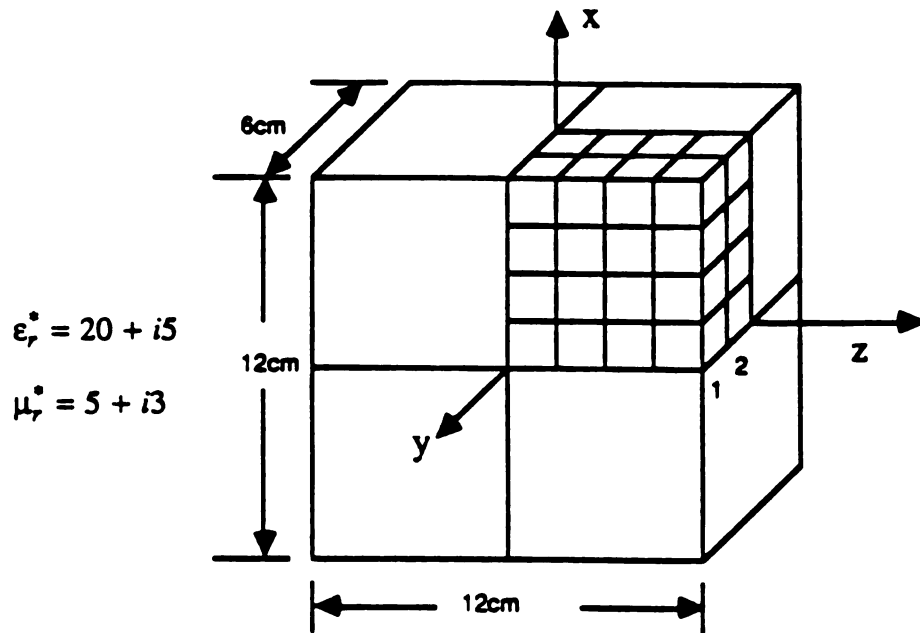
$ E_x $ in (V/m)	.1686	.1688	.1675	.2000	.1351	.1341	.1299	.1623
	-10.6	-10.7	-11.1	-10.6	-11.2	-11.5	-12.3	-11.6
$\angle E_x$ in ($^\circ$)	.2125	.2113	.2079	.2240	.1923	.1884	.1794	.1961
	-9.9	-10.2	-10.9	-10.7	-10.4	-10.9	-12.1	-11.7
	.2361	.2337	.2277	.2353	.2221	.2162	.2030	.2119
	-9.6	-10.0	-10.7	-10.8	-10.1	-10.7	-12.1	-11.8
	.2470	.2440	.2367	.2399	.2365	.2296	.2144	.2190
	-9.5	-9.8	-10.7	-10.8	-9.9	-10.6	-12.1	-11.8
	1				2			

Fig-3.24 Solutions for the symmetric mode of induced electric field obtained from the tensor EFIE in the rectangular magnetic body. (x - component of E field)



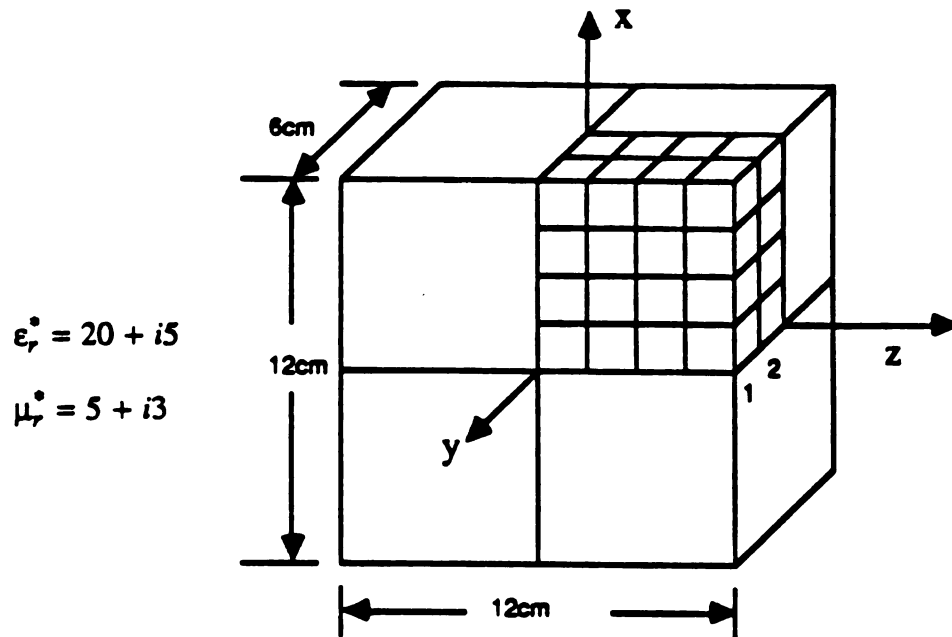
$ E_x $ in (V/m)	.0112	.0341	.0587	.0987	.0122	.0371	.0632	.1037
$\angle E_x$ in ($^\circ$)	93.2	92.8	91.6	89.9	102.1	100.8	98.2	93.2
	.0210	.0642	.1110	.1734	.0252	.0764	.1300	.1949
	98.2	97.5	95.9	93.6	106.2	104.8	104.8	96.9
	.0277	.0843	.1446	.2188	.0339	.1024	.1726	.2499
	100.4	99.6	97.8	95.4	108.1	106.7	103.6	98.8
	.0313	.0942	.1611	.2404	.0383	.1153	.1934	.2760
	101.3	100.5	98.7	96.3	109.0	107.5	104.5	99.7
	1				2			

Fig-3.25 Solutions for the antisymmetric mode of induced electric field obtained from the coupled tensor integral equations in the rectangular magnetic body. (x- component of E field)



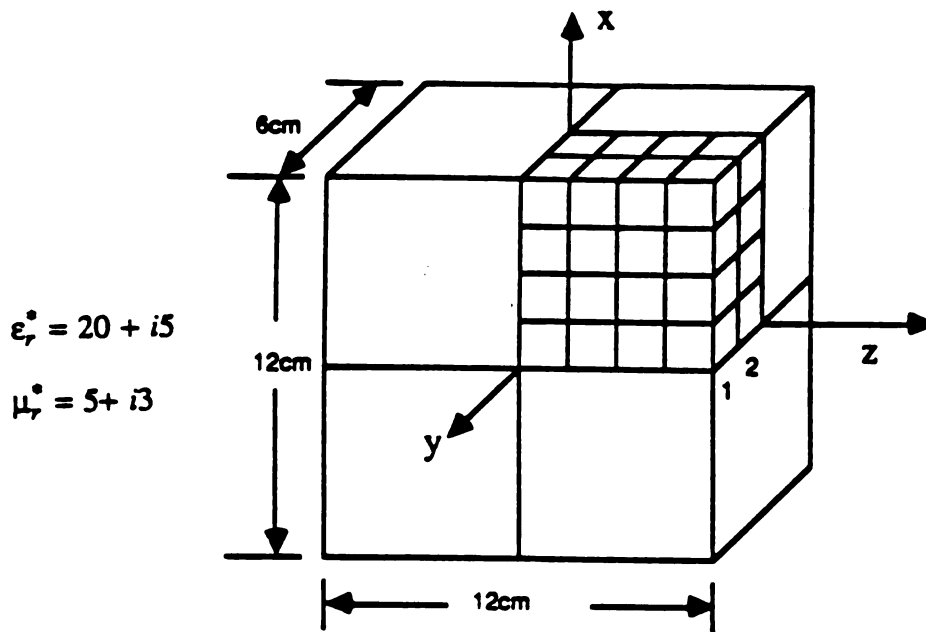
$ E_z $ in (V/m)	.1975	.1739	.1251	.0486	.2372	.2094	.1521	.0622
$\angle E_z$ in ($^\circ$)	-79.2	-79.6	-80.2	-78.3	-76.3	-76.8	-77.7	-76.7
	.1298	.1130	.0793	.0307	.1626	.1419	.1006	.4048
	-76.1	-76.5	-77.1	-76.2	-71.0	-71.4	-72.1	-71.5
	.0748	.0649	.0452	.0175	.0954	.0829	.0583	.0234
	-73.8	-74.2	-74.8	-74.1	-67.4	-67.9	-68.4	-67.6
	.0244	.0211	.0147	.0057	.0314	.0272	.0191	.0077
	-72.7	-73.1	-73.7	-73.1	-65.7	-66.1	-66.6	-65.8
	1				2			

Fig-3.26 Solutions for the antisymmetric mode of induced electric field obtained from the coupled tensor integral equations in the rectangular magnetic body. (z- component of E field)



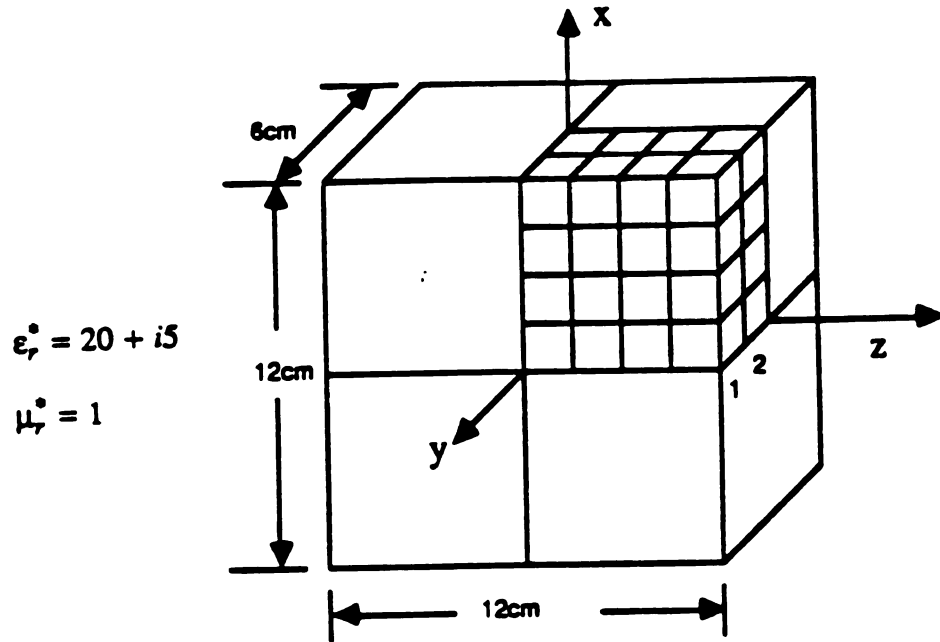
$ E_x $ in (V/m)	.0104	.0314	.0527	.0889	.0103	.0313	.0522	.0894
$\angle E_x$ in ($^\circ$)	86.3	86.1	85.7	85.7	88.7	88.5	87.6	86.9
	.0188	.0571	.0968	.1534	.0208	.0629	.1058	.1668
	89.3	89.1	88.4	88.2	91.7	91.3	90.2	89.4
	.0242	.0734	.1243	.1933	.0275	.0831	.1398	.2153
	90.4	90.1	89.4	89.3	92.8	92.3	91.3	90.5
	.0268	.0813	.1377	.2125	.0308	.0931	.1565	.2388
	90.8	90.5	89.9	89.7	93.3	92.8	91.7	90.9
	1				2			

Fig-3.27 Solutions for the antisymmetric mode of induced electric field obtained from the tensor EFIE in the rectangular magnetic body. (x- component of E field)



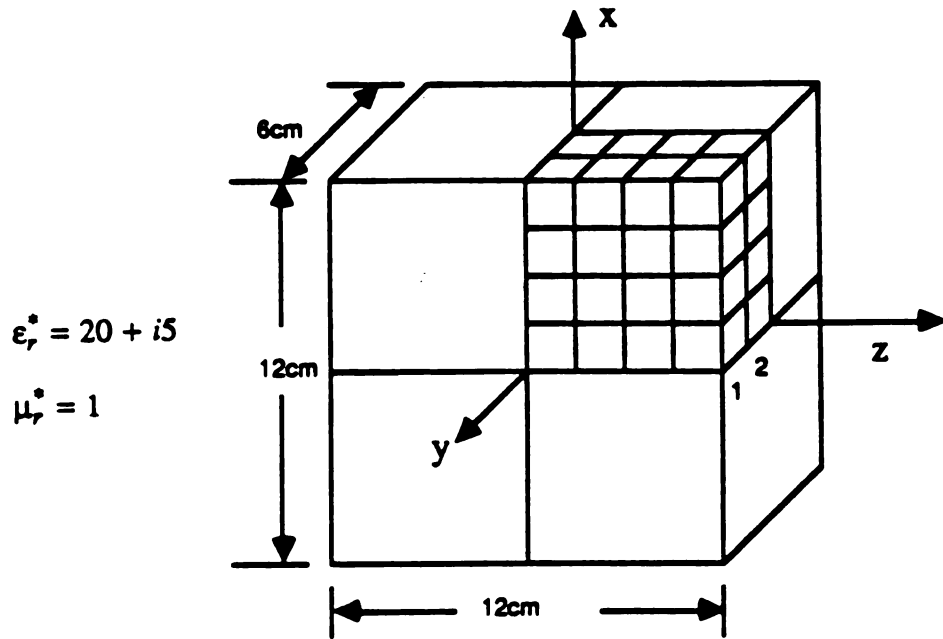
$ E_z $ in (V/m)	.1613	.1415	.1010	.0366	.1922	.1688	.1612	.0468
	-87.1	-87.2	-87.0	-84.2	-86.3	-86.4	-86.4	-84.8
$\angle E_z$ in ($^\circ$)	.1059	.0927	.0660	.0253	.1309	.1146	.0818	.0325
	-86.4	-86.4	-86.3	-85.3	-84.8	-85.0	-85.1	-84.7
	.0617	.0540	.0384	.0149	.0771	.0675	.0481	.0192
	-85.4	-85.5	-85.4	-84.5	-83.5	-83.6	-83.8	-83.3
	.0203	.0177	.0126	.0050	.0254	.0222	.0159	.0064
	-85.0	-85.0	-84.9	-84.3	-82.9	-83.0	-83.1	-82.8
	1				2			

Fig-3.28 Solutions for the antisymmetric mode of induced electric field obtained from the tensor EFIE in the rectangular magnetic body. (z- component of E field)



$ E_x $ in (V/m)	.0078	.0238	.0407	.0672	.0069	.0210	.0360	.0611
$\angle E_x$ in ($^\circ$)	83.2	83.2	83.1	83.3	83.6	83.5	83.4	83.5
	.0133	.0405	.0698	.1076	.0129	.0392	.0676	.1044
	85.9	85.8	85.6	85.6	86.2	86.0	85.8	85.7
	.0168	.0511	.0878	.1318	.0166	.0506	.0868	.1303
	86.8	86.7	86.5	86.5	87.0	86.9	86.6	86.6
	.0185	.0562	.0964	.1432	.0185	.0562	.0961	.1426
	87.2	87.1	86.9	86.9	87.3	87.2	87.0	87.0
	1				2			

Fig-3.29 Solutions for the antisymmetric mode of induced electric field obtained from the tensor EFIE in the rectangular non-magnetic body. (x- component of E field)



$ E_z $ in (V/m)	.0953	.0828	.0569	.0161	.0990	.0863	.0599	.0187
	-89.2	-89.1	-88.5	-82.1	-89.3	-89.2	-88.8	-84.2
$\angle E_z$ in ($^\circ$)	.0635	.0550	.0377	.0125	.0660	.0573	.0395	.0138
	-88.1	-88.4	-87.9	-84.9	-88.6	-88.5	-88.1	-86.3
	.0364	.0314	.0215	.0072	.0379	.0328	.0226	.0079
	-88.0	-87.9	-87.3	-84.7	-88.0	-87.9	-87.5	-85.8
	.0119	.0102	.0070	.0024	.0123	.0107	.0073	.0026
	-87.7	-87.6	-87.0	-84.7	-87.7	-87.6	-87.1	-85.6
	1				2			

Fig-3.30 Solutions for the antisymmetric mode of induced electric field obtained from the tensor EFIE in the rectangular non-magnetic body. (z- component of E field)

figures and the significant differences in the induced fields between magnetic and non-magnetic cases.

The coupled tensor integral equations will become a $6N \times 6N$ matrix equation after transformation via pulse-basis expansion and point-matching if the body is divided into N cells while the decoupled EFIE will become a $3N \times 3N$ matrix equation. Obviously, the former needs four times of the computer memory storage as that of the latter thus requires more computation time to solve the matrix equation by existing numerical methods. However, in the tensor EFIE, we have an extra surface integration term to evaluate when the transformation is performed in contrast to the coupled tensor integral equations. The other advantage of the coupled tensor integral equations is that the heterogeneous problem can be handled easier by applying this set of equations since we only need to vary the parameters τ_e and τ_m in the coefficients of the elements in the transformed matrix equation.

An example of heterogeneous case is given as here. Fig-3.31 shows a heterogeneous body of dimensions $6 \times 6 \times 6$ cm. The shaded region in the center consists of permeable material with $\epsilon_r^* = 20 + i5$ and $\mu_r^* = 5 + i3$ and the rest of the body is non-magnetic material with $\epsilon_r^* = 20 + i5$ and $\mu_r^* = 1$. Again we concentrate on the antisymmetric mode of incident field and omit the case of symmetric mode due to the same reason as previous examples. The frequency is the same 200 MHz.

Fig-3.32 shows the distribution of E_x , E_z and H_y of the first octant of the heterogeneous body described in Fig-3.31. The reason we indicate y - component of induced magnetic field only is simply because this component is the only significant one since H^i is polarized in y - direction and almost uniformly distributed. The body is divided into 64 cubic cells with dimensions of $1.5 \times 1.5 \times 1.5$ cm. Fig-3.33 presents E_x , E_z and H_y of a homogeneous non-magnetic cube with $\epsilon_r^* = 20 + i5$ and of the same

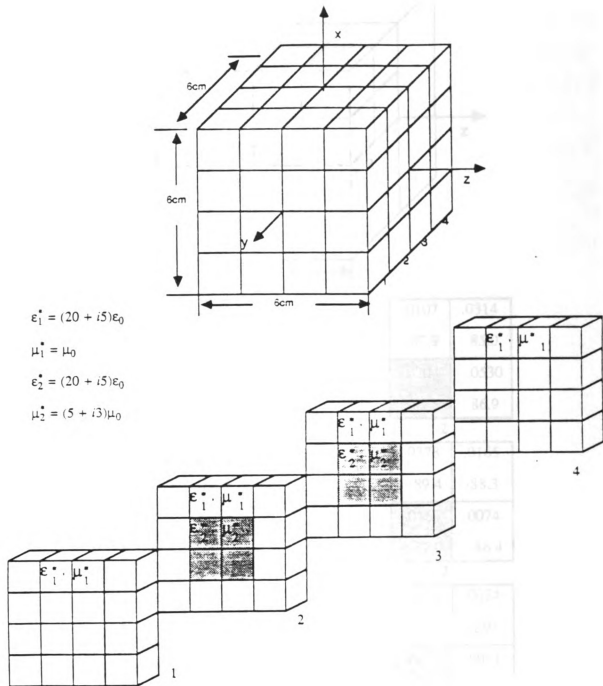
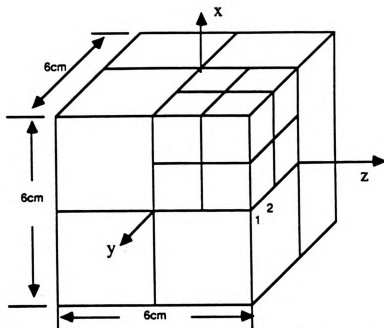


Fig-3.31 A heterogeneous cubic body of dimensions $6 \times 6 \times 6$ cm with different parameters specified in the shaded and unshaded regions.



$|E_x|$ in (V/m)
 $\angle E_x$ in ($^\circ$)

.0087	.0304
83.2	83.2
.0146	.0470
84.9	84.8

1

.0107	.0314
87.9	85.0
.0204	.0530
89.5	86.9

2

$|E_z|$ in (V/m)
 $\angle E_z$ in ($^\circ$)

.0291	.0124
-91.2	-89.6
.0097	.0044
-90.8	-90.1

1

.0378	.0165
-89.4	-88.3
.0164	.0074
-87.0	-86.4

2

$|H_y|$ in (A/m)
 $\angle H_y$ in ($^\circ$)

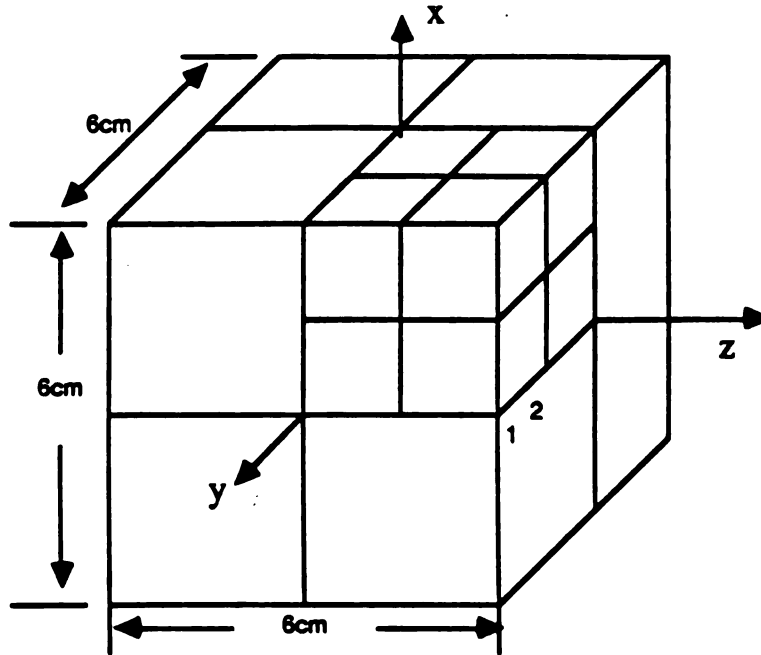
.0029	.0027
1.1	0.2
.0038	.0028
4.5	1.1

1

.0021	.0024
-3.8	-1.9
.0011	.0021
-22.0	-3.9

2

Fig-3.32 Solutions for the antisymmetric mode of induced EM field obtained from the coupled tensor integral equations in the heterogeneous body.



$ E_x $ in (V/m)	.0071	.0271		
	80.4	81.3		
$\angle E_x$ in ($^\circ$)	.0115	.0401		
	81.8	82.5		
	1			
$ E_x $ in (V/m)	.0062	.0246		
	80.1	81.1		
$\angle E_x$ in ($^\circ$)	.0107	.0379		
	81.5	82.3		
	2			
$ E_z $ in (V/m)	.0221	.0090		
	-94.2	-92.4		
$\angle E_z$ in ($^\circ$)	.0065	.0028		
	-94.1	-93.4		
	1			
$ E_z $ in (V/m)	.0226	.0095		
	-94.7	-93.3		
$\angle E_z$ in ($^\circ$)	.0065	.0028		
	-94.7	-94.4		
	2			
$ H_y $ in (A/m)	.0027	.0026		
	0.1	0.0		
$\angle H_y$ in ($^\circ$)	.0027	.0027		
	0.2	0.1		
	1			
$ H_y $ in (A/m)	.0027	.0027		
	0.1	0.0		
$\angle H_y$ in ($^\circ$)	.0027	.0027		
	0.3	0.1		
	2			

Fig-3.33 Solutions for the antisymmetric mode of induced EM field obtained from the coupled tensor integral equations in the non-magnetic homogeneous body.

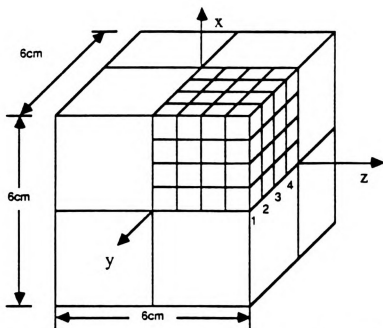
dimensions and incident field for comparison. We observe that the induced electric field in the heterogeneous case is larger than that in the homogeneous case, especially in the cell consisting of magnetic material, but the induced magnetic field becomes smaller in that cell. We may use a simple picture to explain this result. Since the \mathbf{B} field has to be continuous inside the body, the magnetic cell which has larger value of μ then has a smaller strength of the \mathbf{H} field. By the definition of the magnetization \mathbf{M}

$$\mathbf{M} = \frac{\mathbf{B}}{\mu_0} - \mathbf{H} , \quad (3.5.1)$$

the smaller \mathbf{H} implies a larger magnetization \mathbf{M} and hence a larger circulatory electric fields.

Fig-3.34 to Fig-3.36 show the distributions of E_x , E_z and H_y of the above heterogeneous example with 512 subdivisions. A fair convergence is indicated by the comparison of the numbers in Fig-3.33 and Fig-3.34 to Fig-3.36.

The convergence and agreement in the numerical solutions of the coupled tensor integral equations and the tensor EFIE shown in the above examples, however, deteriorate when the relative permittivity ϵ_r goes up to the value about 50. The unsatisfactory results also occur if we increase the frequency of incident EM fields. It appears that there are certain limitations for the numerical solutions of the integral equations. A series of numerical results of the two set of integral equations have been compared to investigate the limitations of the convergence and agreement properties. Table-3.1 and Table-3.1a summarize these properties under various circumstances such as different frequencies of the incident EM fields or parameters of the materials. It is noted that in the cases of $\mu_r^* = 1$, the agreement between two sets of equations is always satisfactory since they are identical equations.



$|E_x|$ in (V/m)
 $\angle E_x$ in ($^\circ$)

.0041	.0124	.0210	.0344
84.4	84.4	84.2	84.1
.0071	.0215	.0368	.0561
87.5	87.4	87.0	86.8
.0092	.0279	.0473	.0701
88.7	88.6	88.3	88.0
.0103	.0311	.0525	.0769
89.2	89.1	88.8	88.6

1

.0038	.0118	.0196	.0318
85.6	86.1	85.8	84.8
.0075	.0231	.0385	.0563
88.7	89.0	88.7	87.7
.0101	.0312	.0515	.0724
89.7	90.2	89.9	89.1
.0114	.0353	.0582	.0805
90.0	90.6	90.4	89.6

2

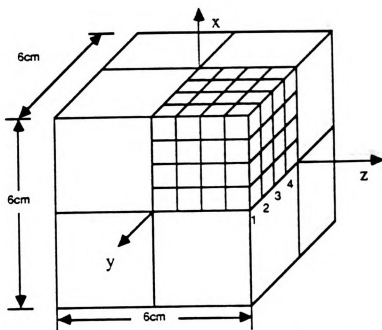
.0042	.0136	.0214	.0323
88.0	89.3	87.9	85.5
.0088	.0285	.0440	.0585
91.5	92.5	91.1	88.7
.0124	.0406	.0613	.0769
92.7	93.7	92.5	90.2
.0143	.0470	.0704	.0863
93.2	94.1	93.0	90.8

3

.0047	.0150	.0226	.0327
90.5	91.4	89.1	85.9
.0102	.0324	.0475	.0601
94.1	94.6	92.4	89.3
.0148	.0476	.0675	.0800
95.5	95.9	93.8	90.9
.0173	.0558	.0782	.0903
96.0	96.3	94.4	91.6

4

Fig-3.34 Solutions for the antisymmetric mode of induced EM field obtained from the coupled tensor integral equations based on 512-cell division in the heterogeneous body. (x - component of E field)



$|E_z|$ in (V/m)
 $\angle E_z$ in ($^\circ$)

.0552	.0477	.0326	.0098
-87.6	-87.6	-87.3	-82.0
.0383	.0329	.0224	.0077
-87.0	-87.0	-86.7	-84.4
.0227	.0195	.0132	.0047
-86.6	-86.6	-86.3	-84.3
.0075	.0064	.0044	.0015
-86.4	-86.3	-86.1	-84.4

1

.0618	.0533	.0365	.0120
-87.0	-87.0	-86.9	-83.4
.0459	.0393	.0266	.0097
-85.8	-85.8	-85.8	-84.6
.0281	.0240	.0162	.0059
-85.7	-85.7	-85.5	-84.6
.0090	.0077	.0052	.0019
-86.2	-86.2	-85.9	-85.4

2

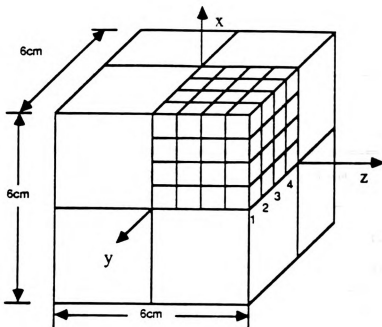
.0687	.0589	.0398	.0132
-86.0	-86.1	-86.2	-83.2
.0589	.0499	.0328	.0120
-83.8	-83.8	-83.9	-82.9
.0402	.0339	.0220	.0081
-82.8	-82.8	-82.7	-82.0
.0120	.0101	.0067	.0024
-83.6	-83.7	-83.7	-83.5

3

.0733	.0625	.0419	.0139
-85.3	-85.5	-85.8	-83.0
.0671	.0565	.0367	.0134
-82.6	-82.7	-82.8	-82.0
.0492	.0411	.0262	.0096
-81.0	-81.0	-81.0	-80.2
.0151	.0126	.0081	.0029
-81.1	-81.2	-81.4	-81.2

4

Fig-3.35 Solutions for the antisymmetric mode of induced EM field obtained from the coupled tensor integral equations based on 512-cell division in the heterogeneous body. (z - component of E field)



$|H_y|$ in (A/m)
 $\angle H_y$ in ($^\circ$)

.0028	.0028	.0027	.0026
1.0	0.9	0.5	0.1
.0031	.0030	.0029	.0027
2.6	2.3	1.5	0.5
.0035	.0034	.0030	.0028
3.8	3.5	2.3	0.9
.0037	.0035	.0031	.0028
4.1	3.8	2.6	1.0

1

.0027	.0027	.0026	.0026
0.3	0.2	-0.1	-0.4
.0031	.0031	.0028	.0026
2.9	2.8	1.2	-0.1
.0043	.0042	.0031	.0026
5.9	6.6	2.8	0.2
.0043	.0043	.0031	.0026
5.1	5.9	2.9	0.2

2

.0024	.0024	.0024	.0025
-2.1	-1.9	-1.6	-1.2
.0021	.0022	.0023	.0024
-4.1	-3.6	-2.2	-1.6
.0011	.0012	.0022	.0024
-21.3	-19.6	-3.6	-2.0
.0010	.0011	.0021	.0023
-23.1	-21.3	-4.1	-2.2

3

.0022	.0022	.0023	.0024
-4.4	-3.9	-2.9	-1.9
.0017	.0018	.0021	.0023
-10.4	-9.3	-5.5	-2.9
.0013	.0014	.0018	.0022
-19.6	-18.9	-9.4	-3.9
.0012	.0013	.0017	.0021
-20.2	-19.7	-10.5	-4.5

4

Fig-3.36 Solutions for the antisymmetric mode of induced EM field obtained from the coupled tensor integral equations based on 512-cell division in the heterogeneous body. (y - component of \mathbf{H} field)

Table-3.1

Summary of Agreement and Convergence Properties for the Coupled tensor IE and tensor EFIE (I)														
Type of Incident Electric Field			$\epsilon_r^* = 50 + i10$						$\epsilon_r^* = 5 + i4$					
			$\mu_r^* = 50+i10$		$\mu_r^* = 5+i3$		$\mu_r^* = 1+i0$		$\mu_r^* = 50+i10$		$\mu_r^* = 5+i3$		$\mu_r^* = 1+i0$	
			E	C	E	C	E	C	E	C	E	C	E	C
$f =$ 750MHz	sin	conv.	X	X	X	X	X	X	F	X	F	O	O	O
		agr.	X		X		O		X		F		O	
	cos	conv.	X	X	X	X	X	X	X	X	O	F	O	O
		agr.	X		X		O		X		X		O	
$f =$ 200MHz	sin	conv.	X	X	X	X	X	X	O	O	O	O	O	O
		agr.	X		X		O		O		O		O	
	cos	conv.	O	X	F	O	O	O	O	O	O	O	O	O
		agr.	X		O		O		F		O		O	

E: Tensor EFIE C: Coupled Tensor IE

O: Satisfactory F: Fair X: Poor

Table-3.1a

Summary of Agreement and Convergence Properties for the Coupled tensor IE and tensor EFIE (II)														
Type of Incident Electric Field			$\epsilon_r^* = 50 + i10$						$\epsilon_r^* = 5 + i4$					
			$\mu_r^* = 50+i10$		$\mu_r^* = 5+i3$		$\mu_r^* = 1+i0$		$\mu_r^* = 50+i10$		$\mu_r^* = 5+i3$		$\mu_r^* = 1+i0$	
			E	C	E	C	E	C	E	C	E	C	E	C
$f =$ 50MHz	sin	conv.	X	X	X	X	F	F	O	O	O	O	O	O
		agr.	X		F		O		O		O		O	
	cos	conv.	O	O	O	O	O	O	O	O	O	O	O	O
		agr.	O		O		O		O		O		O	
$f =$ 10MHz	sin	conv.	X	X	X	X	F	F	O	O	O	O	O	O
		agr.	X		F		O		O		O		O	
	cos	conv.	O	O	O	O	O	O	O	O	O	O	O	O
		agr.	O		O		O		O		O		O	

E: Tensor EFIE C: Coupled Tensor IE

O: Satisfactory F: Fair X: Poor

We now gain some insights about the numerical solution behaviors for the coupled tensor integral equations and the tensor EFIE by comparing the numerical results of the induced electric field distributions presented above. However, to investigate the behavior of the magnetic field distribution, the solutions of tensor MFIE and the coupled equations should be compared. Since both sets of equations are dual in \mathbf{E} and \mathbf{H} , it is logical for us to expect the numerical solution behavior of the induced magnetic field to be similar to that of the electric field if we interchange ϵ^* and μ^* , and also symmetric and antisymmetric modes of incident fields. In fact, the numerical results which are not presented here will confirm our expectation.

There are some advantages in the decoupled tensor EFIE and MFIE which we derived in section 3.2 over the formulations derived by Tai [13] although they are equivalent in the homogeneous case. One thing is that there exist the terms of $\nabla \times \mathbf{E}$ and $\nabla \times \mathbf{H}$ in Tai's equations. This will cause difficulty when one attempts to solve the equations numerically. The other advantage of our equations is that they are derived for a heterogeneous system so that they can be used to handle more complicated cases, although some numerical skill is needed to calculate the terms involving the gradient of the permittivity or permeability functions.

The set of coupled integral equations in terms of the free space scalar Green's functions (3.3.28) and (3.3.29) has also been investigated when it is applied to a homogeneous body. As we mentioned before, there are no induced volume charge inside the homogeneous body therefore the terms of $\nabla \cdot \mathbf{E}$ and $\nabla \cdot \mathbf{H}$ should vanish in the equations. However, if we simply solve the reduced equations (3.4.27) and (3.4.28) via pulse-basis expansion and point-matching, we will find that the numerical results are completely different from what we obtained by the coupled tensor integral equations and tensor EFIE. The reason is that the pulse-basis expansion assumption satisfies the charge free condition inside each cell, but the jump discontinuities created by the

pulse-basis at the boundaries of adjacent cells will imply some charge distributions on the cell surfaces which need to be taken into account in the evaluation of the induced EM fields. Therefore we need to extend the domain of the surface integration from the enclosing surface s to all the surrounding surfaces of each cell in (3.4.27) and (3.4.28). After this extension process, we are able to get numerical results very close to what we have obtained by the tensor integral equations. The numerical results are also omitted.

To compare the advantages and disadvantages of the two sets of coupled integral equations, a few things need to be pointed out. Since these two sets of equations are both transformed into matrix equations of order $6N$, they cost equally in computer memory storage. In the tensor equations, we need to handle the singularity problem with a correction term before we get into computer but the formulations turn out to be easier to program since there are only volume integrations involved. On the other hand, we need to calculate both the volume and surface integrations in the other set of coupled integral equations.

The arguments of the two different formulations of decoupled integral equations are similar to that of the two sets of coupled integral equations except that both sets of decoupled equations contain the surface integrations. We should also notice that only the domains of the surface integrations involving the $\mathbf{n}\cdot\mathbf{E}$ and $\mathbf{n}\cdot\mathbf{H}$ terms which imply surface charge distributions need to be extended to all the surrounding surfaces of each cell.

Let us summarize the relations among the four sets of integral equations briefly. The two sets of coupled integral equations will give similar numerical results provided the surface integration terms are properly treated when we apply the pulse-basis expansion and point-matching to solve the induced field distributions in a homogeneous body, and so will the two sets of decoupled integral equations. The coupled integral

equations can determine both \mathbf{E} and \mathbf{H} simultaneously but will require four times of memory storage in the computer and need a longer CPU time to solve matrix equations of larger size. The agreement of the numerical results between the coupled integral equations and the decoupled ones is satisfactory for certain ranges. However, in the heterogeneous cases, it is easy to program for the coupled tensor integral equations.

CHAPTER IV

PLANE WAVE SPECTRUM ANALYSIS OF A NONUNIFORM PLANE WAVE PASSING THROUGH A LAYER OF LOSSY MATERIAL

This chapter presents an application of electromagnetic wave for detecting a small movement of a biological body behind a barrier. A microwave life detection system operating at a frequency of 10 GHz [20], [21] has been constructed to measure the breathing and heart beats of a human subject located at a distance of 100 feet. The principle of the system is to illuminate a human subject with a low intensity microwave beam, and then extract the breathing and heart signals from the modulated back-scattered wave with a detecting system. In order to detect small body vibrations behind a barrier, a system constructed on the same principle with an operating frequency at 2 GHz is developed because of the better penetration ability of EM waves with a lower frequency. A series of experiments have been conducted to measure the breathing and heart signals of a human subject behind a thick layer of bricks with the microwave life detection systems. Plane wave spectrum theory [17], [18] is used to analyze the nonuniform plane wave radiated from the antenna and passing through a layer of lossy material in order to predict the field distribution on the other side of the barrier. The predicted electric field distributions and experimental results on the detection of breathing and heart signals behind brick wall of various thicknesses are presented.

In section 4.1, the plane wave spectrum analysis is introduced. Some predictions of the electric field distributions of the nonuniform plane wave passing through a layer of lossy material are shown in section 4.2. A brief description of the microwave detection systems is included in section 4.3. Section 4.4 presents experimental results

of detecting the small vibrations due to breathing and heart beats of a human body behind a brick wall.

4.1 Plane Wave Spectrum Analysis

The plane wave spectrum approach has been summarized by Paris [17]. Simply speaking, any arbitrary electric field distribution of a particular frequency can be represented as a superposition of plane waves traveling in different directions with different amplitudes and the same frequency. The resultant expansion is known as a modal expansion of the arbitrary monochromatic wave. The object of this expansion is to determine the unknown amplitudes and directions of propagation of the plane waves in the superposition.

A plane wave in free space must satisfy the Maxwell's equations which lead to the vector Helmholtz equation:

$$\nabla^2 \mathbf{E}(\mathbf{r}) + k_0^2 \mathbf{E}(\mathbf{r}) = 0 \quad (4.1.1)$$

where

$$k_0^2 = \omega^2 \mu_0 \epsilon_0 . \quad (4.1.2)$$

The trial solution of (4.1.1) can be written as

$$\mathbf{E} = \mathbf{A}(\mathbf{k}) e^{-j\mathbf{k} \cdot \mathbf{r}} \quad (4.1.3)$$

where the time harmonic factor of $e^{j\omega t}$ is assumed, $j = \sqrt{-1}$ is used in this chapter and

$$\mathbf{k} = xk_x + yk_y + zk_z \quad (4.1.4)$$

denotes the direction of propagation of the plane wave represented by (4.1.3). The

three Cartesian components of \mathbf{k} should satisfy the following relations:

$$k_x^2 + k_y^2 + k_z^2 = k_0^2 = \omega^2 \mu_0 \epsilon_0 . \quad (4.1.5)$$

Thus at a frequency, only two of the components of \mathbf{k} can be independently specified. Suppose k_x and k_y are independent components, then

$$k_z = \begin{cases} \sqrt{k_0^2 - k_x^2 - k_y^2} , & k_x^2 + k_y^2 \leq k_0^2 \\ -j\sqrt{k_x^2 - k_y^2 - k_0^2} , & k_x^2 + k_y^2 > k_0^2 \end{cases} \quad (4.1.6)$$

The negative radical is chosen specifically in order to ensure that the wave is bounded at infinity.

Since the region is charge free, we have

$$\nabla \cdot \mathbf{E} = 0 . \quad (4.1.7)$$

Substitute (4.1.4) into (4.1.7) gives

$$\mathbf{k} \cdot \mathbf{A}(\mathbf{k}) = 0 \quad (4.1.8)$$

or

$$k_x A_x(\mathbf{k}) + k_y A_y(\mathbf{k}) + k_z A_z(\mathbf{k}) = 0 . \quad (4.1.9)$$

This implies only two components of $\mathbf{A}(\mathbf{k})$ are independent for all \mathbf{k} . Let these be A_x and A_y , then

$$A_z(\mathbf{k}) = -\frac{1}{k_z} [k_x A_x(\mathbf{k}) + k_y A_y(\mathbf{k})] . \quad (4.1.10)$$

The general solution for $\mathbf{E}(\mathbf{r})$ can be constructed as linear combinations over k_x and k_y if $\mathbf{A}(\mathbf{k})$ is known:

$$\mathbf{E}(\mathbf{r}) = \int_{-\infty}^{\infty} \int_{-\infty}^{\infty} \mathbf{A}(\mathbf{k}) e^{-j\mathbf{k} \cdot \mathbf{r}} dk_x dk_y \quad (4.1.11)$$

where $A(\mathbf{k})$ is the so called plane wave spectrum. The expression of (4.1.11) is essentially a 2-dimensional inverse Fourier transform when the z coordinate is specified.

Suppose we aim to predict a electric field distribution of a nonuniform plane wave passing through a layer of lossy barrier with thickness d as shown in Fig-4.1. The complex permittivity of the barrier is ϵ^* and the permeability is μ_0 . An antenna is placed right next to the barrier and the aperture is on the $z=0$ plane. The aperture field of the antenna is then denoted as $E(x,y,0)$. Now we can find the plane wave spectrum of the aperture field on the $z=0$ plane by the two-dimensional Fourier transform:

$$A_x(\mathbf{k}) = \frac{1}{4\pi^2} \int_{-\infty}^{\infty} \int_{-\infty}^{\infty} E_x(x,y,0) e^{j(k_x x + k_y y)} dx dy \quad (4.1.12)$$

$$A_y(\mathbf{k}) = \frac{1}{4\pi^2} \int_{-\infty}^{\infty} \int_{-\infty}^{\infty} E_y(x,y,0) e^{j(k_x x + k_y y)} dx dy \quad (4.1.13)$$

It is noticed that only tangential components of \mathbf{E} field on the $z=0$ plane are needed to determine the spectrum $A(\mathbf{k})$ since A_z can be derived from (4.1.10).

We treat a nonuniform plane wave as a linear combination of uniform plane waves coming from all directions. In order to analyze a single uniform plane wave passing through the one-layer barrier, a very simple approach [19] by means of wave matrix and transmission-line theory is used. This analysis is valid for both cases that the barrier consists of loseless ($\sigma = 0$) or lossy ($\sigma \neq 0$) material. The lossy layer is replaced by an equivalent transmission-line circuit as shown in Fig-4.2. The transmission coefficients of the barrier for an obliquely incident plane wave can be determined as follows:

The reflection and transmission coefficients at the two interfaces are

$$R_1 = \frac{Z - 1}{Z + 1} \quad (4.1.14)$$

$$R_2 = \frac{1 - Z}{1 + Z} \quad (4.1.15)$$

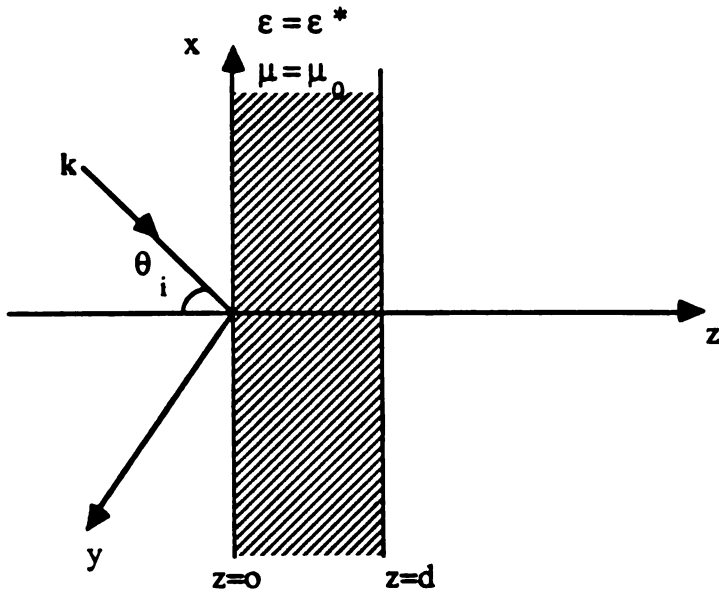


Fig-4.1 An incident plane EM wave on a lossy layer of thickness d .

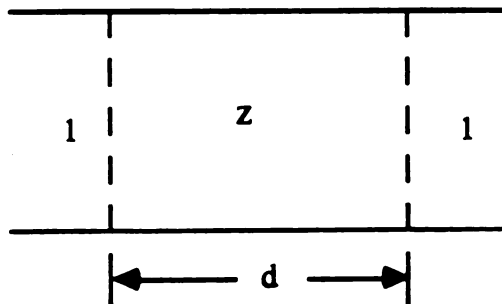


Fig-4.2 Equivalent circuit for a lossy dielectric layer.

$$T_1 = 1 + R_1 = \frac{2Z}{1 + Z} \quad (4.1.16)$$

$$T_2 = 1 + R_2 = \frac{2}{1 + Z} \quad (4.1.17)$$

where Z is the normalized impedance of the section of line representing the lossy layer. Using the wave matrix theory [19] gives the over-all transmission coefficient

$$T = \frac{T_1 T_2}{e^{j\phi} + R_1 R_2 e^{-j\phi}} = \left[\cos\phi + j \frac{1 + Z^2}{2Z} \sin\phi \right]^{-1}, \quad (4.1.18)$$

where

$$\phi = k_0 \sqrt{\kappa - \sin^2\theta_i} d \quad (4.1.19)$$

is the electrical length of the lossy layer of thickness d , $\kappa = \epsilon_r^*$ is the relative complex permittivity and θ_i is the angle of incidence measured from the interface normal in Fig-4.1.

For the cases of perpendicularly polarized and parallelly polarized incident waves, we have different expressions for the normalized impedances:

$$Z_P = \frac{\sqrt{\kappa - \sin^2\theta_i}}{\kappa \cos\theta_i} \quad (4.1.20)$$

$$Z_N = \frac{\cos\theta_i}{\sqrt{\kappa - \sin^2\theta_i}} \quad (4.1.21)$$

where the subscripts N and P stand for perpendicular and parallel polarization, respectively. Similarly for the two different over-all transmission coefficients:

$$T_P = \left[\cos\phi + j \frac{1 + Z_P^2}{2Z_P} \sin\phi \right]^{-1} \quad (4.1.22)$$

$$T_N = \left[\cos\phi + j \frac{1 + Z_N^2}{2Z_N} \sin\phi \right]^{-1} . \quad (4.1.23)$$

Notice that in a particular direction of incidence \mathbf{k} ,

$$\cos\theta_i = \frac{\mathbf{k} \cdot \mathbf{z}}{|\mathbf{k}| |\mathbf{z}|} = \frac{k_z}{k_0} \quad (4.1.24)$$

$$\sin\theta_i = \frac{\sqrt{k_x^2 + k_y^2}}{k_0} . \quad (4.1.25)$$

The normal vector \mathbf{a}_N of the incidence plane for a uniform plane wave traveling in the direction of \mathbf{k} can be expressed as

$$\mathbf{a}_N = \mathbf{z} \times \mathbf{k} = -xk_y + yk_x . \quad (4.1.26)$$

Thus the perpendicularly polarized component of \mathbf{A} , denoted as A_N , is the projection of \mathbf{A} on \mathbf{a}_N :

$$A_N = \frac{(\mathbf{A} \cdot \mathbf{a}_N) \mathbf{a}_N}{|\mathbf{a}_N|^2} , \quad (4.1.27)$$

and the parallelly polarized component of \mathbf{A} , denoted as A_P , can be obtained by subtracting A_N from \mathbf{A} :

$$\mathbf{A}_P = \mathbf{A} - A_N . \quad (4.1.28)$$

The direction of a single uniform plane wave remains the same after passing through the barrier by the Snell's law. So we simply multiply the two different overall transmission coefficients with A_N and A_P to obtain A_N' and A_P' , the two different polarized components of the plane wave spectrum, behind the barrier:

$$A_N' = T_N A_N \quad (4.1.29)$$

$$A_P' = T_P A_P . \quad (4.1.30)$$

The total plane wave spectrum behind the barrier \mathbf{A}' is then

$$\mathbf{A}' = \mathbf{A}'(k_x, k_y) = A_N' + A_P' = T_N A_N + T_P A_P . \quad (4.1.31)$$

Therefore we can determine the electric field distribution behind the barrier at any particular z through the inverse two-dimensional Fourier transform:

$$\mathbf{E}(x,y,z) = \int_{-\infty}^{\infty} \int_{-\infty}^{\infty} \mathbf{A}'(k_x, k_y, k_z) e^{-j[k_x x + k_y y + k_z(z-d)]} dk_x dk_y \quad (4.1.32)$$

where k_z is related to k_x and k_y by (4.1.6).

Now we can predict the \mathbf{E} field distribution at any point behind the barrier for a given antenna aperture field distribution, or in other words, a nonuniform plane wave, passing through a infinite one-layer barrier. Some examples simulating the practical situations are presented in next section.

4.2 Predictions of Field distributions for a Nonuniform Plane Wave Passing through a Layer of Lossy Material

Some examples of the predicted electric field distributions for a nonuniform plane wave passing through a layer of lossy material are presented in this section. Suppose some antenna aperture field distribution are given, we can use the formulas derived in section 4.1 to calculate the desired field distributions behind the layer.

We use the aperture field of an open ended rectangular wave guide with dimension a and b ($b < a$) as the nonuniform plane wave at $z=0$ plane in our example as shown in Fig-4.3. The origin of the coordinate system is set at the center of the aperture. The \mathbf{E} field of TE_{10} mode in a rectangular wave guide is

$$\mathbf{E}(x,y) = \mathbf{x} E_0 \cos \frac{\pi y}{a} e^{-j\beta z} \quad (4.2.1)$$

where

$$\beta = \sqrt{k_0^2 - \frac{\pi^2}{a^2}} \quad (4.2.2)$$

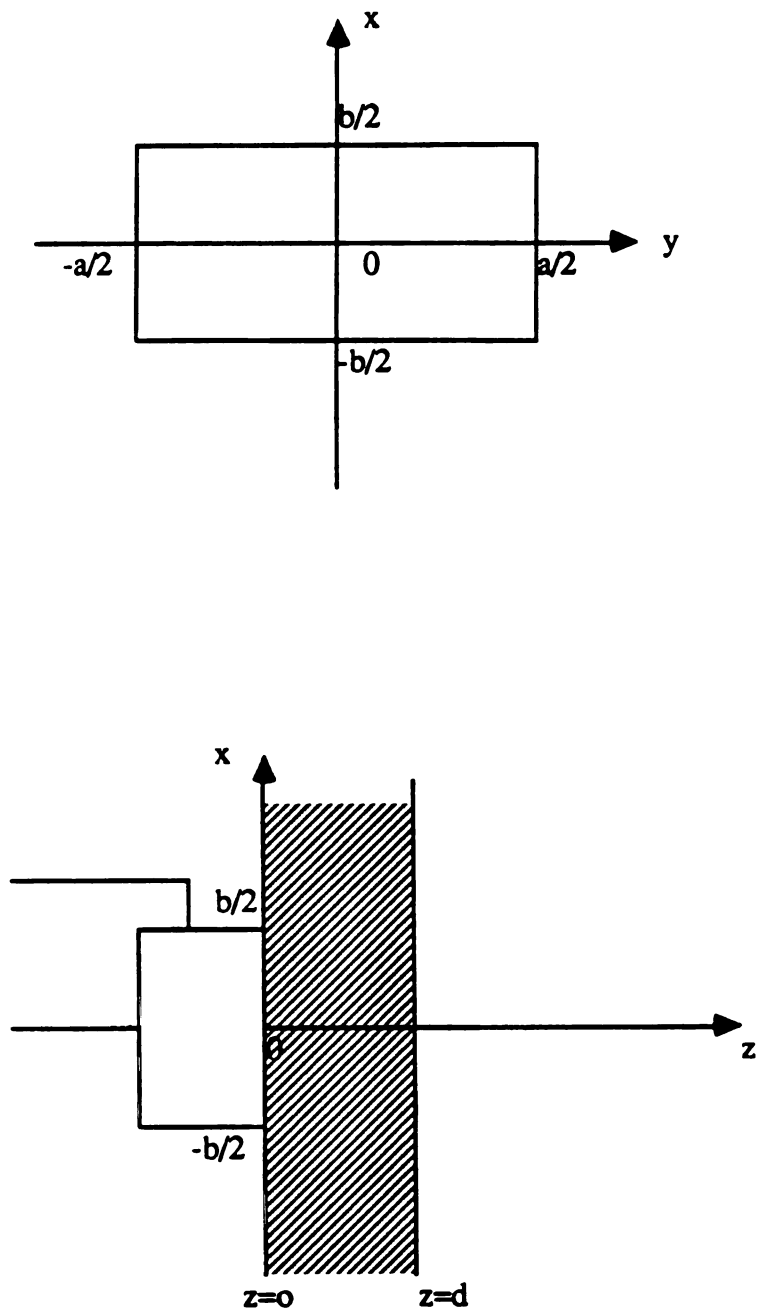


Fig-4.3 The front view and side view of the antenna aperture located next to the lossy layer.

is the propagation constant of the z - direction.

On the $z=0$ plane, we have

$$E_x(x,y,0) = P(x,y) E_0 \cos \frac{\pi y}{a} \quad (4.2.3)$$

$$E_y(x,y,0) = 0 . \quad (4.2.4)$$

where $P(x,y)$ is defined as

$$P(x,y) = \begin{cases} 1, & \text{for } |x| \leq a/2 \text{ and } |y| \leq b/2 \\ 0, & \text{otherwise .} \end{cases} \quad (4.2.5)$$

By using (4.1.12), we obtain the plane wave spectrum of this aperture field:

$$\begin{aligned} A_x(\mathbf{k}) &= \frac{1}{4\pi^2} \int_{-\infty}^{\infty} \int_{-\infty}^{\infty} E_x(x,y,0) e^{j(k_x x + k_y y)} dx dy \\ &= \frac{E_0}{4\pi^2} \int_{-b/2}^{b/2} e^{jk_x x} dx \int_{-a/2}^{a/2} \cos \frac{\pi y}{a} e^{jk_y y} dy \\ &= \frac{E_0}{\pi} \left[\frac{\sin \frac{k_x b}{2}}{k_x} \right] \left[\frac{\cos \frac{k_y a}{2}}{\frac{\pi^2}{a^2} - k_y^2} \right] \end{aligned} \quad (4.2.6)$$

$$A_y(\mathbf{k}) = 0 . \quad (4.2.7)$$

From (4.1.10), we will have

$$A_z(\mathbf{k}) = -\frac{k_x}{k_z} A_x(\mathbf{k}) . \quad (4.2.8)$$

The perpendicularly polarized and parallelly polarized components of the plane wave spectrum \mathbf{A} are

$$A_N = \frac{(\mathbf{A} \cdot \mathbf{a}_N) \mathbf{a}_N}{|\mathbf{a}_N|^2} = -\frac{A_x k_y}{k_x^2 + k_y^2} (-x k_y + y k_x) \quad (4.2.9)$$

$$A_P = A - A_N = A_x \left[x \frac{k_x^2}{k_x^2 + k_y^2} + y \frac{k_x k_y}{k_x^2 + k_y^2} - z \frac{k_x}{k_z} \right]. \quad (4.2.10)$$

Then the total plane wave spectrum A' behind the barrier is

$$\begin{aligned} A'(k_x, k_y) &= T_N A_N + T_P A_P \\ &= A_x \left[x \frac{T_N k_y^2 + T_P k_x^2}{k_x^2 + k_y^2} + y \frac{k_x k_y (T_P - T_N)}{k_x^2 + k_y^2} - z \frac{T_P k_x}{k_z} \right]. \end{aligned} \quad (4.2.11)$$

Suppose we like to know the electric field distribution on the plane at a distance s from the barrier, this field distribution can be obtained from (4.1.32) as

$$E(x, y, d+s) = \int_{-\infty}^{\infty} \int_{-\infty}^{\infty} A'(k_x, k_y, k_z) e^{-j(k_x x + k_y y + k_z s)} dk_x dk_y. \quad (4.2.12)$$

The two-dimensional discrete Fourier transform (DFT) [23], [24] is used to evaluate (4.2.12). The spectrum on the plane at a distance s from the wall can be obtained by multiplying a phase factor $e^{-jk_z s}$ to A' , then we can calculate the value of spectrum at each discrete grid point on the k_x - k_y plane. The electric fields at corresponding grid points on this plane $z = d+s$ can be obtained by taking two-dimensional inverse DFT. The fast Fourier transform (FFT) algorithm was used to perform the DFT in our calculation because for efficiency computation. Fig-4.4 shows the amplitude of the x -component of plane wave spectrum $|A_x'|$ on the plane of $s = 0.2$ m. In this example, the dimensions of the aperture are $a = 32$ cm, $b = 15$ cm and the value of E_0 is assumed to be 1 V/m. The relative complex permittivity ϵ_r^* of the barrier is $5 - j0.3$. Since the field decays very fast when $k_0 \leq \sqrt{k_x^2 + k_y^2}$ (evanescent waves), we can truncate the spectrum at $k_x = \pm 1.1k_0$ and $k_y = \pm 1.1k_0$ and assume that the function values of the spectrum are all zero outside the square. The frequency of this nonuniform wave is 2 GHz, so the boundaries shown on the figure are $k_x = \pm 1.1k_0 = \pm 46.08$ m⁻¹ and

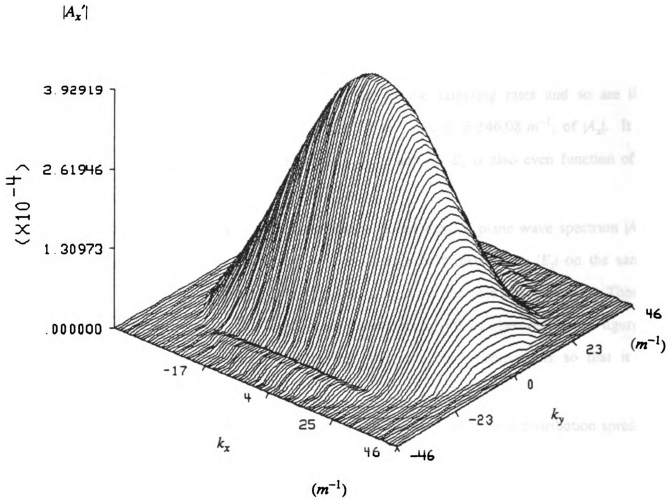


Fig-4.4 The magnitude of the x- component of plane wave spectrum behind the barrier ($d = 0.2 \text{ m}$).

$k_y = \pm 1.1k_0 = \pm 46.08 \text{ m}^{-1}$. We sample 100 points in k_x direction and 30 points in k_y direction. The numbers of sampling points are decided by the Nyquist rate which prevents the aliasing of the result of the inverse DFT. After taking two-dimensional inverse FFT, we obtain the x - component of electric field distribution E_x on the same plane, where $|E_x|$ is shown in Fig-4.5. The bounds for the truncated domain of $|E_x|$, $x \leq \pm 3.4 \text{ m}$ and $y \leq \pm 1.02 \text{ m}$, are determined by the sampling rates and so are the bounds for the truncated domain, $k_x = \pm 46.08 \text{ m}^{-1}$ and $k_y = \pm 46.08 \text{ m}^{-1}$, of $|A_x|$. It is noticed that since A_x' is an even function of k_x and k_y , E_x is also even function of x and y by the Fourier transform theory [22].

Fig-4.6 indicates the amplitude of the z - component of plane wave spectrum $|A_z'|$ and Fig-4.7 the presents z - component of electric field distribution $|E_z|$ on the same plane. Now, since A_z' is odd in k_x but even in k_y , E_z is odd in x and even in y . Therefore $|A_z'|$ is zero when $k_x = 0$ and $|E_z|$ is zero when $x = 0$ as observed in the figures. The y - component is much smaller than the other two components so that it is neglected in this example.

If we increase the distance s to 0.4 m , we expect that the field distribution spreads out and the peak value decreases. The numerical simulations in Figs-4.8 and 4.9 confirm our predictions. Only the electric field distributions are shown in the figures since the amplitude of spectrum remains the same in spite of the variation of s which only introduces a phase change to the spectrum functions.

Another example for the barrier with a different thickness of $d = 0.5 \text{ m}$ is shown in Figs-4.10 to 4.15. We observe similar results except that the amplitudes of both spectrum and electric field are smaller than those in the previous case because of more attenuation caused by the thicker barrier.

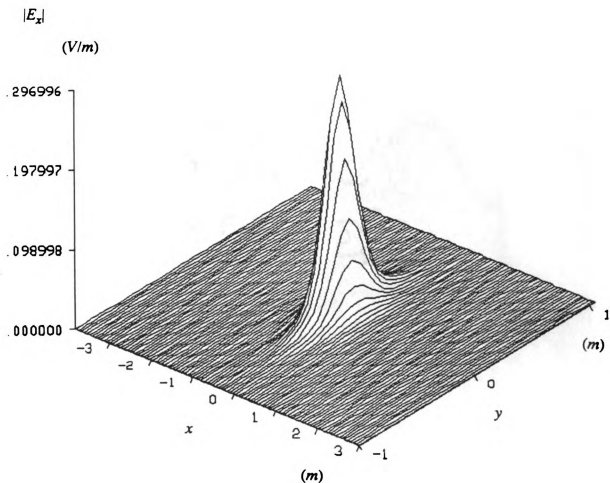


Fig-4.5 The magnitude of the x - component of electric field distribution behind the barrier ($d = 0.2$ m) at a distance of 0.2 m.

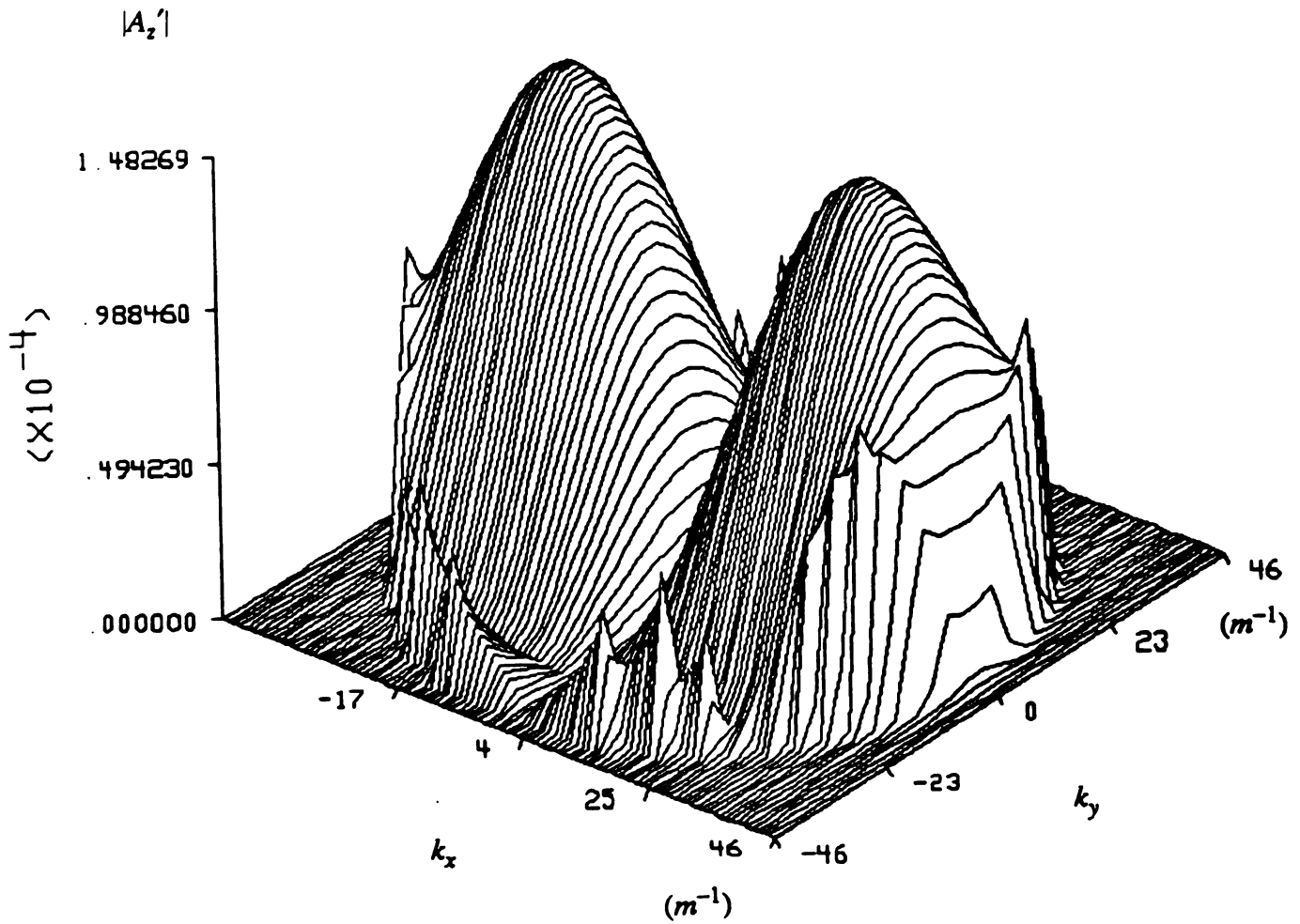


Fig-4.6 The magnitude of the z- component of plane wave spectrum behind the barrier ($d = 0.2 m$).

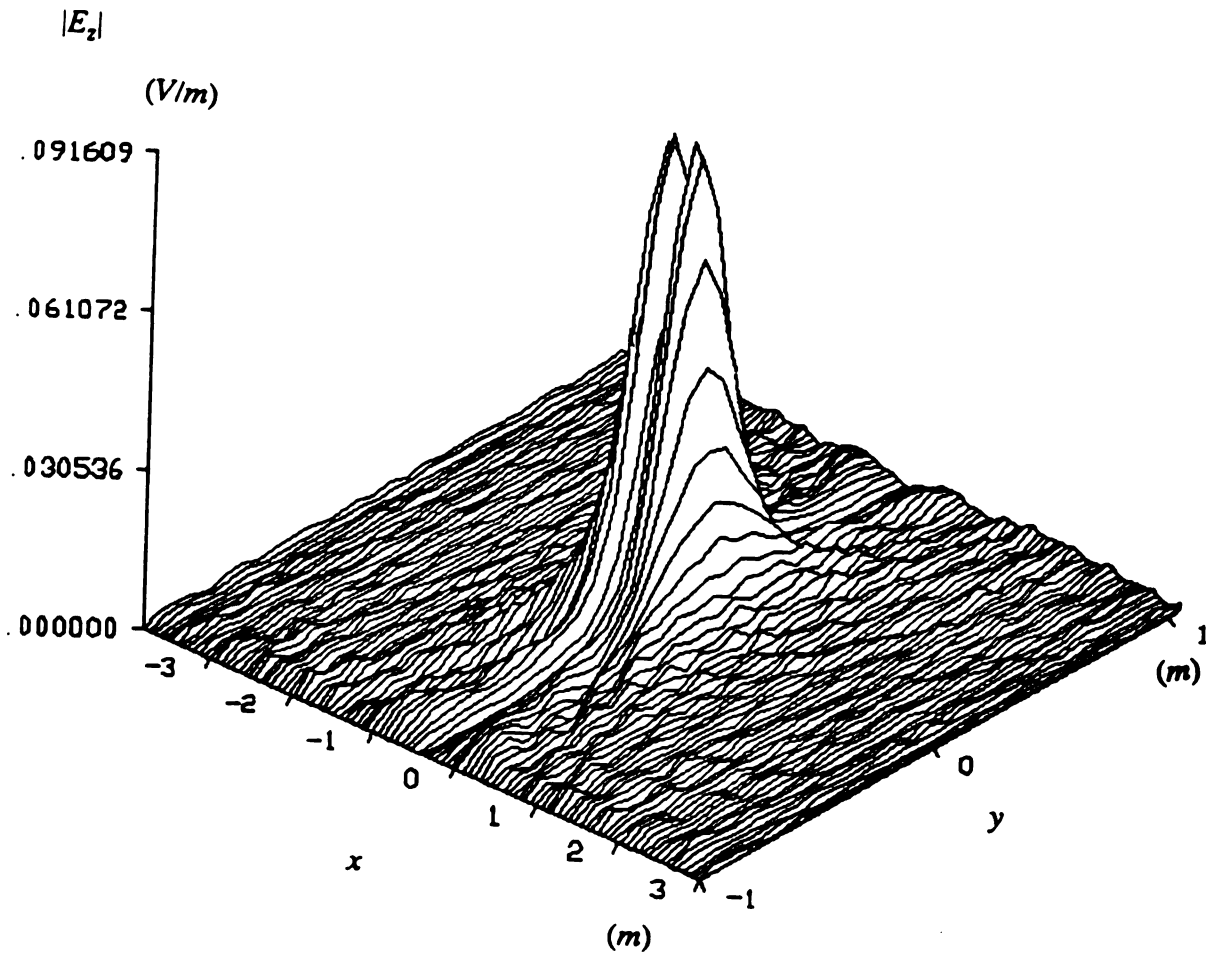


Fig-4.7 The magnitude of the z - component of electric field distribution behind the barrier ($d = 0.2 \text{ m}$) at a distance of 0.2 m .

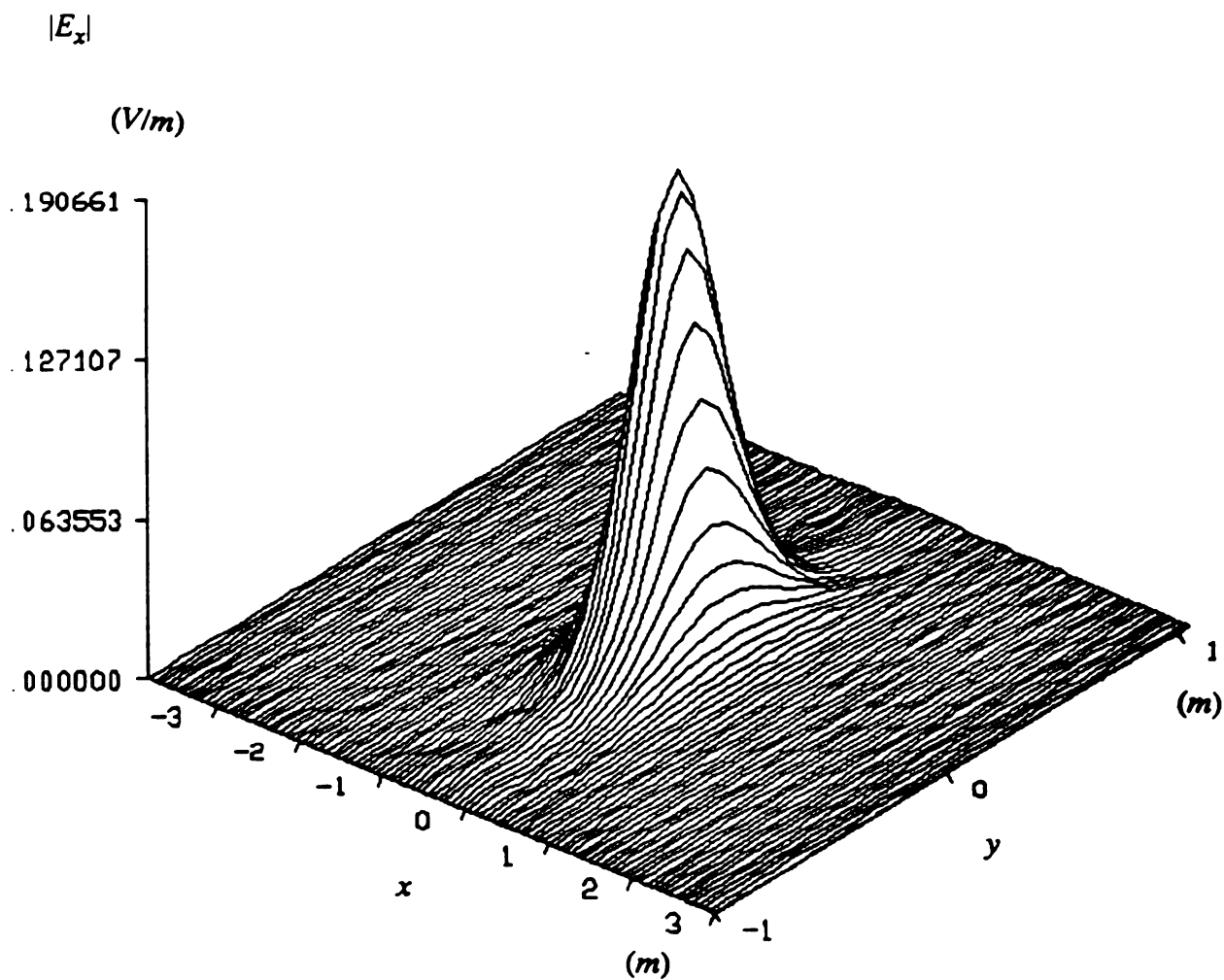


Fig-4.8 The magnitude of the x - component of electric field distribution behind the barrier ($d = 0.2 \text{ m}$) at a distance of 0.4 m .

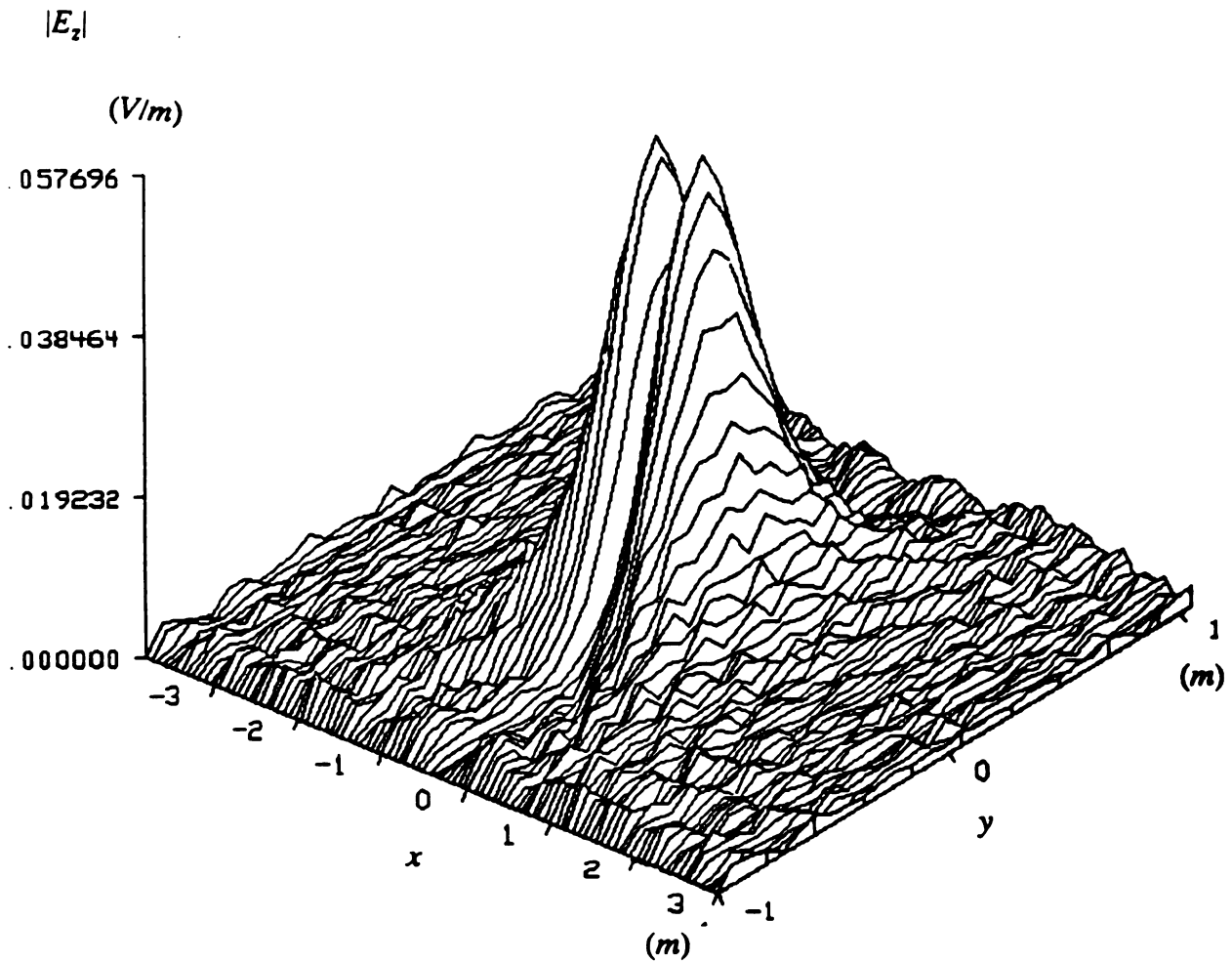


Fig-4.9 The magnitude of the z- component of electric field distribution behind the barrier ($d = 0.2 m$) at a distance of $0.4 m$.

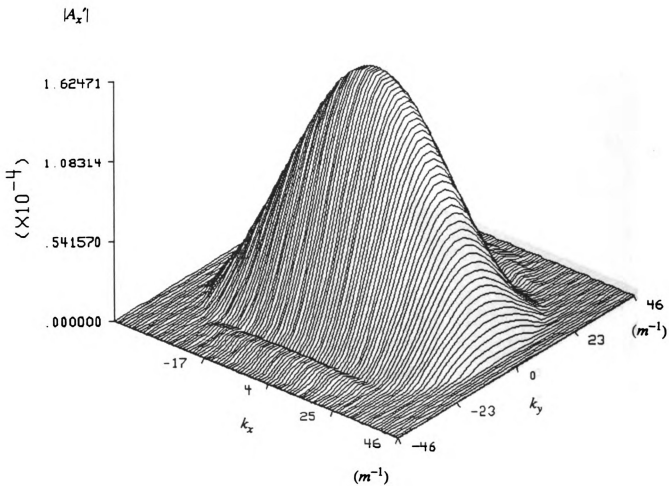


Fig-4.10 The magnitude of the x- component of plane wave spectrum behind the barrier ($d = 0.5 m$).

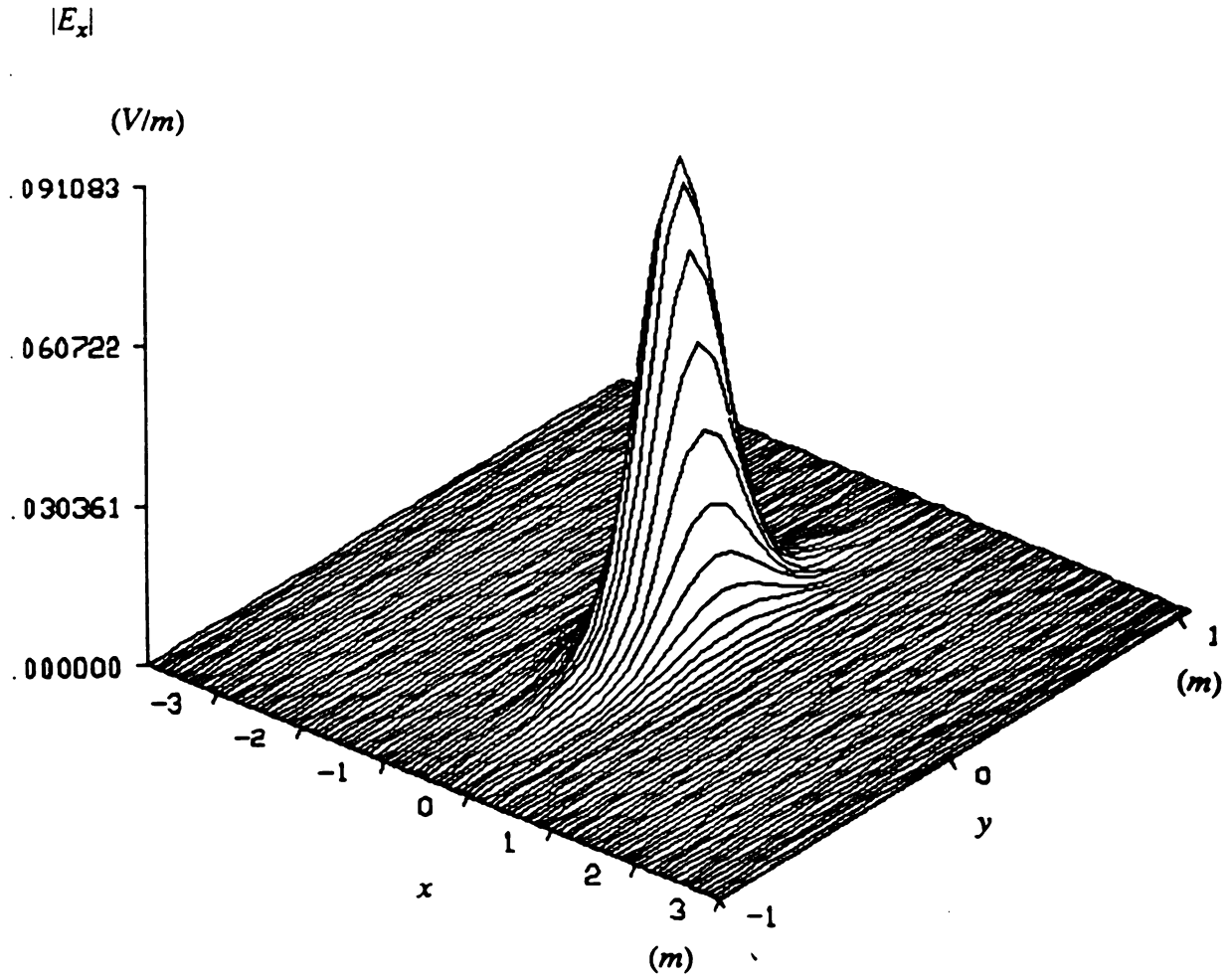


Fig-4.11 The magnitude of the x - component of electric field distribution behind the barrier ($d = 0.5$ m) at a distance of 0.2 m.

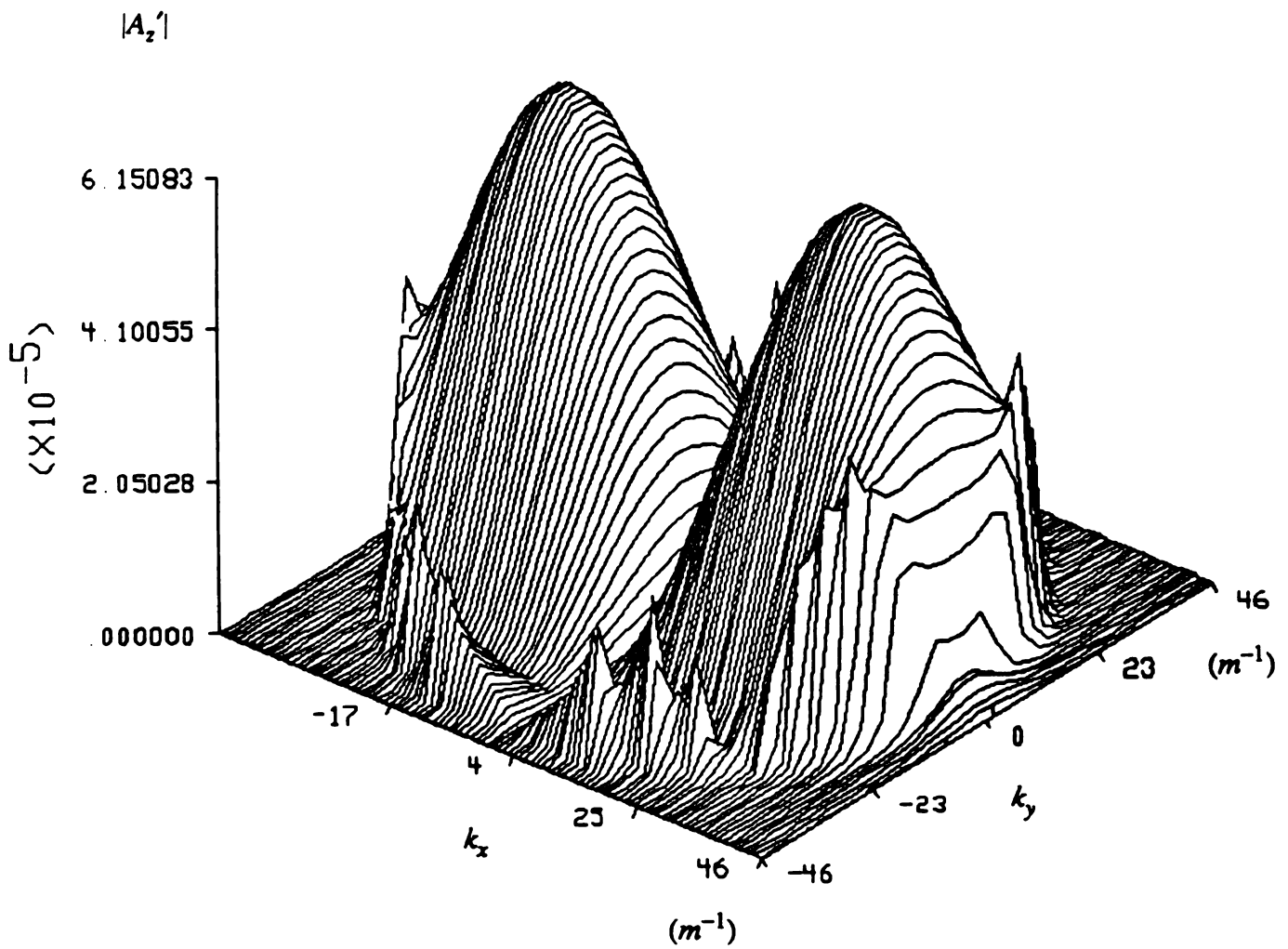


Fig-4.12 The magnitude of the z - component of plane wave spectrum behind the barrier ($d = 0.5 m$).

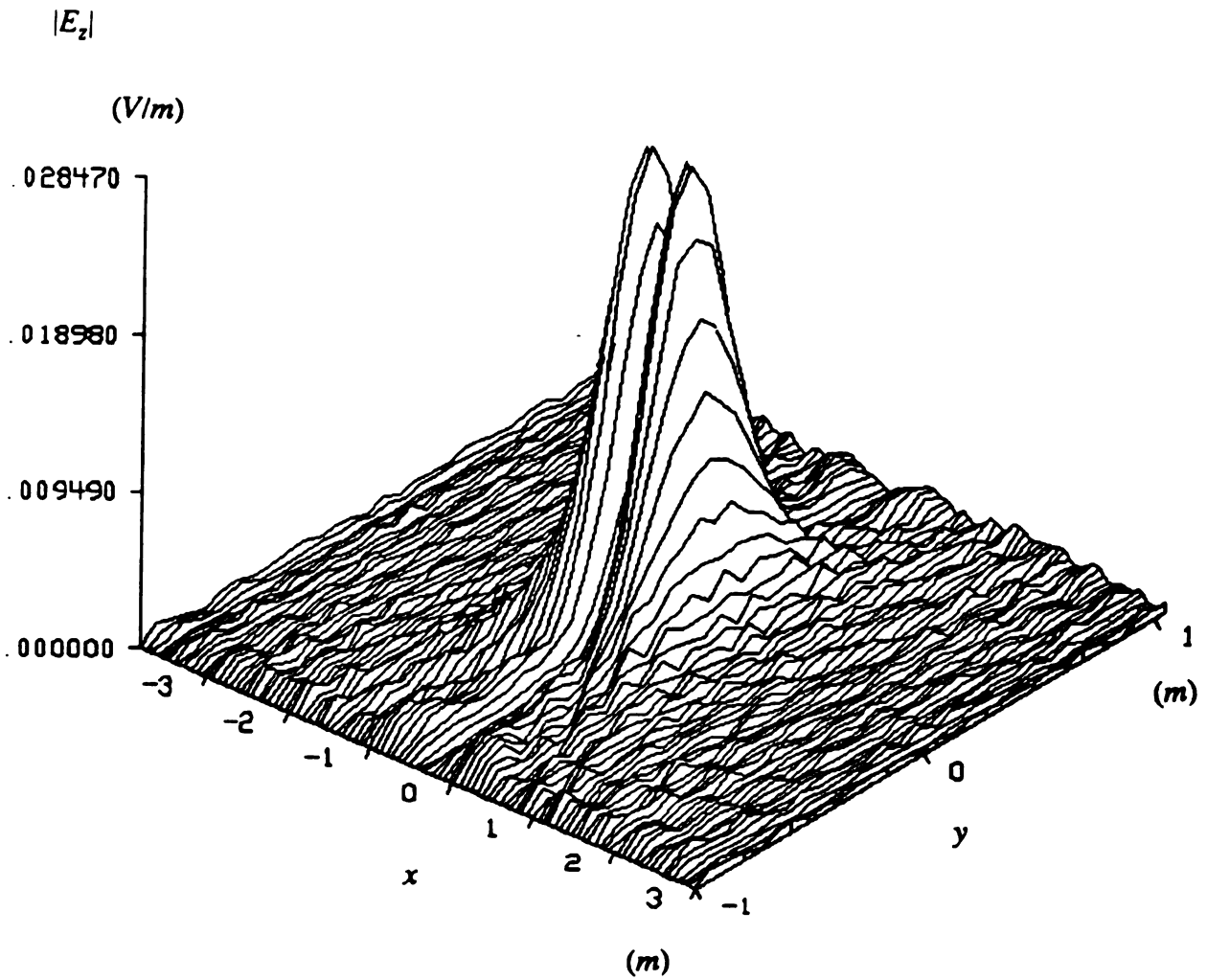


Fig-4.13 The magnitude of the z - component of electric field distribution behind the barrier ($d = 0.5 m$) at a distance of $0.2 m$.

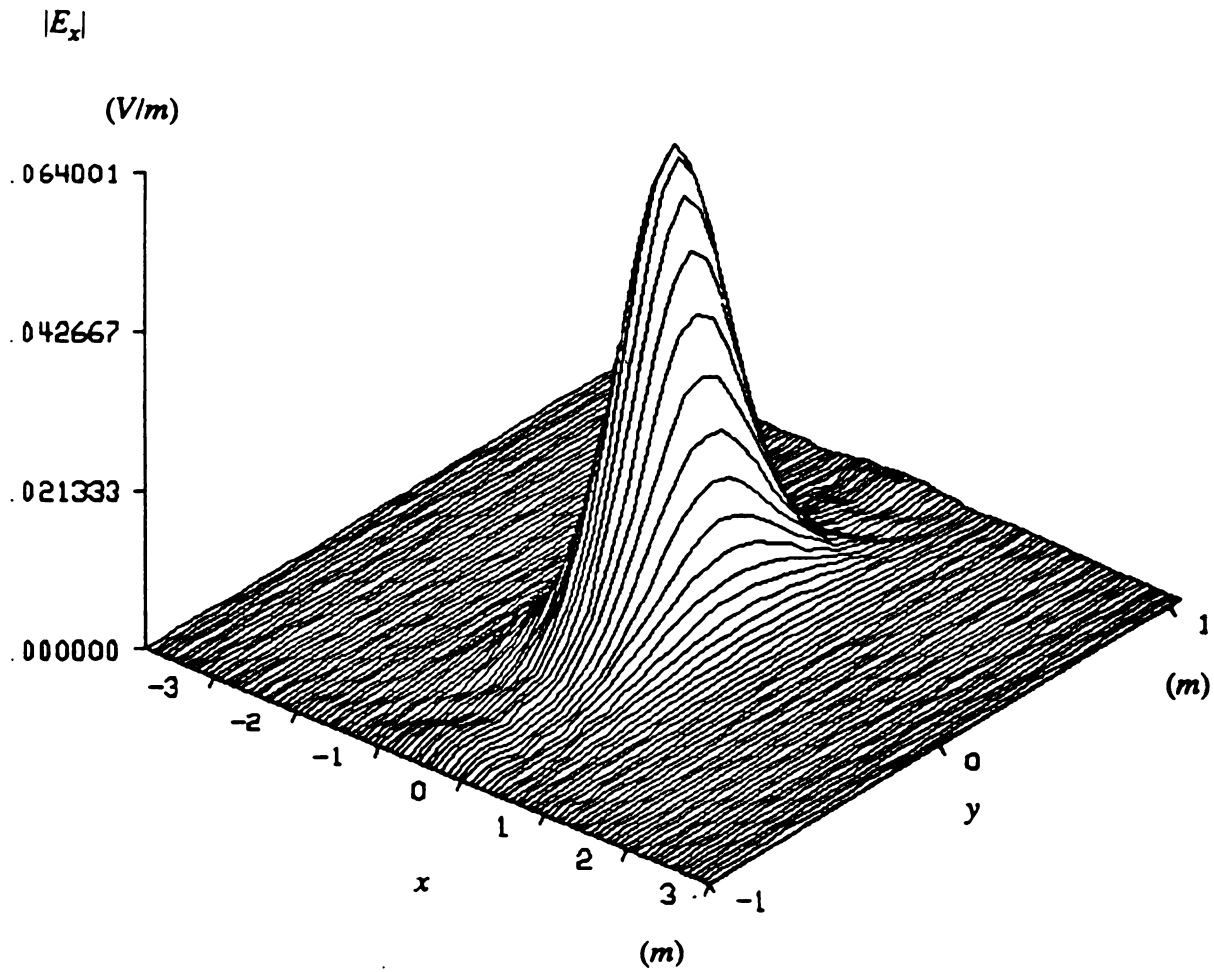


Fig-4.14 The magnitude of the x - component of electric field distribution behind the barrier ($d = 0.5$ m) at a distance of 0.4 m.

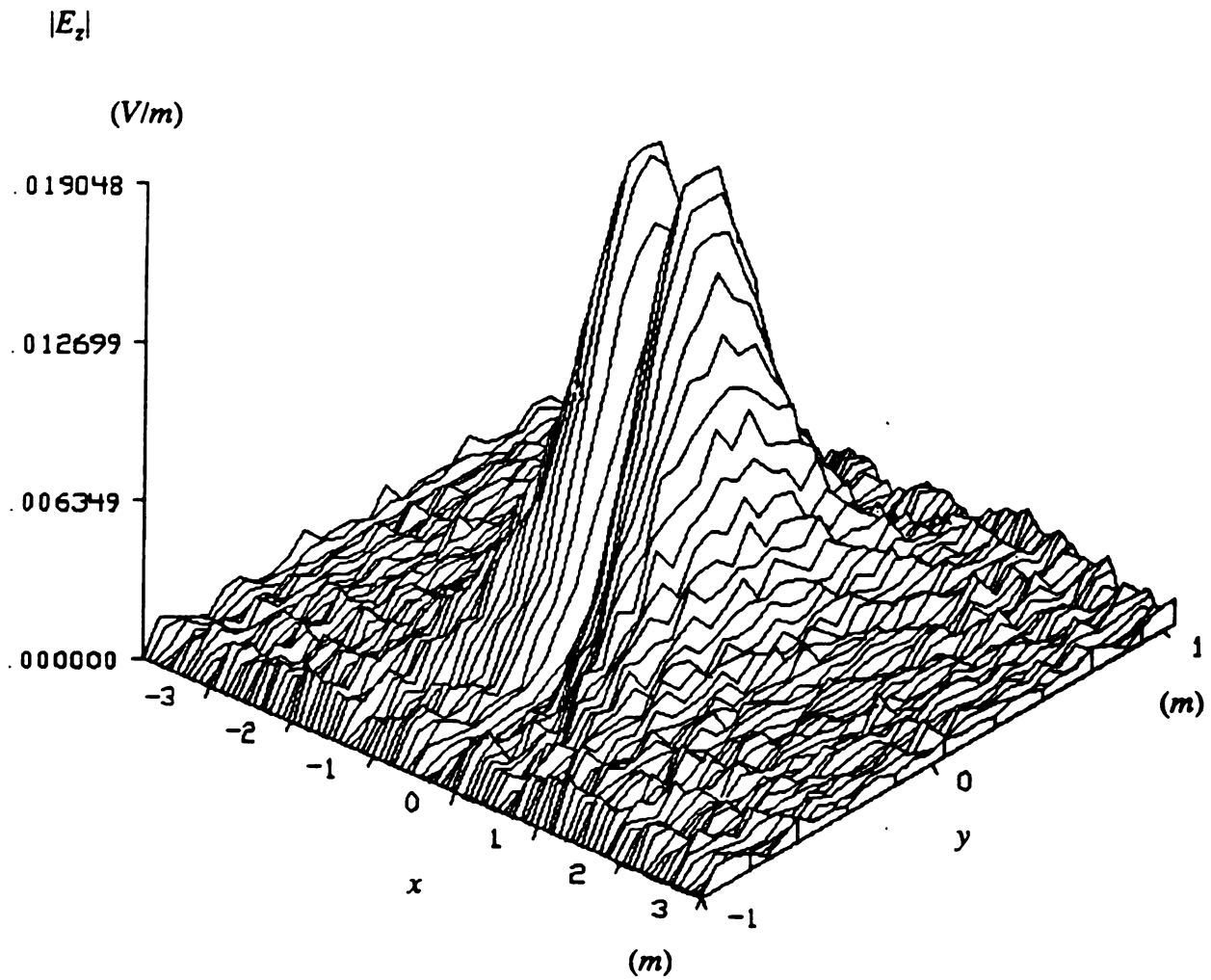


Fig-4.15 The magnitude of the z- component of electric field distribution behind the barrier ($d = 0.5 \text{ m}$) at a distance of 0.4 m .

The DFT scheme we used here to carry out (4.2.12) is restricted to some short distances. Since as the distance goes further, the field distribution will spread more and more. Therefore, very many sampling points are needed to reconstruct the field distribution accurately by means of performing the inverse DFT without aliasing. The array size which the computer is capable of handling indeed limits this distance s .

4.3 Brief Description of Microwave Life Detection Systems

The objectives of the microwave life-detection systems are to sense remotely the breathing and heartbeats of human subjects who are lying on the ground at a distance (about 100 feet) or located behind a wall or other barriers. The principle of the systems is simple. We illuminate the subject with a low-intensity microwave beam. The small amplitude body vibrations due to heartbeat and breathing of the human subject will modulate the back-scattered wave, producing a signal from which information of the heart and breathing rates can be extracted using phase detection in the microwave receiving system.

Two life-detection systems have been developed. The first system is an X-band (10 GHz) system which is capable of detecting the breathing and heartbeats of a human subject lying on the ground at a distance of 100 feet or sitting behind a wall of about 6 inches thickness. The second system is a L-band (2 GHz) radio frequency system which was specially designed for detecting the body movements of human subjects located behind a very thick wall (up to 3 feet brick wall).

The back-scattered wave from the human body is both phase and amplitude modulated by the small amplitude body vibrations. The behavior of the back-scattered wave is analyzed in [25] by assuming that the body is a sphere or an infinite cylinder

of complex permittivity and the breathing and heartbeats cause small vibrations of the spherical or cylindrical surface due to changes in its radius. Since the phase variation is more linear by the analysis in [25] and easier to be detected from the viewpoint of the signal/noise ratio, we detect the phase modulation of the back-scattered wave to measure the vibrations of the body surface caused by the heartbeats and respiration.

The schematic diagram of the microwave life-detection system is shown in Fig-4.16. A phase-locked oscillator produces a stable output of about 20 *mW*. This output is amplified by a low-noise microwave amplifier to a power level of about 200 *mW*. The output of the amplifier is fed through a 6 dB directional coupler, a variable attenuator, a circulator and then to a horn antenna. The 6 dB directional coupler branches out 1/4 of the amplifier output to provide for a reference signal for clutter (the reflected wave due to stationary subjects such as wall, building and ground, etc.) cancellation and another reference signal for the mixer. The variable attenuator controls the power level of the microwave to be radiated by the antenna. Usually, the radiated power is kept at a level of about 10 to 20 *mW*. The microwave coming out of the variable attenuator is fed to the horn antenna through a circulator. The horn antenna radiates a microwave beam of about 15 degrees beamwidth aiming at the human subjects lying on the ground. The received signal by the antenna consists of a large clutter and a weak return signal scattered from the body. The large clutter signal is canceled by a reference signal, amplitude and phase of which are adjusted by a variable attenuator and a phase shifter, in a 10 dB directional coupler. After this clutter cancellation, the output of the 10 dB directional coupler contains mainly the weak scattered signal from the body. This body scattered signal is a CW microwave modulated by the breathing and the heartbeats. This signal is then mixed with another reference signal in a double-balance mixer. In between the microwave pre-amplifier and the double-balance mixer, a 10 dB directional coupler is inserted to take out a small

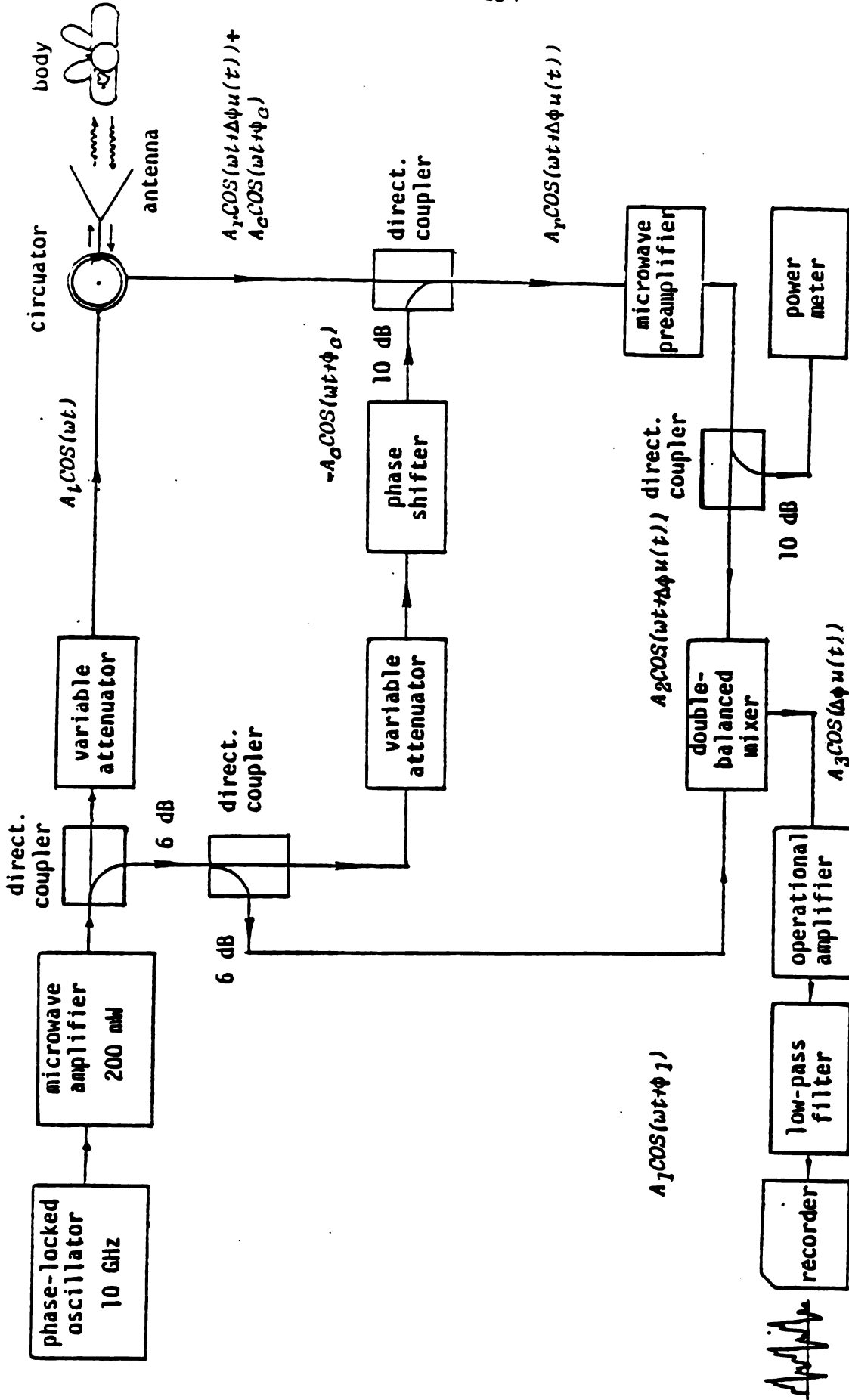


Fig-4.16 Circuit diagram of the microwave life detection system.

portion of the amplifier signal for monitoring its intensity. This monitoring is mainly for checking how well the clutter is canceled. The mixing of the amplified, body scattered signal and a reference signal (7 to 10 *mW*) in the double-balance mixer produces a low-frequency breathing and heart signals which modulate the scattered microwave from the body. This output from the mixer is amplified by an operational amplifier and then it passes through a low-pass filter (4 Hz cut-off) before reaching a recorder.

The two systems of different bands have the same circuit diagram, except that various components for different frequency bands are used.

4.4 Experimental Results of Detecting Movements of a Human Body across a Wall by Using Microwave Detection Systems

The experimental results of detecting movements of a human body at a distance away from the system can be found in [21]. In this section we will present the test results on the detection of the heart and breathing signals of a human subject who is located behind brick walls of various thickness, using both the X-band and the L-band system.

We have found that with the X-band system, it was possible to detect the heart and breathing signals of a human subject through a brick barrier of up to about 15 inches thickness. However, if the wall was thicker than that, the detection become difficult with the X-band system. The L-band (2 GHz) system was then design for the purpose of detecting the heart and breathing signals of human subjects who were behind a very thick wall or buried under a thick layer of rubble.

As mentioned in section 4.3, the L-band system has the essentially same circuit arrangement as that of the X-band system, but the radiation beam of the former can penetrate a thicker wall than the latter due to its lower operating frequency. With the L-band system, it is possible to penetrate the brick barrier of up to about 34 inches thickness.

Fig-4.17 depicts the experimental setup of the first series of experiments. A brick wall (3 feet wide and 4.5 feet high) of various thicknesses was lined with microwave absorbers along the edges. New Orleans's homestead bricks were used. A human subject sat behind the brick wall within a distance of 1 to 2 feet. The antenna of the life-detection system was placed close to the other side of the brick wall.

Fig-4.18 shows the heart and breathing signals of a human subject measured by the 10 GHz system through one layer (3 3/8") and two layers (6 3/4") of dry bricks. In each recorded graph, the breathing signal, the heart signal (the subject holding breath) and the background noise were included. Both the heart and breathing signals were clearly detected. Fig-4.19 shows the heart and breathing signals of a human subject measured by the 10 GHz system through three layers (10 1/8"), four layers (13 1/2") and five layers (16 7/8") of dry bricks. It is observed that both the heart and breathing signals were detected through four layers of bricks, but only the breathing signal was measured through five layers of brick. It is noted that as the thickness of the brick wall was increased, the amplifier gain of the system was increased accordingly. We estimate that with the 10 GHz system, it is possible to penetrate a dry brick wall of about 15 inches thickness.

Fig-4.20 shows the heart and breathing signals of a human subject measured by the 2 GHz system through five layers (16 7/8") and six layers (20 1/4") of dry bricks. In each case, both the heart and breathing signals were easily detected. It is noted that for a thinner brick wall, it was even easier to measure these signals. Fig-4.21 shows

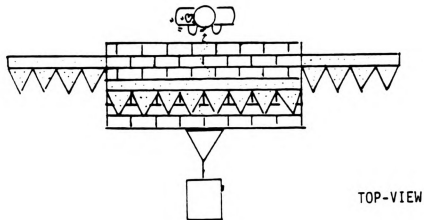
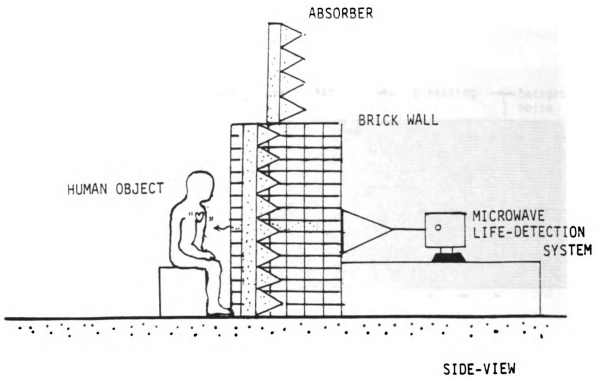


Fig-4.17 Experimental set up for the measurement of heart and breathing signals of a human object through brick wall, using microwave life detection system.

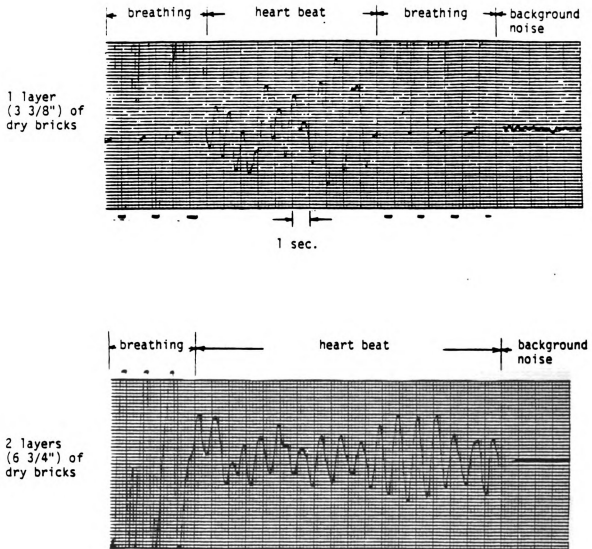


Fig-4.18 Heart and breathing signals of a human subject measured through brick walls of various thicknesses using the 10 GHz life detection system.

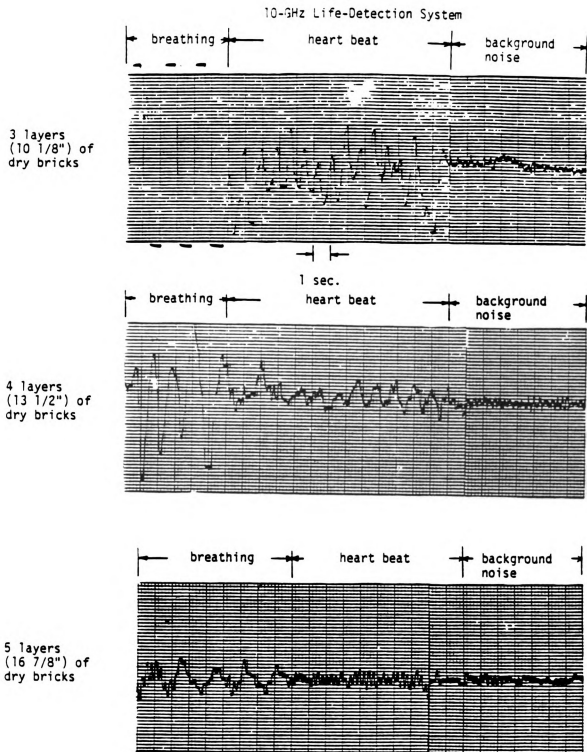


Fig-4.19 Heart and breathing signals of a human subject measured through brick walls of various thicknesses using the 10 GHz life detection system.

2-GHz Life-Detection System

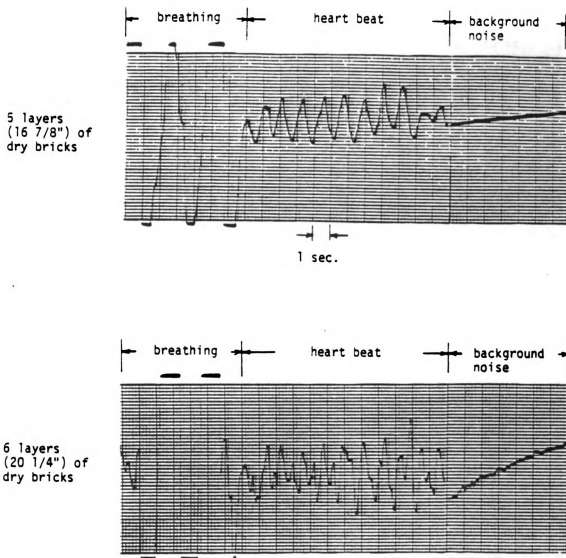


Fig-4.20 Heart and breathing signals of a human subject measured through brick walls of various thicknesses using the 2 GHz life detection system.

2-GHz Life-Detection System

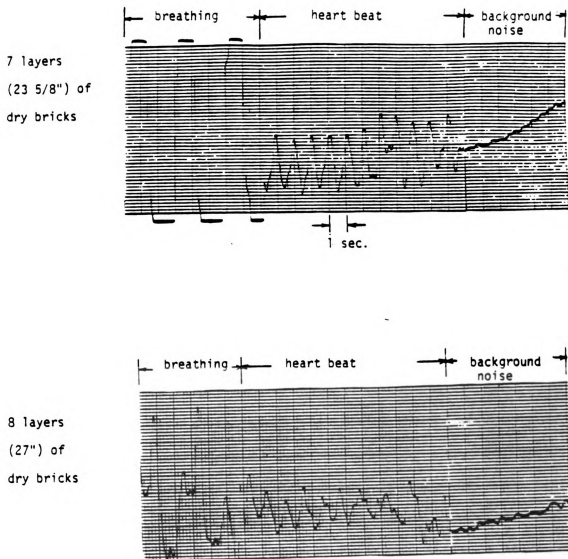


Fig-4.21 Heart and breathing signals of a human subject measured through brick walls of various thicknesses using the 2 GHz life detection system.

the results for the cases of seven layers (23 5/8") and eight layers (27") of dry bricks. Clear heart and breathing signals of a human subject were measured in each case. We were able to measure the heart and breathing signals of a human subject through ten layers of dry bricks with the 2 GHz system. This leads to an estimation that with the 2 GHz system, it is possible to penetrate a dry brick wall of about 34 inches thickness.

We also tested the effect of moisture on the performance of the life-detection systems. For this purpose one layer of the brick wall was constructed with wet bricks. When we used wet bricks which were soaked in water for several hours, the performance of the system was affected insignificantly. However, a significant effect was observed when we used very wet bricks which were soaked in water for three days. Fig-4.22 shows the heart and breathing signals of a human subject measured through three layers (10 1/8") of very wet bricks, using the 10 GHz system. It is observed that with one layer of very wet bricks present, the penetration of 10 GHz microwave beam was severely hampered. It is then conjectured that the 10 GHz system may not be effective in detecting the heart and breathing signals of human subjects through a very wet barrier. This difficulty may be overcome by using the 2 GHz system. Fig-4.23 shows the results of the same experiment of Fig-4.22 except using the 2 GHz system. It is observed that one layer of very wet bricks reduced the magnitudes of the measured heart and breathing signals but we were still able to detect these signals clearly without much difficulty. Therefore, it is reasonable to conclude that for the purpose of detecting vital signs of human subjects through a thick layer of wet rubble, the life-detection system should be designed to operate at low frequencies, such as lower than 1 GHz.

The second series of experiments was conducted with a setup depicted in Fig-4.24. Various layers of bricks were laid on a wooden frame which formed a cavity for a human subject to lie down in it. Microwave absorbers were used to line the sides of

10-GHz Life-Detection System

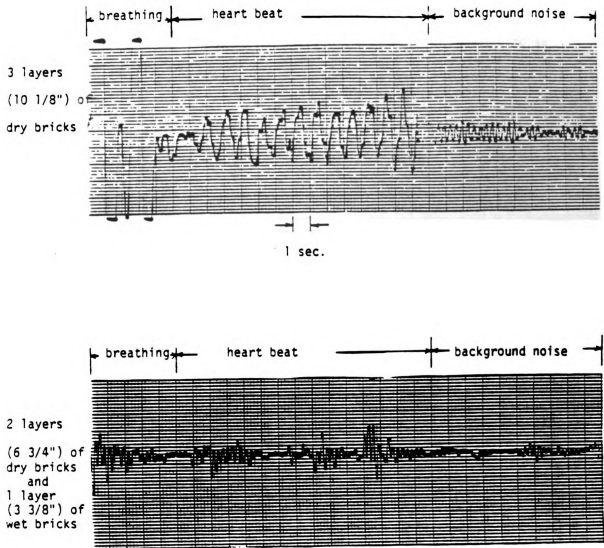


Fig-4.22 Heart and breathing signals of a human subject measured through brick walls of various thicknesses using the 10 GHz life detection system. One layer of wet bricks severely hampered the penetration of the microwave beam.

2-GHz Life-Detection System

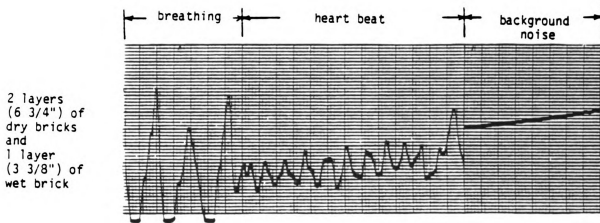
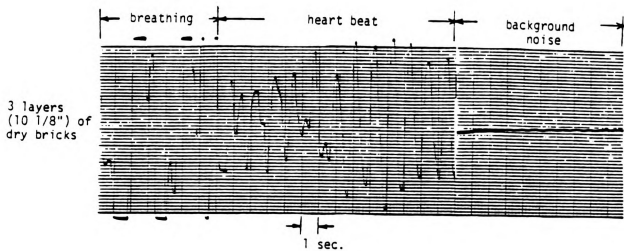
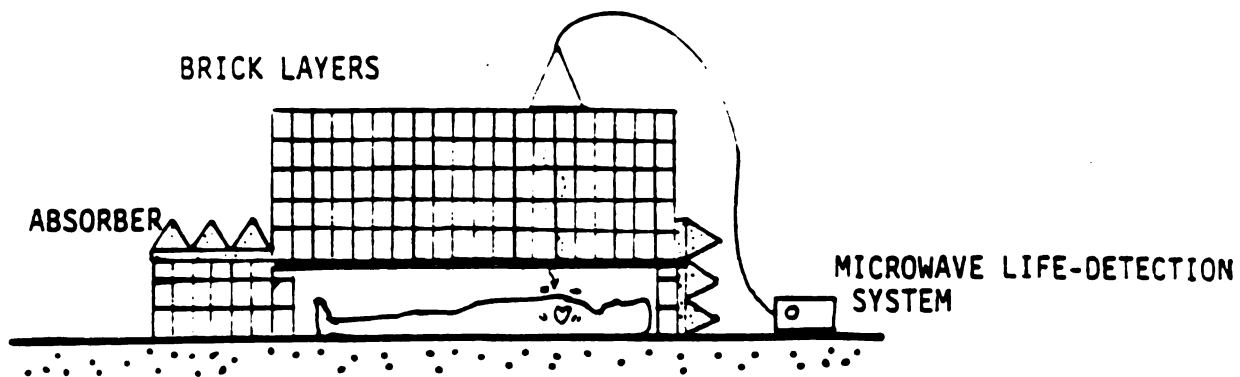
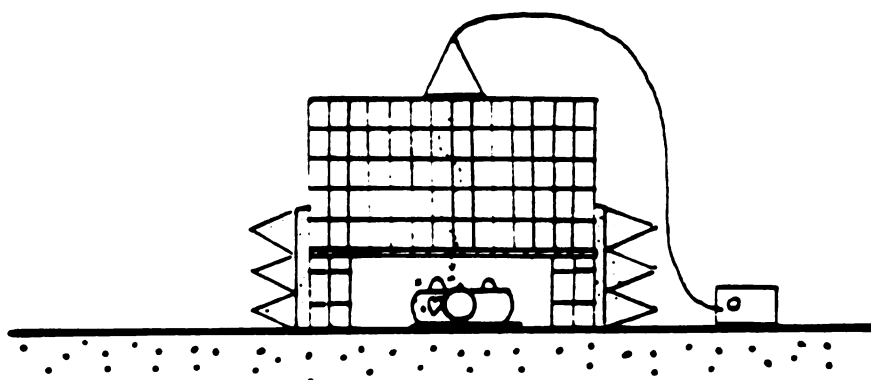


Fig-4.23 Heart and breathing signals of a human subject measured through brick walls of various thicknesses using the 2 GHz life detection system. One layer of wet bricks had a considerable effect on the penetration of the microwave beam.



SIDE-VIEW



FRONT-VIEW

Fig-4.24 Experimental set up for the measurement of heart and breathing signals of a human object under layers of bricks, using microwave life detection system.

this brick structure. This setup simulated a human subject trapped under a thick layer of rubble. The antenna of the life-detection system was placed on the top of the brick structure aiming at the human subject.

Fig-4.25 shows the heart and breathing signals of a human subject lying with face-up or face-down position under three layers (10 1/8") of dry bricks, measured by the 10 GHz system. Both the heart and breathing signals were clearly detected for each position. Fig-4.26 shows the similar results for the case of four layers (13 1/2") of dry bricks, with the 10 GHz system. When the thickness of the brick structure exceeded more than five layers (16 7/8") of bricks, the performance of the 10 GHz system became marginal.

Fig-4.27 to Fig-4.29 show the heart and breathing signals of a human subject lying with face-up or face-down position under five layers (16 7/8"), six layers (20 1/4") and seven layers (23 5/8") of dry bricks, respectively, measured by the 2 GHz system. In each of these figures, the heart and breathing signals were both clearly recorded. As the thickness of the brick structure was increased, the amplifier gain of the system was increased accordingly. It was found that it is easy to penetrate a pile of dry rubble up to about three feet thickness with the 2 GHz life-detection system.

10-GHz Life-Detection System

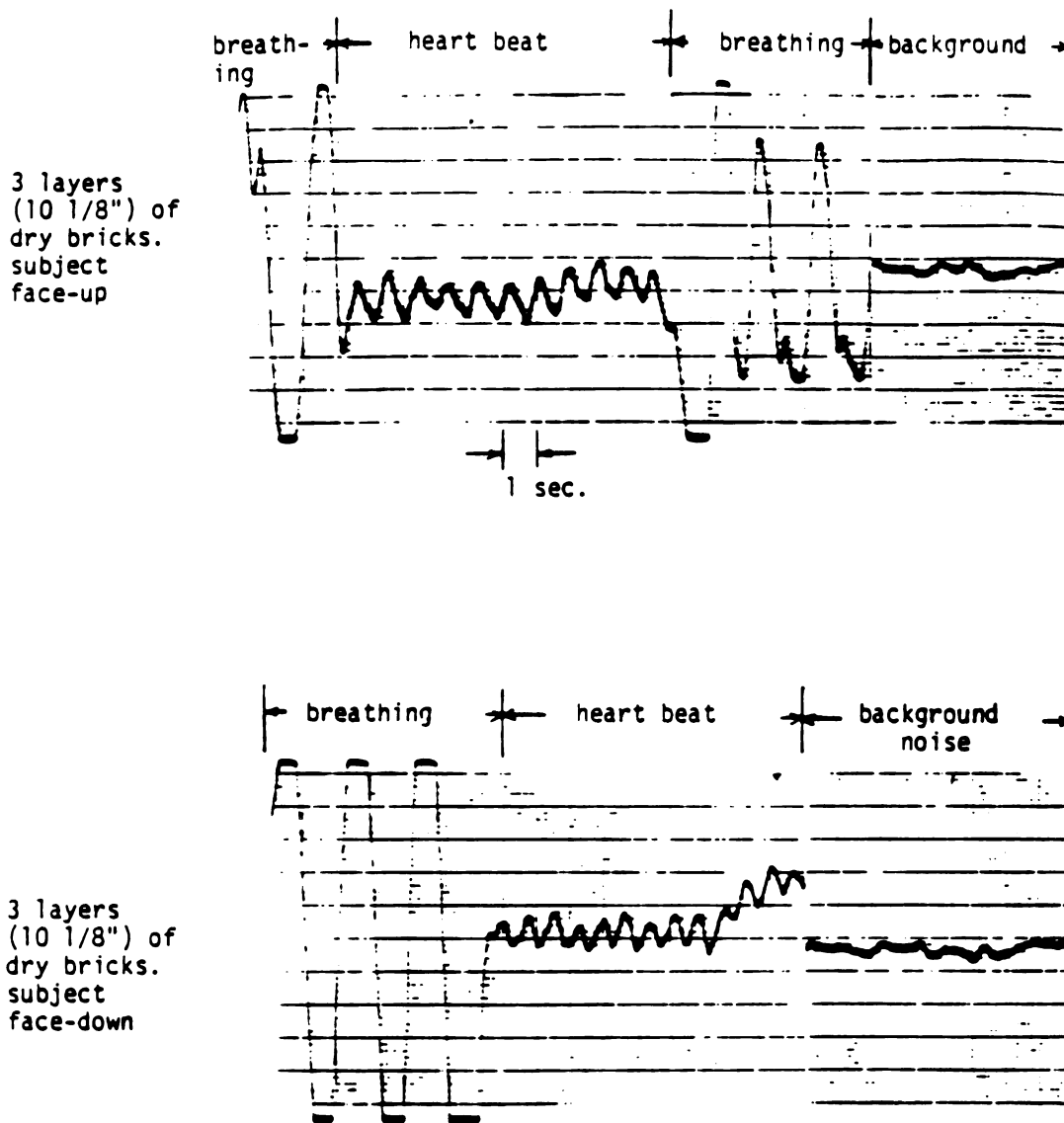


Fig-4.25 Heart and breathing signals of a human subject, lying with face-up or face-down position under 3 layers of bricks, measured by the 10 GHz life detection system.

10-GHz Life-Detection System

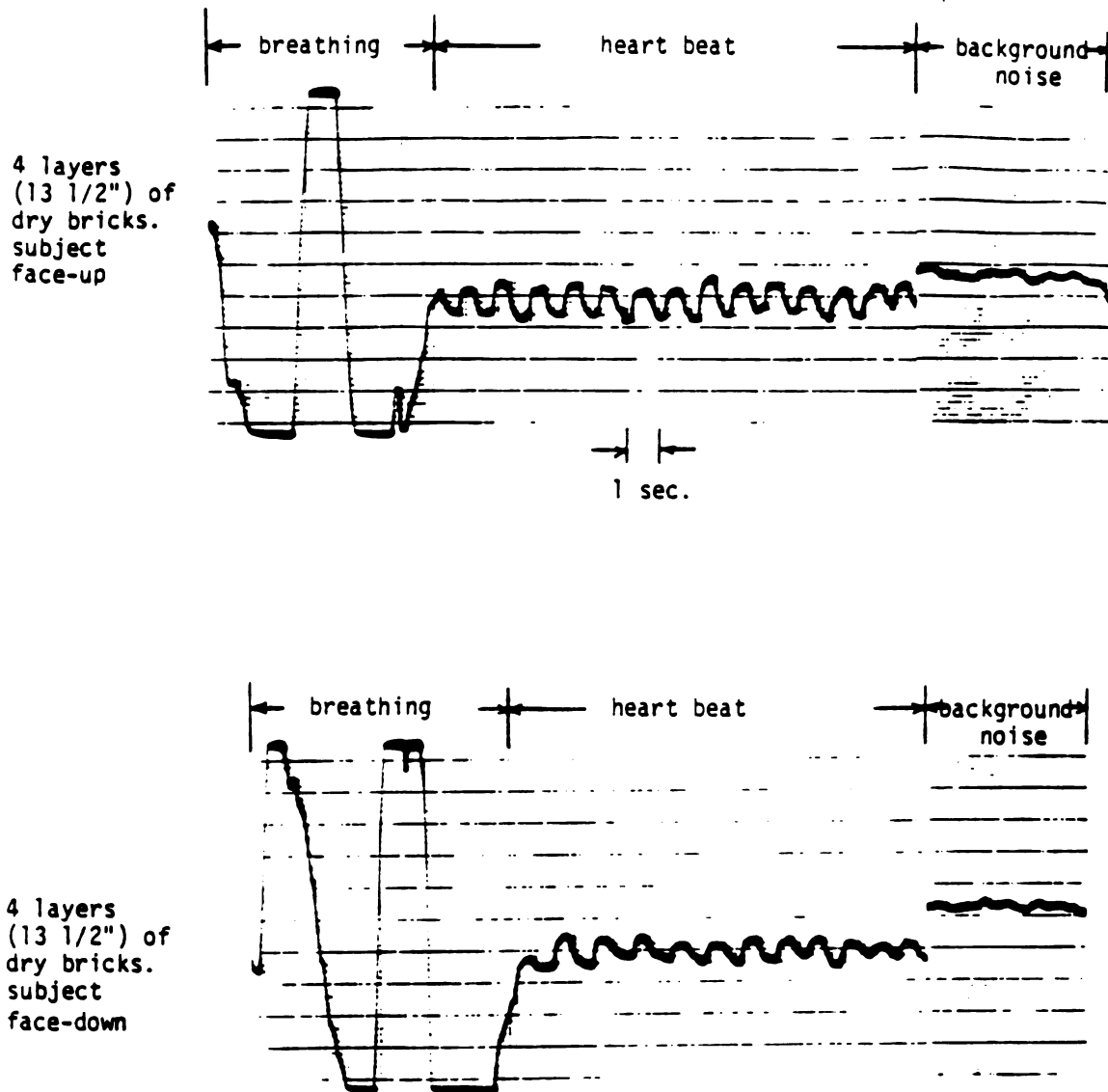


Fig-4.26 Heart and breathing signals of a human subject, lying with face-up or face-down position under 4 layers of bricks, measured by the 10 GHz life detection system.

2-GHz Life-Detection System

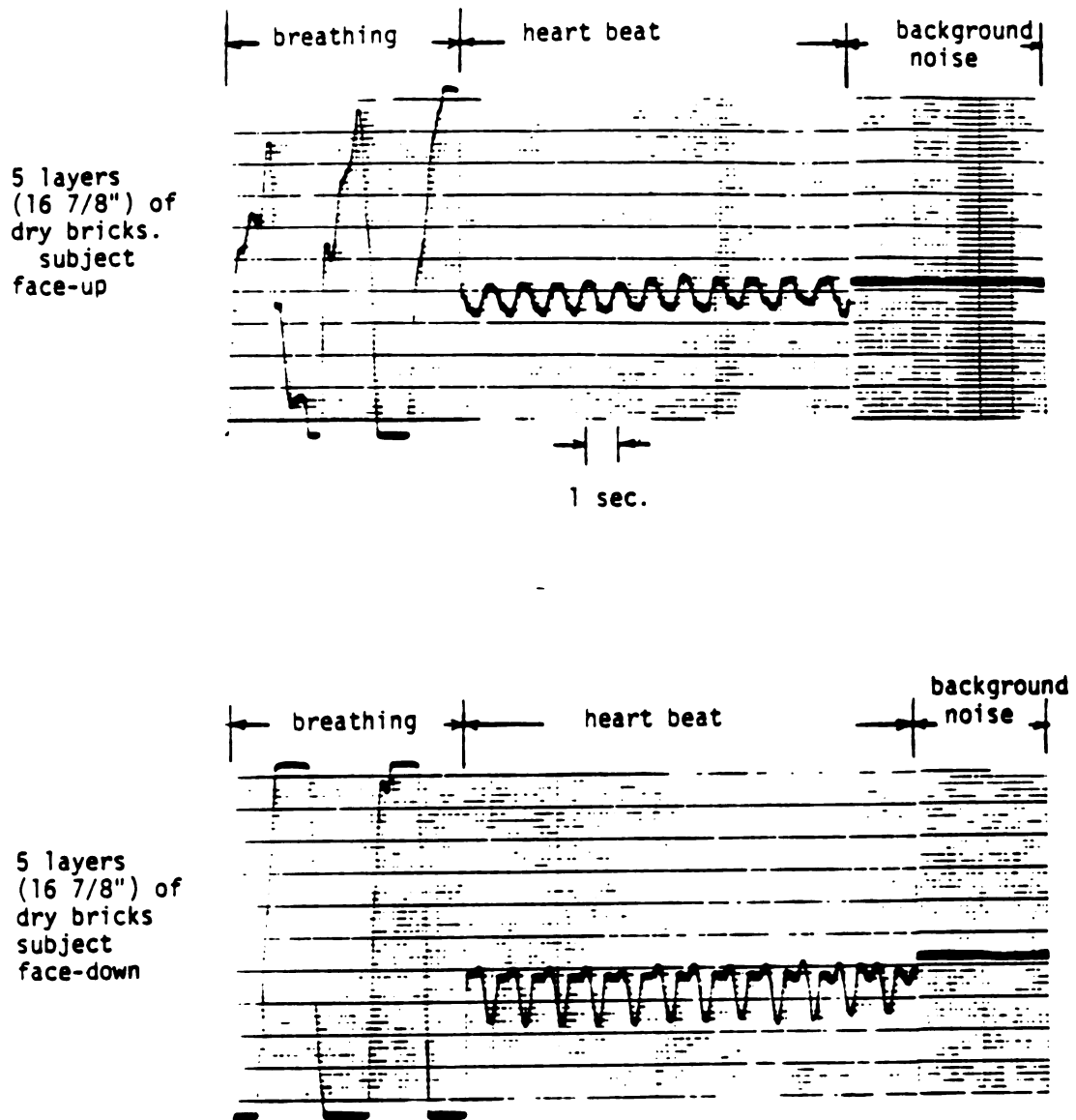


Fig-4.27 Heart and breathing signals of a human subject, lying with face-up or face-down position under 5 layers of bricks, measured by the 2 GHz life detection system.

2-GHz Life-Detection System

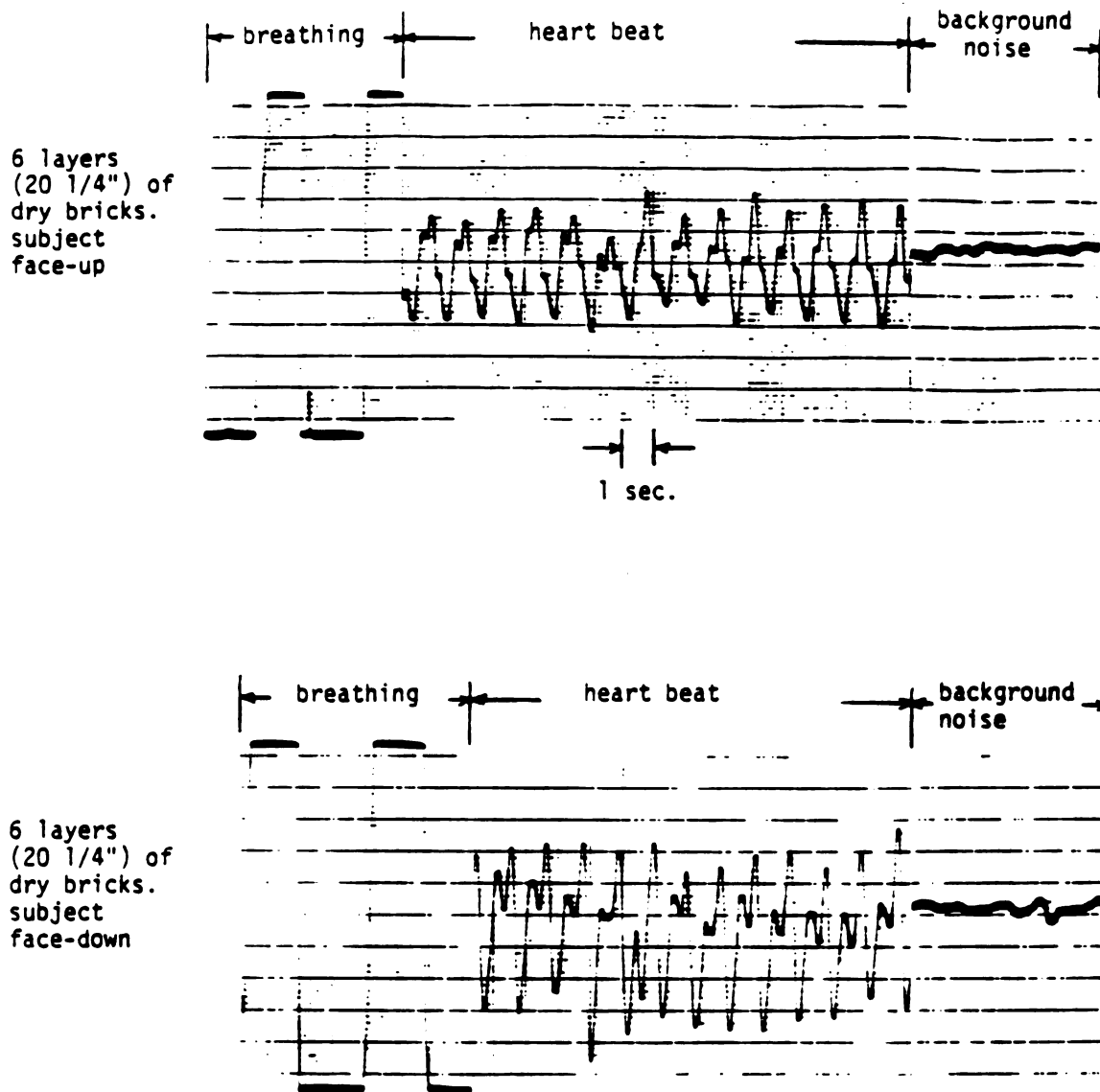


Fig-4.28 Heart and breathing signals of a human subject, lying with face-up or face-down position under 6 layers of bricks, measured by the 2 GHz life detection system.

2-GHz Life-Detection System

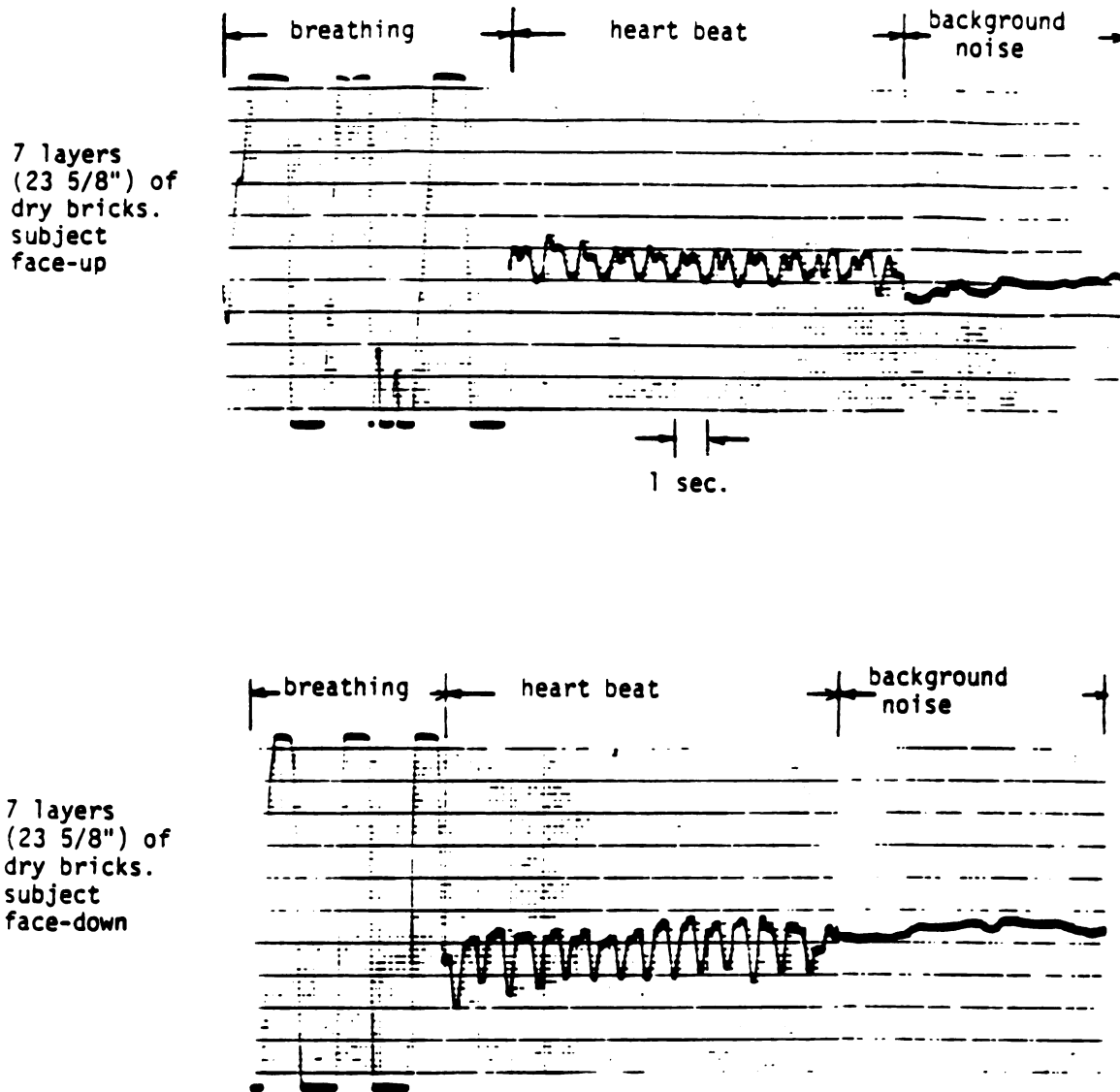


Fig-4.29 Heart and breathing signals of a human subject, lying with face-up or face-down position under 7 layers of bricks, measured by the 2 GHz life detection system.

CHAPTER V

SUMMARY

This thesis presents of the study on the quantification of interaction of electromagnetic fields with finite heterogeneous bodies and an application of electromagnetic waves for detecting a small movement of a biological body behind a barrier.

In the study on the quantification of interaction of electromagnetic fields with finite non-magnetic lossy bodies, an iterative loop-EMF method and an equivalent magnetic current compensation method have been developed to improve the efficiency and accuracy of the existing tensor integral equation method. The induced electric field of electric mode which is excited by symmetrical part of incident electric field can be solved accurately from the tensor EFIE with the method of moment and pulse-basis expansion. However, the induced electric field of the magnetic mode which is excited by the antisymmetrical part of incident electric field can not be determined accurately by the same method. A series of numerical examples at various frequencies for the induced field distributions in a rectangular biological body are presented. It is observed that for an antisymmetric incident electric field in the range of several hundred MHz, the latter method can improve the accuracy of the numerical solution of induced electric field while the former method achieves more improvement. It is felt that the latter method can be further refined if a proper magnetic current can be found to compensate the discontinuity of the tangential electric field at the air-body interface, or the outmost boundary of the body. One can also use the iterative loop-EMF method to calculate the induced fields in a heterogeneous body, but the determination of the impedance at the boundaries of the cells which are of different materials needs

further investigation.

The interaction of EM fields with finite lossy magnetic bodies has also been studied in this thesis. A set of coupled tensor integral equations has been derived to solve for the induced EM field in a finite heterogeneous body with arbitrary electric parameters which is exposed to an incident EM field. This set of equations can be decoupled into a separate tensor EFIE and a separate tensor MFIE. If the coupled tensor integral equations are used, we need to solve for the unknown fields \mathbf{E} and \mathbf{H} simultaneously while we can solve \mathbf{E} and \mathbf{H} separately if the decoupled equations are used. This means twice the number of unknown variables when the coupled equations are solved numerically. Both coupled and decoupled integral equations can be expressed in terms of the free space scalar Green's functions instead of the dyadic Green's functions. With pulse-basis expansion and point-matching, either solving the tensor integral equations or the integral equations in terms of the scalar Green's functions will give similar numerical results. One advantage of the coupled tensor integral equations is that they are easy to be formulated in the heterogeneous case. The agreement of the numerical solutions of the coupled and decoupled equations was observed for the cases of low permittivity ($\epsilon_r < 20$) and frequency below a few hundred MHz. The phenomenon that the induced electric field is enhanced by the magnetic material in a finite body has also been investigated through the comparison of the numerical solutions for a magnetic body and a non-magnetic body with the same dimensions and complex permittivity.

In the study of the application of electromagnetic wave for detecting a small movement of a biological body behind a barrier, a nonuniform plane wave passing through a layer of lossy barrier has been analyzed by using the plane wave spectrum analysis. Also a series of experiments were conducted to measure the breathing and heart signals of a human subject behind a thick layer of bricks with microwave life

detection systems. The predicted electric field behind the barrier distributions calculated by the FFT algorithm indicate some perturbations of the original electric field distributions due to the barrier. Varying the thickness of the barriers causes different attenuations and perturbations to the electric field distributions behind the barrier. Experimental results on the detection of small vibrations of a biological body using the microwave life detection systems clearly indicate the breathing and heart signals of a human subject located behind a brick wall of up to 3 feet thick. The comparison of the results obtained from the X-band and L-band systems confirms that the EM waves of lower frequencies achieve better penetration through a barrier.

APPENDICES

APPENDIX I

We will prove that the decoupled tensor EFIE and MFIE derived in section 3.2 are equivalent to the set of decoupled integral equations derived by Tai [13] when they are applied to a homogeneous body.

When (3.2.18) and (3.2.19) are applied to a homogeneous body, i.e., $\tau_e, \tau_m, \epsilon^*$ and μ are not functions of location, then the equations becomes:

$$\begin{aligned} & \left[\frac{2\mu_0}{3\mu} + \frac{\epsilon^*}{3\epsilon_0} \right] \mathbf{E}(\mathbf{r}) - P.V. \int_v k_0^2 \left[\frac{\epsilon^*}{\epsilon_0} - \frac{\mu_0}{\mu} \right] \mathbf{E}(\mathbf{r}') \cdot \vec{G}_0(\mathbf{r}, \mathbf{r}') dv' \\ & - \int_s \left[\frac{\mu - \mu_0}{\mu} \right] [\mathbf{n} \times \mathbf{E}(\mathbf{r}')] \cdot [\nabla' \times \vec{G}_0(\mathbf{r}, \mathbf{r}')] ds' = \mathbf{E}^i(\mathbf{r}) \end{aligned} \quad (\text{A1.1})$$

$$\begin{aligned} & \left[\frac{2\epsilon_0}{3\epsilon^*} + \frac{\mu}{3\mu_0} \right] \mathbf{H}(\mathbf{r}) - P.V. \int_v k_0^2 \left[\frac{\mu}{\mu_0} - \frac{\epsilon_0}{\epsilon^*} \right] \mathbf{H}(\mathbf{r}') \cdot \vec{G}_0(\mathbf{r}, \mathbf{r}') dv' \\ & - \int_s \left[\frac{\epsilon^* - \epsilon_0}{\epsilon^*} \right] [\mathbf{n} \times \mathbf{H}(\mathbf{r}')] \cdot [\nabla' \times \vec{G}_0(\mathbf{r}, \mathbf{r}')] ds' = \mathbf{H}^i(\mathbf{r}), \end{aligned} \quad (\text{A1.2})$$

The decoupled integral equations by Tai are

$$\begin{aligned} & \mathbf{E}(\mathbf{r}) - (k^2 - k_0^2) \int_v \vec{G}_0(\mathbf{r}, \mathbf{r}') \cdot \mathbf{E}(\mathbf{r}') dv' \\ & + \left[\frac{\mu - \mu_0}{\mu} \right] \int_s \vec{G}_0(\mathbf{r}, \mathbf{r}') \cdot [\mathbf{n} \times \nabla' \times \mathbf{E}(\mathbf{r}')] ds' = \mathbf{E}^i(\mathbf{r}) \end{aligned} \quad (\text{3.2.20})$$

$$\begin{aligned} & \mathbf{H}(\mathbf{r}) - (k^2 - k_0^2) \int_v \vec{G}_0(\mathbf{r}, \mathbf{r}') \cdot \mathbf{H}(\mathbf{r}') dv' \\ & + \left[\frac{\epsilon^* - \epsilon_0}{\epsilon^*} \right] \int_s \vec{G}_0(\mathbf{r}, \mathbf{r}') \cdot [\mathbf{n} \times \nabla' \times \mathbf{H}(\mathbf{r}')] ds' = \mathbf{H}^i(\mathbf{r}) \end{aligned} \quad (\text{3.2.21})$$

where the Cauchy principal value for the volume integration containing $\vec{G}_0(\mathbf{r}, \mathbf{r}')$ and the extra correction term are implied by the usual integral notations.

Suppose we rewrite (A1.1) also by using the usual integral notation to represent the Cauchy principal value for the volume integration containing $\vec{G}_0(\mathbf{r}, \mathbf{r}')$ and the extra correction term, then we can have

$$\begin{aligned} \left[1 - \frac{i\tau_m}{\omega\mu} \right] \mathbf{E}(\mathbf{r}) - \int_v \left(\tau_e + \frac{\epsilon_0\tau_m}{\mu} \right) \mathbf{E}(\mathbf{r}') \cdot \vec{G}_e(\mathbf{r}, \mathbf{r}') dv' \\ - \int_s \frac{i\tau_m}{\omega\mu} \mathbf{n} \cdot [\mathbf{E}(\mathbf{r}') \times \vec{G}_m(\mathbf{r}, \mathbf{r}')] ds' = \mathbf{E}^i(\mathbf{r}) \end{aligned} \quad (\text{A1.3})$$

Let us compare term by term in (A1.3) and (3.2.20). In the second term of the left hand side of (A1.3), we obtain the following equality after some algebraic operations:

$$\left(\tau_e + \frac{\epsilon_0\tau_m}{\mu} \right) \vec{G}_e(\mathbf{r}, \mathbf{r}') = \left(\tau_e + \frac{\epsilon_0\tau_m}{\mu} \right) i\omega\mu_0 \vec{G}_0(\mathbf{r}, \mathbf{r}') = \frac{1}{\mu_r} (k^2 - k_0^2) \vec{G}_0(\mathbf{r}, \mathbf{r}') \quad (\text{A1.4})$$

where

$$\mu_r = \frac{\mu}{\mu_0} \quad (\text{A1.5})$$

is the relative complex permeability of the body. For the first term of the left hand side of (A1.3), we can obtain

$$\left[1 - \frac{i\tau_m}{\omega\mu} \right] \mathbf{E}(\mathbf{r}) = \frac{1}{\mu_r} \mathbf{E}(\mathbf{r}) . \quad (\text{A1.6})$$

The following equality can be proved by using (15), (16) and (17) of Tai's paper [13], the proof is given at the end of this appendix.

$$\int_s \mathbf{n} \cdot [(\nabla' \times \mathbf{E}(\mathbf{r}')) \times \vec{G}_0(\mathbf{r}, \mathbf{r}')] ds' = \mu_r \left[-\mathbf{E}^i(\mathbf{r}) - \int_s \mathbf{n} \cdot [\mathbf{E}(\mathbf{r}') \times (\nabla' \times \vec{G}_0(\mathbf{r}, \mathbf{r}'))] ds' \right] \quad (\text{A1.7})$$

For the rest two terms in (3.2.20), we can have

$$\begin{aligned}
& \mathbf{E}^i(\mathbf{r}) - \left[\frac{\mu - \mu_0}{\mu} \right] \int_s \vec{G}_0(\mathbf{r}, \mathbf{r}') \cdot [\mathbf{n} \times \nabla' \times \mathbf{E}(\mathbf{r}')] ds' \\
&= \mathbf{E}^i(\mathbf{r}) - \left[\frac{\mu - \mu_0}{\mu_0} \right] \left[-\mathbf{E}^i(\mathbf{r}) - \int_s \mathbf{n} \cdot [\mathbf{E}(\mathbf{r}') \times (\nabla' \times \vec{G}_0(\mathbf{r}, \mathbf{r}'))] ds' \right] \\
&= \mu_r \left[\mathbf{E}^i(\mathbf{r}) + \int_s \frac{i\tau_m}{\omega\mu} \mathbf{n} \cdot [\mathbf{E}(\mathbf{r}') \times \vec{G}_m^e(\mathbf{r}, \mathbf{r}')] ds' \right]. \tag{A1.8}
\end{aligned}$$

From (A1.4), (A1.6) and (A1.8), we know that (A1.3) becomes

$$\begin{aligned}
& \frac{1}{\mu_r} \mathbf{E}(\mathbf{r}) - \frac{1}{\mu_r} (k^2 - k_0^2) \int_v \vec{G}_0(\mathbf{r}, \mathbf{r}') \cdot \mathbf{E}(\mathbf{r}') dv' \\
& \quad + \frac{1}{\mu_r} \left[\frac{\mu - \mu_0}{\mu} \right] \int_s \vec{G}_0(\mathbf{r}, \mathbf{r}') \cdot [\mathbf{n} \times \nabla' \times \mathbf{E}(\mathbf{r}')] ds' = \frac{1}{\mu_r} \mathbf{E}^i(\mathbf{r}) \tag{A1.9}
\end{aligned}$$

which is essentially equivalent to (3.2.20).

Therefore we can conclude that (A1.1) is equivalent to (3.2.20) since (A1.3) is simply a short form of (A1.1).

The remaining thing is to prove (A1.7).

Proof: Tai denoted the total electric and magnetic field distributions outside the body as $\mathbf{E}_2(\mathbf{r})$ and $\mathbf{H}_2(\mathbf{r})$, the induced field distributions inside the body as $\mathbf{E}_1(\mathbf{r})$ and $\mathbf{H}_1(\mathbf{r})$ and the incident fields as $\mathbf{E}^{(i)}$ and $\mathbf{H}^{(i)}$, while we use $\mathbf{E}(\mathbf{r})$, $\mathbf{H}(\mathbf{r})$, $\mathbf{E}^i(\mathbf{r})$ and $\mathbf{H}^i(\mathbf{r})$ instead of $\mathbf{E}_1(\mathbf{r})$, $\mathbf{H}_1(\mathbf{r})$, $\mathbf{E}^{(i)}$ and $\mathbf{H}^{(i)}$ as shown in Fig-A.1. Note that the outward normal vector of region I (inside of the body) in the figure of [13] is denoted as \mathbf{n}_1 , and that of region II (outside of the body) as \mathbf{n}_2 . We use the notation $\mathbf{n} = \mathbf{n}_1 = -\mathbf{n}_2$ to denote the normal vector when the boundary conditions are applied on the closed surface s enclosing region I.

Equations (15) to (17) in Tai's paper are needed to prove this equality. On s the boundary conditions are

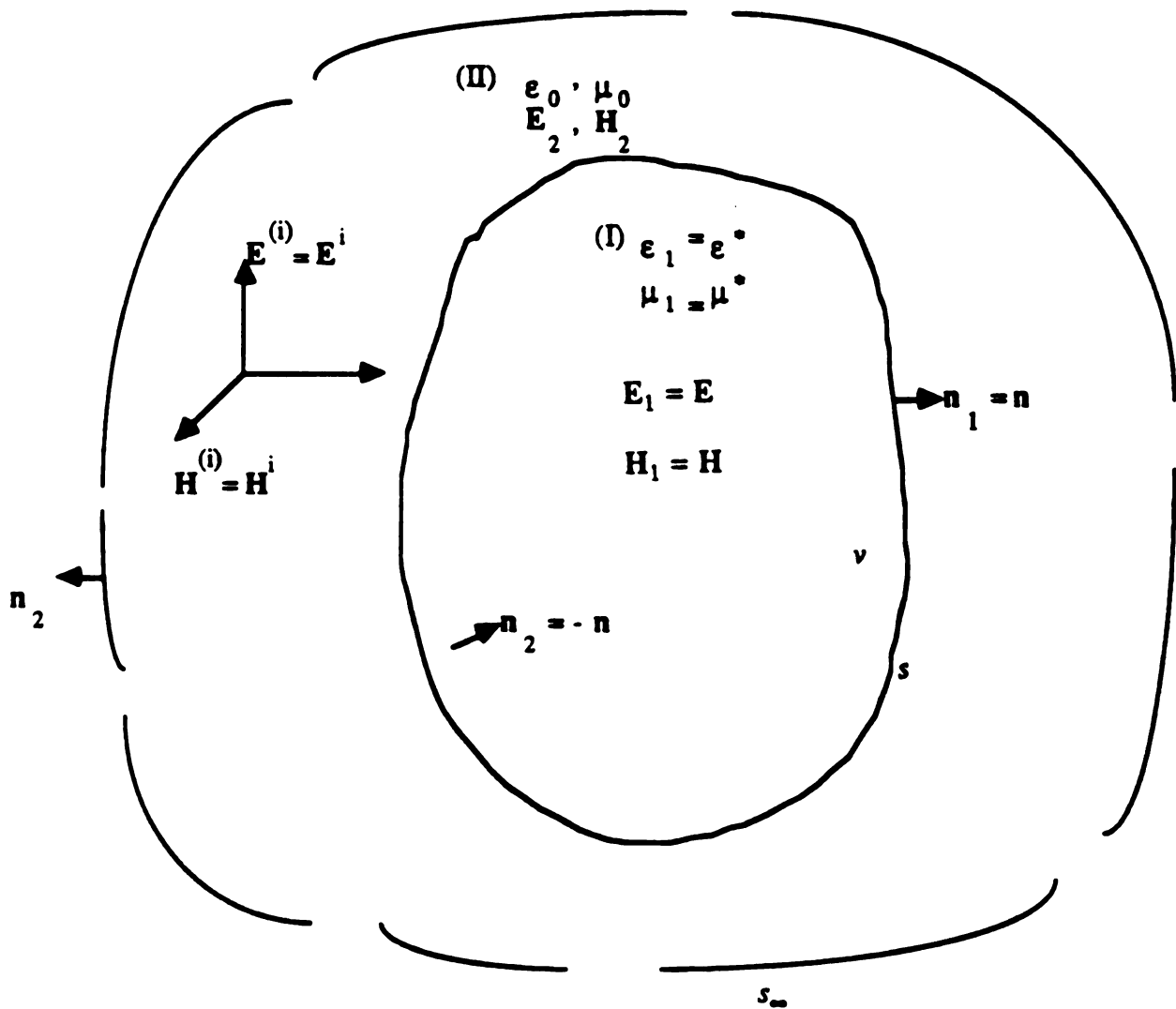


Fig-A.1 Different notations of the parameters and variables in a permeable body used by Tai and this thesis when it is illuminated by a plane wave.

$$\mathbf{n} \times (\mathbf{E} - \mathbf{E}_2) = 0, \quad (15)$$

$$\mathbf{n} \times \left[\frac{\nabla \times \mathbf{E}}{\mu} - \frac{\nabla \times \mathbf{E}_2}{\mu_0} \right] = 0, \quad (16)$$

hence

$$\mathbf{n} \times \nabla \times \mathbf{E} = \frac{\mu}{\mu_0} \mathbf{n} \times \nabla \times \mathbf{E}_2 = \left[1 + \frac{\mu - \mu_0}{\mu_0} \right] \mathbf{n} \times \nabla \times \mathbf{E}_2$$

Thus, we can have

$$\begin{aligned} & - \int_s \mathbf{n} \cdot [\mathbf{E}_2(\mathbf{r}') \times (\nabla' \times \vec{\mathcal{G}}_0(\mathbf{r}, \mathbf{r}')) + (\nabla' \times \mathbf{E}_2(\mathbf{r}') \times \vec{\mathcal{G}}_0(\mathbf{r}, \mathbf{r}')] ds' \\ & - \left[\frac{\mu - \mu_0}{\mu_0} \right] \int_s \mathbf{n} \cdot [(\nabla' \times \mathbf{E}_2(\mathbf{r}') \times \vec{\mathcal{G}}_0(\mathbf{r}, \mathbf{r}')] ds' \\ & = \mathbf{E}^i(\mathbf{r}) - \left[\frac{\mu - \mu_0}{\mu} \right] \int_s \mathbf{n} \cdot [(\nabla' \times \mathbf{E}(\mathbf{r}') \times \vec{\mathcal{G}}_0(\mathbf{r}, \mathbf{r}')] ds'. \end{aligned} \quad (17)$$

From equation (17) of [13], we have

$$\begin{aligned} & \mathbf{E}^i(\mathbf{r}) - \left[\frac{\mu - \mu_0}{\mu} \right] \int_s \mathbf{n} \cdot [(\nabla' \times \mathbf{E}(\mathbf{r}') \times \vec{\mathcal{G}}_0(\mathbf{r}, \mathbf{r}')] ds' \\ & = - \int_s \mathbf{n} \cdot [\mathbf{E}_2(\mathbf{r}') \times (\nabla' \times \vec{\mathcal{G}}_0(\mathbf{r}, \mathbf{r}')) + (\nabla' \times \mathbf{E}_2(\mathbf{r}') \times \vec{\mathcal{G}}_0(\mathbf{r}, \mathbf{r}')] ds' \\ & \quad - \left[\frac{\mu - \mu_0}{\mu_0} \right] \int_s \mathbf{n} \cdot [(\nabla' \times \mathbf{E}_2(\mathbf{r}') \times \vec{\mathcal{G}}_0(\mathbf{r}, \mathbf{r}')] ds' \\ & = - \int_s [(\mathbf{n} \times \mathbf{E}_2(\mathbf{r}')) \cdot (\nabla' \times \vec{\mathcal{G}}_0(\mathbf{r}, \mathbf{r}')) + (\mathbf{n} \times \nabla' \times \mathbf{E}_2(\mathbf{r}')) \cdot \vec{\mathcal{G}}_0(\mathbf{r}, \mathbf{r}')] ds' \\ & \quad - \int_s \left[\frac{\mu - \mu_0}{\mu_0} \right] [\mathbf{n} \times (\nabla' \times \mathbf{E}_2(\mathbf{r}')) \cdot \vec{\mathcal{G}}_0(\mathbf{r}, \mathbf{r}')] ds' \\ & = - \int_s (\mathbf{n} \times \mathbf{E}_2(\mathbf{r}')) \cdot (\nabla' \times \vec{\mathcal{G}}_0(\mathbf{r}, \mathbf{r}')) ds' \end{aligned}$$

$$\begin{aligned}
& - \int_S \left[1 + \frac{\mu - \mu_0}{\mu_0} \right] [\mathbf{n} \times (\nabla' \times \mathbf{E}_2(\mathbf{r}')) \cdot \vec{\mathcal{G}}_0(\mathbf{r}, \mathbf{r}')] ds' \\
& = \int_S (\mathbf{n} \times \mathbf{E}(\mathbf{r}')) \cdot (\nabla' \times \vec{\mathcal{G}}_0(\mathbf{r}, \mathbf{r}')) ds' - \int_S [\mathbf{n} \times (\nabla' \times \mathbf{E}(\mathbf{r}')) \cdot \vec{\mathcal{G}}_0(\mathbf{r}, \mathbf{r}')] ds' ,
\end{aligned} \tag{A1.10}$$

where we have applied the boundary conditions (15) and (16) of [13] in the last step.

Therefore we obtain

$$\begin{aligned}
& - \left[\frac{\mu - \mu_0}{\mu} \right] \int_S \left\{ \mathbf{n} \cdot [(\nabla' \times \mathbf{E}(\mathbf{r}')) \cdot \vec{\mathcal{G}}_0(\mathbf{r}, \mathbf{r}')] \right\} ds' + \int_S \left\{ \mathbf{n} \cdot [(\nabla' \times \mathbf{E}(\mathbf{r}')) \times \vec{\mathcal{G}}_0(\mathbf{r}, \mathbf{r}')] \right\} ds' \\
& = - \mathbf{E}^i(\mathbf{r}) - \int_S (\mathbf{n} \times \mathbf{E}(\mathbf{r}')) \cdot (\nabla' \times \vec{\mathcal{G}}_0(\mathbf{r}, \mathbf{r}')) ds' ,
\end{aligned} \tag{A1.11}$$

or in other words,

$$\frac{1}{\mu_r} \int_S \mathbf{n} \cdot [(\nabla' \times \mathbf{E}(\mathbf{r}')) \times \vec{\mathcal{G}}_0(\mathbf{r}, \mathbf{r}')] ds' = - \mathbf{E}^i(\mathbf{r}) - \int_S \mathbf{n} \cdot [\mathbf{E}(\mathbf{r}') \times (\nabla' \times \vec{\mathcal{G}}_0(\mathbf{r}, \mathbf{r}'))] ds' . \tag{A1.12}$$

Equation (3.2.21) can be proved to be equivalent to (A1.2) in a similar way.

APPENDIX II

A proof of the equivalence between two sets of coupled integral equations is given here.

The coupled tensor integral equations derived in section 3.1 are:

$$\begin{aligned} \left[1 + \frac{i\tau_e(\mathbf{r})}{3\omega\epsilon_0} \right] \mathbf{E}(\mathbf{r}) - P.V. \int_v i\omega\mu_0\tau_e(\mathbf{r}')\mathbf{E}(\mathbf{r}')\cdot\vec{\mathcal{G}}_0(\mathbf{r},\mathbf{r}') d\mathbf{v}' \\ - \int_v \tau_m(\mathbf{r}')\mathbf{H}(\mathbf{r}')\cdot[\nabla \times \vec{\mathcal{G}}_0(\mathbf{r},\mathbf{r}')] d\mathbf{v}' = \mathbf{E}^i(\mathbf{r}) \end{aligned} \quad (3.1.40)$$

$$\begin{aligned} \left[1 + \frac{i\tau_m(\mathbf{r})}{3\omega\mu_0} \right] \mathbf{H}(\mathbf{r}) - P.V. \int_v i\omega\epsilon_0\tau_m(\mathbf{r}')\mathbf{H}(\mathbf{r}')\cdot\vec{\mathcal{G}}_0(\mathbf{r},\mathbf{r}') d\mathbf{v}' \\ + \int_v \tau_e(\mathbf{r}')\mathbf{E}(\mathbf{r}')\cdot[\nabla \times \vec{\mathcal{G}}_0(\mathbf{r},\mathbf{r}')] d\mathbf{v}' = \mathbf{H}^i(\mathbf{r}) . \end{aligned} \quad (3.1.41)$$

The coupled integral equations in terms of the free space scalar Green's function derived in section 3.3 are:

$$\begin{aligned} \mathbf{E}(\mathbf{r}) - \frac{i\zeta}{k_0} \int_v \left\{ [\nabla' \cdot (\tau_e(\mathbf{r}')\mathbf{E}(\mathbf{r}'))]\nabla\phi(\mathbf{r},\mathbf{r}') + k_0^2\tau_e(\mathbf{r}')\mathbf{E}(\mathbf{r}')\phi(\mathbf{r},\mathbf{r}') \right\} d\mathbf{v}' \\ + \frac{i\zeta}{k_0} \int_s [\mathbf{n} \cdot (\tau_e(\mathbf{r}')\mathbf{E}(\mathbf{r}'))]\nabla\phi(\mathbf{r},\mathbf{r}') ds' + \int_v \tau_m(\mathbf{r}')\mathbf{H}(\mathbf{r}') \times \nabla\phi(\mathbf{r},\mathbf{r}') d\mathbf{v}' \\ = \mathbf{E}^i(\mathbf{r}) \end{aligned} \quad (3.3.28)$$

$$\begin{aligned} \mathbf{H}(\mathbf{r}) - \frac{i}{\zeta k_0} \int_v \left\{ [\nabla' \cdot (\tau_m(\mathbf{r}')\mathbf{H}(\mathbf{r}'))]\nabla\phi(\mathbf{r},\mathbf{r}') + k_0^2\tau_m(\mathbf{r}')\mathbf{H}(\mathbf{r}')\phi(\mathbf{r},\mathbf{r}') \right\} d\mathbf{v}' \\ + \frac{i}{\zeta k_0} \int_s [\mathbf{n} \cdot (\tau_m(\mathbf{r}')\mathbf{H}(\mathbf{r}'))]\nabla\phi(\mathbf{r},\mathbf{r}') ds' - \int_v \tau_e(\mathbf{r}')\mathbf{E}(\mathbf{r}') \times \nabla\phi(\mathbf{r},\mathbf{r}') d\mathbf{v}' \end{aligned}$$

$$= \mathbf{H}^i(\mathbf{r}) . \quad (3.3.29)$$

We shall prove that these two sets of integral equations are equivalent. It is sufficient to show (3.1.40) and (3.3.28) to be equivalent since (3.1.41) and (3.3.29) can be proved to be equivalent in a similar way. We need the following relation first:

$$\begin{aligned} & \int_v [\nabla' \cdot \mathbf{A}(\mathbf{r}')] \nabla \phi(\mathbf{r}, \mathbf{r}') dv' - \int_s [\mathbf{n} \cdot \mathbf{A}(\mathbf{r}')] \nabla \phi(\mathbf{r}, \mathbf{r}') ds' \\ &= P.V. \int_v \mathbf{A}(\mathbf{r}') \cdot \nabla \nabla \phi(\mathbf{r}, \mathbf{r}') dv' - \frac{\mathbf{A}(\mathbf{r})}{3} . \end{aligned} \quad (A2.1)$$

for any continuous vector function $\mathbf{A}(\mathbf{r})$.

Proof: Since $\nabla \phi(\mathbf{r}, \mathbf{r}')$ is an integrable vector function for \mathbf{r} and \mathbf{r}' in v , we have

$$\int_v [\nabla' \cdot \mathbf{A}(\mathbf{r}')] \nabla \phi(\mathbf{r}, \mathbf{r}') dv' = \lim_{\varepsilon \rightarrow 0} \int_{v-v_\varepsilon} [\nabla' \cdot \mathbf{A}(\mathbf{r}')] \nabla \phi(\mathbf{r}, \mathbf{r}') dv' . \quad (A2.2)$$

From the dyadic identity

$$\nabla' \cdot [\mathbf{A}(\mathbf{r}') \nabla \phi(\mathbf{r}, \mathbf{r}')] = [\nabla' \cdot \mathbf{A}(\mathbf{r}')] \nabla \phi(\mathbf{r}, \mathbf{r}') + \mathbf{A}(\mathbf{r}') \cdot \nabla' \nabla \phi(\mathbf{r}, \mathbf{r}') , \quad (A2.3)$$

or

$$[\nabla' \cdot \mathbf{A}(\mathbf{r}')] \nabla \phi(\mathbf{r}, \mathbf{r}') = \nabla' \cdot [\mathbf{A}(\mathbf{r}') \nabla \phi(\mathbf{r}, \mathbf{r}')] - \mathbf{A}(\mathbf{r}') \cdot \nabla' \nabla \phi(\mathbf{r}, \mathbf{r}') , \quad (A2.4)$$

we can have

$$\begin{aligned} & \int_{v-v_\varepsilon} [\nabla' \cdot \mathbf{A}(\mathbf{r}')] \nabla \phi(\mathbf{r}, \mathbf{r}') dv' \\ &= \int_{v-v_\varepsilon} \nabla' \cdot [\mathbf{A}(\mathbf{r}') \nabla \phi(\mathbf{r}, \mathbf{r}')] dv' - \int_{v-v_\varepsilon} \mathbf{A}(\mathbf{r}') \cdot \nabla' \nabla \phi(\mathbf{r}, \mathbf{r}') dv' \\ &= \int_{s+s_\varepsilon} [\mathbf{n} \cdot \mathbf{A}(\mathbf{r}')] \nabla \phi(\mathbf{r}, \mathbf{r}') ds' + \int_{v-v_\varepsilon} \mathbf{A}(\mathbf{r}') \cdot \nabla \nabla \phi(\mathbf{r}, \mathbf{r}') dv' \\ &= \int_s [\mathbf{n} \cdot \mathbf{A}(\mathbf{r}')] \nabla \phi(\mathbf{r}, \mathbf{r}') ds' + \int_{s_\varepsilon} [\mathbf{n} \cdot \mathbf{A}(\mathbf{r}')] \nabla \phi(\mathbf{r}, \mathbf{r}') ds' \\ &+ \int_{v-v_\varepsilon} \mathbf{A}(\mathbf{r}') \cdot \nabla \nabla \phi(\mathbf{r}, \mathbf{r}') dv' \end{aligned} \quad (A2.5)$$

where v is the volume source region, s is the closed boundary surface enclosing region v , v_ϵ is a small sphere centered at \mathbf{r} with radius ϵ and s_ϵ is the closed boundary surface enclosing region v_ϵ , as shown in Fig-A.2. Note that the unit normal vector \mathbf{n} of the surfaces $s+s_\epsilon$ enclosing $v-v_\epsilon$ points outward to the the surfaces, i.e., it is in the opposite direction of the outward normal of the small sphere v_ϵ when we consider the surface integration on s_ϵ in (A2.5).

We use the following expression by the definition of Cauchy principal value,

$$P.V. \int_v \mathbf{A}(\mathbf{r}') \cdot \nabla \nabla \phi(\mathbf{r}, \mathbf{r}') dv' = \lim_{\epsilon \rightarrow 0} \int_{v-v_\epsilon} \mathbf{A}(\mathbf{r}') \cdot \nabla \nabla \phi(\mathbf{r}, \mathbf{r}') dv'. \quad (\text{A2.6})$$

Let us take limits for both side of (A2.5) when ϵ goes to zero, we have

$$\begin{aligned} & \int_v [\nabla' \cdot \mathbf{A}(\mathbf{r}')] \nabla \phi(\mathbf{r}, \mathbf{r}') dv' - \int_s [\mathbf{n} \cdot \mathbf{A}(\mathbf{r}')] \nabla \phi(\mathbf{r}, \mathbf{r}') ds' \\ &= \lim_{\epsilon \rightarrow 0} \int_{s_\epsilon} [\mathbf{n} \cdot \mathbf{A}(\mathbf{r}')] \nabla \phi(\mathbf{r}, \mathbf{r}') ds' + P.V. \int_v \mathbf{A}(\mathbf{r}') \cdot \nabla \nabla \phi(\mathbf{r}, \mathbf{r}') dv' \\ &= P.V. \int_v \mathbf{A}(\mathbf{r}') \cdot \nabla \nabla \phi(\mathbf{r}, \mathbf{r}') dv' - \frac{\mathbf{A}(\mathbf{r})}{3}, \end{aligned} \quad (\text{A2.7})$$

since

$$\lim_{\epsilon \rightarrow 0} \int_{s_\epsilon} [\mathbf{n} \cdot \mathbf{A}(\mathbf{r}')] \nabla \phi(\mathbf{r}, \mathbf{r}') ds' = - \frac{\mathbf{A}(\mathbf{r})}{3} \quad (\text{A2.8})$$

for a continuous vector function $\mathbf{A}(\mathbf{r})$. The result of (A2.8) can be carried out by fundamental calculus as shown in [2] and [3].

Now let us compare (3.1.40) and (3.3.28) term by term:

$$\int_v i\omega\mu_0\tau_e(\mathbf{r}')\mathbf{E}(\mathbf{r}')\phi(\mathbf{r}, \mathbf{r}') dv' = \frac{i\zeta}{k_0} \int_v k_0^2\tau_e(\mathbf{r}')\mathbf{E}(\mathbf{r}')\phi(\mathbf{r}, \mathbf{r}') dv'; \quad (\text{A2.9})$$

by (A2.7),

$$\frac{i\tau_e(\mathbf{r})}{3\omega\epsilon_0} \mathbf{E}(\mathbf{r}) - P.V. \int_v \frac{i\omega\mu_0}{k_0^2} \tau_e(\mathbf{r}') \mathbf{E}(\mathbf{r}') \cdot \nabla \nabla \phi(\mathbf{r}, \mathbf{r}') dv'$$

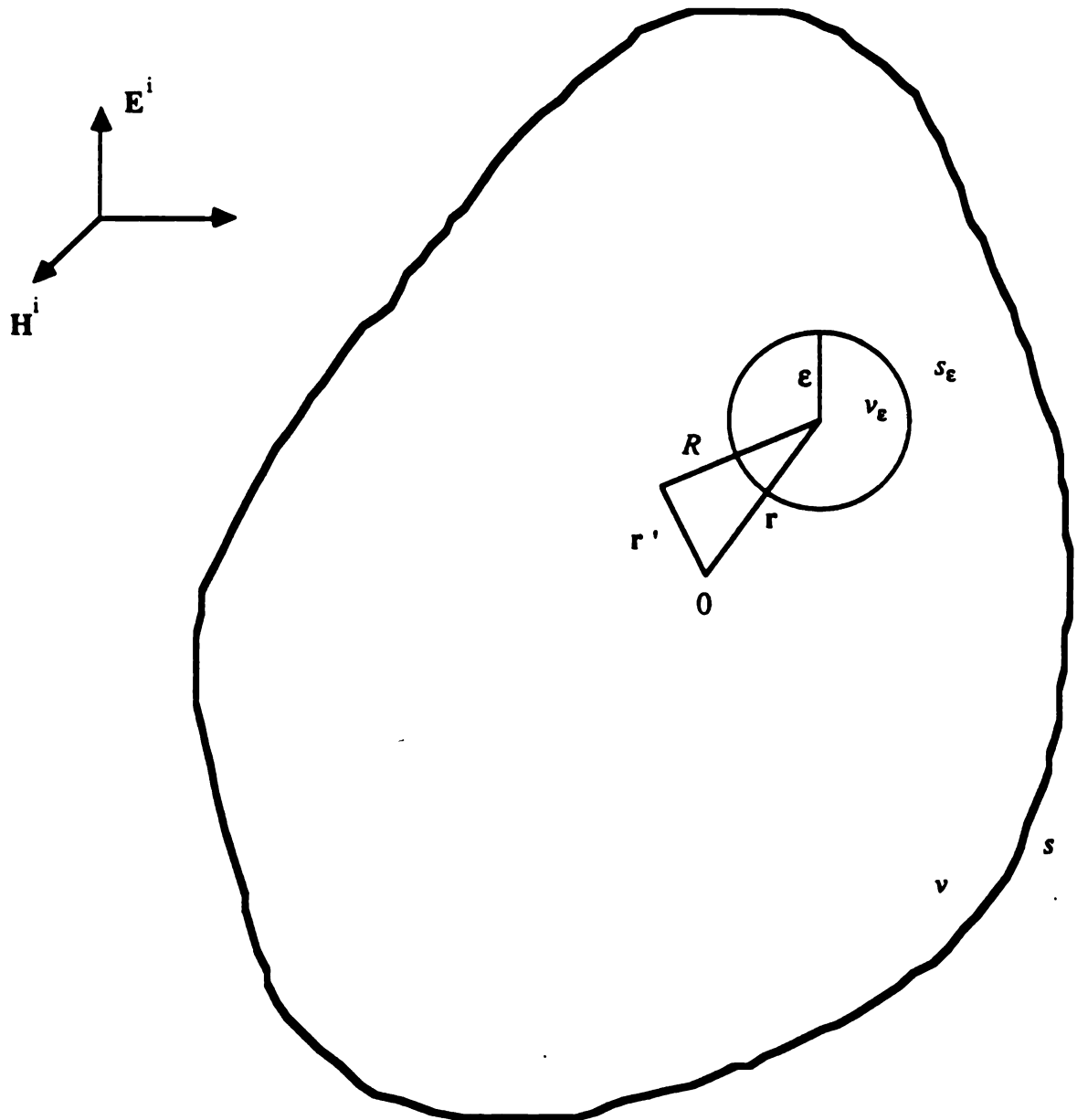


Fig-A.2 Illustration of the exclusion of a small region which contains the singularity point when evaluating the principal integration.

$$= -\frac{i\zeta}{k_0} \int_v [\nabla' \cdot \tau_e(\mathbf{r}') \mathbf{E}(\mathbf{r}')] \nabla \phi(\mathbf{r}, \mathbf{r}') dv' + \frac{i\zeta}{k_0} \int_s [\mathbf{n} \cdot \tau_e(\mathbf{r}') \mathbf{E}(\mathbf{r}')] \nabla \phi(\mathbf{r}, \mathbf{r}') ds' ; \quad (\text{A2.10})$$

and

$$\int_v \tau_m(\mathbf{r}') \mathbf{H}(\mathbf{r}') \cdot [\nabla \times \vec{\mathcal{G}}_0(\mathbf{r}, \mathbf{r}')] dv' = \int_v \tau_m(\mathbf{r}') \mathbf{H}(\mathbf{r}') \times \nabla \phi(\mathbf{r}, \mathbf{r}') dv' \quad (\text{A2.11})$$

since

$$\mathbf{A}(\mathbf{r}') \cdot [\nabla \times \vec{\mathcal{G}}_0(\mathbf{r}, \mathbf{r}')] = \mathbf{A}(\mathbf{r}') \cdot [\nabla \phi(\mathbf{r}, \mathbf{r}') \times \vec{\mathcal{I}}] = \mathbf{A}(\mathbf{r}') \times \nabla \phi(\mathbf{r}, \mathbf{r}') \quad (\text{A2.12})$$

for any vector function $\mathbf{A}(\mathbf{r}')$ and hence in particular, (A2.12) holds when $\mathbf{A}(\mathbf{r}') = \mathbf{H}(\mathbf{r}')$.

From (A2.9), (A2.10) and (A2.11), we can conclude that (3.1.40) and (3.3.28) are equivalent.

It is noted that the limiting processes and the evaluation of the Cauchy principal values are all based on the assumption that the excluded volume v_ϵ is a small sphere. The different infinitesimal geometries will end up with different results as mentioned by Van Bladal [2] and Chen [9].

Similarly, we can prove that (3.1.41) and (3.3.29) are also equivalent.

COMPUTER PROGRAMS

COMPUTER PROGRAM I

Fortran-77 Program Guide for the Coupled Tensor Integral Equations

This program is used to calculate the induced EM field distribution in a finite, heterogeneous, dielectric, magnetic and lossy body exposed to an incident EM field.

Description of key variables and arrays for using the program:

Variable or Array Name	Description
NT	no. of cells in first octant of a symmetric body, integer variable
DL	length of a side of each cubic cell, in (m), real variable
X(L,I)	L coordinate of the center of the I-th cell, in (m), L=1,2,3=x,y,z coordinate, real array
SIG(I)	conductivity of the I-th cell, in (S/m), real array
EPR(I)	relative permittivity of the I-th cell, real array
MUR(I)	relative permeability of the I-th cell, complex array
INCI	symmetry of incident EM field, INCI is 1 or 2. 1 stands for antisymmetric and 2 for symmetric, integer variable
FREQ	frequency of the incident EM field, in (MHz), real variable

Input data file structure:(free formats are used for all the variables)

Line No.	Variable Name
1	NT,DL
2	(X(L,1),L=1,3), SIG(1), EPR(1), MUR(1)
3	(X(L,2),L=1,3), SIG(2), EPR(2), MUR(2)
.....
NT+1	(X(L,NT),L=1,3), SIG(NT), EPR(NT), MUR(NT)
NT+2	INCI, FREQ
The following data are for the symmetry of geometry and EM field distributions and should remain at the end of this data file.	
NT+3	1 1 1
NT+4	-1 1 1
NT+5	-1 -1 1
NT+6	1 -1 1
NT+7	1 1 -1
NT+8	-1 1 -1
NT+9	-1 -1 -1
NT+10	1 -1 -1
NT+11	1 1 1 1 -1 -1 -1 -1
NT+12	1 -1 1 -1 -1 1 -1 1
NT+13	1 -1 -1 1 1 -1 -1 1
NT+14	1 1 1 1 1 1 1 1
NT+15	1 -1 1 -1 1 -1 1 -1
NT+16	1 -1 -1 1 -1 1 1 -1
NT+17	1 -1 1 -1 1 -1 1 -1
NT+18	1 1 1 1 1 1 1 1
NT+19	1 1 -1 -1 -1 -1 1 1
NT+20	1 -1 1 -1 -1 1 -1 1
NT+21	1 1 1 1 -1 -1 -1 -1
NT+22	1 1 -1 -1 1 1 -1 -1

Output data file structure:

There will be 5 numbers in each line. The first one is an integer and indicates the numbering of the cell. The 2nd and 3rd numbers stand for the phasor (real and imaginary parts) of EM field of each cell. The 4th and 5th numbers stand for the amplitude (in V/m or A/m) and phase angle (in degree) of the EM field. Three components of EM field are all printed out.

The program listing is attached from the next page.

```

C*****
C Coupled Tensor Integral Equations
C*****
C This program is used to calculate the induced EM field distribution in
C a finite, heterogeneous, dielectric, magnetic and lossy body exposed to
C an incident EM field
C*****
PROGRAM COUPLEIE
PARAMETER (NTMAX=64,NTMAX3=192,NTMAX6=384,NTMAX61=385
$,NTMAX8=512,NTMAX83=1536)
REAL X(3,NTMAX8),SIG(NTMAX),EPR(NTMAX)
COMPLEX A(2,3,NTMAX83),D(NTMAX6,NTMAX61)
$,MUR(NTMAX),TAUE(NTMAX),TAUM(NTMAX)
$,CON1(NTMAX),CON2(NTMAX),CON3(NTMAX),CON4(NTMAX)
INTEGER NS(NTMAX,6)
C*****
C Input data:
C*****
C NT=No. of cells in first octant of a symmetric body, integer
C DL=length of a side of each cubic cell, in (m)
C X(L,I)=L coordinate of the center of the i-th cell, in (m),
C L=1,2,3=x,y,z coordinate
C SIG(I)=conductivity of the i-th cell, in (S/m)
C EPR(I)=relative permittivity of the i-th cell, a real number
C MUR(I)=relative permeability of the i-th cell, a complex number
C*****
open (1,file='cplin.dat')
read (1,*) NT,DL
do 391 i=1,nt
read (1,*) X(1,I),X(2,I),X(2,I),SIG(I),EPR(I),MUR(I)
C*****
nt3=3*nt
nt6=6*nt
nt8=8*nt
nt83=24*nt
nt61=nt6+1
call main(x,sig,epr,a,d,mur,taue,taum,con1,con2
$,con3,con4,ns,NT,NT3,NT6,NT61,NT8,NT83)
stop
end

subroutine main(x,sig,epr,a,d,,mur,taue,taum,con1,con2
$,con3,con4,ns,NT,NT3,NT6,NT61,NT8,NT83)
REAL MU0,K0,XJV(8,3),X(3,NT8),XC(3),X1(3),SIG(NT),EPR(NT)
COMPLEX A(2,3,NT83),D(NT6,NT61)
$,JC,MUR(NT),MU,mur2,TAUE(NT),TAUM(NT)
$,SUMV,DT1,DT2,CON1(NT),CON2(NT),CON3(NT),CON4(NT)
INTEGER P,Q,NS(NT,6),ISE(2,3,8),ISM(2,3,8),IQ(3,8)
COMMON /A/JC,K0,PI/F/DL,HDL,QDL,DS,DV
OPEN (4,FILE='cplout.dat')
nt2=2*nt
nt4=4*nt
nt5=5*nt
C*****
C Input data:
C*****
C INCI=smetricity of incident EM field, INCI is 1 or 2
C 1 stands for antisymmetric and 2 for symmetric
C FREQ=frequency of the incident EM field, in (MHz)
C*****
READ (1,*) INCI,FREQ
C*****
C Output Format:
C*****
WRITE (4,*) 'HETRO COUPLED IE WITH 8 QUA SYMMETRY'
IF (INCI.EQ.1) WRITE (4,*) 'Ei = x j*sinkz, Hi = y coskz/20'

```

```

      IF (INCI.EQ.2) WRITE (4,*) 'Ei = x coskz,   Hi = y j*sinkz/Z0'
      DO 73 I=1,NT
c*****
73    WRITE(4,50) I,SIG(I),EPR(I),MUR(I)
50    FORMAT (I5,F15.8,3X,F15.8,3X,2F15.8)
c*****
c    IQ(L,J)=sign of L coordnate of center of each cell in J-th octant,
c          IQ is 1 or -1
c    ISE(INCI,L,J)=sign of L component of E field distribution in J-th octant,
c          ISE is 1 or -1, INCI is 1 or 2
c    ISM(INCI,L,J)=sign of L component of H field distribution in J-th octant,
c          ISM is 1 or -1, INCI is 1 or 2
c*****
      DO 31 J=1,8
31    READ (1,*) (IQ(L,J),L=1,3)
      DO 32 I=1,3
32    READ (1,*) (ISE(1,L,J),J=1,8)
      DO 33 I=1,3
33    READ (1,*) (ISE(2,L,J),J=1,8)
      DO 52 I=1,3
52    READ (1,*) (ISM(1,L,J),J=1,8)
      DO 53 I=1,3
53    READ (1,*) (ISM(2,L,J),J=1,8)
c*****
      JC=(0.,1.)
      PI=DATAN(1.D0)*4.
      WG=2.D6*PI*FREQ
      KO=WG/3.D8
      EPO=1.E-9/36./PI
      MU0=4.E-7*PI
      DO 74 I=1,NT
      MU=MUR(I)*MU0
      EP=EPR(I)*EPO
      TAUE(I)=SIG(I)-JC*WG*(EP-EPO)
      TAUM(I)=-JC*WG*(MU-MU0)
      CON1(I)=-K0*TAUE(I)*JC*WG*MU0/4./PI
      CON2(I)=+K0**2*TAUM(I)/4./PI
      CON3(I)=-K0**2*TAUE(I)/4./PI
74    CON4(I)=-K0*TAUM(I)*JC*WG*EPO/4./PI
      DS=DL*DL
      DV=DS*DL
      HDL=DL/2.
      QDL=DL/4.
c*****
c    Calculate the corresponding coordinates from the 2nd to 8th octants
c*****
      DO 15 I=1,NT
      DO 15 M=2,8
      DO 15 L=1,3
15    X(L,I+(M-1)*NT)=X(L,I)*IQ(L,M)
c*****
c    Filling matrix elements
c*****
      DO 18 I=1,NT
      PRINT *,I
      DO 79 L=1,3
79    XC(L)=X(L,I)
      DO 18 MQ=1,2
      DO 17 J=1,NT8
      JMODNT=J-(J-1)/NT*NT
      DO 78 L=1,3
78    X1(L)=X(L,J)
      DO 17 Q=1,3
      LL=J+(Q-1)*NT8
      DO 17 P=1,3
      CALL VPT(X1,XJV,QDL)

```

```

CALL VINTE(I, J, XC, XJV, MQ, P, Q, SUMV)
IF (MQ.EQ.1) THEN
  A(1,P,LL)=CON1(JMODNT)*SUMV
  A(2,P,LL)=CON4(JMODNT)*SUMV
  IF ((I.EQ.J).AND.(P.EQ.Q))
    SA(1,P,LL)=A(1,P,LL)+1.+JC*TAUE(JMODNT)/3./WG/EPO
    IF ((I.EQ.J).AND.(P.EQ.Q))
      SA(2,P,LL)=A(2,P,LL)+1.+JC*TAUM(JMODNT)/3./WG/MUO
  ELSEIF (MQ.EQ.2) THEN
    A(1,P,LL)=CON2(JMODNT)*SUMV
    A(2,P,LL)=CON3(JMODNT)*SUMV
  ENDIF
17  CONTINUE
c*****
c  Using symmetric properties to reduce matrix size
c*****
  DO 41 K=1,NT
  DO 41 P=1,3
  DO 41 Q=1,3
  DT1=(0.,0.)
  DT2=(0.,0.)
  KT=K+(Q-1)*NT
  IF (MQ.EQ.1) THEN
    DO 42 M=1,8
42  DT1=A(1,P,(Q-1)*NT8+K+(M-1)*NT)*ISE(INCI,Q,M)+DT1
    DT2=A(2,P,(Q-1)*NT8+K+(M-1)*NT)*ISM(INCI,Q,M)+DT2
  ELSEIF (MQ.EQ.2) THEN
    DO 43 M=1,8
43  DT1=A(1,P,(Q-1)*NT8+K+(M-1)*NT)*ISM(INCI,Q,M)+DT1
    DT2=A(2,P,(Q-1)*NT8+K+(M-1)*NT)*ISE(INCI,Q,M)+DT2
  ENDIF
  D(I+(P-1)*NT,KT+(MQ-1)*NT3)=DT1
41  D(I+(P-1)*NT+NT3,KT+(2-MQ)*NT3)=DT2
18  CONTINUE
c*****
c  Filling the vector of incident EM field in the center of each cell
c*****
  DO 35 I=1,NT
  B=K0*X(3,I)
  IF (INCI.EQ.1) THEN
    C=SIN(B)
    E=COS(B)
    D(I,NT61)=CMPLX(0.,C)
    D(I+NT4,NT61)=CMPLX(E/120/PI,0.)
  ELSEIF (INCI.EQ.2) THEN
    C=COS(B)
    E=SIN(B)
    D(I,NT61)=CMPLX(C,0.)
    D(I+NT4,NT61)=CMPLX(0.,E/120/PI)
  ENDIF
  D(I+NT,NT61)=(0.,0.)
  D(I+NT2,NT61)=(0.,0.)
  D(I+NT3,NT61)=(0.,0.)
35  D(I+NT5,NT61)=(0.,0.)
c*****
c  Solving the matrix equation
c*****
  CALL CMATPA(-1,D,NT6,1,DET,1.E-38,NT61)
c*****
c  Print out the induced EM fields at the center of each cell
c*****
c  FABS=Magnitude of the EM fields, in (V/m) or (A/m)
c  PHASE=Phase angle of the EM fields, in degree
c*****
  DO 36 K=1,6
  IF (K.EQ.1) WRITE (4,*) 'EX'

```

```

IF (K.EQ.2) WRITE (4,*) 'EY'
IF (K.EQ.3) WRITE (4,*) 'EZ'
IF (K.EQ.4) WRITE (4,*) 'HX'
IF (K.EQ.5) WRITE (4,*) 'HY'
IF (K.EQ.6) WRITE (4,*) 'HZ'
DO 36 I=1,NT
I1=I+NT*(K-1)
FABS=CABS(D(I1,NT61))
PHASE=ATAN2(AIMAG(D(I1,NT61)),REAL(D(I1,NT61)))*180/PI
36 WRITE (4,150) I,D(I1,NT61),FABS,PHASE
150 FORMAT (1X,I4,2E20.11,3X,E15.8,F10.4)
RETURN
END

```

```

c*****
c This subroutine is used to calculate each entry of the matrix except the
c diagonal element via numerical integration, the integration is approximated
c simply by cutting a cell into 8 subcells and summing up the function value
c in each subcell
c*****

```

```

SUBROUTINE VINTE(M,N,X,XJ,MQ,P,Q,ST)
REAL X(3),X1(3),XJ(8,3)
COMPLEX GPQ,GP,ST,GB
INTEGER P,Q
COMMON /F/DL,HDL,QDL,DS,DV
ST=(0.,0.)
IF (MQ.EQ.1) THEN
IF (M.EQ.N) GO TO 69
DO 30 J=1,8
DO 46 L=1,3
46 X1(L)=XJ(J,L)
30 ST=ST+GPQ(P,Q,X,X1)
ST=ST*DV/8.
GO TO 99
69 IF (P.NE.Q) GO TO 99
ST=GB(DL)
ELSEIF (MQ.EQ.2) THEN
IF (P.EQ.Q) GO TO 99
K=6-P-Q
DO 40 J=1,8
DO 56 L=1,3
56 X1(L)=XJ(J,L)
40 ST=ST+GP(K,X,X1)
KD=(P-Q)/2
IF (KD.EQ.0) ST=ST*(P-Q)
IF (KD.NE.0) ST=-ST*KD
ST=ST*DV/8.
ENDIF
99 RETURN
END

```

```

c*****
c This function subroutine is used to evaluate the 2nd derivative of the
c free space Green's function at center of each cell
c*****

```

```

FUNCTION GPQ(P,Q,X,X1)
REAL K0,X(3),X1(3),XD(3)
COMPLEX JC,GPQ,B,C,D
INTEGER P,Q
COMMON /A/JC,K0,PI
DO 75 L=1,3
XD(L)=X(L)-X1(L)
IF (ABS(XD(L)).LT.1.D-8) XD(L)=0.
75 CONTINUE

```

```

R=SQRT(XD(1)*XD(1)+XD(2)*XD(2)+XD(3)*XD(3))
A=K0*R
D=CEXP(JC*A)
C=(3.-A*A-3.*JC*A)*XD(P)*XD(Q)/R/R
IF(P.NE.Q) THEN
GPQ=C*D/A/A/A
ELSEIF(P.EQ.Q) THEN
B=A*A-1.+JC*A
GPQ=(B+C)*D/A/A/A
ENDIF
RETURN
END

```

```

c*****
c This function subroutine is used to evaluate the 1st derivative of the
c free space Green's function at center of each cell
c*****

```

```

FUNCTION GP(P,X,X1)
REAL K0,X(3),X1(3),XD(3)
COMPLEX JC,GP,C,D
INTEGER P
COMMON /A/JC,K0,PI
DO 75 L=1,3
XD(L)=X(L)-X1(L)
IF (ABS(XD(L)).LT.1.D-8) XD(L)=0.
75 CONTINUE
R=SQRT(XD(1)*XD(1)+XD(2)*XD(2)+XD(3)*XD(3))
A=K0*R
D=CEXP(JC*A)
C=(JC*A-1.)*XD(P)/R
GP=C*D/A/A
RETURN
END

```

```

c*****
c This function subroutine is used to calculate the value of the diagonal
c element of the matrix, this value includes a principal integration plus
c a correction term
c*****

```

```

FUNCTION GB(DL)
REAL K0
COMPLEX GB,JC
COMMON /A/JC,K0,PI
DV=DL**3
AN=(3.*DV/4./PI)**(1./3.)
GB=4.*PI*2.*(CEXP(JC*K0*AN)*(1.-JC*K0*AN)-1.)/(3.*K0**3)
RETURN
END

```

```

c*****
c This subroutine is used to calculate the coordinates of 8 subcells
c of each cell in order to perform the numerical integration
c*****

```

```

SUBROUTINE VPT(B,BN,QRDL)
REAL QRDL,B(3),BN(8,3)
BN(1,1)=B(1)+QRDL
BN(1,2)=B(2)+QRDL
BN(1,3)=B(3)+QRDL
BN(2,1)=B(1)+QRDL
BN(2,2)=B(2)+QRDL
BN(2,3)=B(3)-QRDL
BN(3,1)=B(1)+QRDL
BN(3,2)=B(2)-QRDL

```

```

BN(3,3)=B(3)+QRDL
BN(4,1)=B(1)+QRDL
BN(4,2)=B(2)-QRDL
BN(4,3)=B(3)-QRDL
BN(5,1)=B(1)-QRDL
BN(5,2)=B(2)+QRDL
BN(5,3)=B(3)+QRDL
BN(6,1)=B(1)-QRDL
BN(6,2)=B(2)+QRDL
BN(6,3)=B(3)-QRDL
BN(7,1)=B(1)-QRDL
BN(7,2)=B(2)-QRDL
BN(7,3)=B(3)+QRDL
BN(8,1)=B(1)-QRDL
BN(8,2)=B(2)-QRDL
BN(8,3)=B(3)-QRDL
RETURN
END

```

```

c*****
c This subroutine is used to solve the matrix equation via Gaussian
c elimination
c*****
      SUBROUTINE CMATPA(IJOB,A,N,M,DET,EP,N031)
      COMPLEX A,B,DET,CONST,S
      DIMENSION A(N,N031)
30  FORMAT(1X,42HTHE DETERMINANT OF THE SYSTEM EQUALS ZERO./
11X,36HTHE PROGRAM CANNOT HANDLE THIS CASE.//)
      DET=1.
      NP1=N+1
      NPM=N+M
      NM1=N-1
      IF(IJOB) 2,1,2
1   DO 3 I=1,N
      NPI=N+I
      A(I,NPI)=1.
      IP1=I+1
      DO 3 J=IP1,N
      NPJ=N+J
      A(I,NPJ)=0.
3   A(J,NPI)=0.
2   DO 4 J=1,NM1
      C=CABS(A(J,J))
      JP1=J+1
      DO 5 I=JP1,N
      D=CABS(A(I,J))
      IF(C-D) 6,5,5
6   DET=-DET
      DO 7 K=J,NPM
      B=A(I,K)
      A(I,K)=A(J,K)
7   A(J,K)=B
      C=D
5   CONTINUE
      IF(CABS(A(J,J))-EP) 14,15,15
15  DO 4 I=JP1,N
      CONST=A(I,J)/A(J,J)
      DO 4 K=JP1,NPM
4   A(I,K)=A(I,K)-CONST*A(J,K)
      IF(CABS(A(N,N))-EP) 14,18,18
14  DET=0.
      IF(IJOB) 16,16,17
16  PRINT 30
17  RETURN
C   18 DO 11 I=1,N

```

```
C 11 DET=DET*A(I,I)
19 IF(IJOB) 10,10,17
10 DO 12 I=1,N
    K=N-I+1
    KP1=K+1
    DO 12 L=NP1,NPM
        S=0.
        IF(N-KP1) 12,19,19
19 DO 13 J=KP1,N
13 S=S+A(K,J)*A(J,L)
12 A(K,L)=(A(K,L)-S)/A(K,K)
    RETURN
    END
```

COMPUTER PROGRAM II

Fortran-77 Program Guide for the Decoupled Tensor EFIE

This program is used to calculate the induced electric field distribution in a finite, dielectric, magnetic and lossy body exposed to an incident electric field.

Description of key variables and arrays for using the program:

Variable or Array Name	Description
NT	no. of cells in first octant of a symmetric body, integer variable
DL	length of a side of each cubic cell, in (m), real variable
X(L,I)	L coordinate of the center of the I-th cell, in (m), L=1,2,3=x,y,z coordinate, real array
NS(I,K)	surface index, which is actually the sign of the normal vector of the K-th face of the I-th cell, NS is 1, or -1 if the face is on the outmost surface, otherwise NS is 0. K=1,2,...,6 where K=1,2,3 stand for the outward normal vectors pointing to +x,+y,+z directions, and K=4,5,6 for -x,-y,-z directions, integer array
SIG	conductivity, in (S/m), real variable
EPR	relative permittivity, real variable
MUR	relative permeability, complex variable
INCI	symmetry of incident electric field, INCI is 1 or 2. 1 stands for antisymmetric and 2 for symmetric, integer variable
FREQ	frequency of the incident electric field, in (MHz), real variable

Input data file structure:(free formats are used for all the variables)

Line No.	Variable Name
1	NT,DL,SIG,EPR,MUR
2	(X(L,1),L=1,3), (NS(1,K),K=1,6)
3	(X(L,2),L=1,3), (NS(2,K),K=1,6)
.....
NT+1	(X(L,NT),L=1,3), (NS(NT,K),K=1,6)
NT+2	INCI, FREQ
The following data are for the symmetry of geometry and electric field distributions and should remain at the end of this data file.	
NT+3	1 1 1
NT+4	-1 1 1
NT+5	-1 -1 1
NT+6	1 -1 1
NT+7	1 1 -1
NT+8	-1 1 -1
NT+9	-1 -1 -1
NT+10	1 -1 -1
NT+11	1 1 1 1 -1 -1 -1 -1
NT+12	1 -1 1 -1 -1 1 -1 1
NT+13	1 -1 -1 1 1 -1 -1 1
NT+14	1 1 1 1 1 1 1 1
NT+15	1 -1 1 -1 1 -1 1 -1
NT+16	1 -1 -1 1 -1 1 1 -1

Output data file structure:

There will be 5 numbers in each line. The first one is an integer and indicates the numbering of the cell. The 2nd and 3rd numbers stand for the phasor (real and imaginary parts) of electric field of each cell. The 4th and 5th numbers stand for the amplitude (in V/m) and phase angle (in degree) of electric field. Three components of electric field are all printed out.

The program listing is attached from the next page.

```

C *****
C Decoupled Tensor EFIE
C *****
C This program is used to calculate the induced E field distribution in a
C finite, dielectric, magnetic and lossy body exposed to an incident field
C *****
PROGRAM DECOPULEEFIE
PARAMETER (NTMAX=343,NTMAX3=1029,NTMAX31=1030
$,NTMAX8=2744,NTMAX83=8232)
REAL X(3,NTMAX8)
COMPLEX A(2,3,NTMAX83),D(NTMAX3,NTMAX31)
INTEGER NS(NTMAX8,6)
C *****
C Input data:
C *****
C NT=No. of cells in first octant of a symmetric body, integer
C DL=length of a side of each cubic cell, in (m)
C X(L,I)=L coordinate of the center of the i-th cell, in (m),
C L=1,2,3=x,y,z coordinate
C SIG=conductivity, in (S/m)
C EPR=relative permittivity, a real number
C MUR=relative permeability, a complex number
C NS(I,K)=surface index, which is actually the
C sign of the normal vector of the K-th face of the I-th cell,
C NS is 1 or -1 if the face is on the outmost surface,
C otherwise NS is 0. K=1,2,...,6 where K=1,2,3 stand for the outward
C normal point to +x,+y,+z directions, and K=4,5,6 for the -x,-y,-z
C directions
C *****
open (1,file='efiein.dat')
read (1,*) NT,DL,SIG,EPR,MUR
do 391 i=1,nt
read (1,*) X(1,I),X(2,I),X(2,I),
$,NS(I,1),NS(I,2),NS(I,3),NS(I,4),NS(I,5),NS(I,6)
C *****
NT3=3*NT
NT8=8*NT
NT83=24*NT
NT31=NT3+1
CALL EFIE(SIG,EPR,MUR,X,A,D,NS,NT,NT3,NT31,NT8,NT83)
STOP
END

SUBROUTINE EFIE(SIG,EPR,MUR,X,A,D,NS,NT,NT3,NT31
$,NT8,NT83)
REAL MU0,K0,XJV(8,3),XJS(4,3,6),X(3,NT8),XC(3),X1(3)
COMPLEX A(3,NT83),D(NT3,NT31),GD(3,3)
$,JC,EPS,MUR,MU,CON1,CON2,SUMV,SUMS,DT
INTEGER P,Q,NS(NT8,6),IS(2,3,8),IQ(3,8)
COMMON /A/JC,K0,PI,EP0,EP,EPS,MU0,MU,CON1,CON2
$/F/DL,HDL,QDL,DS,DV
OPEN (4,FILE='efieout.dat')
NT2=2*NT
C *****
C Input data:
C *****
C INCI=smetricity of incident E field, INCI is 1 or 2
C 1 stands for antisymmetric and 2 for symmetric
C FREQ=frequency of the incident EM field, in (MHz)
C *****
READ (1,*) INCI,FREQ
C *****
C Output Format:
C *****
WRITE (4,*) 'DECOUPLED EFIE'
IF (INCI.EQ.1) WRITE (4,*) 'INCI = x j*sinkz'

```

```

IF (INCI.EQ.2) WRITE (4,*) 'INCI = x coskz'
WRITE(4,*) 'DL =' ,DL
WRITE(4,*) 'FREQ =' ,FREQ
WRITE(4,*) 'SIG =' ,SIG
WRITE(4,*) 'EPR =' ,EPR
WRITE(4,*) 'MUR =' ,MUR
c*****
c IQ(L,J)=sign of L coordinate of center of each cell in J-th octant,
c IQ is 1 or -1
c IS(INCI,L,J)=sign of L component of E field distribution in J-th octant,
c ISE is 1 or -1, INCI is 1 or 2
c*****
DO 31 J=1,8
31 READ (1,*) (IQ(I,J),I=1,3)
DO 32 I=1,3
32 READ (1,*) (IS(1,I,J),J=1,8)
DO 33 I=1,3
33 READ (1,*) (IS(2,I,J),J=1,8)
c*****
JC=(0.,1.)
PI=ATAN(1.)*4.
WG=2.E6*PI*FREQ
K0=WG/3.E8
EP0=1.E-9/36./PI
MU0=4.E-7*PI
MU=MUR*MU0
EP=EPR*EP0
EPS=EP+JC*SIG/WG
CON1=-K0**3*(EPS/EP0-MU0/MU)/4./PI
CON2=K0**2*(MU-MU0)/MU/4./PI
PRINT *,JC,PI,WG,K0,EP0,MU0,EP,MU,EPS,CON1,CON2
DS=DL*DL
DV=DS*DL
HDL=DL/2.
QDL=DL/4.
c*****
c Calculate the corresponding coordinates and the surface indecies
c from the 2nd to 8th octants
c*****
DO 15 I=1,NT
DO 15 M=2,8
DO 15 L=1,3
15 X(L,I+(M-1)*NT)=X(L,I)*IQ(L,M)
DO 16 I=1,NT
DO 16 M=2,8
DO 16 L=1,3
IF (IQ(L,M).GE.0) THEN
NS(I+(M-1)*NT,L)=NS(I,L)*IQ(L,M)
NS(I+(M-1)*NT,L+3)=NS(I,L+3)*IQ(L,M)
ELSEIF (IQ(L,M).LT.0) THEN
NS(I+(M-1)*NT,L)=NS(I,L+3)*IQ(L,M)
NS(I+(M-1)*NT,L+3)=NS(I,L)*IQ(L,M)
ENDIF
16 CONTINUE
CALL SELF(GD)
c*****
c Filling matrix elements
c*****
DO 18 I=1,NT
PRINT *,I
DO 79 L=1,3
79 XC(L)=X(L,I)
DO 17 J=1,NT8
DO 78 L=1,3
78 X1(L)=X(L,J)
DO 17 Q=1,3

```

```

LL=J+(Q-1)*NT8
DO 17 P=1,3
IF (I.EQ.J) THEN
CALL SPT(X1,XJS,HDL,QDL)
CALL SINTE(XC,J,XJS,P,Q,SUMS,NT8,NS)
A(P,LL)=GD(P,Q)+CON2*SUMS
ELSEIF (I.NE.J) THEN
CALL VPT(X1,XJV,QDL)
CALL VINTE(XC,XJV,P,Q,SUMV)
CALL SPT(X1,XJS,HDL,QDL)
CALL SINTE(XC,J,XJS,P,Q,SUMS,NT8,NS)
A(P,LL)=CON1*SUMV+CON2*SUMS
ENDIF
17 CONTINUE
c*****
c Using symmetric properties to reduce matrix size
c*****
DO 41 K=1,NT
DO 41 P=1,3
DO 41 Q=1,3
DT=(0.,0.)
DO 42 M=1,8
42 DT=A(P,(Q-1)*NT8+K+(M-1)*NT)*IS(INCI,Q,M)+DT
41 D(I+(P-1)*NT,K+(Q-1)*NT)=DT
18 CONTINUE
c*****
c Filling the vector of incident E field in the center of each cell
c*****
DO 35 I=1,NT
B=K0*X(3,I)
IF (INCI.EQ.1) THEN
C=SIN(B)
D(I,NT31)=DCMPLX(0.,C)
ELSEIF (INCI.EQ.2) THEN
C=COS(B)
D(I,NT31)=DCMPLX(C,0.)
ENDIF
35 D(I+NT2,NT31)=(0.,0.)
c*****
c Solving the matrix equation
c*****
CALL CMATPA(-1,D,NT3,1,DET,1.E-38,NT31)
c*****
c Print out the induced EM fields at the center of each cell
c*****
c FABS=Magnitude of the E fields, in (V/m)
c PHASE=Phase angle of the E fields, in degree
c*****
DO 36 K=1,3
IF (K.EQ.1) WRITE (4,*) 'EX'
IF (K.EQ.2) WRITE (4,*) 'EY'
IF (K.EQ.3) WRITE (4,*) 'EZ'
DO 36 I=1,NT
I1=I+NT*(K-1)
EABS=CABS(D(I1,NT31))
PHASE=ATAN2(AIMAG(D(I1,NT31)),REAL(D(I1,NT31)))*180/PI
36 WRITE (4,150) I,D(I1,NT31),EABS,PHASE
150 FORMAT (1X,I4,2E20.11,3X,E15.8,F10.4)
STOP
END

c*****
c This subroutine is used to calculate the volume integration, the
c integration is approximated simply by cutting a cell into 8 subcells

```

c and summing up the function value in each subcell

```

c*****
SUBROUTINE VINTE(X,XJ,P,Q,ST)
REAL X(3),X1(3),XJ(8,3)
COMPLEX GPQ,ST
INTEGER P,Q
COMMON /F/DL,HDL,QDL,DS,DV
ST=(0.,0.)
DO 30 J=1,8
DO 46 L=1,3
46 X1(L)=XJ(J,L)
30 ST=ST+GPQ(P,Q,X,X1)
ST=ST*DV/8.
RETURN
END

```

c*****
c This subroutine is used to calculate the surface integration, the
c integration is approximated simply by cutting a surface into 4 pieces
c and summing up the function value in each piece
c*****

```

SUBROUTINE SINTE(X,M,XJ,P,Q,STT,NT8,NS)
REAL X(3),X1(3),XJ(4,3,6)
COMPLEX GP,ST,STT
INTEGER P,Q,NS(NT8,6)
COMMON /F/DL,HDL,QDL,DS,DV
STT=(0.,0.)
IF (P.EQ.Q) GO TO 39
DO 31 K=P,P+3,3
IF (NS(M,K).EQ.0) GO TO 31
ST=(0.,0.)
DO 30 J=1,4
DO 46 L=1,3
46 X1(L)=XJ(J,L,K)
30 ST=ST+GP(Q,X,X1)
STT=-ST*NS(M,K)+STT
31 CONTINUE
GO TO 99
39 IF (P.EQ.1) THEN
IP1=2
IP2=3
ELSEIF (P.EQ.2) THEN
IP1=1
IP2=3
ELSEIF (P.EQ.3) THEN
IP1=1
IP2=2
ENDIF
DO 41 K=IP1,IP1+3,3
IF (NS(M,K).EQ.0) GO TO 41
ST=(0.,0.)
DO 40 J=1,4
DO 56 L=1,3
56 X1(L)=XJ(J,L,K)
40 ST=ST+GP(IP1,X,X1)
STT=ST*NS(M,K)+STT
41 CONTINUE
DO 51 K=IP2,IP2+3,3
IF (NS(M,K).EQ.0) GO TO 51
ST=(0.,0.)
DO 50 J=1,4
DO 66 L=1,3
66 X1(L)=XJ(J,L,K)
50 ST=ST+GP(IP2,X,X1)
STT=ST*NS(M,K)+STT

```

```

51 CONTINUE
99 STT=STT*DS/4.
   RETURN
   END

```

```

c*****
c This subroutine is used to calculate the volume integrations involved
c with the singularity problem
c*****

```

```

SUBROUTINE SELF(GD)
COMPLEX DT,GNN,GD(3,3)
INTEGER P,Q
COMMON /F/DL,HDL,QDL,DS,DV
DO 81 P=1,3
DO 81 Q=1,3
IF (P.EQ.Q) THEN
DT=GNN(DL)
ELSEIF (P.NE.Q) THEN
DT=(0.,0.)
ENDIF
GD(P,Q)=DT
81 CONTINUE
RETURN
END

```

```

c*****
c This function subroutine is used to evaluate the 2nd derivative of the
c free space Green's function at center of each cell
c*****

```

```

FUNCTION GPQ(P,Q,X,X1)
REAL K0,MU0,X(3),X1(3),XD(3)
COMPLEX JC,EPS,MU,CON1,CON2,GPQ,B,C,D
INTEGER P,Q
COMMON /A/JC,K0,PI,EP0,EP,EPS,MU0,MU,CON1,CON2
DO 75 L=1,3
XD(L)=X(L)-X1(L)
IF (ABS(XD(L)).LT.1.E-8) XD(L)=0.
75 CONTINUE
R=SQRT(XD(1)*XD(1)+XD(2)*XD(2)+XD(3)*XD(3))
A=K0*R
D=CEXP(JC*A)
C=(3.-A*A-3.*JC*A)*XD(P)*XD(Q)/R/R
IF (P.NE.Q) THEN
GPQ=C*D/A/A/A
ELSEIF (P.EQ.Q) THEN
B=A*A-1.+JC*A
GPQ=(B+C)*D/A/A/A
ENDIF
RETURN
END

```

```

c*****
c This function subroutine is used to evaluate the 1st derivative of the
c free space Green's function at center of each cell
c*****

```

```

FUNCTION GP(P,X,X1)
REAL K0,MU0,X(3),X1(3),XD(3)
COMPLEX JC,EPS,MU,CON1,CON2,GP,C,D
INTEGER P
COMMON /A/JC,K0,PI,EP0,EP,EPS,MU0,MU,CON1,CON2
DO 75 L=1,3
XD(L)=X(L)-X1(L)
IF (ABS(XD(L)).LT.1.E-8) XD(L)=0.

```

```

75  CONTINUE
    R=SQRT(XD(1)*XD(1)+XD(2)*XD(2)+XD(3)*XD(3))
    A=K0*R
    D=CEXP(JC*A)
    C=(JC*A-1.)*XD(P)/R
    GP=C*D/A/A
    RETURN
    END

```

```

c*****
c  This function subroutine is used to calculate the value of the diagonal
c  element of the matrix, this value includes a principal integration plus
c  a correction term
c*****

```

```

FUNCTION GNN(DL)
REAL K0,MU0
COMPLEX JC, EPS, MU, CON1, CON2, GNN, GC, GB
COMMON /A/JC, K0, PI, EP0, EP, EPS, MU0, MU, CON1, CON2
DV=DL**3
AN=(3.*DV/4./PI)**(1./3.)
GC=2.*MU0/3./MU+EPS/3./EP0
GB=CON1*4.*PI*2.*(CEXP(JC*K0*AN)*(1.-JC*K0*AN)-1.)/(3.*K0**3)
GNN=GC+GB
RETURN
END

```

```

c*****
c  This subroutine is used to calculate the coordinates of 8 subcells
c  of each cell in order to perform the numerical integration
c*****

```

```

SUBROUTINE VPT(B, BN, QRDL)
REAL QRDL, B(3), BN(8, 3)
BN(1, 1)=B(1)+QRDL
BN(1, 2)=B(2)+QRDL
BN(1, 3)=B(3)+QRDL
BN(2, 1)=B(1)+QRDL
BN(2, 2)=B(2)+QRDL
BN(2, 3)=B(3)-QRDL
BN(3, 1)=B(1)+QRDL
BN(3, 2)=B(2)-QRDL
BN(3, 3)=B(3)+QRDL
BN(4, 1)=B(1)+QRDL
BN(4, 2)=B(2)-QRDL
BN(4, 3)=B(3)-QRDL
BN(5, 1)=B(1)-QRDL
BN(5, 2)=B(2)+QRDL
BN(5, 3)=B(3)+QRDL
BN(6, 1)=B(1)-QRDL
BN(6, 2)=B(2)+QRDL
BN(6, 3)=B(3)-QRDL
BN(7, 1)=B(1)-QRDL
BN(7, 2)=B(2)-QRDL
BN(7, 3)=B(3)+QRDL
BN(8, 1)=B(1)-QRDL
BN(8, 2)=B(2)-QRDL
BN(8, 3)=B(3)-QRDL
RETURN
END

```

```

c*****
c  This subroutine is used to calculate the coordinates of 4 pieces of
c  6 surfaces on a cell in order to perform the numerical integration
c*****

```

```

SUBROUTINE SPT(B,BS,HFDL,QRDL)
REAL QRDL,HFDL,B(3),BS(4,3,6),X(3,5)
DO 20 L=1,3
X(L,1)=B(L)-HFDL
X(L,2)=B(L)-QRDL
X(L,3)=B(L)
X(L,4)=B(L)+QRDL
X(L,5)=B(L)+HFDL
20 BS(1,1,1)=X(1,5)
BS(2,1,1)=X(1,5)
BS(3,1,1)=X(1,5)
BS(4,1,1)=X(1,5)
BS(1,2,1)=X(2,2)
BS(2,2,1)=X(2,2)
BS(3,2,1)=X(2,4)
BS(4,2,1)=X(2,4)
BS(1,3,1)=X(3,2)
BS(2,3,1)=X(3,4)
BS(3,3,1)=X(3,4)
BS(4,3,1)=X(3,2)

BS(1,1,4)=X(1,1)
BS(2,1,4)=X(1,1)
BS(3,1,4)=X(1,1)
BS(4,1,4)=X(1,1)
BS(1,2,4)=X(2,2)
BS(2,2,4)=X(2,2)
BS(3,2,4)=X(2,4)
BS(4,2,4)=X(2,4)
BS(1,3,4)=X(3,2)
BS(2,3,4)=X(3,4)
BS(3,3,4)=X(3,4)
BS(4,3,4)=X(3,2)

BS(1,1,2)=X(1,4)
BS(2,1,2)=X(1,4)
BS(3,1,2)=X(1,2)
BS(4,1,2)=X(1,2)
BS(1,2,2)=X(2,5)
BS(2,2,2)=X(2,5)
BS(3,2,2)=X(2,5)
BS(4,2,2)=X(2,5)
BS(1,3,2)=X(3,2)
BS(2,3,2)=X(3,4)
BS(3,3,2)=X(3,4)
BS(4,3,2)=X(3,2)

BS(1,1,5)=X(1,4)
BS(2,1,5)=X(1,4)
BS(3,1,5)=X(1,2)
BS(4,1,5)=X(1,2)
BS(1,2,5)=X(2,1)
BS(2,2,5)=X(2,1)
BS(3,2,5)=X(2,1)
BS(4,2,5)=X(2,1)
BS(1,3,5)=X(3,2)
BS(2,3,5)=X(3,4)
BS(3,3,5)=X(3,4)
BS(4,3,5)=X(3,2)

BS(1,1,3)=X(1,4)
BS(2,1,3)=X(1,4)
BS(3,1,3)=X(1,2)
BS(4,1,3)=X(1,2)
BS(1,2,3)=X(2,4)
BS(2,2,3)=X(2,2)

```

```

BS(3,2,3)=X(2,2)
BS(4,2,3)=X(2,4)
BS(1,3,3)=X(3,5)
BS(2,3,3)=X(3,5)
BS(3,3,3)=X(3,5)
BS(4,3,3)=X(3,5)

```

```

BS(1,1,6)=X(1,4)
BS(2,1,6)=X(1,4)
BS(3,1,6)=X(1,2)
BS(4,1,6)=X(1,2)
BS(1,2,6)=X(2,4)
BS(2,2,6)=X(2,2)
BS(3,2,6)=X(2,2)
BS(4,2,6)=X(2,4)
BS(1,3,6)=X(3,1)
BS(2,3,6)=X(3,1)
BS(3,3,6)=X(3,1)
BS(4,3,6)=X(3,1)
RETURN
END

```

```

c*****
c This subroutine is used to solve the matrix equation via Gaussian
c ellimination
c*****
SUBROUTINE CMATPA(IJOB,A,N,M,DET,EP,N031)
  COMPLEX A,B,DET,CONST,S
  DIMENSION A(N,N031)
30 FORMAT(1X,42HTHE DETERMINANT OF THE SYSTEM EQUALS ZERO./
11X,36HTHE PROGRAM CANNOT HANDLE THIS CASE.//)
  DET=1.
  NP1=N+1
  NPM=N+M
  NM1=N-1
  IF(IJOB) 2,1,2
1 DO 3 I=1,N
  NPI=N+I
  A(I,NPI)=1.
  IP1=I+1
  DO 3 J=IP1,N
  NPJ=N+J
  A(I,NPJ)=0.
3 A(J,NPI)=0.
2 DO 4 J=1,NM1
  C=CABS(A(J,J))
  JP1=J+1
  DO 5 I=JP1,N
  D=CABS(A(I,J))
  IF(C-D) 6,5,5
6 DET=-DET
  DO 7 K=J,NPM
  B=A(I,K)
  A(I,K)=A(J,K)
7 A(J,K)=B
  C=D
5 CONTINUE
  IF(CABS(A(J,J))-EP) 14,15,15
15 DO 4 I=JP1,N
  CONST=A(I,J)/A(J,J)
  DO 4 K=JP1,NPM
4 A(I,K)=A(I,K)-CONST*A(J,K)
  IF(CABS(A(N,N))-EP) 14,18,18
14 DET=0.
  IF(IJOB) 16,16,17

```

```
16 PRINT 30
17 RETURN
C 18 DO 11 I=1,N
C 11 DET=DET*A(I,I)
19 IF(IJOB) 10,10,17
10 DO 12 I=1,N
    K=N-I+1
    KP1=K+1
    DO 12 L=NP1,NPM
        S=0.
        IF(N-KP1) 12,19,19
19 DO 13 J=KP1,N
13 S=S+A(K,J)*A(J,L)
12 A(K,L)=(A(K,L)-S)/A(K,K)
    RETURN
END
```

BIBLIOGRAPHY

BIBLIOGRAPHY

1. D. E. Livesay and K. M. Chen, "Electromagnetic fields induced inside arbitrarily shaped biological bodies," *IEEE Trans. on Microwave Theory and Techiques*, vol. MTT-22, pp. 1273-1280, December 1974.
2. J. Van Bladel, "Some remarks on Green's dyadic for infinite space," *IRE Trans. on Antennas and Propagation*, vol. AP-9, pp. 563-566, November 1961.
3. K. M. Chen, Interaction of electromagnetic fields with biological bodies, Chapter 13, *Research Topics in Electromagnetic Wave Theory*, edited by J. A. Kong, pp. 290-374, John Wiley and Sons, NY 1981.
4. C. T. Tai, *Dyadic Green's Functions in Electromagnetic Theory*, International Textbook Company, Scraton, PA 1971.
5. H. Massoudi, C. H. Durney and M. F. Iskander, "Limitations of the cubical block model of man in calculating SAR distributions," *IEEE Trans. on Microwave Theory and Techniques*, vol. MTT-32, pp. 746-752, August 1984.
6. K. M. Chen, S. Rukspollmuang and D. P. Nyquist, "Measurement of induced electric fields in a phantom model of man," *Radio Science*, vol. 17, pp. 49S-59S, September-October 1982.
7. O. P. Gandhi, J. F. DeFord and H. Kanai, "Impedance method for calculation of power deposition patterns in magnetically induced hyperthermia," *IEEE Trans. on Biomedical Engineering*, vol. BME-31, October 1984.
8. D. W. Armitage, H. H. LeVeen and R. Pethig, "Radiofrequency-induced hyperthermia: computer simulation of specific absorption rate distributions using realistic anatomical models," *Phys. Med. Biol.*, vol. 28, No. 1, pp. 31-42, 1983.
9. K. M. Chen, "A simple physical picture of tensor Green's function in source region," *Proceedings of the IEEE*, pp. 1202-1204, August 1977.
10. R. F. Harrington, *Time-Harmonic Electromagnetic Fields*, McGraw-Hill, NY 1961.

11. B. S. Guru, "A Experimental and Theoretical Study on the Interaction of Electromagnetic Fields with Arbitrarily Shaped Biological Bodies," Ph. D. Dissertation, Michigan State University, East Lansing, MI 1976.
12. D. E. Livesay, "Electromagnetic Fields Induced in and Scattered by Biological Systems Exposed to Nonionizing Electromagnetic Radiation," Ph. D. Dissertation, Michigan State University, East Lansing, MI 1975.
13. C. T. Tai, "A note on the integral equations for the scattering of a plane wave by an electromagnetically permeable body," *Electromagnetics* 5:79-88, 1985.
14. R. F. Harrington, *Field Computation by Moment Method*, McMillan, NY 1968.
15. J. Van Bladel, Dyadic analysis, Appendix 3, *Electromagnetic Fields*, McGraw-Hill, NY 1964.
16. H. Wang, Y.Q. Liang and K.M. Chen, "Quantification of induced EM fields in finite heterogeneous bodies," *1985 North American Radio Science Meeting and International IEEE/APS Symposium*, Univ. of British Columbia, Vancouver, Canada, June 1985.
17. D. T. Paris, W. M. Leach, Jr. and E. B. Joy, "Basic theory of probe-compensated near-field measurements," *IEEE Trans. on Antennas and Propagation*, vol. AP-26, pp. 373-379, May 1978.
18. I. Chatterjee, O. P. Gandhi, M. J. Hagmann and A. Riazi, "Plane wave spectrum approach for the calculation of electromagnetic absorption under near-field exposure conditions," *Bioelectromagnetics* 1:363-377, 1980.
19. R. E. Collin, *Field Theory of Guided Waves*, McGraw-Hill, NY 1960.
20. K.M. Chen, D. Misra, H. Wang, H.R. Chuang and E. Postow, "An X-band microwave life-detection system," *IEEE Trans. on Biomedical Engineering*, vol. BME-33, pp. 697-701, July 1986.
21. D. Misra, "Scattering of Electromagnetic Wave by Human Body and its Application," Ph. D. Dissertation, Michigan State University, East Lansing, MI 1984.

22. A. Papoulis, *The Fourier Integral and Its Applications*, McGraw-Hill, NY 1962.
23. W. D. Stanley, G. R. Dougherty, R. Dougherty, *Digital Signal Processing*, Reston, Virginia Prentice-Hall, 1984.
24. E. O. Brigham, *The Fast Fourier Transform*, Englewood Cliffs, New Jersey Prentice-Hall, 1974.
25. K. M. Chen and D. Misra, "Microwave Life-Detection Systems," Final Report to Naval Medical Research and Development Command, Contract N00014-82-C-0355, Division of Engineering Research, Michigan State University, East Lansing, MI, November 1986.
26. D. H. Schaubert, D. R. Wilton, and A. W. Glisson, "A tetrahedral modeling method for electromagnetic scattering by arbitrarily shaped inhomogeneous dielectric boies," *IEEE Trans. on Antennas and Propagation*, vol. AP-32, pp. 77-85, January 1984.
27. C. T. Tsai, H. Massoudi, C. H. Durney, and M. F. Iskander, "A procedure for calculation fields inside arbitrarily shaped, inhomogeneous dielectric bodies using linear basis functions with the moment method", *IEEE Trans. on Microwave Theory and Techniques*, vol. MTT-34, November 1986.